Cape Peninsula University of Technology

SCALE-UP DEVELOPMENT FOR THE SYNTHESIS OF COAL FLY ASH BASED ZEOLITE BETA AND ZSM-5 USING A CONTROLLED BENCH PRESSURE REACTOR

by

Nkululeko Zenzele Neville Ndlovu

This thesis is submitted in fulfilment of the requirements for the degree

Doctor of Engineering: Chemical Engineering

in the

Faculty of Engineering and Built Environment

at the

Cape Peninsula University of Technology

Supervisor: Prof TV Ojumu

Co-supervisor: Prof LF Petrik

Bellville

February 2023

DECLARATION

I, Nkululeko Zenzele Neville Ndlovu, declare that the contents of this thesis represent my own unaided work, and that the thesis has not previously been submitted for academic examination towards any qualification. Furthermore, it represents my own opinions and not necessarily those of the Cape Peninsula University of Technology.

09 February 2023

Signed **Date**

ABSTRACT

Coal fly ash (CFA) is the major industrial waste material produced during the combustion of coal to generate electricity. Poor management of this waste causes serious environmental and health problems globally, including contamination of surface and ground waters, air pollution, degradation of land and quality of life of aquatic species, and several diseases to humans. In South Africa, approximately 40 million tons of CFA is produced annually, while only 5.5% is reused in cement and concrete production at a commercial scale, and the rest is disposed of in holding ponds, lagoons, and landfills. The disposal of CFA not only requires a large area of valuable land but is also a major source of environmental pollution. Therefore, more research on the use and recycling of CFA is required to alleviate the environmental burden caused by its disposal. Due to its high Si and Al content, CFA has been used as an inexpensive feedstock in the synthesis of zeolites. Although the synthesis of CFA-based zeolites using various synthesis techniques is well researched, these techniques were limited to laboratory scale. The synthesis of high-silica zeolites such as ZSM-5 from CFA requires the addition of alumino-silicate sources or treatment with a chelating agent to adjust the Si/Al ratio prior to the hydrothermal synthesis. This process leads to a synthesis of low-quality zeolites. The synthesis of high-quality high-silica zeolites requires the extraction of silica followed by treatment with a chelating agent such as oxalic acid. The introduction of an additional chelating agent during the conversion of CFA into zeolites may not be economically and environmentally sustainable. In addition, these processes generate a huge amount of secondary solid and liquid waste, which needs further treatment and disposal, the volume of which may be prohibitive if large-scale synthesis is desired.

This study aimed to synthesise pure phase high-silica zeolite ZSM-5 from CFA silica extract without treatment with oxalic acid or the addition of external aluminium or silicate sources and to use the resultant solid waste in the synthesis of sodalite zeolite, with the view to minimise or completely eliminate the solid waste generated in the process. This aim was achieved by applying a three-step alkaline leaching process, which was comprised of (i) removal of the magnetic fraction at room temperature; (ii) alkaline extraction of silica from CFA (150˚C for 24 h); and (iii) treatment of the silica extract with oxalic acid or water (80˚C for 6 h). The solid residue from the alkaline extraction of silica was transformed into sodalite zeolite. The silica extracts treated with either oxalic acid or water were used as feedstocks in the preliminary synthesis of ZSM-5 zeolite (160˚C for 72 h). The results showed for the first time that a pure phase ZSM-5 zeolite can be synthesised from the water-treated silica extract without the need for the oxalic acid pre-treatment step. The optimum molar composition of 1 Si: 0.003 Al :0.612 Na: 0.190 TPABr: 95.766 H_2O (water-treated silica extract) was used as a basis for further optimisation studies, which investigated the effect of NaOH, TPABr, water content,

hydrothermal synthesis time and temperature on the morphology and crystal size of ZSM-5 zeolite. The variation in concentration of NaOH and water content had a significant impact on the morphology, crystallinity, and crystal size of ZSM-5 zeolite. It was also shown that TPABr within the range $0.3 \leq 0.15 \leq 0.075$ g resulted in the incomplete conversion of the amorphous material during the hydrothermal synthesis and led to impure ZSM-5 zeolite. Furthermore, the study showed for the first time that the previously recorded ZSM-5 hydrothermal synthesis time of 72 h can be reduced to 3 h. This shorter processing time would have significant implications on the economics of the production of CFA-based ZSM-5 zeolites. Recycling protocols to manage the liquid waste generated during the silica extraction treatment step were also explored in this study. It was shown that the liquid waste can be recycled up to four times without compromising the quality of the ZSM-5 products. However, after each treatment cycle, an increase in concentration of Na was observed in the resultant silica extract. This indicated that the resultant liquid waste was highly saturated with Na salts, and that recycling beyond the fourth treatment cycle could compromise the quality of the silica extracts.

A technology economic analysis (TEA) of the synthesis of sodalite and ZSM-5 zeolites from the same CFA batch was also conducted in order to predict their cost of production at a larger scale. The results showed for the first time that the synthesis of ZSM-5 zeolite from CFA-based silica extract was economically viable, with a net present value of approximately R300 M, and a payback period of five years over a 20-year period. This study provides a holistic approach and strategy to using CFA to synthesise sodalite and pure ZSM-5 zeolite with limited to zero solid waste, which in addition to addressing the environmental problems associated with its disposal, presents CFA as a useful resource that can be commercialised.

KEYWORDS: Coal fly ash, silica extract, alkaline leaching, sodalite, ZSM-5 zeolite, recycling, liquid waste, technology economic analysis, cash-flow, sensitivity analysis

ACKNOWLEDGEMENTS

Firstly, I would like to acknowledge the Lord God in His supremacy for affording me the strength, inspiration, and ability to carry out this study, and for His indescribable love and provision throughout this journey. May all the glory and praises be unto Him.

My sincere gratitude to my supervisors, Prof TV Ojumu and Prof LF Petrik, for giving me the opportunity to accomplish my doctoral studies under their supervision. Thank you for believing in me when I doubted myself, for your continuous support, advice, mentorship, patience, guidance, and insight throughout the duration of the project. Thanks for the opportunities you provided to present my work at the national and international level. Thank you for always being available and responsive to all my academic requests. You have made this difficult journey interesting and easy to navigate. Your excellent supervision has contributed enormously to my academic career, and I will forever be grateful.

Dr. Emmanuel Alechine Ameh for his assistance in the lab, for sharing ideas on data acquisition and analysis. Thank you for always being available to assist me whenever I needed assistance, for always being positive, and for your motivation and advice. Thank you very much, Emmy.

Dr Roland Missengue for taking the time to review some of my chapters and sharing ideas on how I can always improve my work; your sacrifices and contributions are highly appreciated.

Dr Miranda Waldron from the Physics Department at UCT for her assistance with SEM analysis.

Mr Remy Bucher from iThemba labs for his assistance with XRD analysis.

Dr Ebrahim Mohiuddin for his assistance with BET and TPD analysis.

Mrs. Ilse Wells from the Environmental and Nanoscience Research Group, Chemistry Department at UWC for her assistance with ICP analysis.

Thank you to Mrs. Hannelene Small for completing my lab orders and guiding me through the laboratories in the new Chemical engineering building. Thank you for fighting for us Hannelene and for making sure we always received our orders on time. Your passion for the work you do is out of this world!

I would also like to thank my colleagues at the Environmental and Nanoscience Department (UWC) and Chemical Engineering Department (CPUT) for their encouragement and support throughout this journey.

To my friends, Dr Sandile Jongile, Dr Chinwe Juliana Iwu-Jaja, Ms Vuyokazi Mmama, Ms Nokubonga Khanyile: this would have been a much more challenging task without you. Thank you for your unwavering support, for sharing your experiences and for holding me accountable. You have made this journey much more bearable.

To my mentors, Dr Michelle Mulder, Dr Ana Casanueva and Dr Janine Chantson, your drive and passion for the work you do encouraged me to always give my best. Thank you for not giving up on me, for reminding me that "*hard work pays*", for your patience and giving me time out to do my experiments when I needed to.

To my partner, Mr. Tshepo Goodwill Mokoena, thank you for believing in me and for supporting my dreams, for driving me to the lab in the early hours of the morning when I needed to monitor my experiments. Thank you for your understanding, unwavering support, encouragement and for reminding me that "little *progress is still progress".*

To my mother, Mrs Delsy Wistance Ndlovu, and my brothers (Dr Rolihlahla Ndlovu and Dr Xolani Ndlovu); this journey would not have been possible without your prayers, support, sacrifices and encouragement.

The financial assistance of the National Research Foundation towards this research is acknowledged. Opinions expressed in this thesis and the conclusions arrived at are those of the author and are not necessarily to be attributed to the National Research Foundation.

DEDICATION

I would like to dedicate this thesis to my family for their encouragement, love and endless support throughout this journey.

Delsy Wistence Ndlovu
Rolihlahla Nandipha Ndlovu
Xolani Kyalami Munene Ndlovu

My gorgeous daughter, Masego Khanya Mokoena

And finally, but not least, my loving partner, Tshepo Goodwill Mokoena

TABLE OF CONTENTS

DECLARATION ii
ABSTRACT iii
ACKNOWLEDGEMENTS v
DEDICATION vi
TABLE OF CONTENTS viii
GLOSSARY xviii
Research outputs xx
CHAPTER 1 1
1.1 Introduction 1
1.2 Background 1
1.3. Problem statement 3
1.4. Motivation of the study 4
1.5. Hypothesis 4
1.6. Aims and objectives 4
1.7 Research questions 5
1.8. Research approach 5
1.9. Scope and delimitations of the study 6
1.10. Thesis structure 6
CHAPTER 2 8
LITERATURE REVIEW 8
2.1 Introduction. 8
2.2 Coal fly ash. 8
2.2.1. Physical appearance of CFA. 8
2.2.2. Chemical composition of CFA. 9
2.2.3 Environmental impact of CFA. 9
2.2.4 Application of CFA. 10
2.2.4.1. Extraction of Iron from CFA 11
2.2.4.2. Extraction of Si from CFA 11
2.3 Zeolite history and formation 12
2.3.1. Classification 14
2.3.2. Properties and applications of zeolites 15
2.3.2.1. Ion-exchange 15
2.3.2.2. Porosity 15
2.3.2.3. Thermal stability 16

2.3.2.4. Acidity 16
2.4 Synthesis of CFA-based zeolites 17
2.4.1 Activation of CFA. 18
2.4.1.1 Fusion assisted method 18
2.4.1.2 Ultrasonic treatment method 20
2.4.1.3 Direct activation method 21
2.4.1.4. Microwave-assisted method 22
2.4.2 Pre-synthesis stage 23
2.4.3 Hydrothermal synthesis of zeolites 23
2.4.3.1. Effect of Si/Al ratio 23
2.4.3.2. Effect of the amount of NaOH 24
2.4.3.3. Effect of water content 24
2.4.3.4. Effect of structure directing agent 25
2.4.4. Hydrothermal physical parameters 25
2.4.4.1. Effect of synthesis time 26
2.4.4.2. Effect of synthesis temperature 26
2.3.4. Recycling of liquid waste during zeolite synthesis 27
2.3.5. Synthesis of zeolite ZSM-5 and sodalite from CFA 27
2.3.5.1. ZSM-5 27
2.3.5.2. Sodalite 29
2.4. Technology economic feasibility 30
2.4.1 Capital cost estimate matrix 30
2.4.2. Capital cost estimation techniques 33
2.4.2.1. Historical cost estimate 33
2.4.2.2. Step counting method 33
2.4.2.3. Factorial methods 34
2.4.2.5. Detailed factorial estimates 35
2.5. Conclusion 35
CHAPTER 3 38
MATERIAL, EXPERIMENTAL & ANALYTICAL TECHNIQUES 38
3.1 Introduction. 38
3.2. Materials and chemicals. 40
3.2.1. Sampling and storage of raw materials. 40
3.2.2. List of Chemicals. 40
3.2.3. List of equipment 40

3.3. Methodology 41
3.3.1. Extraction of magnetic fraction (iron) and silicon from Matla CFA. 41
3.3.1.1. Extraction of iron from CFA. 41
3.3.1.2. Alkaline extract of silicon from IFCFA. 42
3.3.2. Treatment of silica extract 43
3.3.2.1. Recycle of treatment liquid waste 44
3.3.3. Synthesis of high-silica zeolite ZSM-5 from CFA silica extracts 45
3.3.4. Synthesis of zeolite ZSM-5 from CFA silica extracts treated with the recycled liquid waste 48
3.3.5. Techno-economic analysis (TEA) 48
3.4. Analytical techniques 49
3.4.1. Inductively coupled plasma atomic emission spectrometry (ICP-AES). 49
3.4.1.1. Total digestion of solid samples. 49
3.4.2. X-ray fluorescence spectroscopy (XRF) analysis 50
3.4.3. X-ray Diffraction Spectroscopy analysis. 50
3.4.4. Scanning Electron Microscopy (SEM). 51
3.4.5. Fourier Transform Infrared Spectroscopy (FTIR). 51
3.4.7. N_2 Brunauer-Emmett-Teller (BET). 51
3.4.8. Temperature programmed desorption (TPD). 52
3.5 Chapter summary 52
CHAPTER 4 54
SELECTIVE EXTRACTION AND CHARACTERISATION OF COAL FLY ASH SILICA EXTRACT. 54
4.1. Introduction 54
4.2 Characterisation of coal fly ash 55
4.3 Characterisation of magnetic fraction and iron-free solid residue. 58
4.4 Alkaline extract of silicon from iron-free coal fly ash (IFCFA) 63
4.4.1. Elemental composition of the UFSE. 63
4.4.2. Mineral phases of IFCFA, UFSE and SR as determined by XRD. 64
4.4.3. Morphological structure of IFCFA, UFSE and SR as determined by SEM. 66
4.4.4. FTIR spectra for IFCFA, UFSE and SR 66
4.5 Treatment of UFSE with oxalic acid and water 69
4.5.1 Elemental composition of major oxides in UFSE and the TFSE-x 69

4.5.2. Mineral phases of UFSE, TFSE-1.25, TFSE-1, TFSE-0.75, TFSE-0.44, TFSE-0.17 and TFSE-H_2O 72
4.5.3. Morphological structure of UFSE and the TFSE-x 74
4.5.4. FTIR spectra for TFSE-1.25, TFSE-1, TFSE-0.77, TFSE-0.44, TFSE-0.17 and TFSE-H_2O in comparison with UFSE. 76
4.6. Effect of recycled liquid waste on the Si/Al ratio of the treated silica extracts. 77
4.6.1. Elemental composition of TFSE1, TFSE2, TFSE3 and TFSE4 and the generated liquid waste TH-LW1, TH-LW2, TH-LW3 and TH-LW4. 78
4.6.2. Mineral phases of TFSE1, TFSE2, TFSE3 and TFSE4 in comparison with UFSE. 81
4.6.3. Morphological structure of TFSE1, TSFE2, TFSE3 and TFSE4 as determined by SEM. 82
4.6.4 FTIR spectra for TFSE1, TFSE2, TFSE3 and TFSE4 in comparison with UFSE ..84
4.5 Chapter summary 86
CHAPTER 5…… ……..88
5.1. Introduction 87
5.2. Preliminary synthesis of ZSM-5 zeolite using oxalic acid and H_2O treated fly ash silica extracts 88
5.3. Effect of NaOH on the synthesised ZSM-5 zeolite 92
5.4. Effect of TPABr 97
5.5. Effect of water content 101
5.6. Effect of hydrothermal synthesis time 105
5.7. Effect of hydrothermal synthesis temperature 109
5.8. Comparison of the optimum conditions for the synthesis of CFA-based ZSM-5 zeolite 113
5.9. Effect of fly ash silica extract obtained from treatment with recycled liquid waste on the synthesis of ZSM-5 zeolite 127
5.10. Chapter summary 138
CHAPTER 6 139
TECHNOLOGY ECONOMIC ANALYSIS OF ZSM-5 ZEOLITE SYNTHESISED FROM CFA-BASED SILICA EXTRACT 139
6.1. Introduction 139
6.2. Laboratory scale 140
6.2.1. Process description 140
6.2.2 Overall mass balance and product yields 142
6.3. Material cost to produce 1 kg of ZSM-5 144

6.4. Cost estimation and project evaluation at 5 000 kg per year 145
6.4.2. Capital cost estimate 146
6.4.3. Production cost estimate 148
6.4.3.1. Operating labour cost 149
6.4.4. Net Cashflow 151
6.5. Sensitivity analysis 155
6.6. Chapter summary 160
CHAPTER 7 161
CONCLUSION & RECOMMENDATIONS 161
7.1 Introduction 161
7.2 Research main findings 161
7.2.1. Alkaline extraction of silica and treatment 161
7.2.2 Optimisation of ZSM-5 zeolite synthesis from CFA-based silica extract 162
7.2.3. Process technology economic (TEA) analysis 163
7.3 Recommendation for future studies 163
APPENDICES 165
REFERENCES 166

TABLE OF FIGURES

Figure 2.1: Chemical structure of zeolite (Georgiev et al. 2009) 12
Figure 2.2: Formation of zeolite crystal nuclei in a hydrous gel. Source: (Cundy and Cox 2003) 13
Figure 2.3: Coal fly ash-based zeolite synthesis processes, adopted and modified from (Belviso 2018). Note: (1, 7) Ultrasound-assisted method, (2, 3, 4) Fusion-assisted method, (4, 5) Direct activation and (3, 6) Microwave-assisted method 18
Figure 2.4: FAM synthesis process from unseparated and separated fused CFA-NaOH solution (Musyoka et al. 2012) 19
Figure 2.5: Framework structure of ZSM-5 zeolite, adopted from Bindhu and Sugunan (1998) . 28
Figure 2.6: Framework structure of sodalite zeolite, adopted from Kazemimoghadam and Mohammadi (2011) 29
Figure 3.1: Experimental approach process flow diagram 39
Figure 3.2: Iron extraction block flow diagram. Where MFE = magnetic fraction extract process, IFCFA = iron-free coal fly ash and MF = magnetic fraction 42
Figure 3.3: Block flow diagram for alkaline extraction of silica from IFCFA, where IFCFA = iron-free coal fly ash, SR = solid residue and UFSE = untreated coal fly ash silica extract 43
Figure 3.4: Block flow diagram for the oxalic acid and water treated silica extracts. Where TFSE-x = TFSE-1.25, TFSE-1, TFSE-0.78, TFSE-0.44, TFSE-0.17 and TFSE-H_2O 44
Figure 3.5: BFD of the recycled liquid waste during the treatment of UFSE 45
Figure 3.6: BFD for the synthesis of ZSM-5 zeolite from CFA silica extract 46
Figure 4.1: Morphological analysis of South African Class F Matla CFA 56
Figure 4.2: XRD spectra for Matla coal fly ash, where Q = Quartz (SiO_2) and M = Mullite ($Al_6Si_2O_{13}$). 57
Figure 4.3: FTIR spectra for Matla CFA 58
Figure 4.4: XRD spectra for coal fly ash (CFA), magnetic fraction (MF) and iron-free coal fly ash (IFCFA): where M=Mullite, Q=Quartz and Mag=Magnetite 60
Figure 4.5: Morphological analysis for A = CFA, B = MF and C = IFCFA at 1000x magnification 61
Figure 4.6: FTIR spectra for CFA, MF and IFCFA 62
Figure 4.7: XRD patterns of CFA, IFCFA, UFSE and SR, where Q = Quartz, M = Mullite, Th = Thenardite (Na_2SO_4), S = Sodalite and N = Na_2CO_3 65
Figure 4.8: Morphological analysis for IFSA, U-CFASE and SR at 5000x magnification 66
Figure 4.9: FTIR spectra for IFCFA, UFSE and SR 67
Figure 4.10: XRD spectra for UFSE, TFSE-1.25, TFSE-1, TFSE-0.75, TFSE-0.44, TFSE-0.17 and TFSE-H_2O, where Th = Thenardite (Na_2SO_4) 73
Figure 4.11: Morphological analysis for UFSE, TFSE-1.25, TFSE-1. TFSE-0.75, TFSE-0.44, TFSE-0.17 and TFSE-H_2O, Mag 1 000x 75
Figure 4.12: FTIR spectra for TFSE-1.25, TFSE-1, TFSE-0.77, TFSE-0.44, TFSE-0.17 and TFSE-H_2O in comparison with UFSE 76

Figure 4.13: Elemental composition of TFSE1, TFSE2, TFSE3 and TFSE4 in comparison with UFSE 78
Figure 4.14: Elemental composition for TH-LW1, TH-LW2, TH-LW3 and TH-LW4 as analysed by ICP, n = 3 80
Figure 4.15: XRD spectra for UFSE, TFSE1, TFSE2, TFSE3 and TFSE4 in comparison with UFSE, where Th = Thenardite (Na_2SO_4) 81
Figure 4.16: Morphology for TFSE1, TFSE2, TFSE3 and TFSE4 in comparison with UFSE 83
Figure 4.17: FTIR spectra for TFSE1, TFSE2, TFSE3 and TFSE4 compared to UFSE 85
Figure 5.1: XRD spectra showing the effect of oxalic acid treated and water treated fly ash silica extracts on the mineral phase of zeolite ZSM-5, with the following code names: Z-1.25, Z-1, Z-0.77, Z-0.44, Z-0.17 and Z-H_2O 89
Figure 5.2: Morphological structure showing the effect of NaOH on the morphology of ZSM-5 zeolites at 160°C for 72 h, with the following code names: Z-1.25, Z-1, Z-0.77, Z-0.44, Z-0.17 and Z-H_2O 91
Figure 5.3: XRD spectra showing the effect of NaOH on the phase formation of ZSM-5 zeolites at 160°C for 72 h, with the following code names: ZN-0.5, ZN-0.4, ZN-0.3, ZN-0.2, ZN- 0.1 and ZN-0.05, where Z = ZSM-5 94
Figure 5.4: SEM micrographs showing the effect of NaOH on the morphology of ZSM-5 zeolites at 160°C for 72 h, with the following code names: ZN-0.5, ZN-0.4, ZN-0.3, ZN-0.2, ZN- 0.1 and ZN-0.05 96
Figure 5.5: XRD spectra showing the effect of TPABr on the phase formation of ZSM-5 zeolites at 160°C for 72 h, with the following code names: ZTP-0.075, ZTP-0.15, ZTP-0.3, ZTP-0.6, ZTP-0.9, ZTP-1.2 and ZTP-1.5, where Z = ZSM-5 98
Figure 5.6: SEM micrographs showing the effect of TPABr on the morphology of ZSM-5 zeolites at 160°C for 72 h, with the following code names: ZTP-0.075, ZTP-0.15, ZTP-0.3, ZTP-0.6, ZTP-0.9, ZTP-1.2 and ZTP-1.5, where Z = ZSM-5 101
Figure 5.7: XRD spectra showing the effect of water on the phase formation of ZSM-5 zeolites at 160°C for 72 h, with the following code names: ZTHH-20 mL, ZTHH-30 mL, ZTHH-40 mL and ZTHH 50 mL, where Z = ZSM-5. 102
Figure 5.8: SEM micrographs showing the effect of water on the morphology of ZSM-5 zeolites at 160°C for 72 h, with the following code names: ZTHH-20 mL, ZTHH-30 mL, ZTHH-40 mL and ZTHH-50 mL, where Z = ZSM-5 104
Figure 5.9: XRD spectra showing the effect of hydrothermal time on the phase formation of ZSM-5 zeolites at 160°C for (x = 0h, 3h, 6h, 24h, 48h and 72h), with the following codenames: ZTHT-0h, ZTHT-3h, ZTHT-6h, ZTHT-24h, ZTHT-48h and ZTHT-72h where Z = ZSM-5 106
Figure 5.10: SEM micrographs showing the effect of hydrothermal time on the phase formation of ZSM-5 zeolites at 160°C for (x = 0h, 3h, 6h, 24h, 48h and 72h), with the following codes: ZTHT-0h, ZTHT-3h, ZTHT-6h, ZTHT-24h, ZTHT-48h and ZTHT-72h where Z = ZSM-5 108
Figure 5.11: XRD spectra showing the effect of hydrothermal temperature on the phase formation of ZSM-5 zeolites at temperature (x = 40, 70, 100, 130 and 160°C) for 3 h, with the following codes: ZTHT-40°C , ZTHT-70°C, ZTHT-100°C, ZTHT-130°C and ZTHT-160°C, where Z = ZSM-5 110

Figure 5.12: SEM micrographs showing the effect of hydrothermal temperature on the morphology of ZSM-5 zeolites at temperature (x = 40, 70, 100, 130 and 160°C) for 3 h, with the following code, ZTHT-40°C , ZTHT-70°C, ZTHT-100°C, ZTHT-130°C and ZTHT-160°C, where Z = ZSM-5 112

Figure 5.13: Comparison of XRD pattern of H-Z-H_2O, H-ZN-0.3, H-ZTP-1.2, H-ZTHH-20mL and H-ZTHT-3h, where Z = ZSM-5 114

Figure 5.14: Comparison of SEM macrographs of H-Z-H_2O, H-ZN-0.3, H-ZTP-1.2, H-ZTHH-20mL and H-ZTHT-3h 117

Figure 5.15: Comparison of structural profiles of H-Z-H_2O, H-ZN-0.3, H-ZTP-1.2, H-ZTHH-20mL and H-ZTHT-3h obtained by FTIR 118

Figure 5.16: Comparative NH_3-TPD profiles of the optimised H-form ZSM-5 zeolite products obtained by varying the NaOH molar content, TPABr, water, hydrothermal time and temperature 120

Figure 5.17: Adsorption/desorption isotherms of N_2 at 77.41 K of H-Z-H_2O, H-ZN-0.3, H-ZTP-1.2, H-ZTHH-20mL and H-ZTHT-3h 124

Figure 5.18: Pore size distribution curves for H-Z-H_2O, H-ZN-0.3, H-ZTP-1.2, H-ZTHH-20mL and H-ZTHT-3h 127

Figure 5.19: XRD spectra of ZU, ZTHR1, ZTHR2, ZTHR3 and ZTHR4 synthesised under hydrothermal conditions (160°C for 72 h) using the coal fly ash silica extracts (UFSE, TFSE1, TFSE2, TFSE3 and TFSE4) obtained in Chapter 4, Section 4.6 128

Figure 5.20: SEM micrographs of ZU, ZTHR1, ZTHR2, ZTHR3 and ZTHR4 synthesised under hydrothermal conditions (160°C for 72 h) using the coal fly ash silica extracts (UFSE, TFSE1, TFSE2, TFSE3 and TFSE4) obtained in Chapter 4, Section 4.6 131

Figure 5.21: FTIR spectra for ZU, ZTHR1, ZTHR2, ZTHR3 and ZTHR4 synthesised under hydrothermal conditions (160°C for 72 h) using the coal fly ash silica extracts (UFSE, TFSE1, TFSE2, TFSE3 and TFSE4) obtained in Chapter 4, Section 4.6 132

Figure 5.22: Absorption-desorption isotherms of UZ, ZTHR1, ZTHR2, ZTHR3 and ZTHR4 synthesised under hydrothermal conditions (160°C for 72 h) using the coal fly ash silica extracts (UFSE, TFSE1, TFSE2, TFSE3 and TFSE4) obtained in Chapter 4, Section 4.6 134

Figure 5.23: Pore size distribution curves for UZ, ZTHR1, ZTHR2, ZTHR3 and ZTHR4 synthesised under hydrothermal conditions (160°C for 72 h) using the coal fly ash silica extracts (UFSE, TFSE1, TFSE2, TFSE3 and TFSE4) obtained in Chapter 4, Section 4.6 136

Figure 6.1: Block flow diagram for the synthesis of ZTHT-3h (hydrothermally synthesised at 160˚C for 3 h) and SOD zeolite (alkaline treatment at 150˚C for 24 h). X represents the undetermined amount of Na, Si, and Al in the liquid streams (LW2, LW3 and LW4) 141

Figure 6.2: Laboratory scale overall mass balance 142

Figure 6.3: Overall mass balance for 1 kg of ZSM-5 per batch 144

Figure 6.4: Cashflow curve for the manufacture of CFA-based ZTHT-3h zeolite and sodalite zeolite 154

Figure 6.5: Sensitivity analysis of model variables on the net present value 156

Figure 6.6: Sensitivity analysis of profitability for ZSM-5 zeolite 158

Figure 6.7: Sensitivity analysis of profitability for sodalite zeolite 158

TABLES

Table 2.1: Magnetic separation conditions for the extraction of Iron from CFA (adopted and modified from (Cornelius 2019) **11**
Table 2.2: Classification of zeolites by pore diameter (Jacobs et al. 2001) **15**
Table 2.3: Cost estimation classification matrix, adopted from Christensen et al. (2005) **32**
Table 2.4: Lang factor and fixed cost estimation factors for different process plants (Coulson and Richardson 1999) **34**
Table 3.1: List of chemicals, purity and suppliers **40**
Table 3.2: List of equipment **41**
Table 3.3: Experimental conditions for the treatment of CFA-based silica extract (UFSE) with oxalic acid and water **44**
Table 3.4: Preliminary synthesis conditions for the synthesis of ZSM-5 zeolite from silica extract **45**
Table 3.5: Experimental conditions for the synthesis of ZSM-5 zeolite from CFA silica extracts **47**
Table 3.6: ZSM-5 synthesis molar regime from CFA silica extracts treated with recycled liquid waste **48**
Table 3.7: Methodology and corresponding result section **53**
Table 4.1: Composition major oxides present in coal fly ash (n = 3) **55**
Table 4.2: Composition major oxides of coal fly ash, magnetic fraction (MF) and iron-free coal fly ash (IFCFA) **59**
Table 4.3: Composition major oxides in IFCFA, UFSE and SR, as determined by XRF, n = 3 ..... **63**
Table 4.4: FTIR vibration band assignments for IFCFA, UFSE and SR **68**
Table 4.5: Composition major oxides (XRF %) and elemental (ICP %) present in TFSE-1.25, TFSE-1, TFSE-0.75, TFSE-0.44, TFSE-0.77 and TFSE-H_2O in comparison to UFSE **70**
Table 4.6: Purity, Si/Al, yields and efficiency of the untreated and the treated fly ash silica extracts (UFSE and TFSE-x) **72**
Table 4.7: Percentage purity and yields for UFSE, TFSE1, TFSE2, TFSE3 and TFSE4 ..... **79**
Table 5.1: Crystallinity and crystal size for Z-1.25, Z-1, Z-0.77, Z-0.44, Z-0.17 and Z-H_2O **92**
Table 5.2: Crystallinity and crystal size for ZN-0.5, ZN-0.4, ZN-0.3, ZN-0.2, ZN- 0.1 and ZN-0.05 **95**
Table 5.3: Crystallinity and crystal size for ZTP-0.075, ZTP-0.15, ZTP-0.3, ZTP-0.6, ZTP- 0.9, ZTP-1.2 and ZTP-1.5 ..... **99**
Table 5.4: Crystallinity and crystal size for ZTHH-20 mL, ZTHH-30 mL, ZTHH-40 mL and ZTHH-50 mL **103**
Table 5.5: Crystallinity and crystal size for ZTHT-0h, ZTHT-3h, ZTHT-6h, ZTHT-24h, ZTHT-48h and ZTHT-72h **107**
Table 5.6: Crystallinity and crystal size for ZTHT-40°C, ZTHT-70°C, ZTHT-100°C, ZTHT-130°C and ZTHT-160°C **111**
Table 5.7: Summary of the optimum conditions applied for H-Z-H_2O, H-ZN-0.3, H-ZTP-1.2, H-ZTHH-20mL and H-ZTHT-3h **114**

Table 5.8: Comparison of crystallinity, crystal size, Si/Al ratio and yield of the optimised ZSM-5 zeolites **115**
Table 5.9: Acidity (a) and textural properties (b) of zeolite ZSM-5 samples obtained from the optimum conditions **122**
Table 5.10: Percent crystallinity, crystal size, Si/Al ratio and product yield for ZU, ZTHR1, ZTHR2, ZTHR3 and ZTHR4 ..... **130**
Table 5.11: Textural properties UZ, ZTHR1, ZTHR2, ZTHR3 and ZTHR4 ..... **137**
Table 6.1: Product yield for MF, ZTHT-3h and SOD **143**
Table 6.2: Material cost contribution to produce 1 kg of ZSM-5 per batch **144**
Table 6.3: Economic analysis base parameters **146**
Table 6.4: Equipment cost estimate parameters used in equation 6.3 (adapted from Coulson and Richardson (1999) **147**
Table 6.5: Production cost assumptions **149**
Table 6.6:Total labour cost to produce ZSM-5 zeolite **150**
Table 6.7: Net cashflow for the production of ZSM-5 and sodalite zeolite **152**
Table 6.8: Investment performance metric **155**
Table 6.9: Model variables used for the sensitivity analysis **155**

GLOSSARY

Acronyms	Definition
AACE	American Association of Cost Engineers
BET	Brunauer–Emmett–Teller
CEC	Cation exchange capacity
CFA	Coal fly ash
FAM	Fusion assisted method
FTIR	Fourier transform infrared spectroscopy
H_2SO_4	Sulphuric acid
HF	Hydrofluoric acid
ICP-AES	Inductively coupled plasma atomic emission spectrometry
IFCFA	Ion-free coal fly ash
KOH	Potassium hydroxide
LOI	Loss on ignition
LW	Liquid waste
M	Mullite
MAM	Microwave-assisted method
MF	Magnetic fraction
MFE	Magnetic iron extract
Na	Sodium
Na_2CO_3	Sodium Carbonate
Na-P	Zeolite Na-P
NCF	Net cashflow
NPV	Net present value
PC	Plant capacity
PCE	Equipment purchase cost
PPC	Physical plant cost
Q	Quartz
R.T	Room temperature
SDA	Structure directing agent
SEM	Scanning electron microscopy
SR	Solid residue
TEA	Technology economic analysis
TEAOH	Tetraethylammonium hydroxide
TFSE	Treated fly ash silica extract
TPABr	Tetrapropylammonium bromide
TPAOH	Tetrapropylammonium hydroxide
TPD	Temperature programmed desorption

UFSE	Untreated fly ash silica extract
UTM	Ultrasonic treatment method
W-UFSE	Wet untreated fly ash silica extract
XRD	X-ray diffraction spectroscopy
XRF	X-ray fluorescent spectroscopy
ZTHR	ZSM-5 zeolite synthesised from silica extracts treated with the recycled liquid waste
ZSM-5	Zeolite ZSM-5

Research outputs

Publications:

Oral presentations:

Local conference

1. Ndlovu, N.Z.N., Ameh, E.A., Petrik, L.F. & Ojumu, T.V. 2019. Synthesis of pure phase zeolite BEA from high-silica South African coal fly ash (CFA) extracts and its application. Global Experts Meeting on Frontiers in Material Science and Nanotechnology. Rome, Italy. October 17-19, 2019.

2. Ndlovu, N.Z.N., Ameh, E.A., Petrik, L.F. & Ojumu, T.V. 2019. Synthesis of pure phase zeolite BEA from high-silica South African coal fly ash (CFA) extracts and its application. Cape Peninsula University of Technology, Postgraduate Conference, Cape Town 7 November 2019.

International conference

1. Ndlovu, N.Z.N., Ameh, E.A., Petrik, L.F. & Ojumu, T.V. 2019. *Synthesis of ZSM-5 and Beta zeolites from high-silica CFA extracts*. 2nd International Workshop on Porous Materials and their applications, CSIR International Conventional Centre, Pretoria, South Africa. 20 – 21 June 2019

CHAPTER 1

INTRODUCTION

1.1 Synopsis

This chapter gives a brief background to the research topic and highlights the importance and novelty of the study. The problem statement, motivation, research hypothesis, aims and objectives, research questions and approach, scope and delimitations, as well as expected outcomes, institutional contributions and the thesis framework, are also included.

1.2 Background

Coal is universally an important source of energy, generally used as feedstock in the combustion process during electricity generation. The largest coal-producing countries are China, the United States, India, Indonesia, Australia and South Africa (Cronshaw 2015). In 2018, South Africa's coal consumption accounted for 69.6% of the country's total energy consumption, representing more than 88% of Africa's coal consumption (Ma et al. 2018). Coal is classified into two categories: high grade (HG) and low-grade (LG). The HG coal has fewer inorganic minerals and is mainly composed of clays, calcite, dolomite, pyrites and silica, whereas the LG coal is dominated by inorganic minerals. In South Africa, HG coal is mined and exported for economic gain to countries like India, China, Europe and so on, while the LG coal is predominantly used as a source of energy in the combustion processes (Ahmaruzzaman 2010). Burning of LG coal results in a large amount of incombustible material, well known as coal combustion by-products (CCPs) of which coal fly ash (CFA) is the main waste product, accounting for 60% of all CCPs (Musyoka et al. 2012). CFA is abrasive, alkaline and refractory in nature, composed of fine glass-like particles such as Si, Al, O, Fe and Ca and traces of toxic elements such as As, Hg, B, Pb, Ni, Se, Sr, V and Zn (Inada et al. 2005; Musyoka et al. 2012; Querol et al. 2002). Furthermore, with the increase in population, the electricity demand in South Africa has increased proportionally, resulting in the concurrent increase in the amount of CFA produced. Eskom, the country's sole energy supplier, generates approximately 40 Mt of CFA per year and only 5.5% is utilised effectively in the construction industry, while the rest is disposed of in ash dams or stacked on land as ash dumps (Eskom Holdings 2011; Sibanda et al. 2016). The disposal of CFA in landfills has resulted in massive health and environmental problems, due to its fine particle size. The toxic elements contained in CFA have the potential to leach out into the soil during rainy seasons, thereby contaminating the soil, groundwater and surface water. Also, for people living in close proximity to the disposal sites, CFA has been shown to be very detrimental to their health and may cause fatalities (Jala and Goyal 2006). The environmental and health problems associated with the disposal of CFA into the environment has necessitated further research, aiming to investigate alternative disposal or CFA reuse strategies.

CFA has been identified as an inexpensive replacement for the usual sodium silicate and aluminate in the synthesis of zeolites (Hu et al. 2017; Jha and Singh 2016). Zeolites are commonly known as porous crystalline framework materials containing pores of molecular size ranging between 5 to 12 Å (0.5 to 1.2 nm). The elemental composition of a zeolite material includes aluminium, oxygen, and silicon, fused with alkali or alkaline-earth metals such as sodium, potassium, magnesium, and water molecules trapped in the pores between the elements (Chester and Derouane 2009; Papaioannou et al. 2005). There are about 40 naturally-occurring zeolites, which form in both volcanic and sedimentary rocks, and over 300 different types of synthetic zeolites (Du Plessis 2014). Zeolites are classified into low, medium and high-silica with a Si/Al ratio ranging from $1 < Si/Al < 5$, $5 < Si/Al < 10$ and $Si/Al > 10$ respectively (Mosca et al. 2009). The technologies used in producing synthetic zeolites have advanced significantly over the past decade, due to the ability to produce zeolites with specific structural parameters suitable for industrial applications (Wdowin et al. 2014). Zeolites synthesised from CFA have attracted great interest for several industrial applications (Wdowin et al. 2014). Processes used to synthesise CFA-based zeolites have been successful at the laboratory scale. However, there is little research relating to the implementation and application of these processes at an industrial scale (Wdowin et al. 2014). The factors limiting the implementation of CFA-based zeolite synthesis at an industrial scale have been well documented. These include high energy consumption (Mainganye et al. 2013; Musyoka et al. 2012), generation of voluminous liquid and solid waste, which necessitates further treatment (Ojumu et al. 2016), the requirement to purchase expensive reagents, such as sodium aluminate, sodium silicate and organic structure directing agents (Wang et al. 2008) and the production of moderately low yields of the synthesised zeolite product (Wdowin et al. 2014) when fused CFA filtrate is used in the synthesis process, even when energy consumption was minimised by way of sono-chemical treatment (Ojumu et al. 2016). Similarly, when the bulk fused CFA is used, high yields are attainable, though the zeolite product contains mixed phases which then limit its scalability and application in the catalytic industry. Missengue (2016) has developed a process where high-silica zeolites can be synthesised from CFA without the addition of silica or alumina source. However, the process results in zeolites with oversized crystals, which affects the catalytic performance of the synthesised zeolites.

Commercial production of CFA-based zeolites for commercial purposes is reliant on the successful development of a scalable synthesis process, which will enable the valorisation of CFA at a larger scale. At present, this remains an underdeveloped area, which needs further investigation. This study therefore aims to develop a CFA-based zeolite synthesis process which will reduce or eliminate the challenges limiting the implementation of CFA-based zeolite synthesis at an industrial scale. The study will also investigate the effect of Si/Al ratio, NaOH,

structure directing agent and water content on zeolite morphology and crystal size as well as the hydrothermal synthesis parameters (temperature and time). In addition, the study aims to develop a systematic synthesis approach that would holistically convert CFA, such that high yield zeolites can be synthesised from CFA without the addition of a silicon or aluminium source. Further, the technology economic analysis study to investigate the process's feasibility for a production capacity of 5000 kg of ZSM-5 per year will also be investigated. The proposed method should also lead to the production of other zeolites from the solid residue which may find application in water treatment (Prasad and Mortimer 2011) or production of diesel (Manique et al. 2017; Shabani et al. 2022).

1.3 Problem statement

The consumption of coal for domestic use in 2016 (South Africa) was estimated to be 120 Mt per annum, and this figure is expected to increase to 139 Mt by 2023 (Eskom Holdings 2011). Without proper disposal strategies, the environmental burden associated with the disposal of CFA into the environment will continue to increase exponentially. Currently, the rate of CFA generation during the combustion process outweighs the rate of CFA re-use. CFA is a low-cost source of Si and Al and as such, the waste has been applied in the synthesis of alumino-silicate materials. The synthesis of zeolites from CFA has shown a potential for the holistic use of CFA to produce valuable products with important industrial applications. However, considerable research needs to be undertaken to ensure that the developed synthesis processes are not limited to laboratory scale, but could be used to process large amounts of CFA into the creation of commercial products. Different types of zeolites have been successfully synthesized from CFA, though the synthesis of high-silica zeolites from CFA requires a Si/Al ratio of greater or equal to 10. Furthermore, available coal fly ashes have a Si/Al ratio of 1-2 and thus are not suitable for the synthesis of high value zeolites. As such, the synthesis of high-silica zeolites from CFA would require the addition of silica and/or alumina sources in order to adjust the Si/Al ratio. However, the costs of these chemicals are high, and as such the implementation of such processes at a larger scale is at present not economically viable. Missengue (2016) and Ndlovu (2016) have developed a process whereby pure phase high-silica CFA-based zeolites can be synthesized without the addition of an silica or alumina source. Although this process was able to eliminate the need to add silica or alumina source in the CFA precursor, the process required oxalic acid solution to treat the CFA silica extract before use as a feedstock in the synthesis of zeolites. Zeolites synthesised through this route are often lath or coffin-shaped zeolites with large crystal size. Missengue et al. (2017) reported that large zeolite crystal size reduces catalytic efficiency, as the micropores and mesopores might not be easily accessible. It is thus important to develop a process that would produce high-silica zeolites with small crystal sizes suitable for different catalytic applications.

1.4 Motivation of the study

South Africa heavily depends on coal for electricity generation. With the increase in the human population and opening of new industrial parks and residential areas, coal consumption is guaranteed to increase in the coming years. This will lead to an increase in the CFA being produced. Without sustainable, effective and environmentally friendly CFA disposal strategies in place, South Africa is heading into an environmental crisis. Therefore, efficient and effective scalable CFA-based synthesis processes are of utmost importance to ensure that CFA-based zeolites are scalable and competitive in the catalytic industry. The proposed method will not only eliminate the need to add silica or alumina sources but will additionally reduce the costs associated with the synthesis of CFA-based high-silica zeolites, and provide economic feasibility data, which will guide the implementation of this process at a large scale.

1.5 Hypothesis

High-silica pure phase zeolite ZSM-5 can be synthesised directly from CFA silica extracts without prior treatment with oxalic acid or the addition of alumino-silicate sources.

1.6 Aims and objectives

This study aims to synthesise pure phase high-silica zeolite ZSM-5 from CFA silica extracts following the method developed by Ndlovu (2016). The study also aims to conduct a technology economic analysis in order to predict the cost of production for CFA-based ZSM-5 zeolite at a larger scale. The main objectives of the study include:

- Obtain the chemical composition of CFA in order to monitor the Si/Al ratio from the as-received Matla CFA, silica extract, synthesised zeolites and the obtained solid residue.
- Investigate a novel process to extract silica from CFA with adequate Si/Al ratio required to synthesise high-silica ZSM-5 zeolite without the use of oxalic acid treatment process.
- Identify and optimise the synthesis conditions such as NaOH, structure directing agent (TPABr), and water for the synthesis of ZSM-5 zeolite from CFA silica extract.
- Identify and optimise the hydrothermal synthesis conditions, such as temperature and time for ZSM-5, using the optimum molar composition obtained above.
- Investigate the reusability of the liquid waste resulting from the treatment process by way of introducing a recycle stream into the process.
- Investigate the synthesis of ZSM-5 using the silica extract treated with the recycled liquid waste.
- Perform a technology economic analysis study using the optimum formulation and hydrothermal synthesis conditions.

1.7 Research questions

The study intends to achieve the aims and objectives listed above by conducting relevant research that will provide answers to the following research questions.

- Would the Na-rich CFA silica extract have the Si/Al content required to synthesise high-silica zeolite ZSM-5?
- What would be the effect of the water treatment process on the Si/Al ratio of the CFA silica extracted?
- Would variation in NaOH, TPABr and water content have a direct influence on the morphology and crystal size of the synthesised zeolite?
- What would be the effect of silica extract treated with recycled liquid waste on the resultant ZSM-5 zeolite?
- What would be the optimum crystallisation time and temperature for the synthesised zeolite ZSM-5?
- Would the conversion of CFA into ZSM-5 and sodalite using the proposed method be economically viable?

1.8 Research approach

A detailed literature review was conducted to understand previous studies relating to the research topic. The knowledge obtained was used to develop suitable research methodologies which were used to conduct a series of experiments required to achieve the aims and objectives of the study. The research approach for this study is as follows:

- Characterisation of the starting material: The as-received CFA was extensively characterized to determine its physical and chemical properties. The characterisation included X-ray fluorescence (XRF), X-ray diffraction (XRD), scanning electron microscopy (SEM) and Fourier transform infrared (FT-IR).
- Extraction of CFA silica extract: The process included the removal of iron using a magnetic stirrer prior to the extraction of silica. The iron-free CFA was then used as a feedstock to extract silica. This was achieved by treatment with NaOH solution in a reflux system.
- Treatment of CFA silica extract with oxalic acid: The obtained CFA silica extract was then treated with varying concentrations of oxalic acid or deionised water in order to reduce the amount of Al content in the extract to achieve the desired Si/Al ratio suitable for high-silica zeolite synthesis.
- Synthesis of zeolite sodalite from the solid residue: The obtained solid residue after alkaline reflux process was dried overnight and characterised for its physical and chemical properties using XRF, SEM, XRD and FTIR.

- Synthesis of zeolite ZSM-5: The obtained CFA silica extract was mixed with the appropriate amounts of NaOH, H_2O and tetrapropylammonium bromide (TPABr) to acquire a suitable molar formulation required for the synthesis of ZSM-5 zeolite.
- The obtained ZSM-5 zeolite was characterised by XRD, SEM, ICP, FTIR and N_2 adsorption. Temperature-programmed desorption (TPD) and thermogravimetric analysis (TGA) was also performed to measure acid sites and thermal stability of the synthesised zeolites.
- The technology economic analysis was performed using the optimum molar formulation and hydrothermal synthesis conditioned assuming a production capacity of 5000 kg of ZSM-5 zeolite per year.

1.9 Scope and delimitations of the study

High-silica zeolites can be synthesised from different starting materials rich in Si and Al. However, this study will utilise the South African Matla Class F CFA as a source of Si and Al for the purpose of CFA-based zeolite synthesis. Also, among many silica extraction methods, this study will be limited to the alkaline extraction method of fly ash as a Si and Al dissolution technique, followed by the hydrothermal synthesis process. Other dissolution techniques, such as fusion, ultrasound and microwave-assisted methods will not be covered under this study. Due to time and funding constraints, this study will focus on the synthesis of zeolite ZSM-5 and zeolite sodalite from the resultant solid residue. In addition, the technology economic analysis will be based on early-stage economic analyses, where actual equipment data for the large-scale production is not available and would rely on assumptions as suggested by Coulson and Richardson (1999). The cost of liquid waste disposal will not be covered in this study. Alternative ways to manage the liquid waste generated such as recycle protocols will be discussed.

1.10 Thesis structure

This thesis is composed of seven chapters, including this chapter (Chapter One), which presents a brief overview and introduction of the research topic.

Chapter 2: Literature review. This chapter details the generic literature review related to the research topic. The different zeolite synthesis methods used to synthesise CFA-based zeolites and the limitations associated with implementation of current synthesis methods in an industrial scale are discussed. Prior research on the different silica extraction techniques and potential applications of CFA-based zeolites are presented in this chapter. A brief review of literature on the synthesis of zeolite ZSM-5 and sodalite from CFA is included. In addition, the characterisation techniques for the as-received CFA, CFA silica extracts, synthesised zeolite ZSM-5, sodalite zeolite and liquid waste are included. This chapter ends with a summary on the state-of-the-art literature and the gap analysis relating to the current study.

Chapter 3: Material, Experimental and Analytical Techniques. Chapter Three details the materials, experimental methods and analytical techniques used in this study. Background information on the sampling procedure, storage, list of chemicals and equipment used is provided. The methodological approach used to synthesise high-silica zeolite ZSM-5 from South African CFA silica extracts is also presented. The experimental approach applied for the technology economic analysis is also detailed in this chapter.

Chapter 4: Selective Extraction and Characterisation of CFA Silica Extracts. This chapter presents and discusses the characterisation of the as-received South African Matla CFA, silica extracts and the obtained solid residue.

Chapter 5: Synthesis and Characterisation of Zeolite ZSM-5 Synthesised from CFA Silica Extracts. This chapter presents the results and discussions of the synthesised CFA-based high-silica zeolite ZSM-5.

Chapter 6: Technology Economic Analysis of SZM-5 Zeolite Synthesised from CFA-based Silica Extract: This chapter presents the results and discussions of the technology economic analysis performed on the production of ZSM-5 and sodalite zeolite using CFA as a source of Si and Al in a scaled-up continuous process of 5000 kg of ZSM-5 per year.

Chapter 7: Conclusions and Recommendations: Chapter Seven gives a summary of the conclusions and novel findings obtained from this research. It also presents recommendations for future work based on the conclusions and recommendations drawn from the study.

CHAPTER 2
LITERATURE REVIEW

2.1 Synopsis

This chapter presents the review of literature relevant to the research topic under investigation and highlights the gap analysis that this study aims to address. The reviewed literature covers background information on coal fly ash (CFA) formation, its environmental impact and application. Furthermore, the application of CFA as a feedstock in zeolite synthesis, the different synthesis methods and analytical techniques have been carefully reviewed. The applications of zeolites, as well as the challenges associated with the synthesis of CFA-based zeolites at an industrial scale, are also presented. This chapter also proposes a novel process that could lead to the valorisation of CFA in the synthesis of zeolites at an industrial scale with minimal waste generation.

2.2 Coal fly ash

Coal fly ash (CFA) is an incombustible industrial by-product derived from coal combustion in thermal powerplants (Yao et al. 2015). There are approximately 13 Eskom-owned coal fired powerplants in South Africa, the majority of which are situated in Mpumalanga Province (Eskom Holdings 2011). According to Eskom Holdings (2011), South African powerplants generate approximately 40 million tons of CFA every year, from which only 5.5% is being utilised efficiently in the construction industry and the rest has been disposed of on lands. The disposal of CFA has claimed large hectares of land which could have been directed to agriculture or other economic uses. Research on the characterisation of CFA has revealed that the waste contains several toxic elements which can be harmful to human health such as lead, arsenic, chromium and mercury (Musyoka et al. 2012). The poor management of CFA has resulted in serious health and environmental concerns. Exposure to CFA could cause nose and throat irritation, dizziness, nausea, vomiting, lung cancer and shortage of breath. Also, due to the presence of toxic soluble species, the leaching potential of these species into the environment, is extremely high, thereby contaminating the soil, surface and groundwater (Praharaj and Ray 2001).

2.2.1 Physical appearance of CFA

The physical and chemical properties of CFA are dependent on the type and source of coal used in the combustion process. It is well documented in literature that the combustion of powered coal produces several solid coal combustion products (CCPs) including fly ash, flue gas desulphurisation material and bottom ash boiler slag, with fly ash being the main secondary waste of all the CCPs (Vom Berg 1998). CFA is a Si-Al rich material made of

predominantly small spherical particles, ranging in size from 20-80 µm, with specific surface area and specific volume ranging from 21 to 3.0 m^2/kg and 170 to 100 m^3/K respectively, and consists of solid spheres, cenospheres, irregular-shaped debris and porous unburnt carbon (Ahmaruzzaman 2010; Gitari et al. 2016; Yao et al. 2015). Depending on the amount of iron and unburned carbon, the colour of CFA may vary from tan to light and dark grey (Yao et al. 2015). CFA is known to be alkaline, refractory and abrasive in nature and consists of glassy and transparent spherical micro-particles, which indicate the complete melting of silicate minerals during the combustion process (Fisher et al. 1978; Madzivire et al. 2010).

2.2.2 Chemical composition of CFA

CFA is mainly composed of metal oxides such as SiO_2, Al_2O_3, CaO, MgO, K_2O and Fe_2O_3 in varying amounts (Nyale et al. 2013). Fly ash also contains many trace elements, such as Cr, Pb, Ni, Ba, Sr, V and Zn present in significant quantities, some of which are of environmental concern (Musyoka et al. 2012). The characterisation of the CFA material prior to use in various applications is very crucial, as the composition of CFA varies from batch to batch. There are two types of CFA, namely Class F and C. The American Society for Testing Materials (ASTM C618) has classified all CFA containing SiO_2, Al_2O_3 and Fe_2O_3 content of more than 70 wt% and having a low CaO content (< 10%) as Class F type. CFA containing a total SiO_2, Al_2O_3 and Fe_2O_3 content ranged 50 and 70 wt%, with a high CaO content of 10 to 40% is classified as Class C (Ahmaruzzaman 2010). Due to its high CaO content, Class C CFA is known for its cementitious properties, while Class F is well known for its pozzolanic properties (Yao et al. 2015). Class F CFA has been used as a cement replacement in concrete and other building applications due to its ability to act as a binder when combined with an alkaline agent (Ahmaruzzaman 2010). Burning of low-grade coal in South Africa has resulted in the production of only Class F CFA type (Musyoka et al. 2012).

2.2.3 Environmental impact of CFA

The poor management of CFA and its disposal in the environment have resulted in several health and environmental problems due to its chemical composition (Bhanarkar et al. 2008; Du Plessis 2014; Madzivire et al. 2010). Coal consumption is expected to rise considerably, due to the increase in human population worldwide. Consequently, this will cause a proportional rise in the production of CFA. The use of poorer quality coal during the production of electricity in South Africa contributes significantly to the large quantities of CFA produced. Currently, approximately 94.5% of the CFA produced in South Africa is disposed in ash dams or dumps situated near the coal-fired powerplants (Eskom Holdings 2011). CFA has become one of the largest sources of hazardous industrial waste. Without appropriate disposal management strategies, the waste will continue to impose serious health and environmental threats (Querol et al. 2002; Zhang et al. 2013). Increased illness and death in the general

population as a result of air pollution has been reported in recent years (Burt et al. 2013). Burt et al. (2013), reported that for every terawatt-hour of electricity produced from burning coal, there are approximately 25 deaths, 13,288 minor illnesses, 225 serious illnesses, including hospital admissions for congestive heart failures and chronic bronchitis. The health conditions and fatalities associated with direct exposure to CFA result from the toxic constituents such as Pb, Hg, Cd, Ba, Th, Ge, Ce, U, etc. present in CFA (Carlson and Adriano 1993; Davison et al. 1974; Jala and Goyal 2006; Natusch et al. 1974). Fine particles of CFA can easily penetrate the alveolar regions of lungs when inhaled, causing severe damage to the human respiratory system (Bhanarkar et al. 2008; Goodarzi 2006). The environmental issues associated with the disposal of CFA on land include: air pollution, contamination of surface and ground water through disposal of CFA have resulted in leaching of the toxic elements during rainy seasons, thus contaminating ground and surface water, thereby threatening humans, plants and aquatic life (Ahmaruzzaman 2010; Carlson and Adriano 1993). Although some elements found in CFA are deemed beneficial to the growth of plants (Gupta et al. 2002), these benefits are outweighed by the considerable environmental concerns associated with its disposal into the environment.

2.2.4 Application of CFA

Alternative CFA management strategies have been investigated with the aim of eradicating or alleviating the environmental burdens associated with the disposal of CFA into the environment. CFA has been used as a neutralisation agent in alkaline reactions (Daniels et al. 2006), and as a feedstock in the production of porous heat-insulating, soundproof and ceramic materials. These materials have attracted great interest in the defence field (Blissett and Rowson 2012; Zhu et al. 2016), as a low cost adsorbent for the removal of toxic metals, methylene blue and humic acid from aqueous solutions (Wang et al. 2008), as an alkaline agent in the treatment of mine water (Gitari et al. 2016; Moreno et al. 2001), and as a back filling material in open mine voids (Shen et al. 2009; Yao et al. 2015). Due to its physical properties, which include texture, water holding capacity and bulk density, CFA has found application as a soil amendment reagent in agriculture (Gupta et al. 2002). The waste material has also been identified as an inexpensive replacement for the conventionally-used sodium silicate and aluminate in zeolite synthesis (Hu et al. 2017; Jha and Singh 2016) and as feedstock in the synthesis of geopolymers (Bhandari et al. 2012; Nyale et al. 2013).

The extraction of valuable metals from CFA has been considered one of the beneficiation strategies, thus providing an alternative to the disposal of CFA into the environment. Of relevance to this study are studies on the use of CFA as a parent material in the recovery of iron (Gilbert et al. 2019; Sedres 2016) and silicon (Ameh et al. 2020; Cornelius 2019). A review on the selective extraction of these metals from CFA is detailed below.

2.2.4.1 Extraction of Iron from CFA

The recovery of iron from CFA through magnetic separation is well documented (Cornelius 2019; Gilbert et al. 2019; Sedres 2016). Iron is one of the major constituents in CFA, accounting for approximately 4-10% in the form of Fe_2O_3 (Eze 2014). Magnetic separation of iron from CFA consists of three steps: (i) mixing of CFA with deionised water in a fixed solid-to-liquid ratio, (ii) separation of magnetic fraction using a magnetic stirring bar, followed by filtration of the non-magnetic fraction, (iii) drying of the magnetic and non-magnetic fraction. Table 2.1 shows a summary of the recovery of iron through magnetic separation.

Table 2.1: Magnetic separation conditions for the extraction of Iron from CFA (adopted and modified from (Cornelius 2019)

S:L ratio	Temp. (˚C)	Time (h)	Stirring (rpm)	Fe recovery (%)	Reference
1:2	r.t	6	250	63.6	Cornelius, 2019
1:2	r.t	6	250	82	Gilbert *et al.*, 2019
_	r.t	1	750	26	Sedres, 2016

Note: r.t (room temperature), _ (not determined)

As evident in Table 2.1, Gilbert et al. (2019) report the highest Fe% efficiency, followed by Cornelius (2019) and Sedres (2016) using a similar process. Nanoparticle iron has found application as an adsorbent in acid mine drainage remediation (Gilbert et al. 2019), as a catalyst in the removal of uranium from wastewater (Chen et al. 2017), and in protein/enzyme immobilization due to its superparamagnetic properties, high surface area, large surface-to-volume ratio, and easy separation under external magnetic fields (Xu et al. 2014).

2.2.4.2 Extraction of Si from CFA

The recovery of silica from CFA was motivated by earlier studies on the use of CFA as an alternative to bauxite in the recovery of aluminium (Bai et al. 2011; Iyer 2002; Matjie et al. 2005; Wu et al. 2012). The use of inexpensive waste material for metal recovery not only provides a value-add recycling mechanism, but also results in the extraction of valuable elements which can be used in various industrial operations. Silica is the main constituent of CFA, accounting for approximately 58.44% by mass in CFA (Nyale et al. 2013). Studies on the recovery of silica from CFA have been reported by several researchers (Sedres 2016; Seidel et al. 1999). Silica can be extracted from CFA by either the alkaline leaching method (Cornelius 2019; Ndlovu 2016) or fusion method (Ameh et al. 2020; Missengue et al. 2018). Ndlovu (2016) recovered silica extract from CFA using the alkaline reflux extraction method. In the study, iron-free dried CFA was mixed with 500 mL of 8 M NaOH solution in a round-bottom flask and heated at 150˚C under reflux condition for 24 hours. The recovered filtrate was precipitated by a

concentrated amount of H_2SO_4, recovered by vacuum filtration and dried overnight at 70˚C. Prior to the synthesis process, the recovered extracts were treated with a saturated oxalic acid solution in order to reduce the Al content and other elements such as Fe, Ca, Mg, and Ti, which might have an undesirable effect on the quality of the zeolite product. The treated extract with an extraction efficiency of 91.92% was used as feedstock in the synthesis of pure phase ZSM-5 zeolite without the addition of any Si or Al sources. In a similar study, Sedres (2016), investigated the extraction of Si using NaOH as the extraction media. The author reported a silica extraction efficiency of 53.36%.

Detailed literature on the applications of CFA in different fields can be accessed from the comprehensive review by Yao et al. (2015). Despite considerable research on the application of CFA being available in the public domain, research on the implementation of these applications at an industrial scale is lacking. Without viable and sustainable CFA management strategies for the holistic use of CFA in the manufacture of viable products, its disposal into the environment will continue to impose a major environmental health problem in the country. Research on the implementation of existing and viable CFA application strategies on an industrial scale is of great necessity. In this study, the magnetic separation method (Gilbert et al. 2019) and the silica alkaline extraction method (Ndlovu 2016) will be explored further for the preparation of silica extract, which will be used as a feedstock in the synthesis of high value ZSM-5 zeolite and sodalite zeolite from the secondary solid waste (resulting from the alkaline extraction process), with little or no solid waste generated.

2.3 Zeolite history and formation

Zeolites are naturally-occurring aluminosilicate materials characterised by a porous framework structure with aluminate (AlO_4) and silicate (SiO_4) tetrahedra connected to one another, as shown in Figure 2.1 (Georgiev et al. 2009; Passaglia and Sheppard 2001).

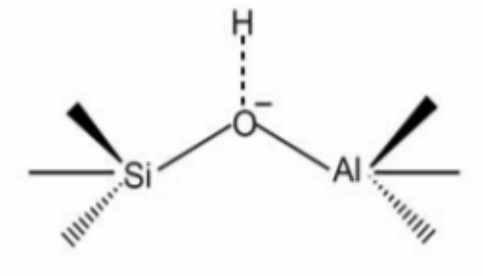

Figure 2.1: Chemical structure of zeolite (Georgiev et al. 2009)

Each AlO_4 tetrahedron in the framework bears a net negative charge which is balanced in an aqueous solution containing a cation, these counter ions are elements from the IA and IIA groups of the periodic table (Weckhuysen and Yu 2015; Wright and Lozinska 2011). The number of tetrahedrally coordinated AlO_4 in the zeolite framework is known to greatly influence

the physicochemical properties of zeolites, such as thermal stability and sorptive, ion-exchange and catalytic abilities (Oumi et al. 2003). Although these materials are naturally occurring, the advancements in technology have enabled the synthesis of these materials in the laboratory leading to the development of new and innovative synthesis methods (Musyoka et al. 2012; Querol et al. 2001; Weitkamp 2000). The mechanism of zeolite synthesis from silica or aluminium rich materials is not a mathematically modelled subject, though it has been proposed based on findings from different experimental observations (Mainganye et al. 2013).

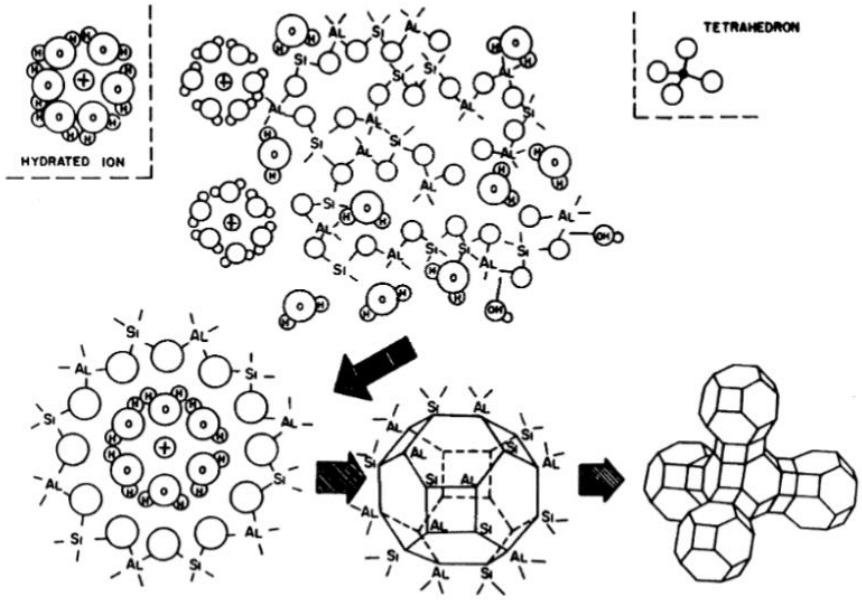

Figure 2.2: Formation of zeolite crystal nuclei in a hydrous gel. Source: (Cundy and Cox 2003)

The science of zeolite synthesis was first developed by Barrer and Milton in the early 1940s (Cundy and Cox 2003). The chemical structure of zeolite is based on the crystallographic unit and its chemical composition can be expressed by the following molecular formula (Georgiev et al. 2009).

$$M_{x/n}[(AlO_2)_x(SiO_2)y].wH_2O$$

Where M is an alkaline earth cation, n is the valence of the cation, w is the number of water molecules per unit cell, x and y are the total number of tetrahedra per unit cell, and the ratio y/x usually has values of 1 to 5. However, for high-silica zeolite, y/x can range from 10 to 100 (Georgiev et al. 2009). Zeolite materials can be synthesised from any SI-Al rich materials, including CFA. Due to the advancements in zeolite synthesis, the technologies and methods for manufacturing synthetic zeolites have been improved and developed such that they can be altered to produce zeolites with specific structural parameters (Wdowin et al. 2014).

Zeolites have various properties (thermal stability, acidity, hydrophobicity/hydrophilicity of surfaces, ion-exchange capacity, low density and large void volume, uniform molecular sized channels, adsorption for gas and vapour and catalytic properties), which make them applicable in a vast range of industrial and environmental applications (Bogdanov et al. 2009). The physical and chemical properties of zeolites are mainly influenced by the Si/Al ratio, which informs the grade and framework structure of the synthesised zeolite.

2.3.1 Classification

One of the most important characteristics of zeolites is their Si/Al ratio, which is inversely correlated with their ion exchange capacity and directly related to their thermal stability. (Ramesh and Reddy 2011). Zeolites can be classified into low silica (Si/Al ≤ 2), intermediate silica (Si/Al 2 to 5) and high silica (Si/Al >5) (Jha and Singh 2011; Ozin et al. 1989). Sodalite zeolite is considered a low Si/Al ratio zeolite, with a Si/Al ratio of ≤ 2 (Cornelius 2019), while high-silica ZSM-5 zeolites contain a Si/Al ratio of ≥10 (Bindhu and Sugunan 1998). Zeolites can also be categorised according to the size of their pore openings (Table 2.2). The pore openings (8, 10 and 12 ring, based on the number of T-atoms) serve as windows into the pore network of a zeolite framework (Hölderich and Van Bekkum 1991). Small-pore zeolites are those containing an 8-membered ring, with free pore diameter of 0.3 to 0.45 nm; medium-pore zeolites have 10-membered rings with a free pore size of 0.45 and 0.6 nm; while large-pore zeolites are characterised by 12-membered rings and have free pores that are at least 0.8 nm in diameter (Ramesh and Reddy 2011). The pore space is typically incorporated into the cavities, or cages, of zeolite, which are located inside the polyhedral units of the zeolite framework (Baerlocher et al. 2007). Due to their unique pore structure and their shape selective capabilities, zeolites have been utilised in the chemical industry as molecular sieves, catalysts, or support materials for the conversion and separation of different compounds (Huang et al. 2014).

Table 2.2: Classification of zeolites by pore diameter (Jacobs et al. 2001)

Zeolite classification	Small pore	Medium pore	Large pore
Pore opening (ring size)	8	10	12
Pore size (nm)	0.3 - 0.45	0.45 - 0.6	0.6 - 0.8
Zeolite framework type	A (LTA), P (GIS), Sodalite (SOD)	Ferrierite (FER), ZSM-5 (MFI), Silicalite-1 (MFI)	Z and Y (FAU), Beta (BEA), Mordenite (Mor)

2.3.2 Properties and applications of zeolites

Zeolites are used in various industrial and environmental applications because of their distinctive physiochemical properties, such as ion exchange, porosity, acidity and thermal stability (Bogdanov et al. 2009; Weitkamp 2000). A summary of the different zeolite properties and their applications is detailed in the subsections below.

2.3.2.1 Ion-exchange

Cation exchange capacity (CEC) is one of the most important characteristics of microporous materials (Musyoka et al. 2012). As such, zeolites can be applied as adsorbents in various industrial applications due to their capacity to exchange cations in aqueous solution, with sodium being the most common extra-framework cation in zeolites (Pfenninger 1999; Valdés et al. 2006). The ion exchange capacity of zeolites can be increased by adding more active sites in the zeolite framework (Koike et al. 2018). Heavy metal removal from sludge, industrial effluents, and other wastewater is a popular use for zeolites with high ion exchange capacities (Na-P, Na-A, FAU, and others) (Scott et al. 2002). Srinivasan and Grutzeck (1999), used CFA-based zeolites such as zeolite X, zeolite Y, zeolite NA-P1, analcime, and sodalite as adsorbents to remove 2000 ppm of SO_2 from a simulated stack gas. Their study showed that these zeolites were efficient in removing all the SO_2, resulting in an adsorption capacity of approximately 0.11 mmol/g. Mercury (II) was removed from aqueous solutions using CFA-based sodalite zeolites as an adsorbent (Tauanov et al. 2019). Studies on the use of zeolite (Clinoptilolite, Mordenite, MesoLite and Chabazitehas) in the removal of ammonia in wastewater have been reported (Booker et al. 1996; Canellas et al. 2019). The usage of CFA-based zeolites for heavy metal removal offers advantages over synthetic zeolites made from pure chemicals in terms of large diffusion and inexpensive production costs (Colella 1999).

2.3.2.2 Porosity

As size- and shape-selective solid acid catalysts, zeolites are extremely useful in achieving optimal catalytic performance in numerous molecular applications (Prasomsri et al. 2015).

However, the use of large-sized zeolites causes diffusion limitations for larger molecules, which can access only the external surface, prohibiting access to the zeolite micropores. These molecules also shorten the diffusion path length through the micropore system of zeolites (BABIC 2021). Thus, much effort has been made toward understanding the synthesis of hierarchically porous materials (Dorin et al. 2014; Yang et al. 2017). These materials have interconnected pores of various sizes, ranging from micropores (≤ 2 nm) through mesopores (2–50 nm) and macropores (> 50 nm), and they have a multimodal hierarchically porous structure (BABIC 2021). Due to their intracrystalline structure and nano-spaces close to the molecular diameters of light hydrocarbons, zeolites exhibit a remarkable molecular-sieving effect for light hydrocarbons and have been widely used as shape-selective catalysts in various hydrocarbon processes (Derouane 1984; Nishiyama et al. 2001). The synthesis of small-sized zeolite crystals creates extra-porosity (meso- and macropores) in the zeolite framework, which contributes to the intra-crystalline diffusion rate and thus improves adsorption and desorption activity, thereby improving catalyst lifetime (Groen et al. 2004). Therefore, the synthesis of multiple pore size structure is of interest in the research area of zeolite synthesis (Ocampo et al. 2009; Zhang and Ostraat 2016).

2.3.2.3 Thermal stability

Thermal stability is a crucial characteristic for zeolites in the catalytic industry, as these processes use high temperatures, especially during the zeolite regeneration step (Trigueiro et al. 2002). Thermal stability is dependent on the Si/Al ratio of the zeolite framework, the higher the Si/Al ratio, the higher the thermal stability of the zeolite (Cruciani 2006). Thus, high-silica zeolites, such as ZSM-5 is mostly applicable in catalytic reactions that require relatively high temperatures to facilitate the conversion of reactant into the desired products (Cornelius 2019). As such, ZSM-5 and Beta zeolites have been used as catalysts in the cracking of n-Hexane (Bleken et al. 2012; Konno et al. 2012), conversion of methanol to hydrocarbons (Bjørgen et al. 2007; Missengue et al. 2018), catalytic pyrolysis and hydro-pyrolysis of biomass (Ding et al. 2020; Iliopoulou et al. 2012), oligomerization of biomass-derived light olefins to light fuel (Wang et al. 2017). The thermal stability of zeolites can be improved through ion-exchange processes by the addition of rare earth cations, principally those from the light group (La, Ce, Nd, Sm, Pr) (Trigueiro et al. 2002).

2.3.2.4 Acidity

The existence of strong and alterable acidity in zeolites has led to their usage as solid catalysts in a large number of oil refining and petrochemical industries (Serrano and Pizarro 2013). Solid acidity in zeolites is caused by the presence of aluminium atoms in the zeolite framework, which results in Si-O-Al sites that may function as either acidic or basic sites in chemical reactions (Cornelius, 2019). Solid acidity is inversely proportional to the Si/Al ratio, thus the

higher the Si/Al ratio in the zeolite framework, the lesser the number of available acid sites. This is caused by the reduction in the Al framework content responsible for zeolite acidity (Na and Somorjai 2015). Moreover, most catalytic reactions thrive in the presence of zeolites with fewer acid sites, as the use of catalysts with high number of acid sites is a disadvantage, because it leads to fast deactivation and shortens the catalytic lifetime (Feng et al. 2019). As such, the Si/Al, strength and distribution of Bronsted or Lewis acid sites, crystal size and framework can be altered accordingly during the synthesis process in order to enhance the catalytic activity of the synthesised zeolite material (Mohiuddin et al. 2018).

2.4 Synthesis of CFA-based zeolites

This section presents the synthesis techniques used to synthesise CFA-based zeolites, with focus on the three critical steps: activation and dissolution, pre-synthesis and hydrothermal treatment.

- Dissolution of Al and Si from CFA using a mineralising agent (hydroxyl anion, OH^-), which is responsible for increasing the solubility of silicon and aluminium from quartz and mullite CFA mineral phases. The OH^- also plays an important role as it facilitates the formation of silicate and aluminate gel (Mainganye et al. 2013).
- The pre-synthesis step involves the preparation of the synthesis solution by mixing the feedstock or reactants together in an arranged order, prior to the hydrothermal treatment step (Cornelius 2015). This step may be carried out under static or stirred conditions at room temperature or at elevated temperatures (Robson 2001).
- The hydrothermal synthesis step involves subjecting the pre-synthesis mixture to elevated temperatures for a set period of time to achieve crystal growth for the desired zeolite (Inada et al. 2005; Moliner et al. 2012).

Figure 2.3 shows a schematic diagram for the different synthesis methods used during the synthesis of zeolites at a laboratory scale. Each method is explicitly described as per the reviewed literature and categorised under either activation, pre-synthesis, or hydrothermal synthesis.

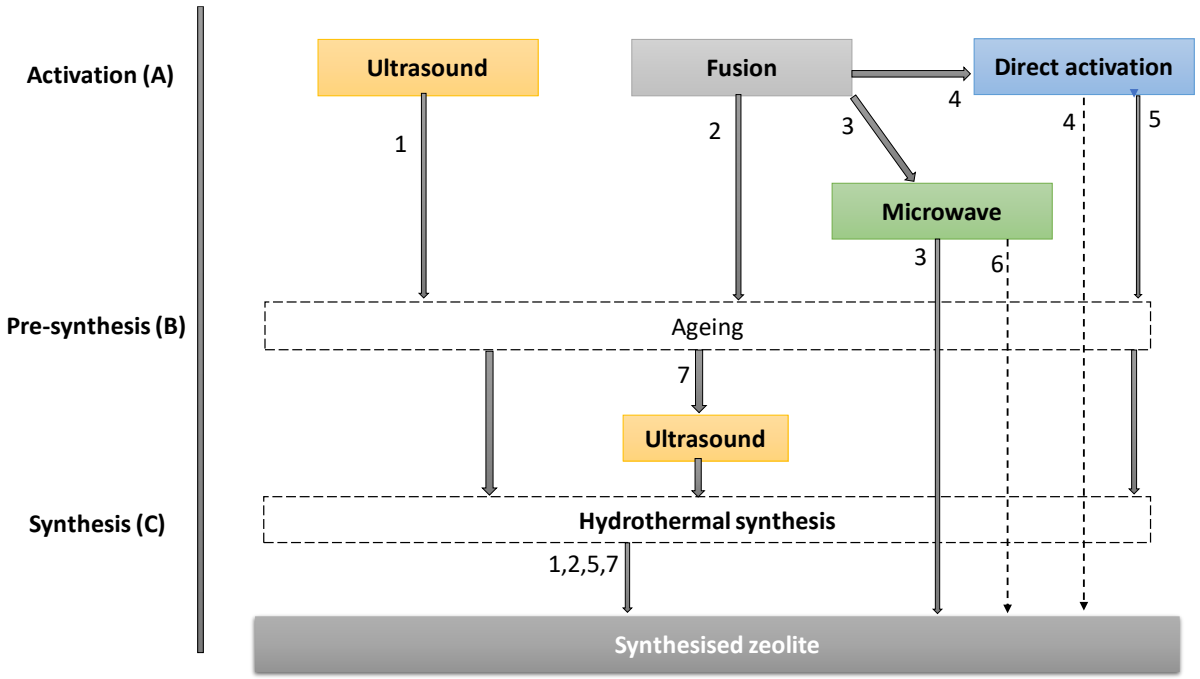

Figure 2.3: Coal fly ash-based zeolite synthesis processes, adopted and modified from (Belviso 2018). Note: (1, 7) Ultrasound-assisted method, (2, 3, 4) Fusion-assisted method, (4, 5) Direct activation and (3, 6) Microwave-assisted method

2.4.1 Activation of CFA

The synthesis of zeolites from fly ash requires the activation of fly ash with an alkaline reagent in order to dissolve Si and Al from quartz and mullite mineral phases. This section presents literature on the conventional pre-treatment methods used during the synthesis of CFA-based zeolites, which includes fusion assisted, microwave, ultrasound and sonochemical methods.

2.4.1.1 Fusion assisted method

The fusion assisted method (FAM) has been widely studied as a CFA activation technique prior to the synthesis of zeolites (Wang et al. 2008). FAM involves the heating of CFA + NaOH mixture at temperatures and times ranging from 450 - 650°C for 1-2 h respectively prior to the hydrothermal process (Figure 2.3 – 2) (Ruen-ngam et al. 2009; Rungsuk et al. 2006). During the fusion process, the crystalline and amorphous Si and Al bearing phases (quartz and mullite) in CFA are converted into sodium silicate and aluminosilicates, which promote the dissolution of Si and Al into the subsequent leachate solution, allowing zeolites to be synthesised from either the bulk fused CFA (process A) or the leachate solution (process B) in Figure 2.4 (Musyoka et al. 2012).

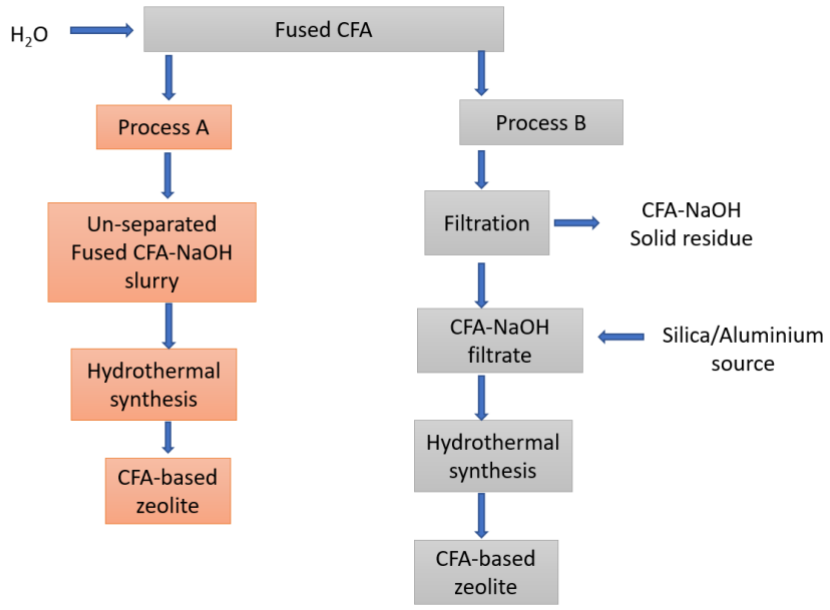

Figure 2.4: FAM synthesis process from unseparated and separated fused CFA-NaOH solution (Musyoka et al. 2012)

Moisés et al. (2013) reported the synthesis of zeolite Na A from sugarcane bagasse ash (SCBA) using the alkaline fusion assisted method. In their study, 30 g of SCBA was homogeneously mixed with NaOH in a ratio of 1:5. The mixture was heated in a nickel crucible in air at a temperature of 550°C for 40 min. The resultant fused mixture was dissolved in 1 L of distilled water and used as feed in the synthesis of zeolite Na A. In another study by Machado and Miotto (2005), zeolite Na A and X were synthesised from oil shale ash generated by the Petrosis process. In their study, oil shale ash of 2 g, Al_2O_3 of 0.95 g and NaOH of 4 g were placed in an open Teflon reactor and heated at 350°C in air for 2 h. The resulting fused mass was allowed to cool and thereafter mixed with 36 mL of deionised water and stirred for 1 h to allow homogenisation of the just-formed gel phase. The hydrothermal process was carried out using the reflux system at 100°C for a maximum time of 2 h.

Musyoka et al. (2012) reported the synthesis of Na A, X and P following the fusion hydrothermal process. In their experimental study, CFA was mixed with fine powder ground NaOH in a CFA/NaOH ratio of 1:1.2. The mixture was transferred into a crucible and heated in a furnace at a temperature of 550°C for 90 min. At completion, the mixture was ground to powder and mixed with ultra-pure water in a fused ash/water mass ratio of 1:5. The resultant slurry was stirred for 2 h to allow the dissolution of the Si and Al into the solution.

Zhang et al. (2011), investigated the synthesis of zeolite Na A, X and P from Chinese Class F fly ash using alkaline fusion followed by hydrothermal treatment. In their experimental study, 9 g of fly ash was mixed with NaOH powder in a ratio of 1:1.3 (w/w). The mixture was then placed

in a nickel crucible and heated in air at 600°C for 1.5 h. The mixture was thereafter transferred into a plastic bottle, followed by the addition of distilled water to form a fused fly ash solution. The respective zeolites were hydrothermally synthesised at 100°C for 9 h and applied as absorbent in the removal of ammonium from aqueous solutions. In another study, magnetically pre-treated fly ash was mixed with 25% $LiOH.H_2O$ and thereafter heated in a ceramic crucible in air at 980°C for 1 h. The resultant mixture was allowed to cool and then dissolved in a $LiOH.H_2O$ solution with a solid-to-liquid ratio of 1:2. The homogeneously mixed solution was thereafter poured into a stainless-steel autoclave and subjected to a hydrothermal process for a maximum temperature of 180°C for 12 h (Yao et al. 2009).

The activation of CFA using an alkaline activation agent represents a critical step in the synthesis of zeolites using any type of fly ash as a starting material. Studies have shown that the use of fusion prior to zeolite crystallisation resulted in a significantly increased dissolution of silicon and aluminium from CFA compared to the conversional synthesis method (Rungsuk et al. 2006). However, zeolites synthesised following the alkaline fusion method prior to the hydrothermal process are often pure phase (*if the clear filtrate was used as a precursor*), with small yields (Musyoka et al. 2012), and those synthesised from the bulk fused solution are often mixed phase with high yields (Du Plessis 2014; Mainganye et al. 2013; Medina et al. 2010). In addition, the average operating temperature for the fusion assisted method is approximately 650°C, making the process unattractive for adoption in industrial operations.

2.4.1.2 Ultrasonic treatment method

The ultrasound treatment method (UTM) has been defined as a range of vibratory waves operating at frequencies greater than 16 kHz, that when applied to a solution, generates a low pressure in the form of a wave which causes the formation of vapour bubbles, which then collapse at a high resolution, causing an intense acoustic cavitation (Ensminger and Bond 2011; Ojumu et al. 2016). Belviso et al. (2011) define ultrasound cavitation as a phenomenon that facilitates the growth and explosive collapse of microscopic bubbles, which creates hot spots in the solution or local temperatures greater than 4726°C, and cooling rates greater than 10^7°C/s (Ensminger and Bond 2011). The pressure and the high local temperatures, combined with extraordinarily rapid cooling, provide a unique means for dissolution and chemical reactions (Ojumu et al. 2016). Studies on the use of UTM in the conversion of different types and classes of CFA into zeolites prior to the hydrothermal process have been reported (Figure 2.3 - 1) (Aldahri et al. 2016; Belviso et al. 2011; Musyoka et al. 2012). Ultrasound treatment has been shown to accelerate the dissolution of Al and Si in the amorphous aluminosilicate mineral phase of CFA and increase the crystal growth during zeolite synthesis (Bukhari et al. 2016). Accordingly, Ojumu et al. (2016) investigated the possibility of replacing the high energy intensive fusion step with UTM during the activation of CFA prior to the hydrothermal synthesis

of zeolite Na A. In their study, 20 g of CFA was mixed with 100 mL of 5 M NaOH in a plastic sonication container and sonicated at 100% amplitude using 600 W Misonix S-400 sonicator. The recovered mixture was filtered, and the Si/Al ratio of the solution was adjusted accordingly using a sodium aluminate powder prior to the hydrothermal process. The authors reported that 10 min of high ultrasound intensity irradiation successfully replaced the high energy fusion step. They also reported that only the amorphous phase can be dissolved from CFA when the ultrasound treatment method was used with a Si and Al dissolution of 24%, compared to the 32% obtained through the fusion process. However, since the early disclosure by Ojumu et al. (2016), no other findings have been reported on the use of UTM as a replacement for the fusion step, although studies on the application of ultrasound energy on the synthesis precursor during the pre-synthesis step prior to the hydrothermal process are well documented (Figure 2.3 – 7) (Andaç et al. 2005; Belviso et al. 2013; Musyoka et al. 2012). The application of ultrasound during the pre-synthesis step has shown improvements in the rates, crystallisation time, yields and properties of the synthesised zeolite product (Andaç et al. 2005).

2.4.1.3 Direct activation method

The synthesis of zeolites from CFA by the direct activation method was first initiated by (Holler and Wirsching 1985). The method is carried out at low temperatures without significant energy consumption (Inada et al. 2005). The direct activation method involves mixing of the starting material (fly ash) with a mineralising agent (NaOH or KOH) and heating of the mixture at a temperature of 80-100°C for a specific time ranging from 24 to 72 h, depending on the desired zeolite product (Figure 2.3 – 5). In simple terms, this method involves direct hydrothermal conversion of a mixture of CFA and alkaline solution to zeolites (Berkgaut and Singer 1996). This method was considered to be fast, economical and less involved, and for some years was a preferred method to synthesise zeolites over the other methods, such as fusion, ultrasound and microwave (Chigondo et al. 2013). As a result, different types of zeolites in mixed phases have been synthesised using the direct activation method (Querol et al. 2001). The findings from these studies have led to several patents and publications in high impact journals (Harja et al. 2016; Inada et al. 2005). Studies on the effect of synthesis temperature, synthesis time, aging, Si/Al molar ratio and CFA/NaOH ratio during the synthesis of CFA-based zeolites using the direct activation method have been investigated (Izidoro et al. 2012; Juan et al. 2007; Querol et al. 1997). Kolay and Singh (2002), investigated the activation of lagoon CFA using NaOH and KOH as alkaline activation agents. The authors reported that the activation of lagoon CFA with 1 M NaOH led to the formation of zeolite NaP1 and hydroxysodalite using activation times of 12 and 24 h respectively. It was also shown that the activation of CFA with KOH did not lead to the formation of a zeolite. In another study, Querol et al. (1997) used CFA from different sources to investigate the effect of NaOH and KOH as activating agents prior to the synthesis of zeolites. The results obtained from their research showed a higher conversion

efficiency of NaOH solution than that of KOH solution; even at higher KOH concentrations of 1×0 M and 473 K, quartz and mullite could not be dissolved. Therefore, NaOH has been a preferred dissolution alkaline reagent compared to KOH, due to its high dissolution efficiency. Chareonpanich et al. (2011) reported the synthesis of zeolite A using subbituminous coal ashes with high crystalline silica content following the direct synthesis method. The authors reported that, in cases where low hydrothermal temperatures and low alkaline concentrations were used, the obtained zeolite was dominated by α-quartz as the main crystalline mineral phase. However, at slightly higher temperatures, the crystalline silica can be dissolved, which resulted in the formation of sodalite octahydrate. In addition to its dissolution inefficiencies, the direct activation method has also led to long synthesis time and mixed phases of zeolites with uneven zeolite crystals, due to the low heating rates in the synthesis mixture (Li and Yang 2008). As a result, there have been increasing efforts aimed at investigating alternative zeolite synthesis methods with improved heating mechanisms to achieve better purity and quality of zeolite materials. The direct activation method has been modified by introducing microwave heating mechanisms, which have been very instrumental in improving the dissolution of amorphous silica and in reducing the synthesis time required for zeolite synthesis. The use of the microwave-assisted method was first disclosed by the Mobil group in 1988 (Panzarella et al. 2007). The replacement of the conventional heating method by microwave heating has been considered a promising approach to significantly reduce the temperature, synthesis time, and eventually the costs associated with the synthesis of CFA-based zeolites (Schmidt et al. 2015).

2.4.1.4 Microwave-assisted method

The microwave-assisted method (MAM) is based on the application of electromagnetic radiation with wavelengths ranging from 1 m to 1 mm, with corresponding frequencies ranging between 300 MHz to 300 GHz (Musyoka et al. 2012). A brief overview on the use of MAM to synthesise different types of zeolites has been published by (Conner et al. 2004). The microwave process has been proven to reduce zeolite synthesis time from 48 h to 30 min (Behin et al. 2014; Conner et al. 2004; Querol et al. 1997). Arafat et al. (1993), have shown that the synthesis time can be reduced to as little as 10 min when compared to the conventional hydrothermal process, which could take up to 50 h. The microwave-assisted method has also been used as a silicon and aluminium dissolution process, whereby CFA + NaOH undergo a microwave heating for 30 min, in order to release the Si-Al bearing particles in CFA to facilitate the synthesis of the desired zeolite product (Jha and Singh 2016). Different types of zeolites (Na-P1, Na-X and Na-A) have been successfully synthesised using the microwave-assisted method (Ansari et al. 2014; Chandrasekhar and Pramada 2008; Querol et al. 1997). However, the purity of the zeolite products has been of great concern. Jha and Singh (2016), reported that the zeolites obtained from the microwave-assisted method contain unreacted CFA, which

can affect the characteristics of the synthesised zeolite and limit its industrial application. Although the use of the microwave-assisted technique can significantly reduce zeolite synthesis time, the method often results in zeolite products with small pore sizes, thereby limiting their industrial applications. The reviewed literature has shown that the use of microwave heating in zeolite synthesis has been successful at the laboratory scale, although studies on the industrial application of this method are not well reported.

2.4.2 Pre-synthesis stage

The pre-synthesis step (Figure 2.3 - B) involves mixing of the synthesis mixture in a synthesis vessel to allow aging and achieve homogeneity prior to the hydrothermal treatment step (Cornelius 2019). The process has been shown to have a significant influence on the crystallisation rate and time, crystal size and morphology of the zeolite product (Askari et al. 2013). The pre-synthesis step could either be carried out under static or stirred conditions at room temperature or at elevated temperatures in order to enhance zeolite nucleation (Robson 2001). Figure 2.3-B shows that aging during pre-synthesis is a crucial step and applicable in different synthesis processes, including fusion assisted, ultrasound as well as the direct activation method (Missengue et al. 2018; Musyoka et al. 2012; Ojumu et al. 2016). The effect of Si/Al ratio of the starting material, NaOH, water and the structure directing agent, hydrothermal synthesis time and temperature on the synthesis of zeolite ZSM-5 will be investigated in this study. These parameters are discussed in detail in the subsequent sections.

2.4.3 Hydrothermal synthesis of zeolites

Hydrothermal treatment (Figure 2.3 - C) is carried out (after mixing reagents and aging of the synthesis mixture) at a set temperature and time under static or stirred conditions, in order to convert the aluminosilicates in the pre-synthesis mixture into crystalline zeolitic materials. These parameters vary widely depending on the desired zeolite product (Mallapur and Oubagaranadin 2017). The hydrothermal synthesis step is also known as an incubation stage for crystal growth (Inada et al. 2005; Moliner et al. 2012). In order to understand the mechanism of zeolite formation, the effect of chemical (Si/Al ratio, NaOH structure, directing agent and water – instrumental in the composition of the molar regime) and physical parameters (time and temperature) on zeolite synthesis are investigated during this step.

2.4.3.1 Effect of Si/Al ratio

The Si/Al ratio of the synthesis gel plays a vital role in zeolite synthesis, as it determines the crystal structure of the end zeolite product (Cejka et al. 2007; Purnomo et al. 2012). Lower Si/Al ratio of the synthesis mixture favours the synthesis of low-silica zeolites such as zeolite A, P, sodalite etc (Chang and Shih 2000), while high-silica zeolites such as ZSM-5 and Beta crystallise at a Si/Al ratio ≥ 10 (Ameh 2019; Missengue et al. 2017). Alkalinity plays a vital role

in the Si/Al ratio of the synthesis mixture. Köroğlu et al. (2002) studied the effect of different alkalinities on the Si/Al ratio of zeolite synthesis gel. The authors showed that the use of low alkaline concentration hydrogel could enhance the Si/Al of the synthesised product, thereby improving its chemical and physical properties. In addition, ageing of the reaction or synthesis mixture at colder and less alkaline environments could have a significant effect on the Si/Al ratio of the synthesis mixture (Köroğlu et al. 2002; Shirazi et al. 2008). Shirazi et al. (2008), studied the effect of Si/Al ratio of ZSM-5 zeolite on its morphology, acidity and crystal size. The authors found that the crystal size of the synthesised zeolite ZSM-5 increased as Si/Al molar ratio increased. In addition, the authors showed that zeolites with low Si/Al ratios and small crystal size affect the stability of the zeolite framework (Shirazi et al. 2008). In this study, ZSM-5 zeolite will be synthesised from a CFA-based silica extract (extracted using an alkaline leaching method), in the presence of a structure directing agent. The Si/Al ratio of the feedstock (CFA-based silica) will be monitored to ensure the successful formation of the desired zeolite product.

2.4.3.2 Effect of the amount of NaOH

The synthesis of zeolites normally requires the use of a mineralising agent, with NaOH being the most commonly used. The OH- is known to enhance the solubility of silicate or aluminosilicate species in zeolite synthesis mixture (Xu et al. 2001). However, alkalinity could affect the stability of the organic structure directing agent at certain concentrations in the synthesis gel (Missengue 2016). Ren et al. (2011) reported that alkalinity has a great influence on the Si/Al molar ratio of zeolite ZSM-5 crystals and plays a major role in the dissolution rate of amorphous silica and aluminium hydroxide during the pre-synthesis process. Shigemoto et al. (1993), reported that higher alkaline concentrations enhanced the crystallisation kinetics of zeolite X from CFA. However, in another study Missengue (2016), elevated concentrations above 0.25 g of NaOH were reported to impede the formation of zeolite ZSM-5. Alkalinity has been reported to have an effect on the morphological structure, as well as the crystal size of the synthesised zeolite product (Köroğlu et al. 2002). Larlus and Valtchev (2004), studied the effect of KOH concentration on the particle size and morphology of LTL-type zeolite. The authors observed a gradual decrease in crystal size with an increase in alkalinity, shorter prismatic faces, and an abundant overgrowth of the crystals. In conclusion, increasing alkalinity concentrations in the synthesis gel has been shown to increase the nucleation of zeolite and decrease the crystal size. In the current study, the effect of NaOH on the morphology and crystal size of the zeolite products will be investigated.

2.4.3.3 Effect of water content

Water content plays a significant role in the crystallization rate of zeolites and may be varied in a specific range in order to alter the concentration of the synthesis reaction to achieve a

specific zeolite product (Cornelius 2015; Shirazian et al. 2014). The use of low water content in the synthesis hydrogel has been shown to accelerate the growth of zeolite crystals Shirazian et al. (2014) and in contrast, a diluted synthesis hydro gel reduces the concentration of reactive species in liquid phase, and thus decreases the crystal growth rate (Mousavi et al. 2013). Yu (2007), reported that diluting the synthesis hydrogel results in lower supersaturation, which favours the crystal growth process over the nucleation process, thus resulting in zeolite with large crystal size. Water content can also be used to control the crystallinity, particle size and yields of zeolite products (Shirazi et al. 2008). The variation of water content during zeolite synthesis was also shown to enhance the quality of the product and could be used to monitor the crystallisation efficiency of zeolite products (Missengue 2016). Furthermore, the increase in water content during the synthesis of high-silica zeolite ZSM-5 was shown to increase the purity of the zeolite product (Missengue 2016). This study also aims to investigate the effect of water content during the crystallisation of zeolite products synthesised from the CFA-based silica extracts.

2.4.3.4 Effect of structure directing agent

Structure directing agents (SDA) are inorganic or organic molecules that are used to facilitate the crystallisation of the synthesis hydrogel into specific zeolite structures (Itabashi et al. 2012). The most commonly used structure directing agents for high-silica zeolite synthesis are tetrapropylammonium bromide (TPABr), tetraethylammonium hydroxide (TEAOH) and tetrapropylammonium hydroxide (TPAOH) (Abrishamkar et al. 2010; Askari et al. 2013; Missengue 2016). SDA play an important role on the type and quantity of zeolite produced, crystal size and the morphology (Miar Alipour et al. 2016). Crea et al. (1988) investigated the effect of TPABr/SiO_2 ratio on the crystallisation of Silicalite 1 and the results showed that the crystallisation rates of silicalite increased with the increase in TPABr concentrations. In another study by Xue et al. (2012), it was shown that the use of higher TPABr/SiO_2 ratio promoted additional nucleation in the synthesis hydrogel due to its strong nucleation ability, which resulted in smaller crystal size of the synthesised zeolite product. Similarly, Modhera et al. (2009) studied the effect of the TEAOH/SiO_2 ratio on the crystallisation of zeolite BEA and concluded that the use of a higher TEAOH/SiO_2 ratio favoured the crystallisation of smaller zeolite crystals. This study will also investigate the effect of TPABr on the morphology and crystal size of zeolite ZSM-5.

2.4.4 Hydrothermal physical parameters

The hydrothermal synthesis time and temperature have an important role on crystal size, morphology, crystallinity and surface area of the synthesised zeolite product. This section presents literature on the effect of these parameters on zeolite synthesis.

2.4.4.1 Effect of synthesis time

Bohra et al. (2014) investigated the crystallisation of Na-A and Na-P with respect to the synthesis time using agro-waste as a source of silica and aluminium. The results obtained from their study showed that, with the increase in synthesis time, metastable Na A zeolite was transformed to a more thermodynamically stable small-pore Na-P zeolite, showing that increased hydrothermal time can cause phase change to occur. In contrast, Dey et al. (2013) studied the effect of time on the synthesis of a template-free zeolite ZSM-5 from rice husk ash. The authors reported that the surface area and pore volume of the synthesised zeolite increased significantly with the increase in the synthesis time, which shows that an adequate synthesis time is required to acquire a good quality zeolite product. Prasetyoko et al. (2012) studied the phase transformation of rice husk ash in the synthesis of ZSM-5 without organic template and found that, at crystallisation times of greater than 48 h, zeolite ZSM-5 crystals had completely transformed into a more stable quartz phase. Their study showed that prolonged crystallisation time could result in several phase transformations in the synthesis mixture. The same findings are also reported by Mallapur and Oubagaranadin (2017). Bayati et al. (2008) studied the hydrothermal synthesis of nanostructure Na A zeolite and found that the reaction time had a great effect on the crystallinity of the synthesised zeolites. Moreover, the crystal size of ZSM-5 increased with an increase in synthesis time (Kumar et al. 2002). Surface area and crystal size play an important role in the catalytic application of zeolites. Zeolites with small crystal size have high external surface areas and short diffusional paths, which can have significant effect on product distribution in catalytic reaction (Shirazi et al. 2008), hence the synthesis time can be used to tailor zeolite particle size for specific reactions.

2.4.4.2 Effect of synthesis temperature

The effect of synthesis temperature on zeolite synthesis has been studied by many researchers due to its significant effect on zeolites synthesis (Bayati et al. 2008; Kovo 2012; Musyoka et al. 2012). Temperature plays a significant role on the rate of crystallisation, crystal size and morphology of the synthesised zeolite materials (Cornelius 2015; Liu et al. 2010). Bayati et al. (2008) indicate that an increase in the reaction temperature results in larger zeolite crystal sizes. Hui and Chao (2006), studied the effect of the synthesis temperature on the crystallisation of CFA-based zeolite material. The authors reported that at higher synthesis temperatures, the rate of crystallisation was greater. In addition, the synthesis time was reduced significantly without compromising the crystallisation of the final product. The hydrothermal synthesis temperature can cause phase change if too high or low, or can be used to tailor zeolite properties if optimised (Shirazi et al. 2008). Oleksiak and Rimer (2014) showed that higher temperatures form denser zeolite phases and promote Ostwald ripening. It is thus crucial to monitor and control the hydrothermal synthesis temperature in order to achieve the desired zeolite product. Kovo (2012) reported that the use of shorter synthesis time in zeolite

synthesis can potentially reduce the cost of energy and time required to obtain a zeolite material. It is therefore important to investigate the effect of temperature during the hydrothermal synthesis of CFA-based zeolite ZSM-5 in order to have a broader understanding of the production cost.

2.3.4 Recycling of liquid waste during zeolite synthesis

The processes listed in Figure 2.3 generate enormous volumes of liquid waste (often containing complex chemical composition), at different synthesis stages, which requires further management strategies. The disposal or treatment of complex liquid waste is costly and thus requires cost-effective and efficient waste management strategies. To this effect, Du Plessis (2014) has design a liquid waste management protocol, whereby the liquid waste resulting from the hydrothermal synthesis can be minimised by means of recycling. The author showed for the first time that 100% of the liquid waste can be recycled without compromising the quality of the zeolite product. The adoption of the recycling protocols developed by the author at a larger scale would not only offer financial relief, but also counter the environmental burden associated with processing the synthesised liquid waste. However, the treatment of liquid waste generated during the pre-synthesis step, such as treatment of the silica extract, has not yet been reported. Hence this study aims to introduce a recycling mechanism after the silica treatment step in order to minimise the liquid waste generated.

2.3.5 Synthesis of zeolite ZSM-5 and sodalite from CFA.

A summary of the literature on the synthesis of ZSM-5 and sodalite zeolite from CFA and their applications is presented in this section.

2.3.5.1 ZSM-5

The first report on the synthesis of zeolite ZSM-5 was published by Argauer and Landolt from Mobil.Co in 1972 (Xue et al. 2012). ZSM-5 is a member of the MFI structure type with 10-membered ring pore windows made of a Si/Al ratio ranging between 10 and several thousands (Bindhu and Sugunan 1998). As shown in Figure 2.5, the MFI framework incorporates S5Rs that combine to generate pentasil units (5^8 units). A three-dimensional network of interconnected pores is created when pentasil units are linked together by oxygen bridges to create pentasil chains (Cornelius 2019).

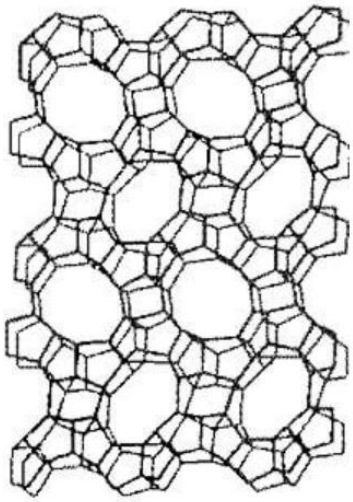

Figure 2.5: Framework structure of ZSM-5 zeolite, adopted from Bindhu and Sugunan (1998)

ZSM-5 zeolite is synthesised from silica-rich materials in the presence of an organic template agent such as TPABr, TPAOH and TEABr (Kasture et al. 2005; Rani et al. 2016). However, recent studies have shown that, in a much narrower compositional space, template-free zeolites can be achieved (Pan et al. 2014; Prasetyoko et al. 2012). ZSM-5 zeolites are well known for their shape-selective properties, and as a result have been used as solid catalysts and as shape selective matrices in hydrocarbon transformation reactions (Bindhu and Sugunan 1998). Due to their unique physicochemical properties, these zeolites have a wide range of industrial applications. ZSM-5 zeolite is primarily used as a catalyst in a number of catalytic reactions, due to its acid strength, which is inversely proportional to the number of Al in the framework. The acid strength decreases more specially when there are more Al atoms affects the acidity of zeolite acid strength and it decreases in series Al(OH)Si > Ga(OH)Si > Fe(OH)Si > In(OH)Si > B(OH)Si (Palčić and Valtchev 2020).

The synthesis of zeolite ZSM-5 from different fly ashes has been reported by several researchers, although this required the addition of aluminosilicate reagent into the hydrogel solution to adjust the Si/Al ratio (Anuwattana et al. 2008; Chareonpanich et al. 2004; Kalyankar et al. 2011). Missengue et al. (2017), studied the transformation of South African fly ash into ZSM-5 and its application as catalyst for the conversion of methanol to Olefin reactions. The authors showed for the first time that high-silica zeolites can be synthesised from fly ash without the addition of an aluminosilicate material, by selectively extracting silica from CFA using the fusion process. The synthesis hydrogel contained the following molar regimes: 10 Si, 1 Al, 50 Na, 3473 H_2O, 4 TPABr, and the hydrothermal synthesis was carried out at 160 ^oC for 72 h. In contrast, Cornelius (2019) showed that high-silica zeolite such as ZSM-5 can be synthesised from Si-extract obtained from the alkaline extraction process without oxalic acid treatment. However, this method required the addition of sodium aluminate, and the product was a mixed phase of ZSM-5 and mordenite. The current study seeks to explore the synthesis

conditions developed by Missengue et al. (2017) to investigate the synthesis of ZSM-5 zeolite using fly ash silica extract obtained through the alkaline leaching process without the oxalic acid Si/Al ratio adjustment step. Moreover, to investigate the conversion of the secondary solid waste generated during the extraction process into a low-cost sodalite zeolite of commercial value.

2.3.5.2 Sodalite

Sodalite zeolite is a cubo-octahedra unit (Figure 2.6), with a framework structure consisting of a six-membered ring aperture with a pore size of 2.8 Å (Yao et al. 2006). This type of zeolite is well known for its hydrophilicity and dense phase, with a Si/Al ratio of 1 (Van Niekerk 2005). Its pore sizes are less than those of zeolites with eight-membered rings, such as Na A, which has a pore size of 3.8 Å (Chudasama et al. 2005). The extreme similarities of sodalite zeolite with other low-silica zeolites such as Na-X, NaP, Na-A zeolites, with high ion-exchange capabilities, has led to great interest in sodalite synthesis processes (Novembre et al. 2010).

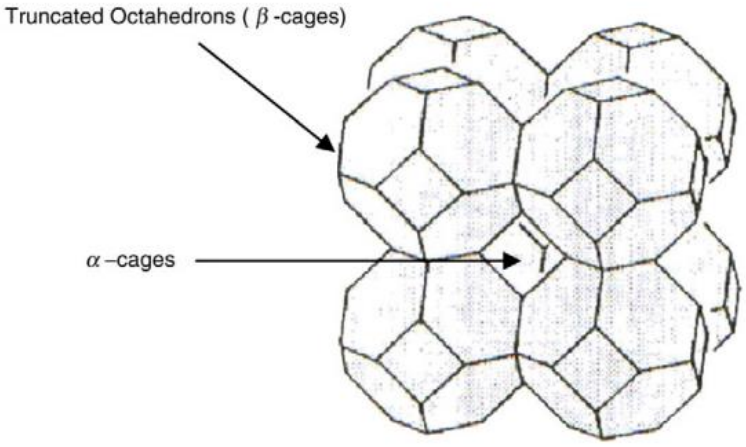

Figure 2.6: Framework structure of sodalite zeolite, adopted from Kazemimoghadam and Mohammadi (2011)

Sodalite zeolite can be synthesised from commercially-sourced and natural Si- and Al-rich materials through a direct hydrothermal process in the presence of an alkaline agent such as NaOH. Kazemimoghadam and Mohammadi (2011) investigated the synthesis of sodalite using natural kaolin as a feedstock. The process was carried out as follows: kaolin was calcined in a furnace at 700˚C for 3 h, and the resultant kaolinite was mixed with NaOH in an autoclave and subjected to a hydrothermal process at 100˚C for 24 h. The authors reported that the zeolite formed was a mixture of sodalite and mullite mineral phase. In another study, Shabani et al. (2022) investigated the synthesis of sodalite from coal fly ash. This was achieved by mixing CFA and 5M of NaOH in a solid-to-liquid ratio of 1:1. The mixture was thereafter transferred into a 100 mL Teflon container and hydrothermally synthesised in an oven at 140˚C for 48 h. However, the resultant product was a mixed phase of sodalite, Na P, Na X and quartz mineral

phases, which shows incomplete dissolution of the quartz mineral phase initially present in CFA. In a recent study, Cornelius (2019) directly synthesised sodalite zeolite from a solid residue obtained after the alkaline leaching of amorphous silica (150˚C for 24 h), and the zeolite product was also a mixed phase of sodalite, quartz and mullite.

Owing to its small pore size, sodalite zeolite has been used as a molecular sieve or membrane in the separation of small molecule gases such as H_2, He, H_2O or NH_3 from various gas streams (Gouzinis and Tsapatsis 1998; Julbe et al. 2003; Lee et al. 2006). Sodalite zeolite has also been used as a catalyst in the production of biodiesel (Shabani et al. 2022). Due to its high ion exchange capability, sodalite zeolite has been used as an adsorbent in wastewater management (e.g. removal of lead ions in water) (Golbad et al. 2017). This study will explore the transformation of the solid waste resulting from the alkaline leaching process into a low-cost sodalite zeolite using the method reported by Cornelius (2019).

2.4 Technology economic feasibility

Zeolite synthesis from fly ash has advanced greatly in the past decade (Cornelius 2019; Missengue 2016; Musyoka et al. 2011; Shabani et al. 2022), however technology feasibility studies to determine their viability are lacking. Technology cost estimation plays an integral part in chemical and manufacturing processes in determining their viability and scalability in order to guide investment strategies for large scale production (Aboudi et al. 2021; Rani et al. 2016). Strategic decisions on whether to approve a project for further development in most chemical industries (including research institutions) are guided by counterbalance estimates of operational expenditure (OpEx) and capital expenditure (CapEx) (van Amsterdam 1918). With the rate of CFA generation and its disposal into the environment, the development of scalable synthesis processes for the valorisation of the waste material is a matter of urgency. Recently, Hong et al. (2017) designed a cost estimation model with a capacity of 5000 kg/h for the production of Na A zeolite from CFA using the fusion method. The authors showed that their process was profitable and achieve a net present value of approximately R2 billion for a 20-year plant operating life, within a payback period of 7.1 years. Their study also showed that the conversion of CFA into valuable products as an alternative to current CFA disposal strategies is promising. Inevitably, the economic feasibility of ZSM-5 and sodalite zeolite synthesised from CFA will also be investigated in this study (Chapter 6). This section presents literature on the importance of conducting a technology economic analysis, cost estimate classifications and available methodologies.

2.4.1 Capital cost estimate matrix

The cost estimation classification matrix is used as a guide to determine project cost estimates in order to evaluate, approve, and/or fund projects in research and development or process

industries (Christensen et al. 2005). The process flow diagrams (PFDs), and pipe and instrument diagrams (P&IDs) are used as the main defining scope for the cost estimation. Cost estimates can be categorised into five classes (Table 2.3) by the American Association of Cost Engineers (AACE), ranging from 5 to 1, with Class 5 being the most imprecise assessment, and Class 1 the most certain. In the conceptual phase, estimates for Classes 3, 4, and 5 are prepared to compare alternative methods or processes. The cost of conducting a cost estimate is closely linked to the preparation effort, since it mainly consists of engineering salaries. As such, cost estimates for projects categorised under Class 5, 4 and 3 would require a minimal budget compared to those in Classes 2 and 1 (van Amsterdam 1918). In addition, cost estimates for projects under Class 4 and 5 are commonly used in processes with limited costing information, and subsequently have a wide accuracy range (Christensen et al. 2005). Due to the level of project maturity for projects categorised under Classes 4 and 5, the AACE recommends that cost estimations be performed using the factored estimating technique. This relies mainly on historical data, using statistical inferential or modelling (Walton and Sorrels 2017). Given the scale of the project, as technically demonstrated in the previous chapters, the cost estimation performed in this study was based on assumptions generally applied for projects within the Class 5 cost category, as recommended by AACE (shown in Chapter 6, Table 6.3).

Table 2.3: Cost estimation classification matrix, adopted from Christensen et al. (2005)

	Primary characteristic	Secondary characteristic			
Estimate class	**Level of project definition (expressed as % of complete definition)**	**End usage (purpose of estimate)**	**Methodology**	**Expected accuracy range (variation in low and high ranges (a))**	**Preparation effort (degree of effort relative to least cost index 1 (b)**
Class 5	0% - 2%	Concept screening	Capacity factored, parametric models, Lang factor and etc.	L: -20% to -50 %, H: +20% to +100%	1
Class 4	1% - 15%	Study or feasibility	Equipment factored or parametric models	L: -15% to -30 %, H: +20% to +50%	2 to 4
Class 3	10% - 40%	Budget, authorisation, or control	Semi-detailed unit costs with assembly-level line items	L: -10% to -20 %, H: +10% to +30%	3 to 10
Class 2	30% - 70%	Control or bid/tender	Detailed unit cost with forced detailed take-off	L: -5% to -15 %, H: +5% to +20%	4 to 20
Class 1	50% - 100%	Check estimate or bid/tender	Detailed unit cost with detailed take-off	L: -3% to -10 %, H: +3% to +15%	5 to 100

Note: (a) The state of process technology and availability of applicable reference cost data affect the range markedly. The +/- value represents typical percentage variation of actual costs from the cost estimate after application of contingency (typically at a 50% level of confidence) for given scope.

(b) If the range index value of “1” represents 0.005% of project costs, then an index value of 100 represents 0.5%. Estimate preparation effort is highly dependent upon the size of the project and the quality of estimating data and tools.

2.4.2 Capital cost estimation techniques

Capital cost estimation can be performed using different techniques or methods, and each technique may be associated with a level of accuracy or class (Table 2.3) (Christensen et al. 2005). However, the selection criteria for the type of technique to be used is informed by the process stage of development, during which a cost estimation is performed. Presented below is a list of capital cost estimation techniques based on the work of Coulson and Richardson (1999).

2.4.2.1 Historical cost estimate

Historical cost estimates are commonly used to perform a quick estimate of the total investment required, based on historical knowledge (e.g., plant capacity and capital cost) of similar manufacturing processes. The capital cost is thus expressed as:

$$C_2 = C_1\left(\frac{S_2}{S_1}\right)^n \quad \ldots\ldots\ldots\ldots\ldots\ldots \textbf{Equation 2.1}$$

Where C_1 and C_2, denotes capital cost of the project with capacity S_1 and S_2 respectively. n represents the index, traditionally taken as 0.6. This method, however, is only applicable if sufficient data is available.

2.4.2.2 Step counting method

Step counting techniques are useful during the conceptual stage, where approximate cost estimations are needed to compare alternative processes and/or inform the next steps in the process design (Coulson and Richardson 1999). This method uses a number of significant processing steps in the overall process to determine the capital cost. Equation 2.2 (used for plants with capacity under 60 000 tonne per year) and 2.3 (used for plants with capacity above 60 000 tonne per year) are commonly used to estimate the capital cost in plants that are predominantly liquids and/or solids (Sinnott and Towler 2019).

$$C = 130{,}000\, N\left(\frac{Q}{s}\right)^{0.30} \quad \ldots\ldots\ldots\ldots\ldots\ldots \textbf{Equation 2.2}$$

$$C = 150\, N\left(\frac{Q}{s}\right)^{0.675} \quad \ldots\ldots\ldots\ldots\ldots\ldots \textbf{Equation 2.3}$$

Where C = capital cost in pounds sterling, N = Number of functional units, Q = plant capacity, tonnes per year and s = reactor conversion (see equation 2.4.)

$$s = \frac{\boldsymbol{mass\ of\ desired\ product}}{\boldsymbol{mass\ reactor\ input}} \ldots\ldots\ldots\ldots\ldots \boldsymbol{Equation\ 2.4}$$

2.4.2.3 Factorial methods

The factorial cost estimation technique is often used in the early stages of project design. This technique is based on preliminary flowsheets and lists of sized equipment, using equation 2.5. The factors give an estimate of the equipment costs, which is then used to estimate the indirect and direct costs. The technology economic analysis performed in this study was based on the factorial method, using costing flowsheet data available in literature Coulson and Richardson (1999).

$$\boldsymbol{Cf = f_L C_e} \ldots\ldots\ldots\ldots\ldots\ldots \boldsymbol{Equation\ 2.5}$$

where Cf = fixed capital cost, C_e = the total cost of all the major equipment's, and f_L = the "Lang factor" (depends on the type of process used).

Table 2.4: Lang factor and fixed cost estimation factors for different process plants (Coulson and Richardson 1999)

	Process type		
	Solids	**Fluids**	**Mixed fluids-solids**
Lang factor	3.1	4.7	3.6
f_1	0.5	0.4	0.45
f_2	0.2	0.7	0.45
f_3	0.1	0.2	0.15
f_4	0.1	0.1	0.1
f_5	0.05	0.15	0.1
f_6	0.25	0.5	0.45
f_7	0.25	0.15	0.2
f_8	0.05	0.05	0.05
f_9	0.3	0.15	0.2
f_{10}	0.2	0.3	0.25
f_{11}	0.05	0.05	0.05
f_{12}	0.1	0.1	0.1

2.4.2.5 Detailed factorial estimates

The detailed factorial estimates are used to conduct a more precise and accurate capital cost estimation. This technique relies on the accuracy of the available cost data and the design of the process, with all the costs identified and included (Coulson and Richardson 1999). This technique is generally used to estimate costs for more advanced processes, where costing data for the overall process is available. More information on the different cost estimation methods are detailed elsewhere (Christensen et al. 2005; Mewes 1997; Sinnott and Towler 2019).

2.5 Conclusion

This review aimed to highlight the literature relevant to the research topic and pinpoint the gaps that the current study aimed to investigate. The focus of this study is on the synthesis of high-silica zeolite ZSM-5 and sodalite zeolite from coal fly ash. The conversion of CFA into zeolite materials has been studied extensively, resulting in several new approaches being researched and adopted to utilise CFA, not only to reduce the impact of its disposal upon the environment but also to advance the production of value-added products (Ameh et al. 2020; Cornelius 2019; Ndlovu 2016; Shabani et al. 2022)

The synthesis of pure phase zeolite is mainly dependent upon the dissolution technique employed to release the Si and Al bearing phases of CFA into the synthesis solution. Recent research has shown that pure phase ZSM-5 zeolite can be synthesised from CFA without the addition of silica or alumina sources, through selective extraction of silica from CFA using either the fusion process (Missengue et al. 2018) or alkaline treatment (Cornelius 2019; Ndlovu 2016). However, the extracted silica requires further treatment with oxalic acid in order to adjust the Si/Al ratio and the removal of excess sodium and other impurities in the extract prior to the hydrothermal process. Although pure phase high-silica ZSM-5 zeolite can be synthesised successfully through this method, the process involves several challenges or drawbacks, which could limit its implementation at a larger scale.

- The use of a chelating agent, such as oxalic acid, during the treatment step (Si/Al adjustment) comes with exorbitant costs, including the purchase of the reagent and disposal of the resultant liquid waste. The treatment of highly concentrated waste streams in chemical processes is generally high, and these costs may not be justified if large scale production is desired. This study aims to reduce the cost associated with producing ZSM-

5 from CFA by eliminating the use of the oxalic acid step and employing recycling mechanisms in order to minimise the liquid waste generated during the treatment process.

- CFA-based ZSM-5 zeolite has been produced at a hydrothermal synthesis temperature of 160˚C for 72 h (Cornelius 2019). These conditions are extreme and could negatively impact on the production rate and viability of the synthesis process. The impact of reduced synthesis time or temperature on the quality of ZSM-5 zeolite will also be investigated, with the view to minimising the energy implication arising from its synthesis over an extended period of time, and to boost its market competitiveness.

- The synthesis of zeolites from CFA is also known to generate massive secondary solid waste, which is often left untreated (Missengue 2016). This study also aims to investigate the synthesis of sodalite zeolite in order to achieve a zero-waste synthesis process that could easily be optimised and adopted at industrial scale.

- The technology economic analysis is important in the design and viability of a process. Although the synthesis of CFA-based zeolites has successfully been demonstrated at a laboratory scale, the adoption of these processes in the market relies significantly in the economic viability of the synthesis process. Recently, cost estimations for the production of low-silica zeolites such as Na A and X have been reported: Hong et al. (2017) investigated the synthesis of zeolite Na A from the bulk fused CFA, and added $NaAlO_2$ to adjust the Si/Al ratio. The recovered product was a mixture of Na A and hydroxysodalite zeolite. A techno-economic analysis was performed for the production of Na A from CFA using the fusion method. The authors showed that the process, with a capacity of 5000 kg/h, achieved high profitability, resulting in a payback period of 7.1 years over a 20-year operating period. Although the process has been deemed profitable, the quality and purity of the zeolite product will affect its intended commercial selling price, which might have a huge impact on the viability of the overall process

- In another study, Panitchakarn et al. (2014) synthesised zeolite Na A and X from CFA using acid pre-treated fused bulk CFA. The resultant product was a mixed phase of Na A, Na X and sodium aluminium silicate hydrate. The authors performed a rough cost estimate for producing CFA-based zeolites using the fusion method. Their cost estimate considered only the total equipment and material costs of producing the zeolites at a laboratory scale

(13 g of zeolite per batch), then scaled this to a larger scale (1.5 kg per batch). The authors reported that the total expense for producing zeolite at a laboratory-scale was approximately R8 400 per kilogram and the price was significantly reduced to R330 per kilogram in a scaled-up process. These studies present a roadmap towards commercialisation of low-value CFA-based zeolites. However, there is still a need to perform a techno-economic analysis for CFA-based zeolites synthesised using various synthesis methods in order to identify a marketable CFA-based zeolite synthesis process:

- Low and high content silica zeolites,
- Pure and mixed phase zeolites,
- Zeolites synthesised using bulk CFA, liquid and solid CFA extracts,
- Zeolites synthesised through alternative synthesis processes, e.g., direct hydrothermal process, ultrasound-assisted, sono-chemical treatment, microwave-assisted method and alkaline leaching-assisted method.

Despite the limited information on techno-economic analyses for the production of CFA-based zeolites, this study seeks to perform a techno-economic analysis with particular focus on pure and high-silica ZSM-5 zeolite (synthesised from an alkaline leaching process) and low-value sodalite zeolite (synthesised from solid residue resulting from the alkaline leaching process).

CHAPTER 3
MATERIAL, EXPERIMENTAL AND ANALYTICAL TECHNIQUES

3.1 Synopsis

This chapter details the materials, chemicals and equipment used in this study. It also highlights the experimental procedure, material sampling and storage procedures followed to achieve the aims and objectives outlined in Chapter One. Furthermore, the analytical techniques used to analyse the starting materials and final products are also presented in this chapter. The experimental approach was systematically designed in order to address the research questions set out in Chapter One of this thesis, and is presented in Figure 3.1.

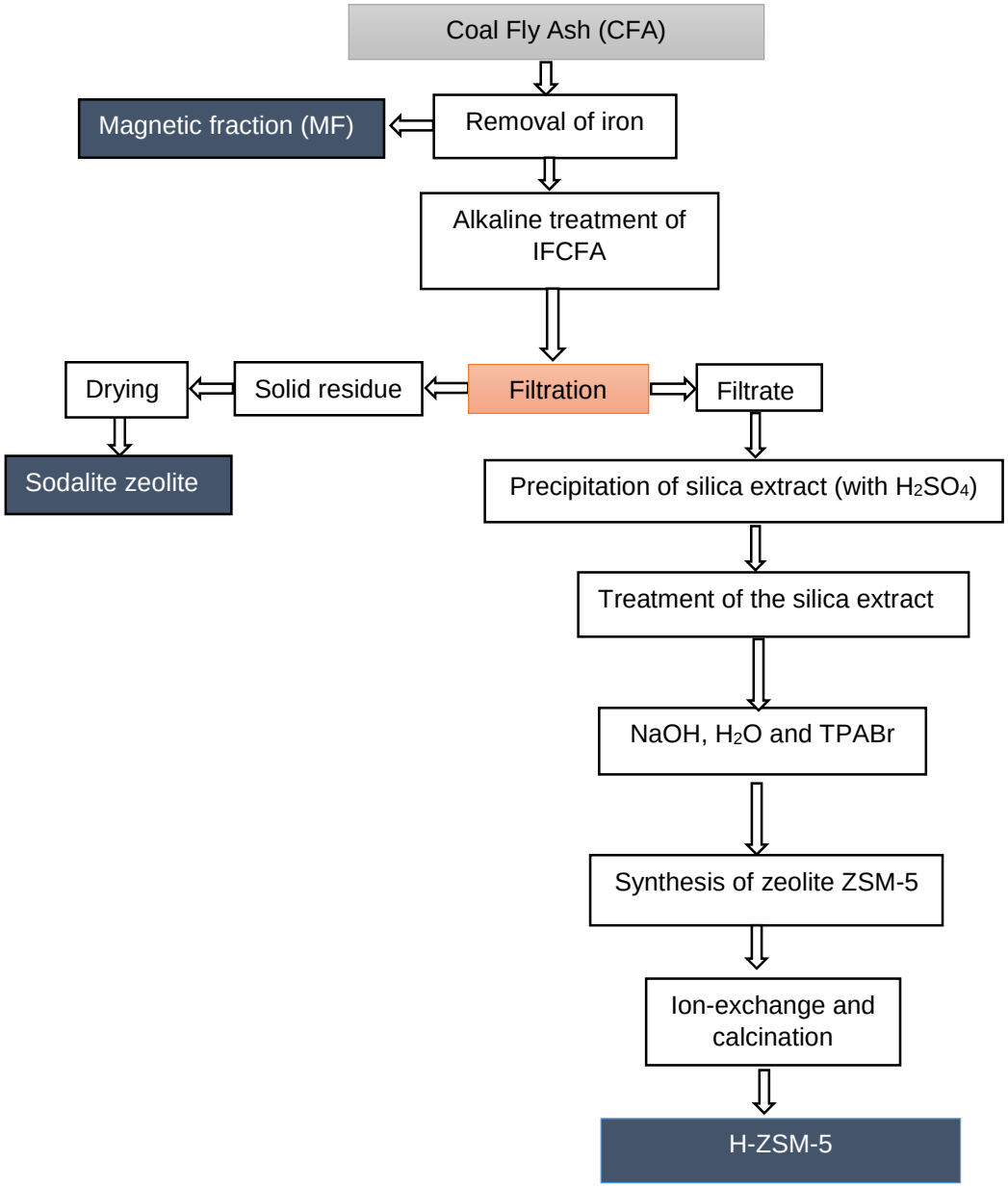

Figure 3.1: Experimental approach process flow diagram

3.2 Materials and chemicals

The storage, sampling procedure of the as-received Matla CFA, list of chemicals, and equipment used in this study are presented in this Section.

3.2.1 Sampling and storage of raw materials

The CFA used in this study was sampled from the Matla Eskom power station, situated in the Mpumalanga province in South Africa. The ash was sampled using 25 L containers, which were then sealed and stored in a dark place at room temperature to limit changes in CFA composition. For the purpose of this research, only one batch was used throughout the duration of the project to minimise variations in quality and quantity of the final products.

3.2.2 List of chemicals

The list of chemicals used in this study, their purity and suppliers is presented in Table 3.1 below.

Table 3.1: List of chemicals, purity and suppliers

Chemicals	Supplier	Purity (%)
Sulphuric acid (H_2SO_4)	Sigma-Aldrich	95 – 99
Sodium Hydroxide (NaOH) pellets	Kimix	98
Hydrochloric Acid (HCl)	Science World	32
Hydrofluoric Acid (HF)	Kimix	48
Nitric Acid (HNO_3)	Kimix	55
Boric Acid (H_3BO_3)	Kimix	99.5
Tetrapropylammonium bromide (TPABr)	Sigma-Aldrich	98
Ammonium nitrate (NH_4NO_3)	Sigma-Aldrich	98
Oxalic acid (OA)	Kimix	99.8
Silicone oil 350 VISCOSITY 5LT	Science World	350 viscosity

3.2.3 List of equipment

The list of equipment for extraction, synthesis and characterisation used in this study is presented in Table 3.2 below.

Table 3.2: List of equipment

Equipment name	Model	Specifications
Round-bottom flask	/	250 mL
Magnetic stirrer	/	/
Teflon-lined stainless autoclave	*	100 mL
Hot plate	Lab Smart MS-H-Pro	T_{max}=340°C
Heavy duty laboratory oven or dryer	Scientific Series 2000	T_{max} =250°C
Laboratory furnace	Thermo Scientific	T_{max} =1000°C

Note: * custom made, / Information not available.

3.3 Methodology

The different methods, experimental setup, conditions and parameters applied during the experimental work of this research are presented in this section. This chapter also includes the methods applied during the characterisation of the starting materials, intermediate and final products.

3.3.1 Extraction of magnetic fraction (iron) and silicon from Matla CFA

Iron and silicon were extracted from the as-received Matla CFA following the experimental procedure developed by Ndlovu (2016).

3.3.1.1 Extraction of iron from CFA

100 g of CFA was mixed with 250 mL of deionised water in a solid-to-liquid ratio of 1:2.5 and stirred for 6 h at room temperature (Figure 3.2). A magnetic stirrer was used to recover the magnetic fraction (MF) from the slurry, which was achieved by placing the stirrer inside the CFA slurry. The MF was recovered from the magnetic stirrer by washing using deionised water. The process was repeated three times to ensure that most of the iron was recovered. The remaining iron-free CFA (IFCFA) slurry and the recovered MF were both filtered and dried overnight at 70°C. At completion, a portion of the solids were sampled separately and digested following the procedure presented in Section 3.4.1.1, and analysed by inductively coupled plasma atomic emission spectrometry (ICP-AES) as detailed in Section 3.4.1 of this chapter. The remaining IFCFA was used as a feedstock in the extraction of silicon.

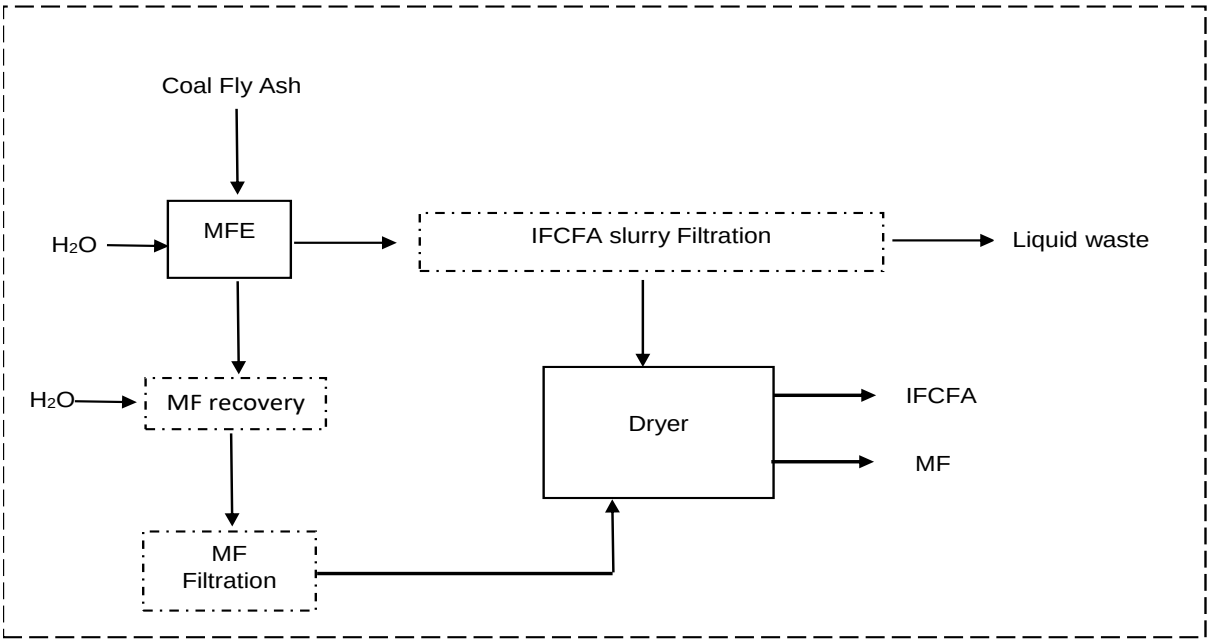

Figure 3.2: Iron extraction block flow diagram. Where MFE = magnetic fraction extract process, IFCFA = iron-free coal fly ash and MF = magnetic fraction

3.3.1.2 Alkaline extraction of silicon from IFCFA

To extract silicon, 50 g of the dried IFCFA was weighed and mixed with 8 M NaOH solution of 250 mL in a round-bottom beaker and heated at 150˚C under reflux conditions for 24 h (Figure 3.3), while stirring at 250 rpm. At completion, the mixture was filtered while still hot and the recovered silicon-rich filtrate was collected and poured inside a conical flask. The filtrate was thereafter precipitated by adding concentrated H_2SO_4 dropwise, while stirring at 100 rpm until the solution reached a pH of ~10. The formed untreated CFA silica extract (UFSE) precipitate was then filtered and dried overnight at 70°C. The resulting solid residue (SR) and UFSE were thereafter dried overnight at 70°C and analysed by XRF, XRD, SEM and FTIR. The dried SR was transformed into a low-silica sodalite zeolite, as shown in Figure 3.3.

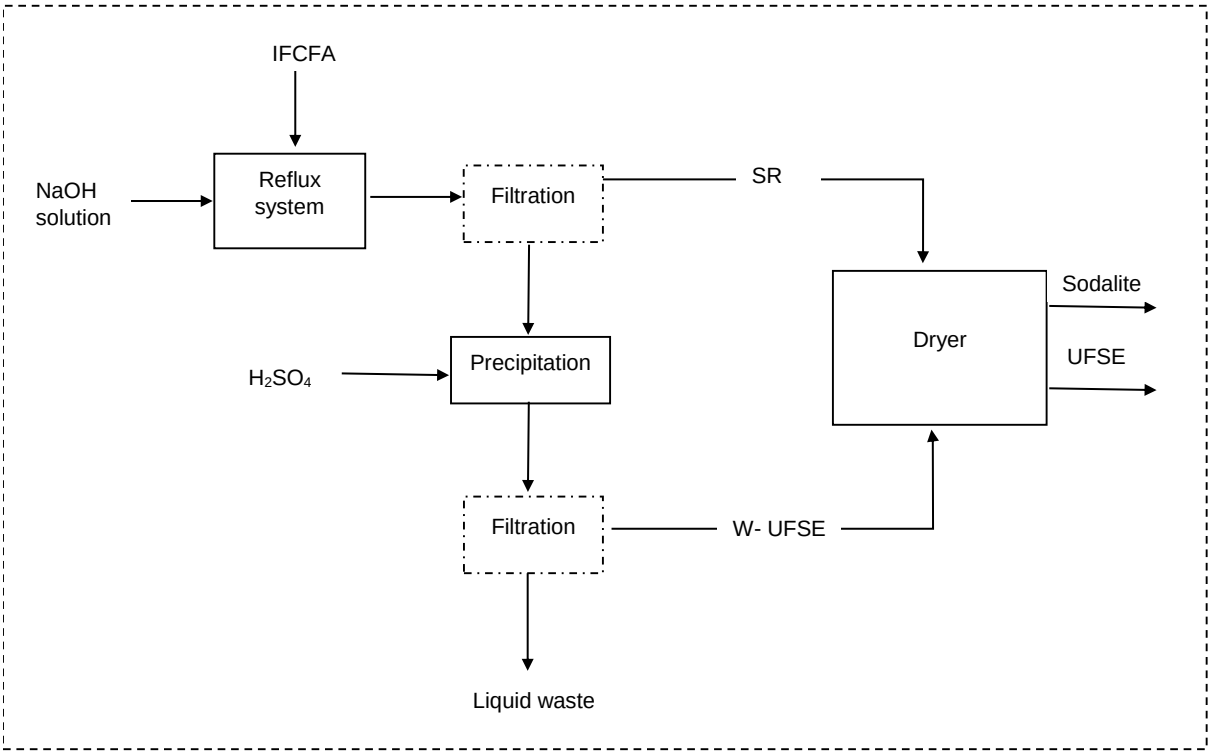

Figure 3.3: Block flow diagram for alkaline extraction of silica from IFCFA, where IFCFA = iron-free coal fly ash, SR = solid residue and UFSE = untreated coal fly ash silica extract

3.3.2 Treatment of silica extract

The effect of varying oxalic acid concentration and water on the treated coal fly ash silica extracts (TFSEs) was investigated, as shown in Table 3.3 and Figure 3.4, using fresh UFSE for each cycle. For this, 30 g of UFSE was weighed and mixed with 200 mL of oxalic acid solution of varying concentrations (1.25, 1, 0.78, 0.44 or 0.17 M) or water in a 250 mL round-bottom flask. The mixture was heated under reflux conditions at 80°C for 6 h, while stirring at 250 rpm. At completion, the mixture was filtered while still hot and the recovered TFSE-x (x = 1.25, 1, 0.78, 0.44 and 0.17 (oxalic acid treated) and H_2O (water treated)) were dried overnight at 70°C. The treated extracts were all analysed for chemical and structural properties by means of XRF, XRD, SEM, and FTIR.

Table 3.3: Experimental conditions for the treatment of CFA-based silica extract (UFSE) with oxalic acid and water

Variable parameters		Fixed parameters			
Sample code	**Oxalic acid (g)**	**UFSE (g)**	**Stirring speed (rpm)**	**Temperature (˚C)**	**Time (h)**
TFSE-1.25	22.5	30	250	80	6
TFSE-1	18.5				
TFSE-0.78	13.5				
TFSE-0.44	8				
TFSE-0.17	3.5				
TFSE - H_2O	0				

Figure 3.4 shows an illustration of the BFD for the treatment process.

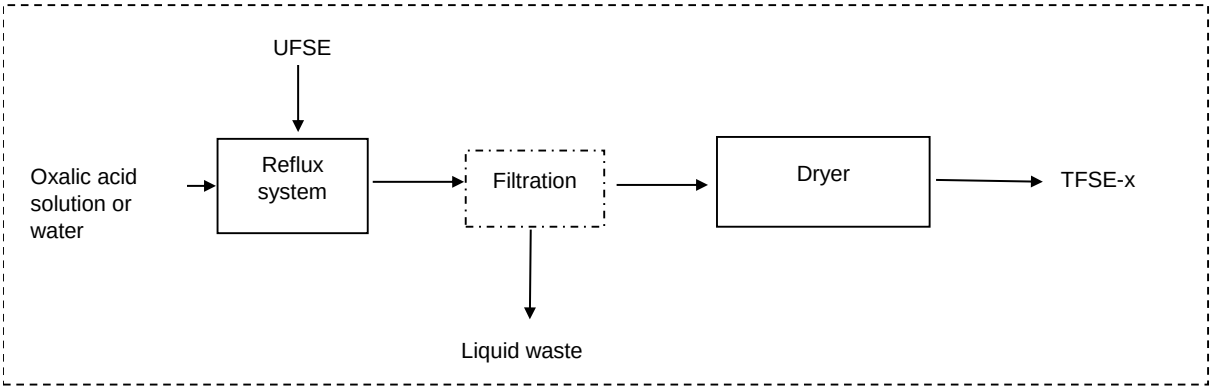

Figure 3.4: Block flow diagram for the oxalic acid and water treated silica extracts. Where TFSE-x = TFSE-1.25, TFSE-1, TFSE-0.78, TFSE-0.44, TFSE-0.17 and TFSE-H_2O

3.3.2.1 Treatment with recycled liquid waste

The liquid waste recovered from Section 3.3.1.3 (Figure 3.4) was used as feed to investigate the effect of recycled liquid waste on the treated silica extracts. The liquid waste was recycled four times using the fresh UFSE for each treatment cycle. The effect of the recycled liquid waste on the TFSEs was investigated using the treatment conditions detailed in Section 3.3.1.3. The recovered TFSEs (TFSE 1, TFSE 2, TFSE 3 and TFSE 4) were thereafter analysed by XRD, ICP and SEM, and the respective liquid wastes were analysed by ICP to determine the elemental composition. Figure 3.5 shows the BFD of the recycled liquid waste process.

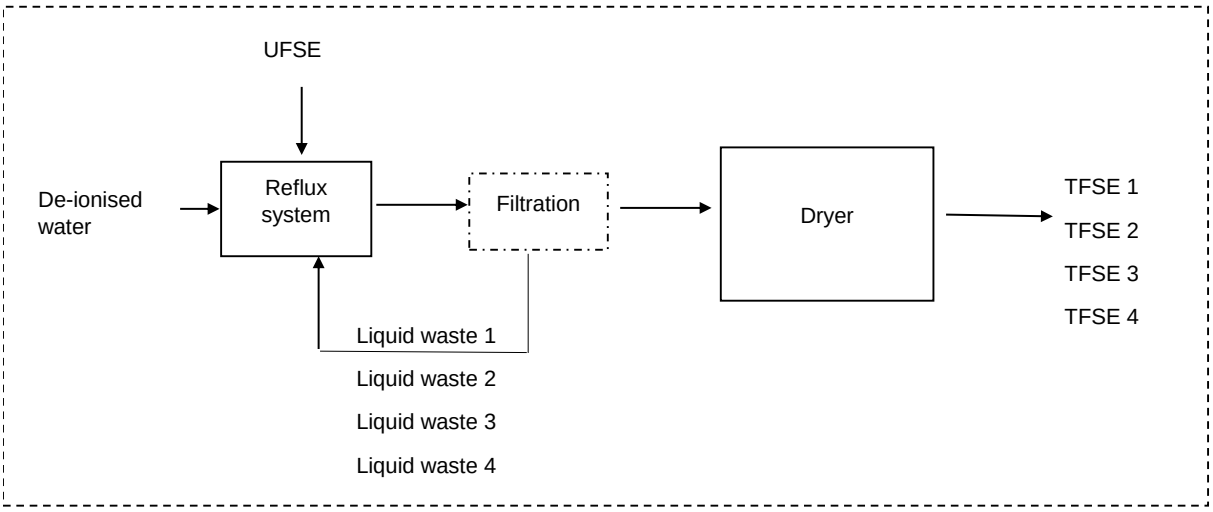

Figure 3.5: BFD of the recycled liquid waste during the treatment of UFSE

3.3.3 Synthesis of high-silica zeolite ZSM-5 from CFA silica extracts

This section presents the synthesis of ZSM-5 zeolite from CFA-based silica extracts (TFSE-1.25, TFSE-1, TFSE-0.78, TFSE-0.44, TFSE-0.17 and TFSE-H_2O), with correct Si/Al ratio required for high-silica zeolite synthesis (Figure 3.6). The detailed experimental conditions and molar compositions are described in Table 3.4.

Table 3.4: Preliminary synthesis conditions for the synthesis of ZSM-5 zeolite from silica extract

Feedstock code name	Product code name	Molar regimes				
TFSE-1.25	Z-1.25	1 Si	0.002 Al	0.587 Na	95.088 H_2O	0.180 TPABr
TFSE-1	Z-1	1 Si	0.009 Al	1.250 Na	121.171 H_2O	0.241 TPABr
TFSE-0.78	Z-0.78	1 Si	0.003 Al	0.762 Na	101.381 H_2O	0.202 TPABr
TFSE-0.44	Z-0.44	1 Si	0.003 Al	0.575 Na	94.721 H_2O	0.188 TPABr
TFSE-0.17	Z-0.17	1 Si	0.004 Al	0.628 Na	96.399 H_2O	0.192 TPABr
TFSE-H_2O	Z-H_2O	1 Si	0.011 Al	1.282 Na	122.034 H_2O	0.243 TPABr

The synthesis conditions used for the preliminary study were modified from Missengue (2016). In this set of experiments, 2 g of TFSE-x (each treated extract) was weighed and mixed with 0.4 g of NaOH and 50 mL of H_2O in a 100 mL Teflon-lined stainless autoclave and aged for 40 min at room temperature. After ageing, the autoclave containing the homogeneous mixture was placed in a pre-heated oven at 160°C for 72 h. At completion, the autoclave was removed from the oven and allowed to cool down to room temperature. The synthesised zeolite was recovered by

filtration, washed with deionised water and dried overnight at 70°C. Thereafter, dried zeolite products (Z-1.25, Z-1, Z-0.78, Z-0.44, Z-017 and Z-H_2O) were de-templated in a pre-heated furnace at 120°C for 2 h, then at 550°C for 3 h in air with a ramping temperature of 15°C/min to remove the structure-directing agent (TPABr) in the zeolite structure.

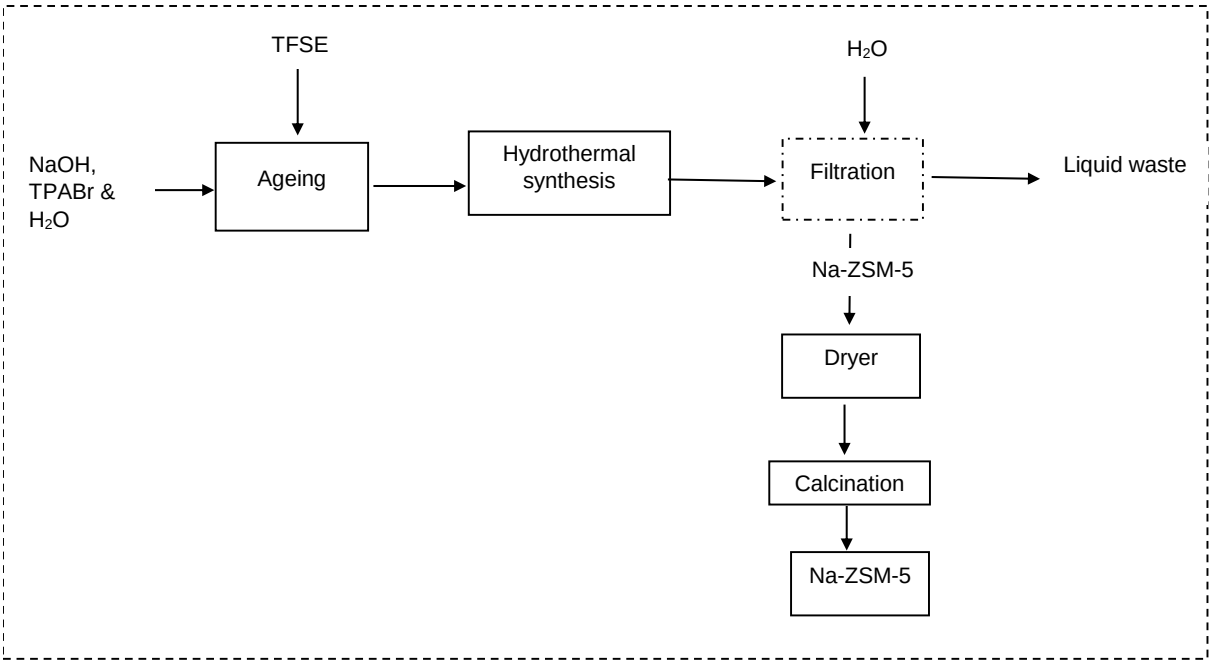

Figure 3.6: BFD for the synthesis of ZSM-5 zeolite from CFA silica extract

The effects of NaOH, TPABr, water content, hydrothermal time and temperature on ZSM-5 zeolite were investigated further, based on the optimum conditions obtained from the preliminary synthesis conditions (TFSE-H_2O silica extract). Table 3.5 provides information on the varying and fixed conditions for each parameter and their respective molar regimes.

Table 3.5: Experimental conditions for the synthesis of ZSM-5 zeolite from CFA silica extracts

Variables	Variable code name	Product code name	Molar regimes				Physical parameters
	NaOH (g)						
Effect of NaOH	0.5	ZN-0.5	1 Si	0.003 Al	0.696 Na	95.766 H_2O	0.190 TPABr	Ageing time (40 min), Hydrothermal temperature (160 °C), time (72 h)
	0.4	ZN-0.4	1 Si	0.011 Al	1.282 Na	122.034 H_2O	0.243 TPABr	
	0.3	ZN-0.3	1 Si	0.003 Al	0.529 Na	95.766 H_2O	0.038 TPABr	
	0.2	ZN-0.2	1 Si	0.003 Al	0.445 Na	95.766 H_2O	0.190 TPABr	
	0.1	ZN-0.1	1 Si	0.003 Al	0.361 Na	95.766 H_2O	0.190 TPABr	
	0.05	ZN-0.05	1 Si	0.003 Al	0.319 Na	95.766 H_2O	0.190 TPABr	
	TPABr (g)						
Effect of TPABr	1.5	ZTP-1.5	1 Si	0.003 Al	0.529 Na	95.766 H_2O	0.038 TPABr	Ageing time (40 min), Hydrothermal temperature (160 °C), time (72 h)
	1.2	ZTP-1.2	1 Si	0.003 Al	0.529 Na	95.766 H_2O	0.152 TPABr	
	0.9	ZTP-0.9	1 Si	0.003 Al	0.529 Na	95.766 H_2O	0.114 TPABr	
	0.6	ZTP-0.6	1 Si	0.003 Al	0.529 Na	95.766 H_2O	0.076 TPABr	
	0.3	ZTP-0.3	1 Si	0.003 Al	0.529 Na	95.766 H_2O	0.038 TPABr	
	0.15	ZTP-0.15	1 Si	0.003 Al	0.529 Na	95.766 H_2O	0.019 TPABr	
	0.075	ZTP-0.075	1 Si	0.003 Al	0.529 Na	95.766 H_2O	0.010 TPABr	
	H_2O mL						
Effect of H_2O	50	ZTHH-50 mL	1 Si	0.003 Al	0.529 Na	95.766 H_2O	0.152 TPABr	Ageing time (40 min), Hydrothermal temperature (160 °C), time (72 h)
	40	ZTHH-40 Ml	1 Si	0.003 Al	0.529 Na	78.613 H_2O	0.190 TPABr	
	30	ZTHH-30 mL	1 Si	0.003 Al	0.529 Na	57.459 H_2O	0.190 TPABr	
	20	ZTHH-20 mL	1 Si	0.003 Al	0.529 Na	38.306 H_2O	0.190 TPABr	
	Time (h)						
Effect of time	72	ZTHT-72 h	1Si	0.003 Al	0.529 Na	38.306 H_2O	0.190 TPABr	Ageing time (40 min), Hydrothermal temperature (160 °C)
	48	ZTHT-48 h						
	24	ZTHT-24 h						
	6	ZTHT-6 h						
	3	ZTHT-3 h						
	0	ZTHT-0h						
	Temperature (°C)						
Effect of temperature	160	ZTHT-160˚C	1 Si	0.003 Al	0.529 Na	38.306 H_2O	0.190 TPABr	Ageing time (40 min), time (3 h)
	130	ZTHT-130˚C						
	100	ZTHT-100˚C						
	70	ZTHT-70˚C						
	40	ZTHT-40˚C						

The zeolite products (Table 3.5) were also de-templated, at a ramping rate of 2°C/min for 2 h at 120°C and then at 550°C for 3 h in air with a ramping rate of 3°C/min to remove the structure-directing agent (TPABr). SEM and XRD characterisation techniques were used as the main response factor throughout the experimental process.

The obtained zeolite products from the optimisation study (Z-H_2O, ZN-0.3, ZTHP-1.2, ZTHH-20 mL, ZTHH-3 h) were ion-exchanged by mixing 0.5 M NH_4NO_3 solution at a zeolite/ NH_4NO_3 ratio of 1:10 at 80˚C under reflux system for 1 h while stirring at 100 rpm. The treatment was repeated four times using a fresh aliquot. At completion, the mixture was filtered, and the recovered zeolite products were dried overnight at 70˚C and calcined again as described above. The recovered zeolite products in H-form (H-Z-H_2O, H-ZN-0.3, H-ZTHP-1.2, H-ZTHH-20 mL, H-ZTHH-3 h) were characterised further by means of XRD, SEM, FTIR, BET and TPD.

3.3.4 Synthesis of zeolite ZSM-5 from CFA silica extracts treated with the recycled liquid waste

The treated fly ash silica extracts (TFSE 1, TFSE 2, TFSE 3 and TFSE 4) obtained after each recycle process were thereafter used as feedstock in the synthesis of ZSM-5 zeolite. The synthesis conditions were the same as those described in Section 3.3.2. The molar regimes for the different feedstock are presented in Table 3.6.

Table 3.6: ZSM-5 synthesis molar regime from CFA silica extracts treated with recycled liquid waste

Sample code	Molar regimes	Hydrothermal conditions
ZTHR1	1Si: 0.02Al: 0.39 Na: 23.41 H_20: 0.05 TPABr	160 ˚C for 72 h
ZTHR2	1Si: 0.01 Al: 0.41 Na: 53.06 H_20: 0.11 TPABr	
ZTHR3	1Si: 0.01 Al: 0.81 Na: 28.34 H_20: 0.06 TPABr	
ZTHR4	1Si: 0.01 Al: 0.91 Na: 29.45 H_20: 0.06 TPABr	

The resulting zeolite products (ZTHR1, ZTHR2, ZTHR3 and ZTHR4) were thereafter calcined and characterised by XRD, SEM, FTIR and BET analysis.

3.3.5 Techno-economic analysis (TEA)

The TEA performed was based on the production of ZSM-5 zeolite using the optimum synthesis conditions (ZTHH-3h) and sodalite zeolite. The factorial cost estimation methodology described

by Coulson and Richardson (1999) was used as the basis for the cost estimation performed. The summary of the procedure is presented below:

- Detailed process flow diagram.
- Material and energy balances of the process (if no equipment energy data available, the energy consumed can be estimated as in the process provided by Coulson and Richardson (1999)).
- Major equipment items sizing and selection of materials of construction.
- Estimation of the purchase cost of the major equipment items, using Figures 6.3 to 6.6 and Tables 6.2 and 6.3 of Coulson and Richardson (1999).
- Calculation of the total physical plant cost (PPC), using the factors given in Table 2.4 of this study.
- Calculation of the indirect costs from the direct costs, using the factors given in Table 6.1 of Coulson and Richardson (1999).
- Calculation of the fixed capital cost.
- Estimation of the working capital as a percentage of the fixed capital; and estimation of the total investment required.

3.4 Analytical techniques

This section presents the different analytical techniques and procedures followed to characterise the liquid and solid samples obtained from the experiments conducted in this study.

3.4.1 Inductively coupled plasma atomic emission spectrometry (ICP-AES)

The ICP-AES analytical technique was used to identify and quantify the presence of trace and major elements in both liquid and solid samples. Prior to the analysis, all solid samples were digested following the digestion method presented in Section 3.4.1.1 below. After digestion, all samples were diluted using the 10- and 100-times dilution method, using a 2% HNO_3 solution. The samples were analysed using the Varian 710-ES ICP-AES instrument based in the Chemistry Department at the University of the Western Cape. The analysis was conducted in triplicate to investigate the replicability of the results.

3.4.1.1 Total digestion of solid samples

The total digestion method used in this study was adopted from that used by Missengue (2016). A solid sample of 0.25 g was mixed with 2 mL of concentrated hydrofluoric acid (HF) and 5 mL of

aqua regia (HNO_3/HCl, 1:3) in a 50 mL digestion vessel. The digestion vessel was thereafter placed in a preheated oven and heated at 100°C for 2 h. After the reaction was complete, the mixture was allowed to cool for at least 1 h before opening the vessel. 25 mL of saturated boric acid was thereafter prepared and used to neutralise the excess HF in the digestate. The mixture was filtered, and the supernatant was diluted to 50 mL with deionised water. The samples (TSFE1, TFSE2, TFSE3, TFSE4, H-Z-H_2O, H-ZN-0.3, H-ZTP-1.2, H-ZTHH-20 mL and H-ZTHH-3h) were then analysed using ICP-AES, as described in Section 3.4.1.

3.4.2 X-ray fluorescence spectroscopy (XRF) analysis

The XRF analysis was used to determine the elemental composition of the as-received Matla CFA, UFSE and the fly ash-treated silica extracts (TFSE-1.25, TFSE-1, TFSE-0.78, TFSE-0.44, TFSE-0.17 and TFSE-H_2O) by measuring the percentage of major oxides in each sample. The oxides measured included SiO_2, Al_2O_3, Fe_2O_3, CaO, TiO_2, MgO, K_2O, P_2O_5, MnO and Cr_2O_3. Prior to the analysis, the samples were dried overnight at 110°C to remove excess moisture content. Thereafter, 0.65 g of each sample and 5.60 g of a flux (containing 66.67% of $Li_2B_4O_7$, 32.83% of $LiBO_2$ and 0.50% of LiBr) were prepared, mixed and fused to a glass bead. The instrument used for the analysis was a wavelength dispersive Philips PW 1480 X-ray spectrometer. The spectrometer was fitted with a chromium tube, analysing crystals (namely LIF 200, LIF 220, GE, PE and PX) and the detectors were a combination gas-flow proportional counter and a scintillation detector. The gas-flow proportional counter uses P10 gas, which is a mixture of argon and methane at a ratio of 9:1. The analysis was conducted four times using a fresh sample each time in order to determine the integrity (by means of standard deviation) of the results.

3.4.3 X-ray diffraction spectroscopy analysis

The X-ray diffraction (XRD) analysis was carried out in order to determine the mineral phases in the identified samples. For this project, the analysis was performed on all solid samples to determine the composition of the sample of interest. The analysis was carried out using a Philips X-pert pro MPD X-ray diffractometer with Cu-K radiation at 40 KV and 40 mA instrument. For the analysis, 0.5 g of the solid sample was weighed and placed onto a sample holder. The sample height was levelled to the edge of the sample holder and inserted into the XRD instrument. The analysis was performed between 0° and 60° 2Θ and the obtained mineral phases were identified using High Score Xpert software. The XRD graphs were then prepared using Origin Pro 8.4 software. The spectra obtained were compared with standard patterns from the powder diffraction database supplied by the International Centre for Diffraction Data (ICDD).

3.4.4 Scanning electron microscopy (SEM)

SEM was used to determine the morphological characteristics and particle size of the as-received Matla CFA, CFASEs, solid residue and the synthesised zeolite ZSM-5. The analysis was performed using a Hitachi X-650 Scanning Electron Micro-analyser equipped with a CDU-lead detector at 25 kV, and a tungsten filament. The samples were prepared by placing a carbon adhesive tape onto an aluminium stub. A small amount of each sample was applied onto the carbon adhesive tape, which was coated with carbon in an Emitech K950X carbon evaporator for 6 sec to enable the conductivity. The samples were placed in the column of the SEM instrument and the scanning electron micrographs of each sample were captured and displayed on an LCD computer screen. ImageJ.exe software was used to determine the average crystal size of each analysed sample.

3.4.5 Fourier Transform Infrared Spectroscopy (FTIR)

FTIR was performed in order to identify the surface functionalities and structural configurations of solid samples. Approximately 15 mg of each sample was placed on the Attenuated Total Reflectance (ATR) sample holder of a Perkin Elmer spectrum 100 FT-IR spectrometer. An equal force was then applied to the sample and the infrared (IR) spectra were then collected within a range of 4000 – 400 cm^{-1} to identify structural configuration and provide information about the bonds in the sample. Before data collection, baselines were corrected for background noise, which was subtracted from the spectra. OriginPro 8.4 software was used to draw the IR spectra and identify the structural configurations for each sample.

3.4.7 N_2 Brunauer-Emmett-Teller (BET)

BET analysis was used to determine the surface area and porosity of the synthesised CFA-based zeolite ZSM-5 and BEA using the Micromeritics Tristar 3000 analyser. For this analysis, approximately 0.2 g of the zeolite was weighed and placed inside a BET glass tube. The sample was thereafter degassed at 90°C for 2 h and 400°C for 4 h in order to remove moisture adsorbed inside the porous network of the synthesised zeolites using helium. At completion, the BET tube was removed from the degas pod and left to cool for at least 15 min. The N_2 physisorption was thereafter carried out at 196°C. The Brunauer-Emmett-Teller (BET) model was used to compute the samples' microporous and mesoporous surface areas, as well as their pore volumes. T-plot measurements were used to distinguish between the samples' exterior surface area and microporous area. The total pore volume was calculated using the Horvath-Kawazoe (HK) model

at P/Po 0.99, whereas the pore size distributions were obtained using the density functional theory (DFT) model.

3.4.8 Temperature programmed desorption (TPD)

Temperature programmed desorption (TPD) was used to determine the amount and strength of acid sites in the synthesised zeolite ZSM-5 and BEA. The TPD profiles were obtained using an Autochem II Micromeritics chemisorption analyser. For the analysis, 0.1 g of the synthesised zeolite was placed on a glass tube and loaded into the instrument. The zeolite was then activated by heating to 500°C and holding for 20 min under helium flow at 30 mL/min. At completion, the zeolite material was then cooled to 120°C under helium flow at 30 mL/min. After cooling, the sample was exposed to 5% NH_3 in balance helium and the NH_3 was adsorbed at 120°C for 30 min at a flow rate of 15 ml/min. Each of the zeolite samples was then purged under flowing helium for 30 min and the NH_3 desorption was recorded by heating the zeolite to 700°C using a 10°C/min ramp. The TPD profiles were then measured using a thermal conductivity detector (TCD) and the outputs were recorded on a computer.

3.5 Chapter summary

This section provides a synopsis of where the results obtained from the research methodologies and characterisation techniques described in earlier sections are presented and discussed in the upcoming chapters: The overview of the methodology, characterisation and the corresponding chapters are summarised in Table 3.7.

Table 3.7: Methodology and corresponding result section

		Characterisation						
Methodology	**Chapter**	**XRF (Section 3.4.2)**	**ICP (Section 3.4.1 - 3.4.1.1)**	**XRD (Section 3.4.3)**	**SEM (Section 3.4.4)**	**FTIR (Section 3.4.5)**	**BET (Section 3.4.7)**	**TPD (3.4.8)**
	Chapter 4							
Section 3.3.1 (3.3.1.1)	(a) Magnetic fraction extraction	Table 4.2	_	Figure 4.4	Figure 4.5	Figure 4.6	_	_
Section 3.3.1 (3.3.1.2)	(b) Alkaline extraction of silica and synthesis of sodalite zeolite	Table 4.3	_	Fig. 4.7	Fig. 4.8	Fig. 4.9	_	_
Section 3.3.2	(c) Treatment of silica extract	Table 4.5	Table 4.5	Fig 4.10	Fig 4.11	Fig. 4.12	_	_
Section 3.3.2.1	(d) Treatment with recycled liquid waste	_	Fig. 4.13 and 4.14	Fig. 4.15	Fig. 4.16	Figure 4.17	_	_
	Chapter 5							
Section 3.3.3	(a) Synthesis of high silica zeolite ZSM-5 from CFA silica extracts		Annexure 5.1	Figure 5.1, 5.3, 5.5, 5.7, 5.9, 5.11, 5.13	Figure 5.2, 5.4, 5.6, 5.8, 5.10, 5.12, 5.14	Figure 5.15	Figure 5.17, Table 5.9 (b)	Figure 5.16, Table 5.9 (a)
Section 3.3.4	(b) Synthesis of zeolite ZSM-5 from CFA silica extracts treated with the recycled liquid waste.		Annexure 5.2	Figure 5.19	Figure 5.20	Figure 5.21	Figure 5.22, Table 5.11	

CHAPTER 4

SELECTIVE EXTRACTION AND CHARACTERISATION OF COAL FLY ASH SILICA EXTRACT.

4.1 Synopsis

This chapter presents and discusses the characterisation of CFA, coal fly ash silica extracts and solid residue obtained from the 3-step silica extraction process which is comprised of removal of iron from CFA, an alkaline extraction process and the silica extract treatment step, as discussed in Chapter 3, Section 3.3.1.1, 3.3.1.2, and 3.3.2 respectively. Results of the effect of recycled liquid waste on the silica extract during the treatment process are also discussed in this chapter. The experimental procedure followed in this study was adopted and modified from Ndlovu (2016). Different analytical techniques such as XRF/ICP, SEM, XRD and FTIR were used in order to understand the physical and chemical properties of the coal fly ash silica extracts prior to use as feedstock in zeolite synthesis.

4.2 Characterisation of coal fly ash

The elemental composition of the Matla CFA used in this study was determined by XRF, as detailed in Chapter 3, Section 3.4.2. Table 4.1 shows the composition of major oxides in dry weight present in Matla coal fly ash (CFA).

Table 4.1: Composition major oxides present in coal fly ash (n = 3)

	XRF (%)			
Major oxides	**CFA A**	**CFA B**	**CFA C**	**Average %**
Al_2O_3	29.26	29.24	29.17	29.22 ± 0.05
CaO	7.91	7.97	7.95	7.94 ± 0.03
Cr_2O_3	0.03	0.02	0.02	0.02 ± 0.01
Fe_2O_3	3.19	3.17	3.20	3.19 ± 0.02
K_2O	0.69	0.67	0.67	0.68 ± 0.01
MgO	2.06	2.11	2.11	2.09 ± 0.03
MnO	0.04	0.04	0.04	0.04 + 0.00
Na_2O	0.37	0.38	0.40	0.38 ± 0.01
P_2O_5	0.89	0.89	0.89	0.89 ± 0.00
SiO_2	53.44	53.38	53.40	53.41 ± 0.03
TiO_2	2.11	2.13	2.14	2.13 ± 0.01
Total	**100.00**	**100.00**	**100.00**	**100.00**
Si/Al	**1.61**	**1.61**	**1.62**	**1.61**
LOI	**1.52**	**1.59**	**1.58**	**1.56**

Table 4.1 summarises the amount in percentage of major oxides present in CFA on a dry basis without loss of ignition (LOI = 1.56). It can be seen from Table 4.1 that SiO_2 and Al_2O_3 are the main constituents in CFA, accounting for 82.63% of the total major oxides. According to the American Society for Testing Materials (ASTM C618), any fly ash material containing a SiO_2, Al_2O_3 and Fe_2O_3 content of more than 70 wt% with a low CaO content (< 10%) is classified as Class F type fly ash. CFA containing a total SiO_2, Al_2O_3 and Fe_2O_3 content ranging between 50 and 70 wt%, with a high CaO content of 10 to 40% is classified as Class C fly ash. The total mass percentage of SiO_2, Al_2O_3 and Fe_2O_3 as shown in Table 4.1 is 85.82%, and as such, the as-

received Matla CFA can be classified as Class F type, as its total mass content is greater than 70%. It can be seen from the results that, apart from the major oxides, CFA contains other oxides such as TiO_2, P_2O_2, Na_2O, MnO, MgO, K_2O, Cr_2O_3 and CaO present in trace amounts of 2.13, 0.89, 0.38, 0.04, 2.09, 0.68, 0.02 and 7.94 %, respectively. The result is consistent with other Matla CFA samples analysed by XRF (Madzivire et al. 2010; Ndlovu 2016; Nyale et al. 2013). The average Si/Al ratio as presented in Table 4.1 was 1.61. According to Missengue (2016), fly ashes typically have a Si/Al ratio of 1- 2 and as such, CFA has been used for direct synthesis of low-cost alumino-silicate zeolites (Jha and Singh 2011; Musyoka et al. 2012). However, this Si/Al ratio is not suitable for the synthesis of high-silica zeolites, such as ZSM-5, that require a Si/Al ≥ 10 (Missengue 2016).

The morphological structure of Matla CFA was analysed as described in Chapter 3, Section 3.4.4. Figure 4.1 presents the SEM micrograph of Matla CFA.

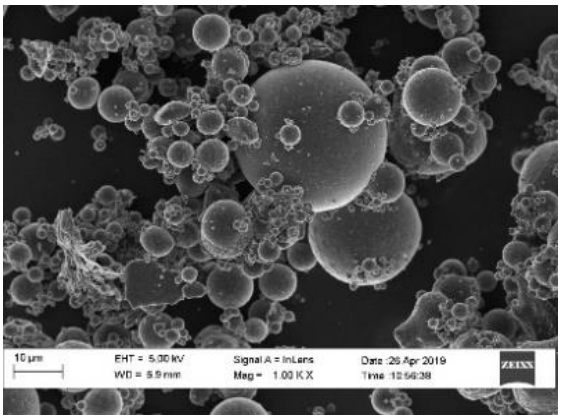

Figure 4.1: Morphological analysis of South African Class F Matla CFA

The morphological structure of Matla CFA is composed of irregular and spherical shaped particles of varying sizes formed as a result of the thermal chemical reaction between Al_2O_3 and SO_2 during the combustion of coal. The CFA micrograph is dominated by glassy spherical particles. These spheres are mostly transparent, indicating complete melting of silicate minerals (Fisher et al. 1978). This observation supported the major oxides composition results presented in Table 4.1 that showed that CFA is mainly composed of SiO_2 and Al_2O_3.

The mineralogical phases of Matla CFA was determined by the XRD technique, as discussed in Chapter 3, Section 3.4.3. Figure 4.2 shows the mineral phases of Matla CFA.

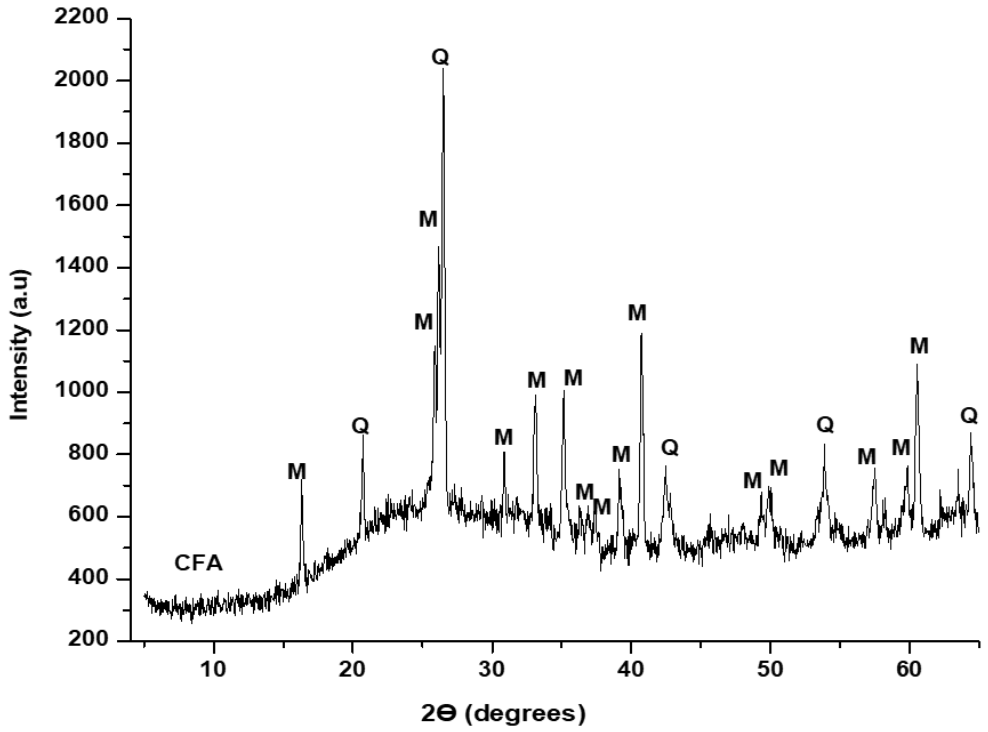

Figure 4.2: XRD spectra for Matla coal fly ash, where Q = Quartz (SiO_2) and M = Mullite ($Al_6Si_2O_{13}$).

It can be seen from Figure 4.2 that the as-received Matla CFA was composed of quartz and mullite mineral phases. A broad hump in the region of 16 to 35 2Θ was observed. This hump is associated with the presence of amorphous silica, as reported by (Missengue et al. 2017). The XRD spectra showed no presence of hematite mineral phases, as observed by other researchers (Du Plessis 2014; Musyoka et al. 2012). The XRD result presented in Figure 4.2 is in agreement with the elemental composition and morphological analysis presented in Table 4.1 and Figure 4.1 respectively.

The structural analysis of Matla CFA as represented by Figure 4.3 was characterised by FTIR spectroscopy, as detailed in Chapter 3, Section 3.4.5.

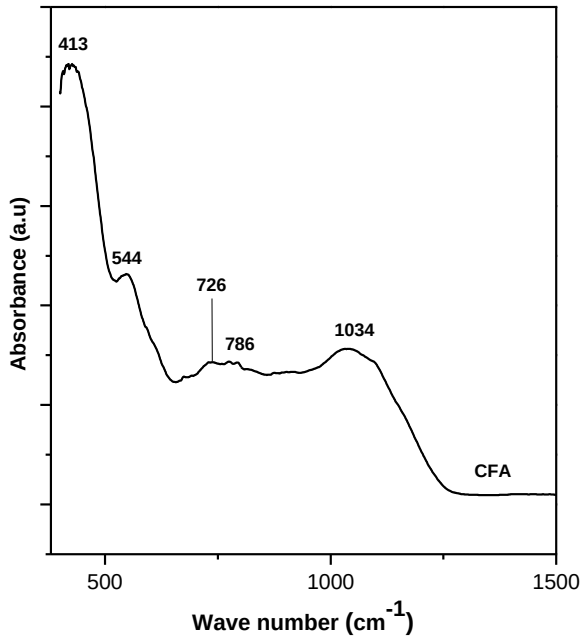

Figure 4.3: FTIR spectra for Matla CFA

FTIR vibration bands in the region of 413, 544, 726, 788 and 1034 cm^{-1} were observed. The band appearing at 413 cm^{-1} relates to the silicate tetrahedron, which is indicated by the banding vibration of O-Si-O (Mozgawa et al. 2014). The band appearing at 544 cm^{-1} can be attributed to Si-O-Al vibration, which occurs as a result of structural rearrangement during coal combustion (Mukherjee and Srivastava 2006). The presence of quartz is indicated by Si-O-Si symmetric stretching vibrations, which are shown by the bands appearing at 726 and 786 cm^{-1} (Hahn et al. 2018). The intense and broad band appearing at 1034 cm^{-1} can be assigned to Si-O-Al asymmetric stretch for mullite and quartz mineral phase in CFA (Liu et al. 2019).

4.3 Characterisation of magnetic fraction and iron-free solid residue

The magnetic fraction of CFA was removed following the extraction process detailed in Chapter 3, Section 3.3.1.1. Table 4.2 presents the composition of major oxides present in Matla CFA compared to magnetic fraction (MF) and the resulting iron-free solid residue (IFCFA), as analysed by XRF. The removal of magnetic iron oxide from CFA prior to the extraction of silica was carried out in order to enhance the extraction efficiency of Si and Al, as suggested by Sedres (2016).

Table 4.2: Composition major oxides of coal fly ash, magnetic fraction (MF) and iron-free coal fly ash (IFCFA)

	XRF (%)		
Species	**CFA**	**MF**	**IFCFA**
SiO_2	54.40 ± 0.24	0.02 ± 2.00	53.63 ± 0.29
Al_2O_3	29.22 ± 0.10	33.90 ± 0.02	31.45 ± 0.92
CaO	7.95 ± 0.06	7.85 ± 1.02	7.20 ± 0.00
Fe_2O_3	3.18 ± 0.03	45.34 ± 2.05	1.50 ± 0.01
TiO_2	2.13 ± 0.02	0.00 ± 0.12	1.76 ± 0.12
MgO	2.10 ± 0.04	0.49 ± 0.01	2.16 ± 0.01
P_2O_5	0.89 ± 0.00	4.22 ± 0.02	0.91 ± 0.02
K_2O	0.68 ± 0.01	2.20 ± 0.00	0.76 ± 0.00
Na_2O	0.39 ± 0.01	0.68 ± 0.00	0.58 ± 0.00
MnO	0.04 ± 0.00	0.53 ± 0.01	0.04 ± 0.03
Cr_2O_3	0.02 ± 0.01	4.78 ± 0.00	0.02 ± 0.00
Total	100	100	100
Si/A	1.64	0.00	1.5
LOI	1.56	n/a	1.53

The concentration of major oxides in CFA, MF and IFSR is presented on a dry basis without LOI. The XRF results shows that SiO_2 and Al_2O_3 were the major oxides present in the CFA, accounting for 83.62% in total composition (54.40% SiO_2 + 29.22% Al_2O_3). After the MF recovery process, the total amount of SiO_2 and Al_2O_3 increased in the resultant IFCFA, with a composition of 53.63% SiO_2 + 31.45% Al_2O_3. A decrease in the Fe_2O_3 content from 3.18 to 1.5% in CFA and IFCFA was also observed. The decrease in Fe_2O_3 resulted in a MF recovery rate of 52.83% (determined using equation 4.1), where Fe_{CFA} and Fe_{IFCFA} represent the amount of Fe present in CFA and IFCFA, as determined by XRF.

$$Recovery\ rate = \frac{Fe_{CFA} - Fe_{IFCFA}}{Fe_{CFA}} * 100 \ldots\ldots\ldots\ldots\ldots\ldots Equation\ 4.1$$

The MF recovery rate achieved in this study was comparable to the 63.6% Fe recovery rate reported by Cornelius (2019). The slightly lower MF recovery rate obtained in this study could be due to the presence of Al_2O_3 in the MF extract at high amounts (33.90%), as shown in Table 4.3. This could be indicative of the presence of quartz and mullite mineral phases in the MF extract. Gilbert et al. (2019) showed that higher Fe recovery of 82% can be achieved through repeated washing of the magnetic fraction extract, or through purification with HCl (Sedres 2016), however this falls outside the scope of this study. Notwithstanding this observation, the MF recovery rate of 52.83% suggests that the iron removal process was efficient. This result corroborates studies on the removal of iron from CFA (Lv et al. 2014; Valeev et al. 2018). The priority removal of Fe in CFA is essential and has an adverse effect on the selective recovery of Si and Al and other metals of interest (Wang et al. 2020). The recovered IFCFA was thereafter used as a feedstock for the alkaline extraction process. Figure 4.4 presents the mineral phases of CFA, MF and IFCFA, as determined by XRD.

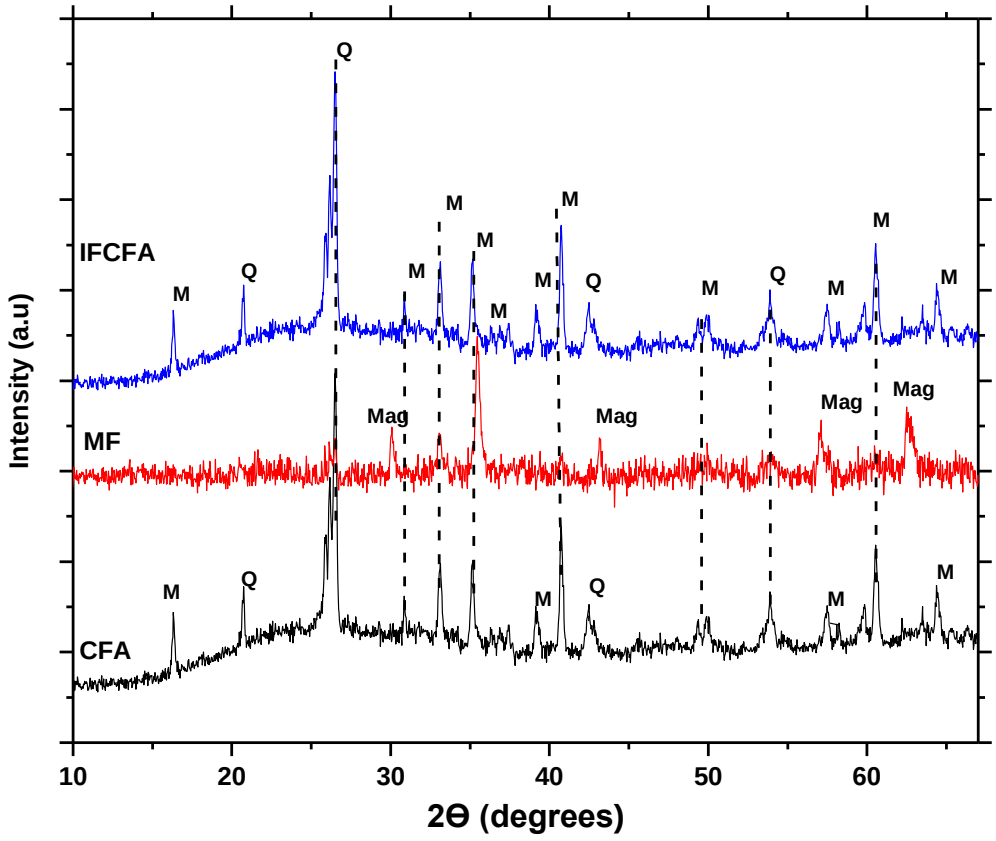

Figure 4.4: XRD spectra for coal fly ash (CFA), magnetic fraction (MF) and iron-free coal fly ash (IFCFA): where M=Mullite, Q=Quartz and Mag=Magnetite

The XRD spectra of IFCFA is identical to that of CFA, represented by quartz and mullite mineral phases. The MF spectra is dominated by magnetite. Trace mineral phases of quartz and mullite could also be seen. Mullite spectra of high intensity was observed at 35 Θ degrees. This supported the XRF result presented in Table 4.2, which showed a high concentration of Al_2O_3. This result confirmed the results presented by Cornelius (2019) and Ndlovu (2016).

The SEM micrographs showing the morphological structure of CFA, MF and IFCFA are presented in Figure 4.5. The structure of IFCFA is similar to that of CFA, which contained irregular, spherical particles. However, the shapes of particles of IFCFA are more variable incomparison to those of CFA, with a rough surface of smaller CFA and magnetic particles (Cornelius 2019). The morphology of MF shows spheres of varying sizes, with various surface textures. The presence of small granular crystals on MF indicate the presence of iron oxide (Xue and Lu 2008). The small granular crystals in MF confirm the presence of magnetite, as detected by XRF (Table 4.3) and XRD (Figure 4.4).

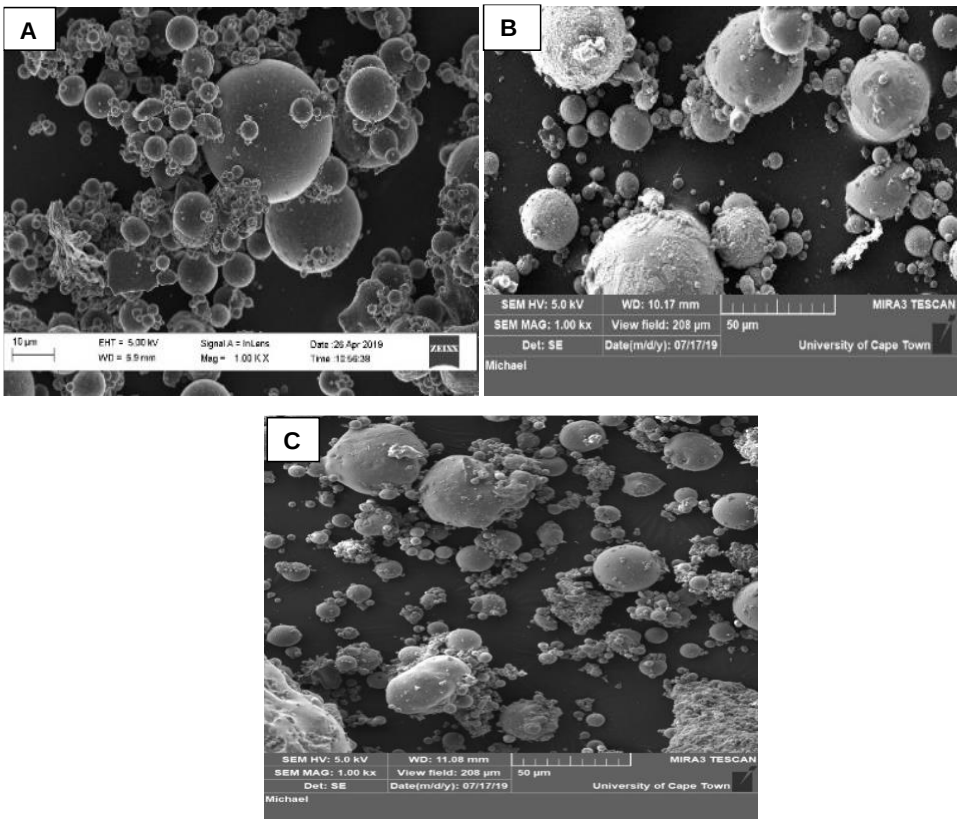

Figure 4.5: Morphological analysis for A = CFA, B = MF and C = IFCFA at 1000x magnification

Figure 4.6 presents the structural patterns of CFA, MF and IFCFA, as analysed by FTIR.

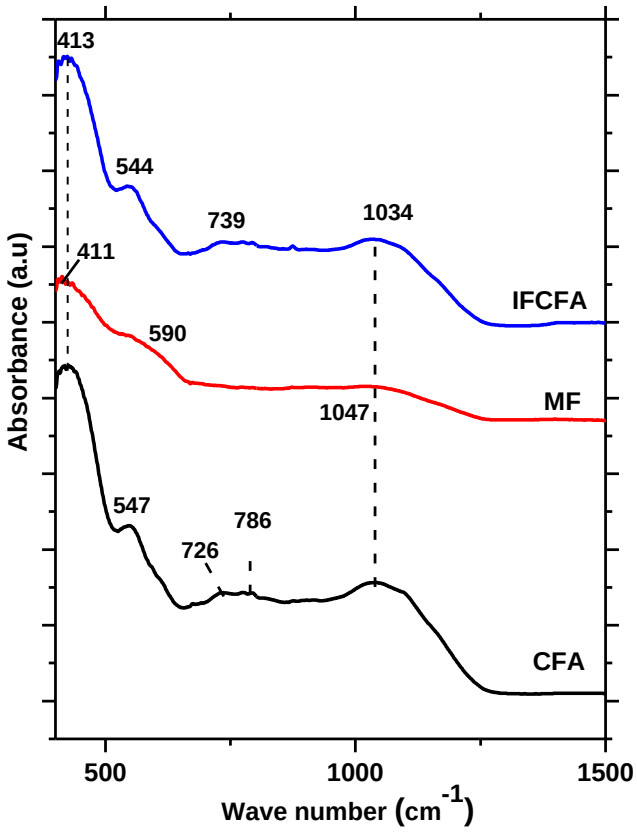

Figure 4.6: FTIR spectra for CFA, MF and IFCFA

A similar trend between CFA and IFCFA is observed, with vibration bands appearing at 413, 544, 547, 726, 739, 786 and 1034 cm^{-1}. The vibration band appearing at 413 cm^{-3} in both CFA and IFCFA relates to the silicate tetrahedron, which is indicated by the bending vibration of O-Si-O (Mozgawa et al. 2014). A shift in the Si-O-Al band appearing at 547 cm^{-1} in CFA to 544 cm^{-1} in IFCFA was observed, the shift could be due to the magnetic extraction process. The vibration bands appearing at 726, 739, 786 and 1034 cm^{-1} can be assigned to the symmetric and asymmetric stretching vibration bands, which indicate the presence of quartz and mullite in both CFA and IFCFA samples (Hahn et al. 2018). The MF sample only revealed three bands, which appeared at 411, 590 cm^{-1} and a stretched vibration band at 1034 cm^{-1} respectively. The bands at the lower wavelength of 411 and 590 cm^{-1} indicate the presence of Fe-O stretching, corresponding to magnetite (Parikh and Chorover 2006). This observation corroborates the XRF, XRD and SEM results presented in Table 4.3, Figure 4.4 and 4.5 respectively.

4.4 Alkaline extract of silicon from iron-free coal fly ash (IFCFA)

The IFCFA recovered from the magnetic fraction extraction process was used as a feedstock in the alkaline extraction of silica. The methodology used for alkaline extraction was adopted and modified from Ndlovu (2016). The method involves two consecutive steps, namely alkaline reflux and a precipitation process. In the reflux process, IFCFA is mixed with sodium hydroxide solution in a ratio of 1:2.5, followed by heating under reflux conditions at 150˚C for 24 h, as detailed in Chapter 3, Section 3.3.1.2. At completion, the solution was filtered, and silica was recovered by adding H_2SO_4 dropwise into the filtrate until a white precipitate was formed, which was then named 'untreated coal fly ash silica extract' (UFSE). The UFSE and solid residue (SR- obtained after the alkaline extraction process) were dried overnight at 70˚C. The products were thereafter characterised by XRF, XRD, SEM and FTIR, as detailed in Chapter 3, Section 3.4.2, 3.4.3, 3.4.4 and 3.4.5 respectively. The results are presented in the subsections below.

4.4.1 Elemental composition of the UFSE

Table 4.4 presents the composition of major oxides present in the IFCFA, UFSE and the SR, as analysed by XRF.

Table 4.3: Composition major oxides in IFCFA, UFSE and SR, as determined by XRF, n = 3

	XRF (wt%), n = 3		
Species	**IFCFA**	**UFSE**	**SR**
SiO_2	53.63 ± 0.29	27.28 ± 0.12	33.97 ± 0.70
Al_2O_3	31.45 ± 0.92	0.21 ± 0.21	22.82 ± 1.21
CaO	7.20 ± 0.00	0.02 ± 0.00	5.15 ± 0.03
Fe_2O_3	1.50 ± 0.01	nd	1.05 ± 0.02
TiO_2	1.76 ± 0.12	0.08 ± 0.00	1.25 ± 0.04
MgO	2.16 ± 0.01	nd	1.51 ± 0.03
P_2O_5	0.91 ± 0.02	0.42 ± 0.03	0.40 ± 0.00
K_2O	0.76 ± 0.00	0.67 ± 0.00	0.19 ± 0.00
Na_2O	0.58 ± 0.00	71.32 ± 0.00	33.62 ± 1.21
MnO	0.04 ± 0.03	nd	0.03 ± 0.00
Cr_2O_3	0.02 ± 0.00	nd	0.01 ± 0.00
Si/Al	**1.5**	**114.73**	**1.31**
Si/Na	58.57	0.24	0.64

**Note: nd – not detected*

Table 4.3 presents the major oxides composition of IFCFA, untreated fly ash silica extract (UFSE) and solid residue (SR) obtained after the alkaline leaching process respectively. The starting material (IFCFA) was composed mainly of (Si>Al>Na) in oxide form, accounting for 83.62% of the total composition (Table 4.3). After the alkaline leaching and precipitation process, the resulting UFSE showed a total composition of 98.81 for the major oxides (Na>Si>Al). The percentage oxides of Cr, Fe, Mg and Mn originally present in IFCFA were not detected in the recovered UFSE. This suggests that the major impurities in IFCFA were removed during the alkaline leaching and precipitation process. However, a high percentage of Na, in excess of 71.32%, was observed in UFSE. The high Na content in UFSE is attributed to the addition of NaOH during the alkaline leaching process. In addition, Si/Al ratio of 114.75 was achieved on the UFSE sample. The high Si/Al ratio shows the possibility of using the extracted silica for the synthesis of high-silica zeolites. This is in agreement with the Si/Al ratio of the silica feedstock used for the synthesis of ZSM-5 zeolite reported by Missengue et al. (2018). However, the high Na content present in UFSE might affect the chemical structure of the desired zeolite product. The treatment of the recovered UFSE was therefore deemed a necessary step in order to reduce the Na content, as well as other impurities, and improve the purity of the recovered UFSE (Missengue et al. 2017)

The recovered secondary solid residue (SR) was mainly composed of 90.29% major oxides (Si>Na>Al), with a Si/Al of 1.31 (Table 4.3). The high percentages of Si and Al indicated that some of the mullite and quartz were not dissolved during the alkaline extraction process. The Si/Al ratio observed in SR is within the recommended Si/Al ratio for achieving zeolites with low silica content (Cornelius 2019; Shabani et al. 2022). The successful extraction of silica from UFCFA shows that the alkaline leaching process can be used as an alternative to the high energy consumption fusion process, thus lowering the cost of recovering silica from CFA.

4.4.2 Mineral phases of IFCFA, UFSE and SR as determined by XRD

The mineral phases of IFCFA, UFSE and SR in comparison to CFA are presented in Figure 4.7.

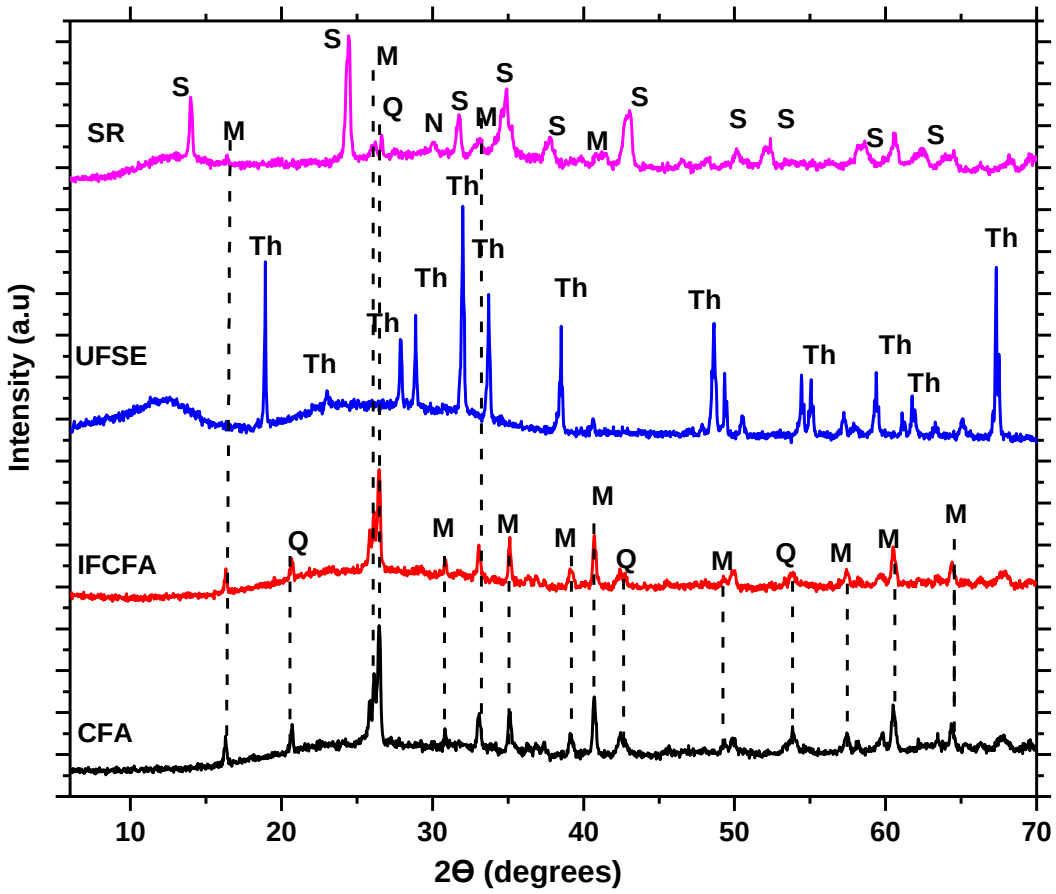

Figure 4.7: XRD patterns of CFA, IFCFA, UFSE and SR, where Q = Quartz, M = Mullite, Th = Thenardite (Na_2SO_4), S = Sodalite and N = Na_2CO_3

The XRD for IFCFA, UFSE and SR are presented in Figure 4.7. The XRD spectra of UFSE shows the presence of thenardite (Na_2SO_4) in mineral phase and the presence of sodium sulphate salts formed during the precipitation of the alkaline extracted solution with sulphuric acid. The presence of Na_2SO_4 in UFSE confirms the XRF results, which showed a high content of Na. Two broad humps are observed in the region between 6-14° and 16-35° 2θ in UFSE spectra. These humps are characteristic of amorphous silica (Madrid et al. 2012; Missengue et al. 2018). The XRD pattern of the recovered SR is mostly dominated by sodalite phases, alongside a small signal of sodium carbonate. Mullite and quartz mineral phases of low intensities were also observed. The low residual content of quartz and mullite phases observed in SR indicates that the alkaline leaching process conditions were adequate to break down these refractory mineral phases initially present in CFA and release Si and Al, the elemental building blocks needed for zeolite synthesis. In addition, the remaining Si and Al in the SR after the alkaline leaching process underwent a further dissolution and condensation during the drying process at 70˚C, resulting in crystalline

sodalite mineral phases. This finding supports the report by Cornelius (2019) where a low-silica zeolite sodalite was achieved as a secondary product of the alkaline leaching process.

4.4.3 Morphological structure of IFCFA, UFSE and SR as determined by SEM

The morphological structure of IFCFA, UFSE and SR is presented in Figure 4.8.

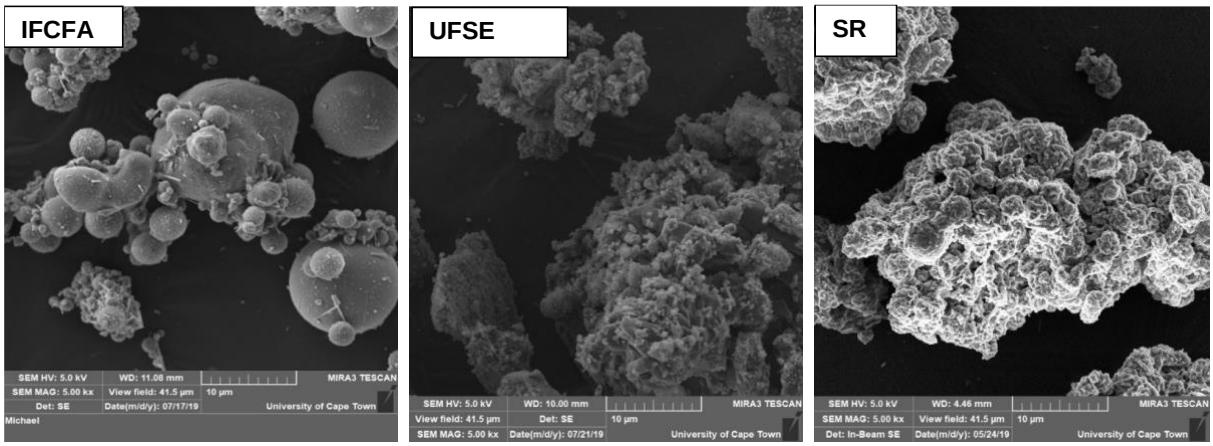

Figure 4.8: Morphological analysis for IFSA, U-CFASE and SR at 5000x magnification

The morphology of IFCFA, UFSE and SR, as depicted in Figure 4.8 shows that the well-defined spherical particles observed in IFCFA were transformed into agglomerated irregular particles in the UFSE sample after the alkaline leaching process. Such morphology is known to be characteristic of amorphous silica (Mor et al. 2017). In addition to the agglomerated spheroidal particles, the presence of crystalline rod-like structures were observed, which can be associated with the presence of Na and other metals in UFSE that precipitated with the silica during the alkaline leaching process (Cornelius 2019). The SEM micrograph of the solid residue (SR) obtained as a secondary waste after the alkaline leaching process shows a woolly ball-like crystalline morphology, which exhibited a typical sodalite structure (Hums 2017; Li et al. 2015; Shabani et al. 2022). The transformation of IFCFA to amorphous silica and zeolite sodalite (Figure 4.7), as clearly shown by the SEM micrographs, confirms that the dissolution of mullite and quartz minerals present in IFCFA during the alkaline leaching process was a success.

4.4.4 FTIR spectra for IFCFA, UFSE and SR

This section discusses the FTIR structure of IFCFA, UFSE and SR.

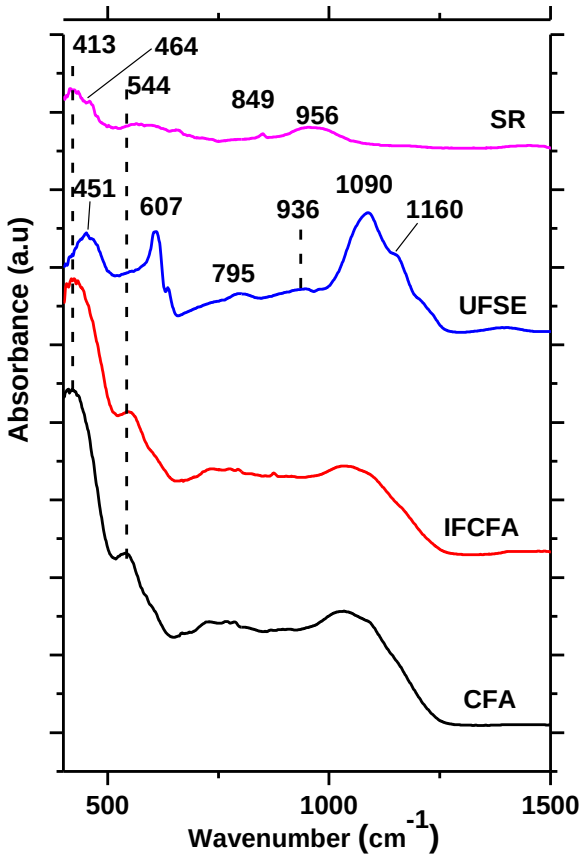

Figure 4.9: FTIR spectra for IFCFA, UFSE and SR

The structural configuration of UFSE and SR was analysed by FTIR spectroscopy and compared to that of CFA and IFCFA, as shown in Figure 4.9. The summary of the vibration bands with corresponding assignments for IFCFA, UFSE and SR are presented in Table 4.4.

Table 4.4: FTIR vibration band assignments for IFCFA, UFSE and SR

Wavenumber cm^{-1}				
IFCFA	**UFSE**	**SR**	**Band**	**Assignment**
413	451	413, 464	Si-O-T (T = Al or Si)	Symmetric stretching
544	_	544	Si-O-Al	Stretching vibration
_	607		Al-O	
726	795	849	Si-O	Symmetric stretching
_	936	956	Si-O	Asymmetric stretching
1038	1090	_	Si-O-T	Asymmetric stretching

A significant change in the chemical structure of IFCFA to UFSE and SR was observed. Five vibration bands were identified for the UFSE sample. These bands appeared at 451, 607, 795, 936, 1090 and 1160 cm^{-1}. The vibration bands at 451 and 607 cm^{-1} are attributed to Si-O-T and Al-O vibration bands respectively. A chemical shift at 413 to 451 cm^{-1} was observed when comparing IFCFA to UFSE. According to Shirazi et al. (2008), this shift indicates an increase in Si/Al ratio. This confirmed the XRF results shown in Table 4.4, where an increase in Si/Al ratio from 1.50 in IFCFA to 114.73 in UFSE was observed. The bands at 795, 936 and 1090 cm^{-1} can be assigned to Si-O and Si-O-T asymmetric stretching vibration, and the broad band at 1090 cm^{-1} indicates that the UFSE sample is dominated by silicate materials (Fu et al. 2017). The structural configuration of IFCFA is similar to that of CFA, which shows vibration bands that correlate to the presence of mullite and quartz (Cornelius 2019). However, the FTIR spectra for SR shows five bands at 413, 464, 544, 849 and 959 cm^{-1}, which correlates to Si-O-T, Al-O and Si-O. These bands indicate the presence of an alumino-silicate structure, in this case, that of a sodalite zeolite, as observed by Musyoka et al. (2011) and Vaičiukyniene Vaičiukyniene et al. (2009). These bands appeared at a relatively lower wavenumber in the SR spectra due to the high content of aluminium in this material (Fernández-Jiménez and Palomo 2005). The high concentration of Al in SR at 22.82, as shown in Table 4.4, is supported by the decrease in Si/Al ratio from 1.50 in IFCFA to 1.31 in SR. This could be due to the extraction of Si into the liquid phase and its subsequent separation and precipitation. This result shows that the alkaline leaching process was more susceptible to the dissolution of silica than aluminium.

4.5 Treatment of UFSE with oxalic acid and water

The obtained U-CFASE from the alkaline silica extraction process was then treated with varying concentrations of oxalic acid (X = 1.25, 1, 0.75, 0.44, 0.77 and 0 M) in order to remove the excess Na content and other impurities contained in the extract. The treatment process was carried out as follows: 30 g of the UFSE was mixed with X M oxalic acid solution in a 250 mL round-bottom beaker and heated at 80˚C under reflux conditions for 6 h while stirring at 250 rpm, as described in Chapter 3, Section 3.3.2. Subsequently, the solution was filtered, and the recovered treated silica extracts were dried overnight at 70˚C. The treated silica extracts were then named TFSE-1.25, TFSE-1, TFSE-0.75, TFSE-0.44, TFSE-0.77 and TFSE-H_2O respectively. The TFSE-x were thereafter characterised by XRF, XRD, SEM and FTIR in order to understand the effect of oxalic acid concentration and water on the TFSE-x chemical and physical properties.

4.5.1 Elemental composition of major oxides in UFSE and the TFSE-x

Table 4.5 compares the composition of major oxides in TFSE-1.25, TFSE-1, TFSE-0.75, TFSE-0.44, TFSE-0.77 and TFSE-H_2O, as analysed by XRF.

Table 4.5: Composition major oxides (XRF %) and elemental (ICP %) present in TFSE-1.25, TFSE-1, TFSE-0.75, TFSE-0.44, TFSE-0.77 and TFSE-H_2O in comparison to UFSE

XRF (wt%), n = 3							
Species	**UFSE (%)**	**TFSE-1.25 (%)**	**TFSE-1 (%)**	**TFSE-0.75 (%)**	**TFSE-0.44 (%)**	**TFSE-0.17 (%)**	**TFSE-H_2O (%)**
SiO_2	27.28 ± 0.12	87.68 ± 0.62	68.8 ± 0.02	82.23 ± 1.05	88.02 ± 0.03	86.47 ± 0.11	68.32 ± 0.20
Al_2O_3	0.21 ± 0.21	0.17 ± 0.40	0.57 ± 1.02	0.23 ± 0.30	0.23 ± 0.02	0.30 ± 0.39	0.61 ± 0.20
CaO	0.02 ± 0.00	0.01 ± 0.00	0.12 ± 0.00	Nd	0.01 ± 0.00	0.01 ± 0.00	0.03 ± 0.00
Fe_2O_3	Nd	Nd	0.01 ± 0.94	Nd	Nd	Nd	0.01 ± 0.59
TiO_2	0.08 ± 0.00	0.05 ± 0.00	0.04 ± 0.01	0.05 ± 0.02	0.06 ± 0.01	0.07 ± 0.02	0.07 ± 0.00
MgO	Nd	Nd	Nd	Nd	Nd	Nd	Nd
P_2O_5	0.42 ± 0.03	0.05 ± 0.00	0.05 ± 0.23	0.07 ± 0.00	0.06 ± 0.00	0.07 ± 0.00	0.18 ± 0.00
K_2O	0.67 ± 0.00	0.51 ± 0.00	1.08 ± 0.00	0.11 ± 0.00	0.54 ± 0.00	0.09 ± 0.00	0.65 ± 0.00
Na_2O	71.32 ± 0.00	11.53 ± 0.01	29.33 ± 0.01	17.3 ± 0.03	11.08 ± 0.01	12.98 ± 0.00	30.13 ± 0.00
MnO	Nd	Nd	Nd	Nd	Nd	Nd	Nd
Cr_2O_3	Nd	Nd	Nd	Nd	Nd	Nd	Nd
SiO_2/Al_2O_3	**129.55**	**506.87**	**119.74**	**355.68**	**382.95**	**284.69**	**114.05**
ICP (%)							
Si	19.18	81.81	58.22	74.59	82.31	80.27	57.79
Al	0.17	0.18	0.55	0.24	0.24	0.33	0.58
Ca	0.02	0.01	0.16	Nd	0.01	0.01	0.04
Fe	Nd	Nd	0.01	Nd	Nd	Nd	0.01
Ti	0.07	0.06	0.04	0.06	0.07	0.08	0.08
Mg	Nd	Nd	Nd	Nd	Nd	Nd	Nd
P	0.14	0.02	0.02	0.03	0.03	0.03	0.07
K	0.84	0.84	1.62	0.18	0.90	0.15	0.98
Na	79.58	17.07	39.38	24.91	16.44	19.12	40.45
Mn	Nd	Nd	Nd	Nd	Nd	Nd	Nd
Cr	Nd	Nd	Nd	Nd	Nd	Nd	Nd
Si/Al	**114.73**	**455.55**	**106.61**	**315.78**	**338.02**	**246.37**	**98.92**

*Note: nd – not detected

The total percentage oxides of Si>Na>Al present in the oxalic acid treated silica extracts (TFSE-1.25, TFSE-1. TFSE-0.75, TFSE-0.44, TFSE-0.17) accounted for 99.38%, 98,70%, 99.76%, 99.33%, and 99.75%, with a Si/Al ratio of 456, 107, 316, 338 and 246 respectively. The total percentage of Si>Na>Al in the water treated extract (TFSE-H_2O) was similar, with a total percentage of 99.05% and a Si/Al ratio of 99. As evident in Table 4.5, the percentage oxides of Cr, Mg, Mn and Fe remained either undetected or in insignificant amounts after the treatment process with both oxalic acid and water. However, the other oxides (Ca, K, P and Ti) regarded as sources of impurities were detected in trace amounts of < 1. A significant decrease in the Na content from 79.58% in the UFSE to a maximum of 16.44% in the oxalic acid treated extracts was also observed, with an Na removal efficiency within the range of 84.46 to 58.87. The Na removal efficiency in TFSE-H_2O was similar, at 57.75%. This result indicates that the treatment with H_2O alone could also remove the unwanted impurities (mainly Na) and still retain the high Si/Al ratio required for the synthesis of high-silica zeolites such as ZSM-5. The degree of Na removal efficiency, purity and yield were calculated using equation 4.2, 4.3 and 4.4 respectively.

$$ŋ = \frac{U_{NA} - T_{Na}}{U_{NA}} * 100 \ldots\ldots\ldots\ldots\ldots\ldots Equation\ 4.2$$

$$Yield = \frac{M_{TFSE}}{M_{TFSE} - M_{UFSE}} \ldots\ldots\ldots\ldots\ldots Equation\ 4.3$$

$$P\ (\%) = 1 - \sum_{i-1} M_i\ (\%) \ldots\ldots\ldots\ldots\ldots Equation\ 4.4$$

Where ŋ denotes the removal efficiency, U_{Na} is the percentage of Na in the UFSE and T_{Na} represents the percentage of Na in the TFSE-x (x = 1.25, 1, 0.75, 0.44, 0.17 and H_2O). M_{TFSE} and M_{UFSE} denote the mass of Si in the TFSE and UFSE, and M_i represents the mass of the components in the TFSE, except that of SiO_2.

Table 4.6: Purity, Si/Al, yields and efficiency of the untreated and the treated fly ash silica extracts (UFSE and TFSE-x)

			Percentage		
Concentration of OA (M)	**Sample Code name**	**Si/Al**	**Purity (%)**	**Yield (%)**	**Na removal ŋ (%)**
Untreated CFASE	UFSE	114.73	46.27	33.72	_
1.25	TFSE-1.25	455.55	90.89	76.27	83.83
1	TFSE-1	106.61	76.92	71.61	58.88
0.75	TFSE-0.75	315.78	86.91	75.09	75.74
0.44	TFSE-0.44	338.02	91.15	76.34	84.46
0.17	TFSE-0.17	246.37	90.07	76.02	81.80
H_2O	TFSE-H_2O	98.92	76.68	71.46	57.75

The purity and yield of the oxalic acid and water treated extracts, as shown in Table 4.6, indicate that the percentage of purity and yield increased significantly, from 46.27 and 33.72% to approximately 91 and 76% respectively, when UFSE was treated with oxalic acid (1.25, 1, 0.75, 0.44 and 0.17). Notably, the treatment with water (TFSE-H_2O) resulted in percentage purity of the Si and yield of 76.68 and 71.46% respectively. The increase in product yield in all the treated fly ash silica extracts suggests that the major impurity (Na) was removed during the oxalic acid treatment step and that the main component of the treatment of UFSE with either oxalic acid or water is predominantly silica. In a similar study by Ameh (2019), fused fly ash silica extract was treated with oxalic acid concentrations of 1.3, 1.5 and 1.7 M. The author reported a maximum purity and yield of 94 and 45% respectively, with a Si/Al ratio of between 48 and 61. These extracts were further used as feedstock in the synthesis of a high-silica zeolite (Ameh et al. 2020). The Si/Al ratio of TFSE-H_2O achieved after treatment with water in this study is within the required Si/Al ratio of >10 for high-silica zeolite synthesis. This result shows for the first time that the use of oxalic acid during the treatment step is not necessary, as suggested by Missengue et al. (2018) and Ndlovu (2016), and can be replaced by a simple water treatment step.

4.5.2 Mineral phases of UFSE, TFSE-1.25, TFSE-1, TFSE-0.75, TFSE-0.44, TFSE-0.17 and TFSE-H_2O

Figure 4.9 shows the comparison of the mineral phases contained in the untreated fly ash silica extract (UFSE) and the subsequent oxalic acid and water treated silica extracts (TFSE-x, where x represent the concentration of oxalic acid used during the treatment process) as determined by XRD analysis.

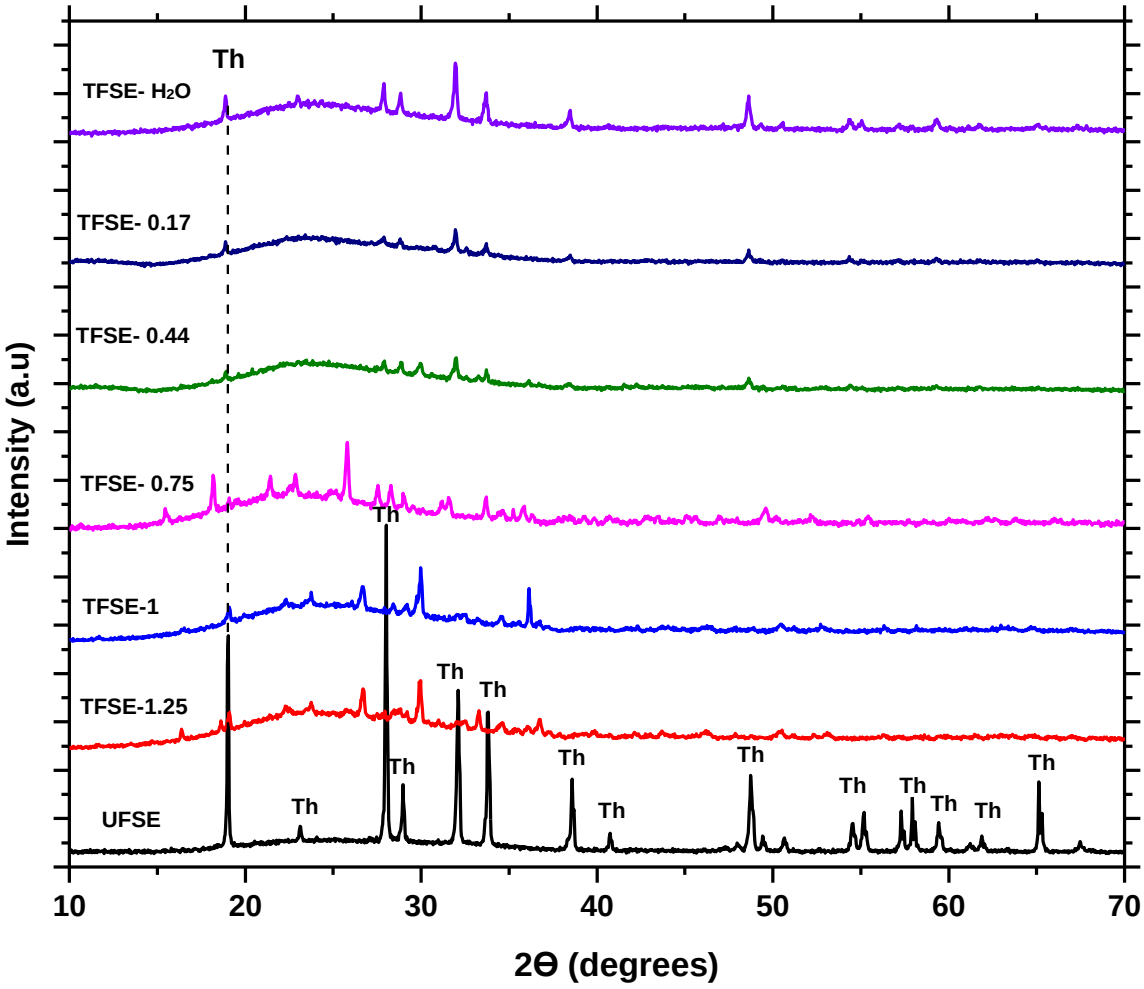

Figure 4.10: XRD spectra for UFSE, TFSE-1.25, TFSE-1, TFSE-0.75, TFSE-0.44, TFSE-0.17 and TFSE-H_2O, where Th = Thenardite (Na_2SO_4)

The XRD patterns of TFSE-1.25, TFSE-1. TFSE-0.75, TFSE-0.44, TFSE-0.17 and TFSE-H_2O are presented in Figure 4.10. The oxalic acid treated extracts and the water treated extract has a similar XRD pattern, which shows a broad diffusion peak within the region 16-35° 2θ. This structure can be ascribed to amorphous silica, as reported by Santos et al. (2020) and Morsi and Mohamed (2018). A single mineral phase of thenardite in varying intensities at 19° 2θ in the TFSE-x is also observed, which indicates the presence of Na (in sulphate form), as evident from the chemical composition presented in Table 4.5. The presence of thenardite mineral phases in the silica extracts shows that the sulphuric acid used during the precipitation stage reacted with Na to form Na_2SO_4, as shown in Figure 4.10. It can be seen that the intensity of the thenardite mineral phase in TFSE-1 and TFSE-H_2O is higher than the other TFSE-x (TFSE-1.25, TFSE-0.77, TFSE-

0.44 and TFSE-0.17), and this could be due to the high Na content in these samples at 29.33 and 30.13% respectively (Table 4.5). Similarly, the percentage purity was also lowest in these extracts, at 76.92 and 76.68% respectively (Table 4.6). The treatment process was not only instrumental in removing excess Na in the silica extracts, but also in removing some of the impurities such as SO_4 inherited during the precipitation of UFSE.

4.5.3 Morphological structure of UFSE and the TFSE-x

Figure 4.11 compares the morphological structure of UFSE and the TFSE-x (TFSE-1.25, TFSE-1. TFSE-0.75, TFSE-0.44, TFSE-0.17 and TFSE-H_2O), as analysed by SEM analysis.

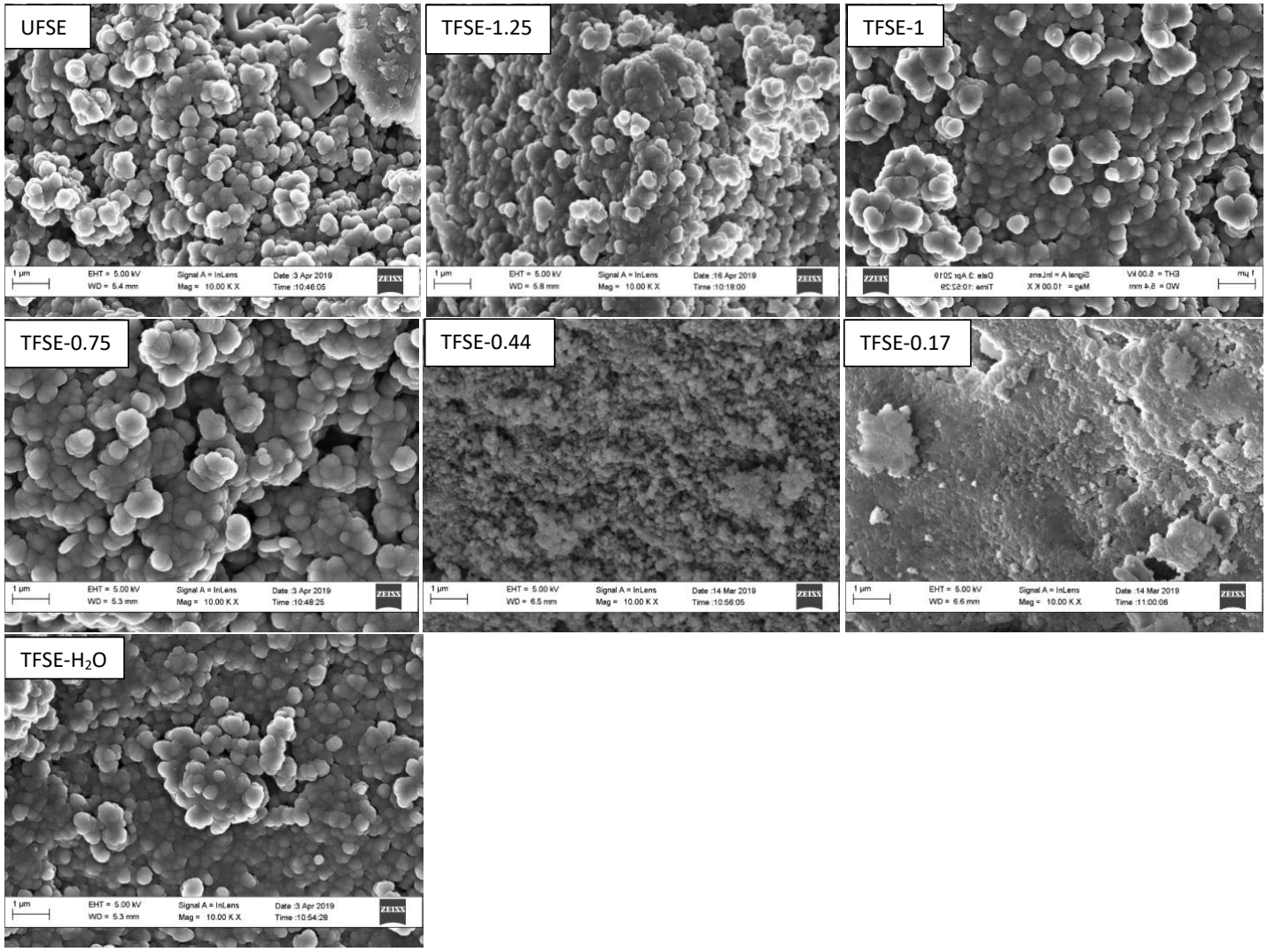

Figure 4.11: Morphological analysis for UFSE, TFSE-1.25, TFSE-1. TFSE-0.75, TFSE-0.44, TFSE-0.17 and TFSE-H_2O, Mag 1 000x

As expected, the morphology of the TFSE-x shows agglomerated spheroid nanoparticles which indicates the presence of amorphous silica, as discussed in Section 4.4.2. It can be seen from the SEM micrographs presented in Figure 4.11 that the treatment with lower concentrations of oxalic acid (0.44 and 0.17 M) had a direct impact on the morphological structure of the TFSE-0.44 and TFSE-0.17 samples. At high purity of > 90% (Table 4.6), smaller agglomerated crystal sizes are observed (Figure 4.11). This observation is similar to that reported by Yuvakkumar et al. (2014). This result not only shows that the treatment step was beneficial in terms of impurity removal, but that it could also be used for amorphous silica crystal size alteration.

4.5.4 FTIR spectra for TFSE-1.25, TFSE-1, TFSE-0.77, TFSE-0.44, TFSE-0.17 and TFSE-H_2O in comparison with UFSE

Figure 4.12 presents the comparison of the structural analysis of the treated silica extracts (TFSE-x) obtained after the treatment with varying concentrations of oxalic acid (1.25, 1, 0.75, 0.44 and 0.17 M) and water.

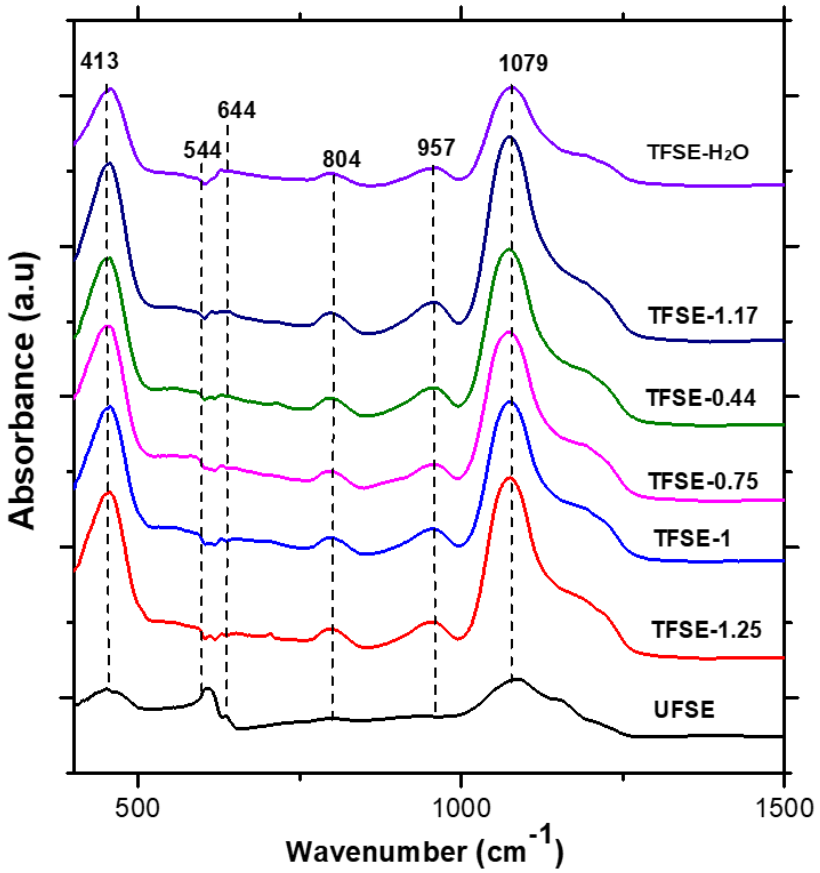

Figure 4.12: FTIR spectra for TFSE-1.25, TFSE-1, TFSE-0.77, TFSE-0.44, TFSE-0.17 and TFSE-H_2O in comparison with UFSE

The FTIR spectra of the oxalic acid-treated and water-treated extracts are shown in Figure 4.12. The chemical structures of all the samples were similar and contained six vibration bands appearing at 413, 544, 644, 804, 957 and 1079 cm^{-1}. The absorption band at 413 cm^{-1} can be assigned to a Si-O band that characterises highly siliceous materials and double ring vibration bands respectively (Shirazi et al. 2008). A change in the absorption intensity to a higher wavelength was observed from UFSE to the TFSE-1.25, TFSE-1, TFSE-0.77, TFSE-0.44, TFSE-0.17 and TFSE-H_2O. However, the wavelength for the water treated sample (TFSE-H_2O) was lower than that of the oxalic acid treated extracts (TFSE-1.25, TFSE-1, TFSE-0.77, TFSE-0.44, TFSE-0.17). Shirazi et al. (2008) reported that the shift in the internal asymmetric stretch band towards higher wavelength is due to the increase in Si/Al ratio. Based on this observation, it can be concluded that the higher absorption wavelength in the oxalic acid treated extracts is due to the high Si/Al ratio (between 106 – 456) in these samples, and was lowest for TFSE-H_2O, with a Si/Al ratio of 99. The vibration bands at 544 and 644 cm^{-1} are associated with the stretching vibration of the Al-O with coordinated aluminium ions (Aronne et al. 1997). A significant decrease in the peak intensity of UFSE and the respective TFSE-x between the region 544 and 644 cm^{-1} was observed. This could be due to the decrease in Na metal (initially present in the UFSE) after treatment with oxalic acid or water. The vibration bands at 804 and 957 cm^{-1} can be related to the Si-O symmetric stretching vibration, and the band at 1079 cm^{-1} is associated with Si-O-T asymmetric stretching vibration, where T = Si or Al (Li et al., 2014). The FTIR pattern for all the treated silica extracts (TFSE-1.25, TFSE-1, TFSE-0.77, TFSE-0.44, TFSE-0.17 and TFSE-H_2O) correlates to that of amorphous silica (Saikia and Parthasarathy 2010). In addition, it can be observed that the intensity of the absorption vibration at 804, 975 and 1079 cm^{-1} relating to the asymmetric stretching vibration increased in proportion with the percentage purity, as shown in Table 4.6.

4.6 Effect of recycled liquid waste on the Si/Al ratio of the treated silica extracts

It has been shown in prior sections that the oxalic acid treatment step can be eliminated by using a single-step water treatment process. However, in order to minimise the generation of liquid waste during the treatment process, a recycling stream was introduced in the treatment process, with a view to enhancing the feasibility and minimising the liquid waste generated during the treatment process. The treatment conditions used to investigate the effect of recycled liquid waste on the Si/Al of the treated silica extracts is detailed in Chapter 3, section 3.3.2.1. The liquid waste

was recycled four times using a fresh feed (UFSE) for each cycle. The obtained TFSEs for each cycle (coded TFSE1, TFSE2, TFSE3 and TFSE4) were dried overnight at 70°C and characterised by ICP, SEM, XRD and FTIR. The subsequent liquid waste after each treatment cycle (coded, TH-LW1, TH-LW2, TH-LW3 and TH-LW4) were thereafter characterised by ICP in order to gain a better understanding of the elemental distribution of the resulting TFSEs.

4.6.1 Elemental composition of TFSE1, TFSE2, TFSE3 and TFSE4 and the generated liquid waste TH-LW1, TH-LW2, TH-LW3 and TH-LW4.

The elemental composition of TFSE1, TFSE2, TFSE3 and TFSE4 and TH-LW1, TH-LW2, TH-LW3 and TH-LW4 as characterised by ICP is presented in Figure 4.13 and Figure 4.14 respectively.

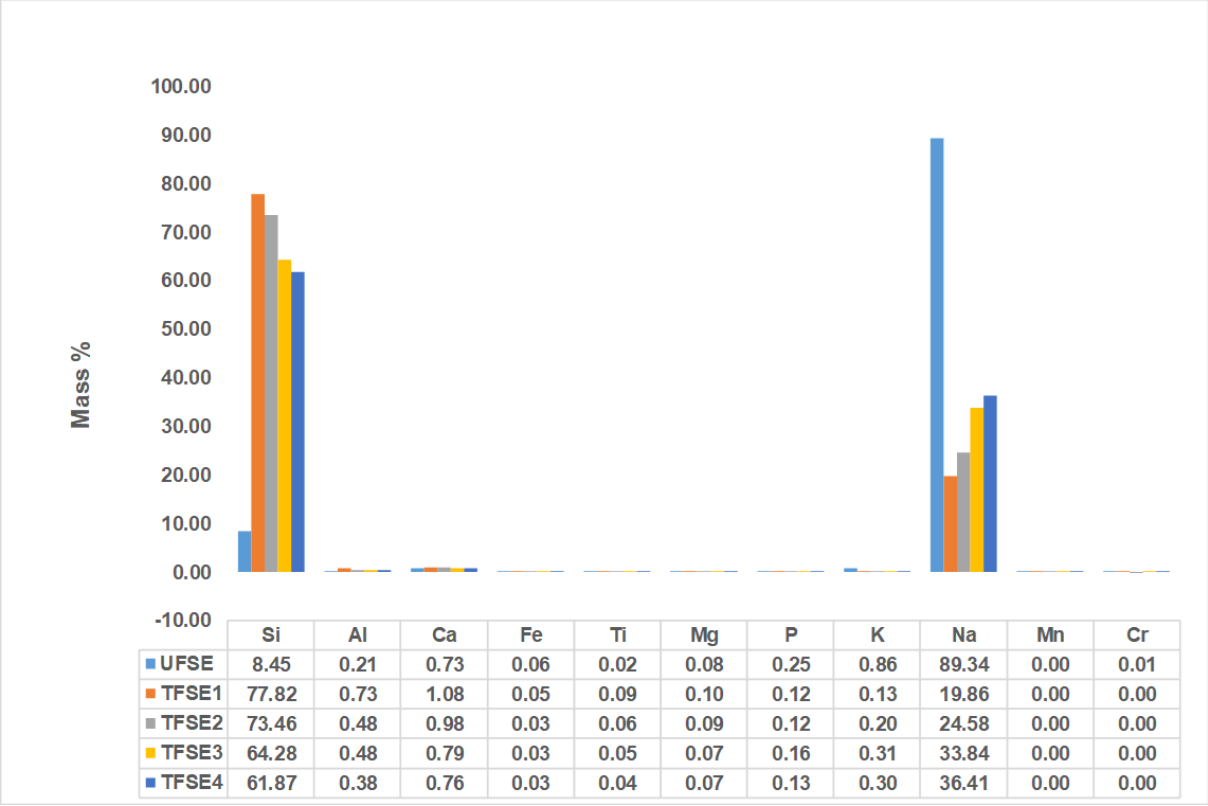

	Si	Al	Ca	Fe	Ti	Mg	P	K	Na	Mn	Cr
UFSE	8.45	0.21	0.73	0.06	0.02	0.08	0.25	0.86	89.34	0.00	0.01
TFSE1	77.82	0.73	1.08	0.05	0.09	0.10	0.12	0.13	19.86	0.00	0.00
TFSE2	73.46	0.48	0.98	0.03	0.06	0.09	0.12	0.20	24.58	0.00	0.00
TFSE3	64.28	0.48	0.79	0.03	0.05	0.07	0.16	0.31	33.84	0.00	0.00
TFSE4	61.87	0.38	0.76	0.03	0.04	0.07	0.13	0.30	36.41	0.00	0.00

Figure 4.13: Elemental composition of TFSE1, TFSE2, TFSE3 and TFSE4 in comparison with UFSE

The major elements (Na>Si>Al) present in TFSE1, TFSE2, TFSE3 and TFSE4 accounted for 98.41, 98.52, 98.60 and 98.66%, with a Si/Al ratio of 106, 153, 133 and 161 respectively (Figure 4.13). It can be seen from Figure 4.13 that the mass percentage of Si decreased from 77.82, 73.46, 64,28 and 61,87, accounting for Na/Si ratios of 0.26, 0.33, 0.53 and 0.59 after each cycle

respectively. The percentage purity and yield of the recovered TFSE (1,2,3 and 4) after each treatment cycle, in comparison with UFSE, was calculated and the results are presented in Table 4.7.

Table 4.7: Percentage purity and yields for UFSE, TFSE1, TFSE2, TFSE3 and TFSE4

Sample code name	Si/Al	Na/Si	Percentage		
			Purity (%)	Yield (%)	Na remove ŋ (%)
UFSE	114.73	4.15	46.27	33.72	_
TFSE1	106.13	0.26	69.25	92.88	77.77
TFSE2	152.99	0.33	63.51	48.56	72.48
TFSE3	133.47	0.53	51.02	46.28	62.12
TFSE4	160.97	0.59	47.96	45.72	59.25

It can be seen that the purity of the silica extracts (TFSE1, TFSE2, TFSE3 and TFSE4) decreased with the increased Na content, as shown in Figure 4.13 and Table 4.7 respectively. The increase in Na-content on TFSE1, TFSE2, TFSE3 and TFSE4 is influenced by the excess Na carried over by the recycled stream. Singh and Dutta (2003) reported that an increase in Na/Si to ≥ 0.4 in the synthesis precursor resulted in co-crystallisation of ZSM-5 and α-SiO_2, which then compromised the stability of the formed zeolite. In another study, (Missengue et al. 2017) reported that high Na/Si of 5 prevented the formation of ZSM-5 zeolite. Although the purity of the recovered TFSEs were compromised (due to the increased Na content in each extract), the Na/Si ratio is still within the required range for high-silica zeolite synthesis.

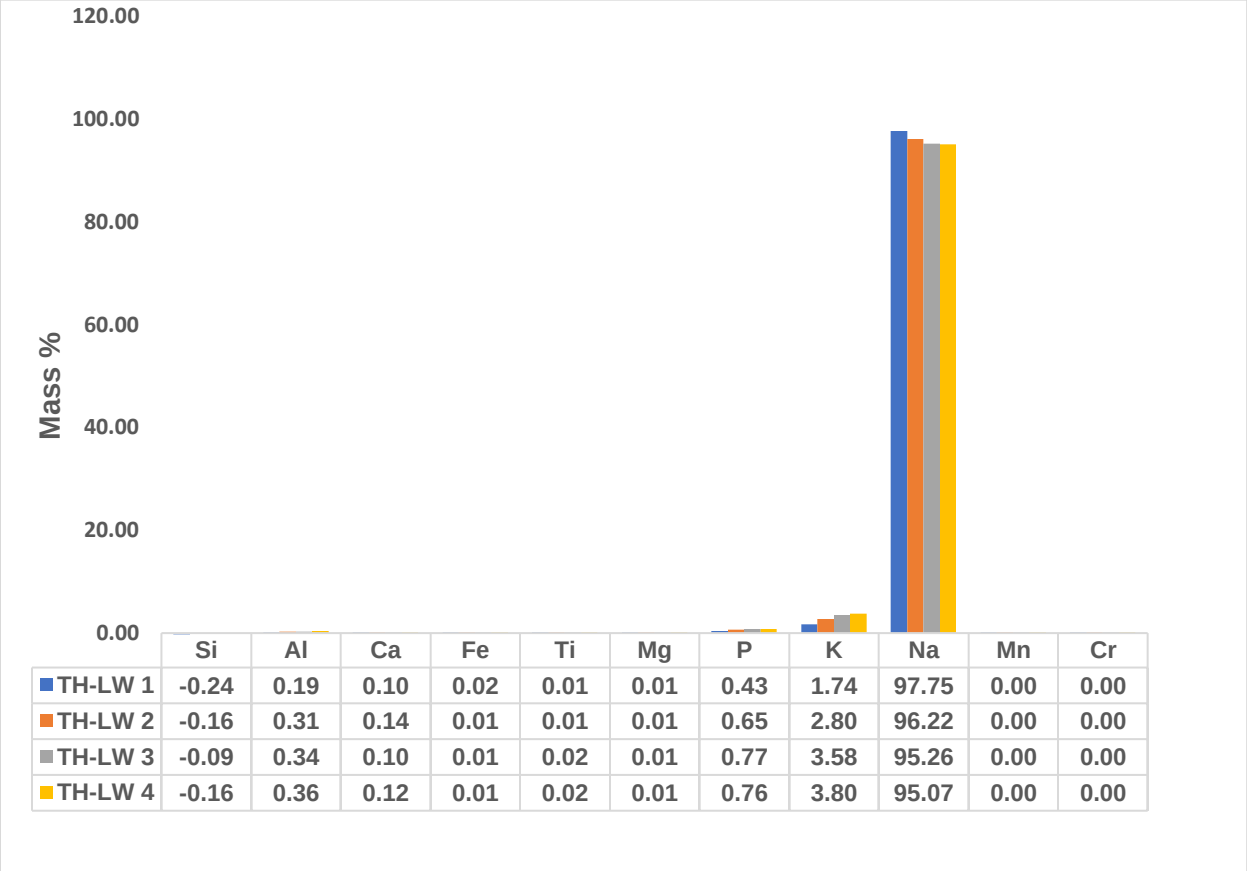

	Si	Al	Ca	Fe	Ti	Mg	P	K	Na	Mn	Cr
TH-LW 1	-0.24	0.19	0.10	0.02	0.01	0.01	0.43	1.74	97.75	0.00	0.00
TH-LW 2	-0.16	0.31	0.14	0.01	0.01	0.01	0.65	2.80	96.22	0.00	0.00
TH-LW 3	-0.09	0.34	0.10	0.01	0.02	0.01	0.77	3.58	95.26	0.00	0.00
TH-LW 4	-0.16	0.36	0.12	0.01	0.02	0.01	0.76	3.80	95.07	0.00	0.00

Figure 4.14: Elemental composition for TH-LW1, TH-LW2, TH-LW3 and TH-LW4 as analysed by ICP, n = 3

Figure 4.14 shows a decrease in the Na content (97.75, 96.22, 95.26 and 95.07%) in the resulting liquid waste (TH-LW1, TH-LW2, TH-LW3 and TH-LW4), while concentration of other impurities such as Al, Ca, Ti, P and K increased in the liquid waste resulting from each treatment cycle (TH-LW1, TH-LW2, TH-LW3 and TH-LW4). The increase in concentration of these elements from TH-LW1 – TH-LW4 is due to the build-up of elements initially present in TH-LW1. Du Plessis (2014) reported that recycling of the liquid waste stream is necessary and could promote the scale-up of zeolite synthesis processes, although the build-up of elements initially present in the mother liquor is unavoidable. The production of highly concentrated liquid waste (TH-LW4) at the end of the treatment cycle poses a serious economic and environmental problem, as treatment or disposal of highly concentrated liquid waste can be costly. To minimise the liquid waste generated, the recovered TH-LW beyond the 4th recycle may be recycled back to the alkaline extraction step as process water or source of Na. The results obtained in this study have shown that even after a treatment cycle beyond 4 cycles, the process managed to achieve a Na removal efficiency of more than 50%. This process presents an opportunity to eliminate the liquid waste generated

during the treatment process and reduce the costs associated with the treatment of liquid streams with complex compositions.

4.6.2 Mineral phases of TFSE1, TFSE2, TFSE3 and TFSE4 in comparison with UFSE

Figure 4.15 presents the mineralogical structure of TFSE1, TFSE2, TFSE3 and TFSE4 as determined by XRD.

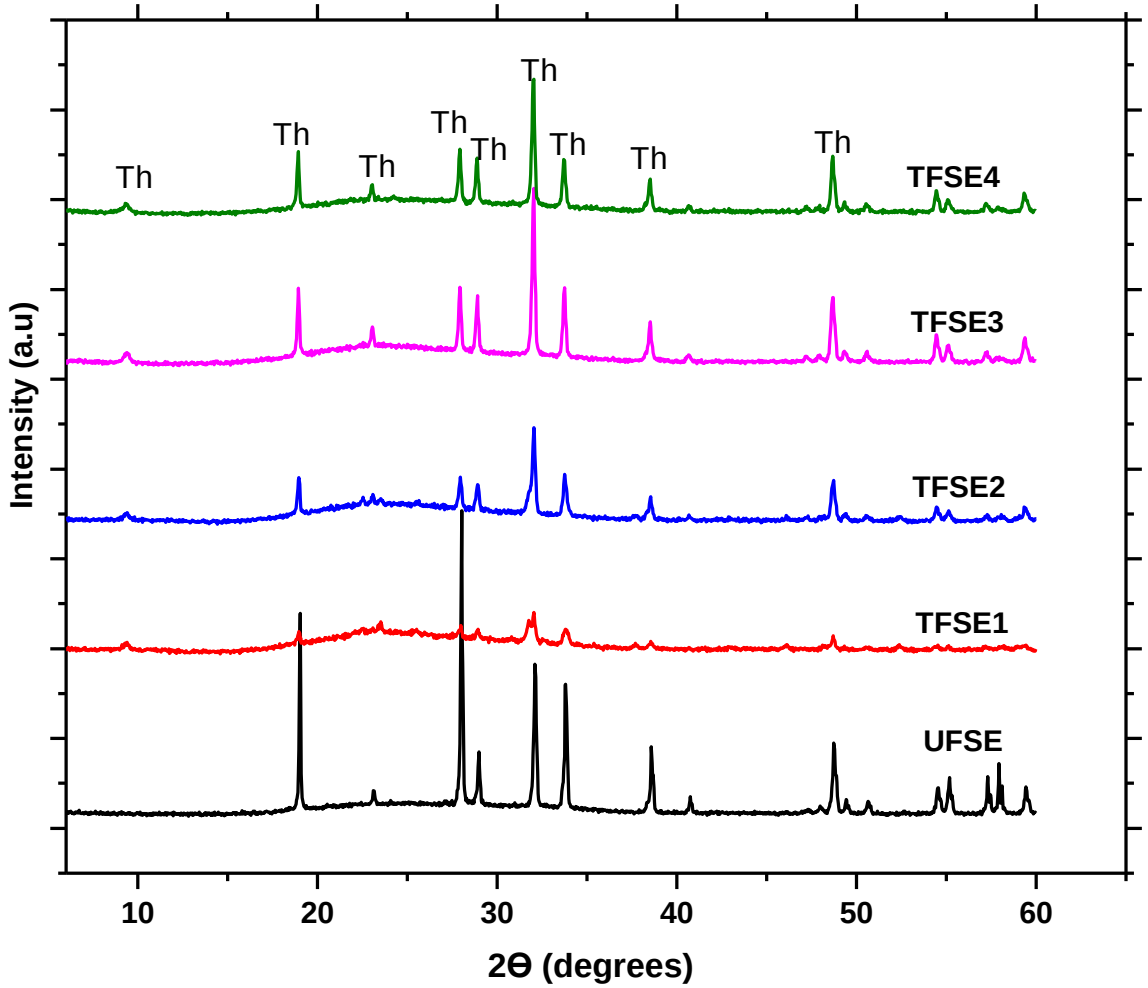

Figure 4.15: XRD spectra for UFSE, TFSE1, TFSE2, TFSE3 and TFSE4 in comparison with UFSE, where Th = Thenardite (Na_2SO_4)

The XRD spectra presented in Figure 4.15 show that the silica extracts treated with recycled liquid waste (TFSE1, TFSE2, TFSE3 and TFSE4) are composed of thenardite crystalline mineral phases which indicates the presence of sodium sulphate. A broad hump in the region 16-35 2Θ

of all the TFSEs is observed, which indicated the presence of amorphous silica. It can be seen that the intensity of the thenardite mineral phase increased from UFSE to TFSE1, TFSE2, TFSE3 and TFSE4. This observation is due to the increase in Na content of the TFSEs, as shown in Figure 4.13. The high intensity of thenardite on the respective extracts could also be related to the degree of impurity, as shown in Table 4.7. It could then be concluded that the higher the intensity of thenardite, the less pure the TFSE. This result confirmed the ICP and XRD results presented in Figures 4.13 and 4.15 respectively.

4.6.3 Morphological structure of TFSE1, TSFE2, TFSE3 and TFSE4, as determined by SEM

Figure 4.16 presents the SEM micrographs of TFSE1, TFSE2, TFSE3 and TFSE4 in comparison with UFSE, as characterised by SEM analysis.

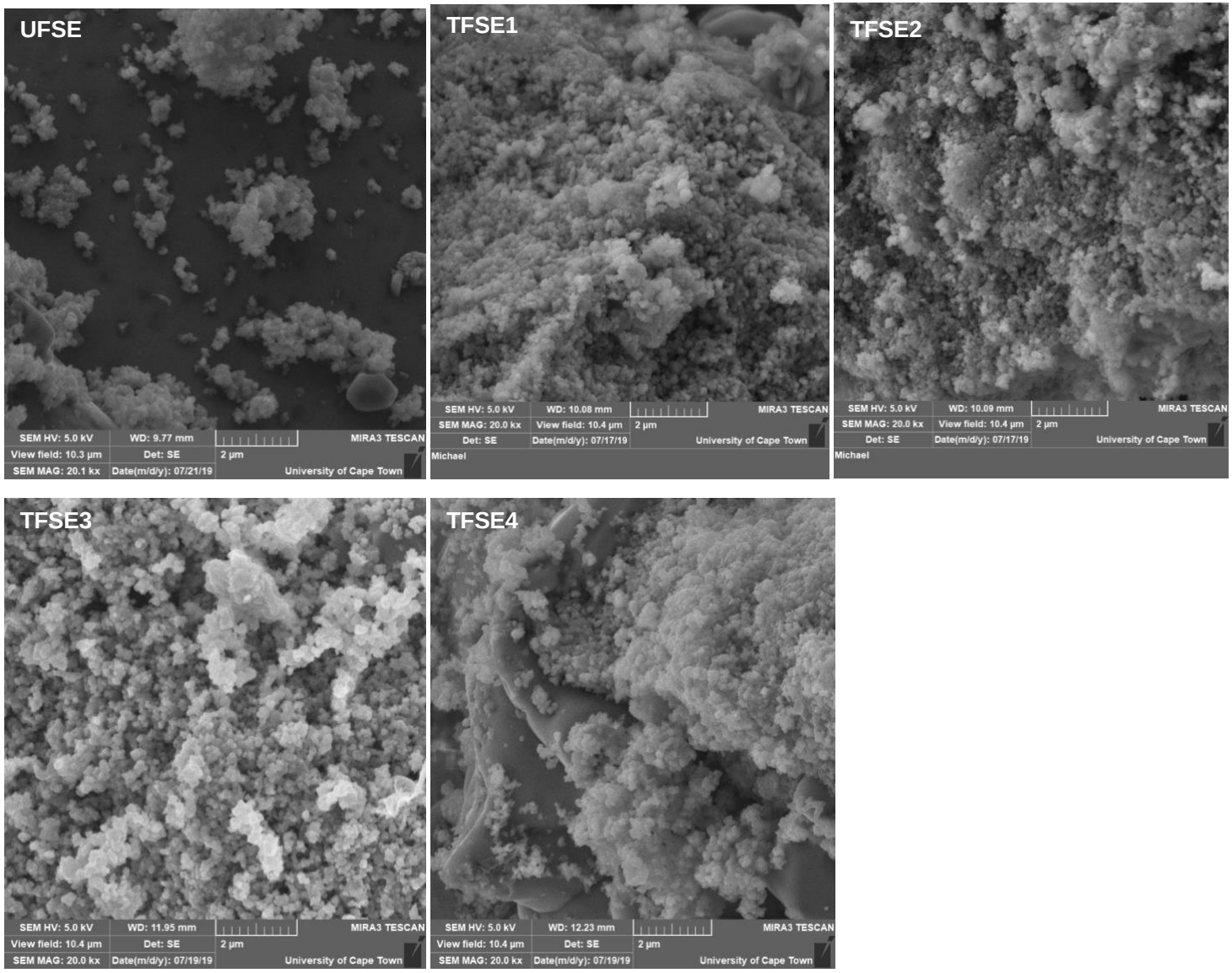

Figure 4.16: Morphology for TFSE1, TFSE2, TFSE3 and TFSE4 in comparison with UFSE

.

The morphological structures of TFSE1, TFSE2, TFSE3 and TFSE4 were similar to that of UFSE, with an irregular shape of varying sizes. Agglomerated smaller particles were observed on the surface of the larger particles, which indicate the presence of amorphous silica (Mor et al. 2017).

4.6.4 FTIR spectra for TFSE1, TFSE2, TFSE3 and TFSE4 in comparison with UFSE

The FTIR spectra presented in Figure 4.17 show the FTIR patterns for TFSE1, TFSE2, TFSE3 and TFSE4.

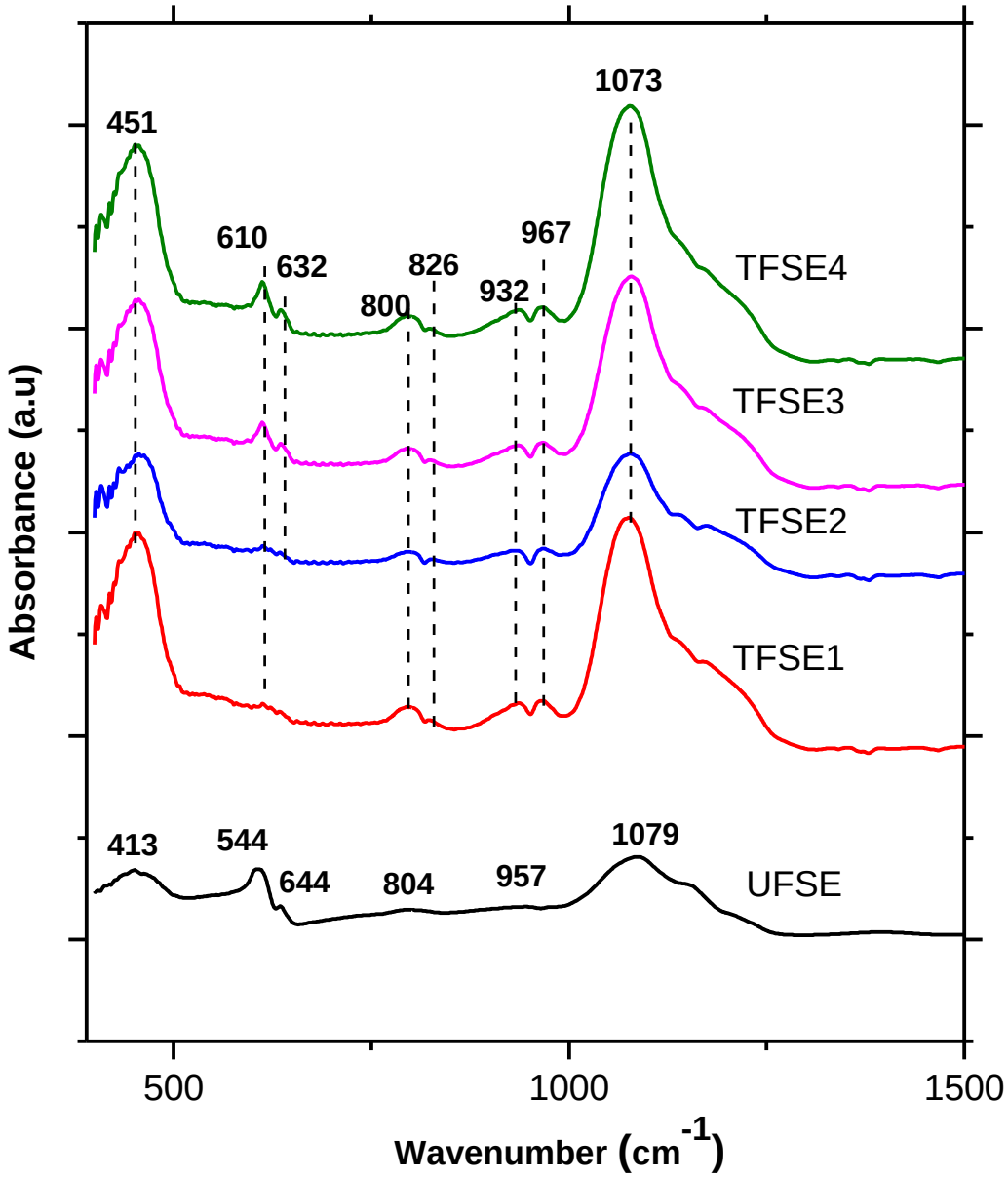

Figure 4.17: FTIR spectra for TFSE1, TFSE2, TFSE3 and TFSE4 compared to UFSE

The FTIR pattern of TFSE1, TFSE2, TFSE3 and TFSE 4 recovered from the treatment process using recycled liquid waste is identical to that of the TFSE-H_2O treated with water (Figure 4.12). This shows that the recycling of the liquid waste in the treatment process was a success, as no structural changes were observed in the treated silica extracts. The absorption bands appearing at 451, 800, 826 and 1073 cm^{-1} are attributed to Si-O-Si bonds, which can be assigned to symmetric and asymmetric vibration bands (Fu et al. 2017; Mor et al. 2017). The band at 610 and 632 cm^{-1} can be assigned to stretching vibration of the Al-O, which indicated the presence of

.

aluminium in the TFSEs. The band at 932 and 967 cm^{-1} can be assigned to Si-O symmetric stretching vibration. The results show that selective extraction of silica from CFA can be achieved using alkaline extraction techniques with minimal waste generation.

4.5 Chapter summary

The extraction of high-silica fly ash extracts suitable for use as feedstock in synthesis of ZSM-5 zeolite was achieved in this chapter using the alkaline extraction process. The process was comprised of: removal of magnetic fraction (MF) (in order to enhance the dissolution of silica), alkaline extraction of silica (UFSE) (reflux at 150˚C for 24 h) from the iron-free coal fly ash (IFCFA). The alkaline extraction process resulted in a solid residue (SR), which was thereafter transformed into a low-cost sodalite zeolite. Lastly, there followed the treatment of the extracted silica (UFSE) with oxalic acid of varying concentration (1.25, 1, 0.77, 0.44, 0.17 M) or water to reduce the excess Na content and other undesirable impurities present in UFSE. The oxalic acid and water treated silica extracts (TFSE-1.25, TFSE-1, TFSE-0.77, TFSE-0.44, TFSE-0.17 and TFSE-H_2O) resulted in high purity (77-91% and 77%) and yields (72-76% and 71%), respectively. The results showed that treatment of UFSE with water achieved high purity and yield comparable to those treated with oxalic acid and a Si/Al ratio of 98.92.

The water treatment process generates voluminous liquid waste, which requires further treatment. Considering scale-up, processing large volumes of highly concentrated liquid waste can be costly. As such, in this study, recycle protocols during the treatment process were implemented with a view to minimise the waste generated in the process and enhance the feasibility of process at a large scale. The results obtained showed that the recycling of the liquid waste compromised the purity and yields of the treated silica extracts (TFSE1, TFSE2, TFSE3 and TFSE4), however the obtained Si/Al (106 - 160) and Na/Si (0.26 – 0.59) were still within the range required for ZSM-5 zeolite synthesis.

This chapter has shown that CFA can be used as a feedstock to extract highly siliceous materials suitable for the synthesis of ZSM-5 zeolite using alkali as an extraction medium, which also resulted in a low-cost zeolite sodalite leading to a zero-waste extraction process. A cost saving model was also proposed by way of introducing recycle streams to reduce wastage of resourceful materials during the alkaline and treatment process.

.

CHAPTER 5
SYNTHESIS AND CHARACTERISATION OF ZEOLITE ZSM-5 SYNTHESISED FROM CFA SILICA EXTRACTS.

5.1 Synopsis

The synthesis of ZSM-5 zeolite from standard chemical reagents or in combination with either rice husk or CFA has been extensively studied (Dey et al. 2013; Gao et al. 2016; Mohiuddin et al. 2016; Nada et al. 2019). However, studies on the use of CFA as the sole source of silicon and aluminium in the synthesis of ZSM-5 is limited. This is due to its low Si/Al ratio and the difficulty of dissolving sufficient Si and Al required for the synthesis of high-silica zeolites. The synthesis of ZSM-5 from CFA often requires the addition of aluminosilicate sources to adjust the Si/Al ratio. These reagents are costly, and could limit the potential application of CFA-based zeolite at an industrial scale. Most recently, the synthesis of CFA-based ZSM-5 zeolite without the addition of aluminosilicate sources has been reported on (Ndlovu 2016). The method involved a three-step alkaline leaching process, which included a Si/Al ratio adjustment step with saturated oxalic acid solution, followed by a standard hydrothermal process. Considering scale-up, the use of concentrated oxalic acid solution during the treatment process will contribute a significant amount to the production costs for CFA-based zeolites, making the process uneconomical for industrialization.

In this chapter, the synthesis and optimisation of ZSM-5 zeolite from the oxalic acid or water-treated silica extracts prepared from CFA (as discussed in Chapter 4) was investigated. The verified synthesis method for ZSM-5 zeolite was used for the preliminary synthesis, as described in Chapter 3, Section 3.3.3. The optimum conditions obtained were thereafter used as a baseline to investigate the effect of NaOH, the structure directing agent (TPABr), water content and the hydrothermal time on the phase purity and morphology of ZSM-5 zeolite. The effect of the treated fly ash silica extracts (TFSE1, TFSE2, TFSE3 and TFSE4) treated with recycled liquid waste (as discussed in Chapter 4, section 4.6) on the phase purity and morphology of ZSM-5 zeolite was also investigated. The crystal size and crystallinity (obtained from the SEM and XRD diffraction) were used as a response factor and monitored throughout the experimental process. Detailed characterisations, such as ICP, FTIR, BET, TGA and TPD, were performed on selected zeolite samples following the optimisation process. A summary, which outlines major discussions and findings is also included in this chapter.

.

5.2 Preliminary synthesis of ZSM-5 zeolite using oxalic acid and H_2O treated fly ash silica extracts

In this section, oxalic acid and water treated fly ash silica extracts (TFSE- x, where x = 1.25, 1, 0.77, 0.44, 0.17 and H_2O, as shown in Chapter 4, Section 4.5) were used as feedstock in the preliminary synthesis of ZSM-5 zeolite. The synthesis, as detailed in Chapter 3 (Section 3.3.3) was carried out by mixing 2 g of TFSE-x, 0.4 g of NaOH and 50 mL of H_2O in a 100 mL Teflon-lined stainless autoclave. This was followed by ageing for 40 min at room temperature and the addition of 1.5 g of TPABr, after which the autoclave containing the homogeneous mixture made of different molar regimes (see below the different molar regimes) was placed in a pre-heated oven at 160°C for 72 h. The obtained results were characterised by SEM and XRD as the main response factor to evaluate the performance of each fly ash extract on the synthesis of ZSM-5 zeolite. The selected fly ash silica extract after the preliminary synthesis was thereafter used as the sole source of Si and Al for further optimisation studies in the subsequent subsections.

Z-1.25	1 Si: 0.002 Al: 0.587 Na: 0.189 TPABr: 95.088 H_2O
Z-1	1 Si: 0.009 Al: 1.250 Na: 0.241 TPABr: 121.171 H_2O
Z-0.77	1 Si: 0.003 Al: 0.762 Na: 0.202 TPABr: 101.381 H_2O
Z-0.44	1 Si: 0.003 Al: 0.575 Na: 0.188 TPABr: 94.721 H_2O
Z-0.17	1 Si: 0.004 Al: 0.628 Na: 0.192 TPABr: 96.399 H_2O
Z-H_2O	1 Si: 0.003 Al :0.612 Na: 0.190 TPABr: 95.766 H_2O

Figure 5.1 presents the x-ray diffraction patterns of the ZSM-5 zeolite products obtained after the preliminary synthesis.

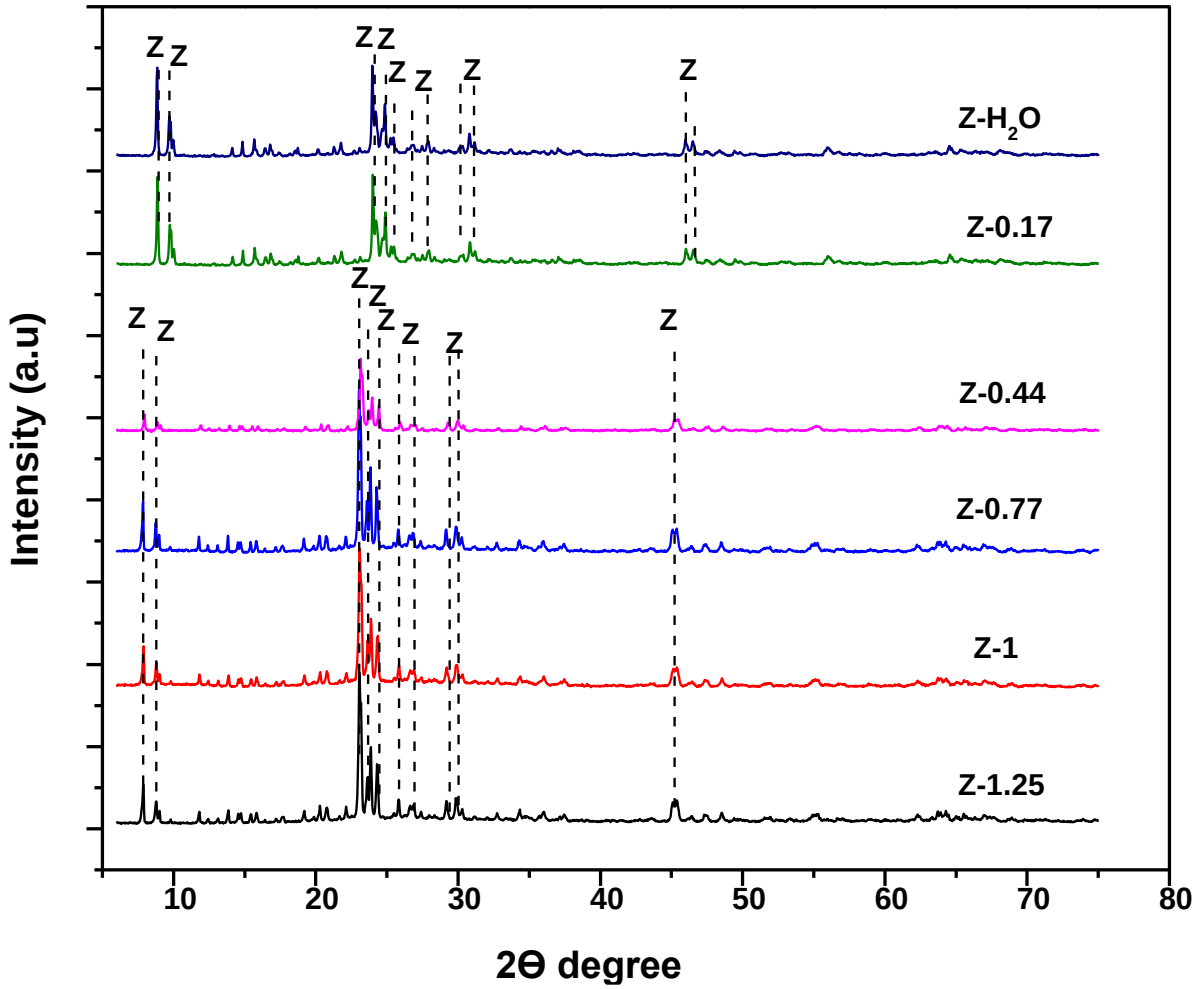

Figure 5.1: XRD spectra showing the effect of oxalic acid treated and water treated fly ash silica extracts on the mineral phase of zeolite ZSM-5, with the following code names: Z-1.25, Z-1, Z-0.77, Z-0.44, Z-0.17 and Z-H_2O

The XRD patterns of Z-1.25, Z-1, Z-0.77, Z-0.44, Z-0.17 and Z-H_2O are compared in Figure 5.1, with the characteristic of ZSM-5 zeolite peaks observed at 7.7, 8.9, 12.5, 13.8, 14.6, 14.9, 15.8, 21.2, 23, 23.9, 24.4, 25.6, 29, 29.7, 44.9 and 45.4° 2Θ as confirmed by the XRD patterns of the commercial ZSM-5 zeolite (Missengue et al. 2017) and the collection of simulated XRD powder patterns for zeolites (Treacy and Higgins 2007). However, a slight increase in the peak intensities in the zeolite products from Z-1.25 to Z-0.77 can be observed, with sample Z-0.77 having the highest peak intensity in the region 23, 24 and 25° 2θ. The lowest peak intensities were observed in Z-0.44 and Z-0.17, synthesised from TSFE containing lower concentrations of oxalic acid. The peak intensity of the Z-H_2O sample was the lowest in comparison to samples Z-1.25 and Z-0.77, although it was comparable to sample Z-1. It is evident from the XRD spectrum that the synthesis

.

of ZSM-5 zeolite from fly ash silica extract treated with varying concentrations of oxalic acid or H_2O had no effect on the phase purity of the zeolite structure.

The main diffraction peaks for zeolite ZSM-5 (2θ = 7.7, 8.9, 23, 23.9 and 24.4 °) were used to calculate the relative percentage crystallinity (using Equation 5.1) of zeolite products in relation to the highly crystalline sample Z-0.77.

$$Relative\ crystallinity = \frac{P}{P_O} * 100 \ldots\ldots\ldots\ldots\ldots\ldots\ldots\ldots\ldots\ldots\ldots Equetion\ 5.1$$

where P is the total area of the diffraction peaks at 7.7, 8.9, 23, 23.9 and 24.4 ° 2θ and Po is the equivalent area in the case of the height selected value of P.

The percentage crystallinity, as calculated from the XRD spectra, showed that sample Z-0.77 was highly crystalline, at 100%, followed by Z-1.25, Z-H_2O, Z-1, Z-0.17 and Z-0.44 with crystallinity of 98%, 84%, 81%, 47% and 38% respectively (5.1). The results show that the water treated fly ash silica extract (TFSE- H_2O) contained sufficient Si/Al ratio (98.92) required for the synthesis of pure phase ZSM-5 zeolite, as evident in Figure 5.1. In addition, this result validated that the percentage purity, as shown in Chapter 4, Table 4.6, was sufficient to allow for complete conversion of the amorphous silica into pure phase ZSM-5 without any trace impurities.

The morphological structure as resolved by SEM of Z-1.25, Z-1, Z-0.77, Z-0.44, Z-0.17 and Z-H_2O, presented in Figure 5.2, shows that the fly ash silica extracts (TFSE-1.25, TFSE-1, TFSE-0.77, TFSE-0.44, TFSE-0.17 and TFSE-H_2O) used as sources of Si and Al during the synthesis process were transformed into intergrowth prismatic morphology of different crystal sizes (as shown in Table 5.1), characteristic of ZSM-5.

.

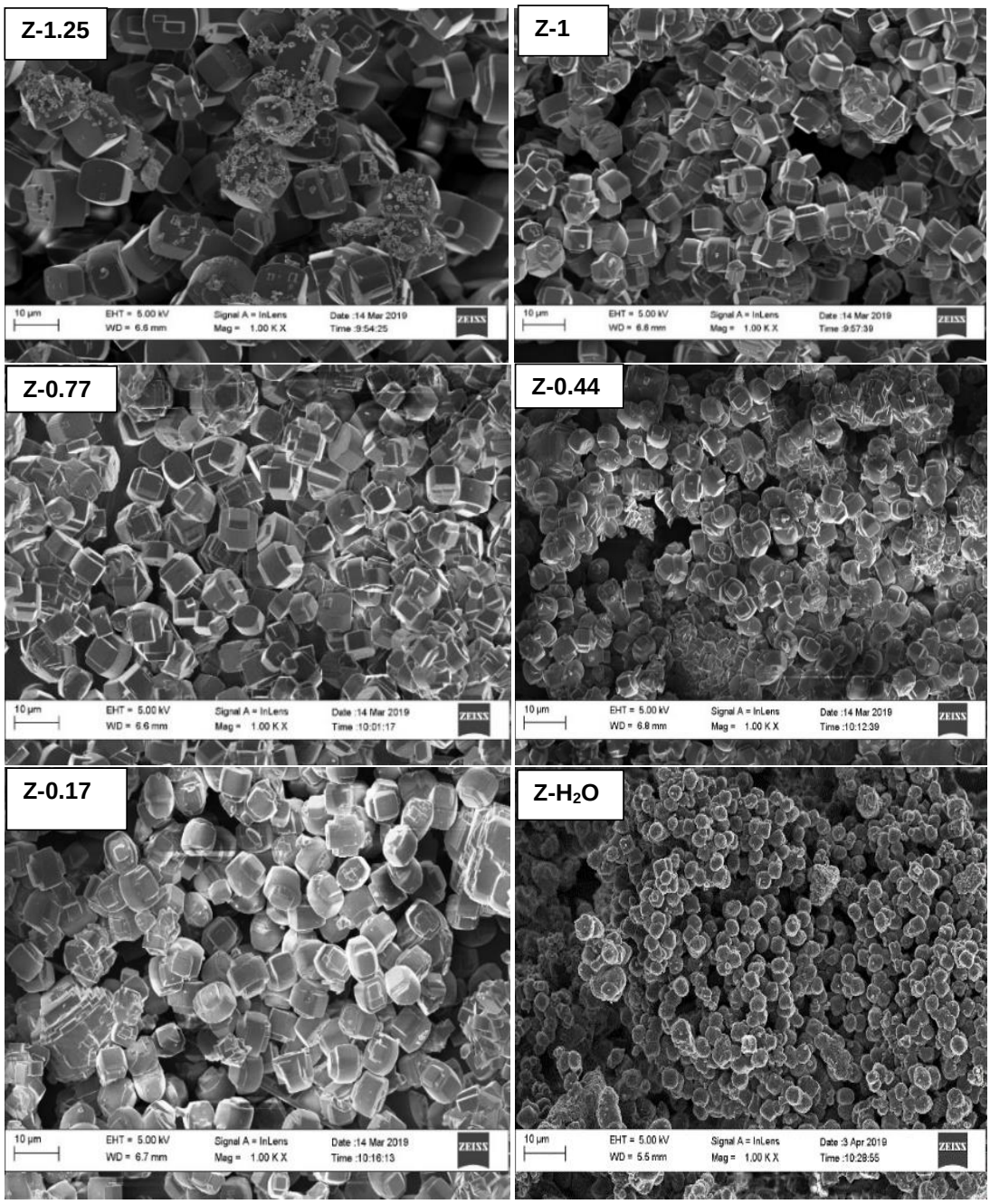

Figure 5.2: Morphological structure showing the effect of NaOH on the morphology of ZSM-5 zeolites at 160°C for 72 h, with the following code names: Z-1.25, Z-1, Z-0.77, Z-0.44, Z-0.17 and Z-H_2O

The crystal shapes of Z-1.25, Z-1, Z-0.77, Z-0.17 and Z-H_2O are pronounced and well-defined compared to sample Z-0.44, which revealed smaller crystallites, indicating shorter range repeating crystalline ordering. The crystal size (length and width), determined using ImageJ software, and their percentage crystallinity, are presented in Table 5.1

.

Table 5.1: Crystallinity and crystal size for Z-1.25, Z-1, Z-0.77, Z-0.44, Z-0.17 and Z-H_2O

		Crystal size (µm)	
Sample	Crystallinity (%)	Length (µm)	Width (µm)
Z-1.25	98	7.10	5.53
Z-1	81	6.80	3.42
Z-0.77	100	7.10	3.78
Z-0.44	38	5.30	2.77
Z-0.17	47	7.70	4.51
Z-H_2O	84	3.60	1.59

Table 5.1 shows that Z-0.77 was the most crystalline (100%), followed by Z-1.25 (98%), Z-1 (81%), Z-0.17 (47%) and Z-0.44 at 38%. It is noteworthy that the crystallinity of Z-H_2O was comparable to Z-1, at 84%. In addition, the crystal sizes of Z-1.25, Z-1, Z-0.77, Z-0.44, and Z-0.17 were within the range of 7.70 - 5.30 µm (length) and 5.53 – 2.77 µm (width), and that of sample Z-H_2O was the smallest, at 3.60 x 1.59 µm. The crystal sizes of Z-1.25, Z-1, Z-0.77, Z-0.44, and Z-0.17 were comparable to those reported by Missengue et al. (2017), who also synthesised ZSM-5 from oxalic acid treated silica extracts. The authors showed that the crystals of the synthesised ZSM-5 zeolites ranged in size from 9.50 – 3.75 µm (length) and 4.99 – 2.11 µm (width). Shirazi et al. (2008), reported that the increase in ZSM-5 crystal size was directly related to the increase in Si/Al molar ratio of the precursor hydrothermal gel. However, the results of this study showed no direct relationship between the Si/Al of the precursor gel and the obtained crystal size of the respective zeolite products. The results of this study clearly indicate that the treatment of the fly ash silica extracts with oxalic acid prior to the synthesis of high-silica zeolites was not necessary, and can be replaced with a water treatment step to achieve a pure phase zeolite ZSM-5 product of high quality. Sample Z-H_2O was selected as the best candidate due to its high crystallinity and small crystal size when compared to the other zeolite products. The synthesis conditions for Z-H_2O, including its molar composition, were thereafter used as the basis for further optimisation studies in the subsequent subsections.

5.3 Effect of NaOH on the synthesised ZSM-5 zeolite

.

The alkalinity of the synthesis solution is one of the most important parameters to control the crystallization of zeolite synthesis. This section investigates the effect of NaOH on the crystallinity, phase purity and morphology of ZSM-5 zeolite. The optimum molar composition for Z- H_2O (1 Si :0.003 Al :0.612 Na: 0.190 TPABr: 95.766 H_2O) was used as the basis for this set of experiments. The synthesis was carried out by mixing 2 g of TFSE-H_2O, x g of NaOH (x = 0.5, 0.4, 0.3, 0.2, 0.1 and 0.05 M) and 50 mL of H_2O in a 100mL Teflon-lined stainless autoclave, followed by the addition of 1.5 g of TPABr, while the hydrothermal conditions were kept constant at 160°C for 72 h, as described in Chapter 3, Section 3.3.2. The subsequent molar regimes were assigned the following code names: ZN-0.5, ZN-0.4, ZN-0.3, ZN-0.2, ZN- 0.1 and ZN-0.05. The relative crystallinity, crystal size and the quality of the crystalline phase were used to determine the optimal conditions for the synthesis of ZSM-5 zeolite in this section. The selected zeolite product with the optimal NaOH content was used for further investigations in the following subsections.

Figure 5.3 presents the XRD pattern of the products ZN-0.5, ZN-0.4, ZN-0.3, ZN-0.2, ZN-0.1 and ZN-0.05 obtained by varying the amount of NaOH, as described above.

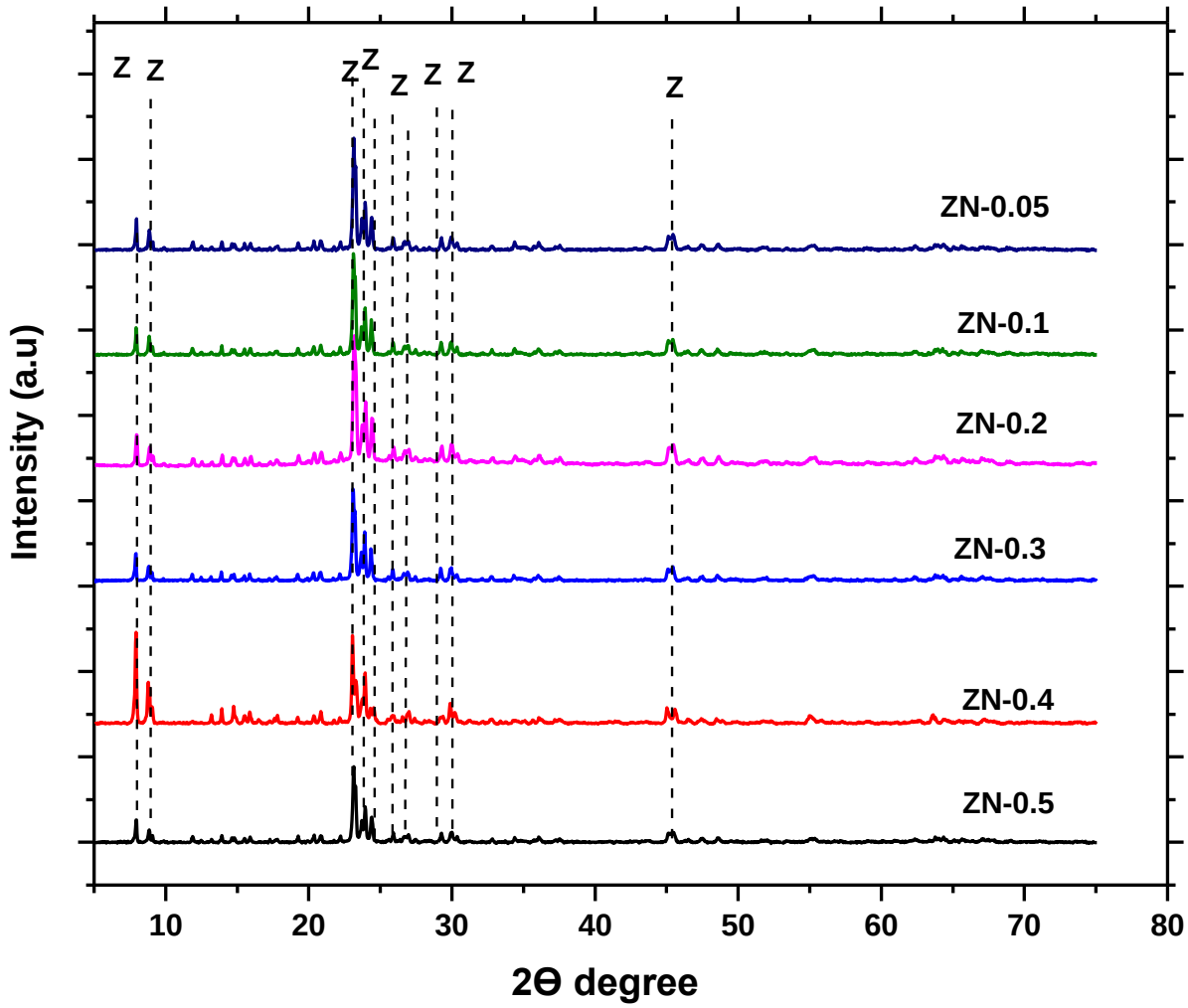

Figure 5.3: XRD spectra showing the effect of NaOH on the phase formation of ZSM-5 zeolites at 160°C for 72 h, with the following code names: ZN-0.5, ZN-0.4, ZN-0.3, ZN-0.2, ZN- 0.1 and ZN-0.05, where Z = ZSM-5

Figure 5.3 shows that the characteristic peaks of pure phase ZSM-5 zeolite were observed in all the samples, with no impurities detected. It is also evident from the XRD spectra that the increase in the NaOH amount had a reducing effect on the peak intensities of the products within the region 2θ = 23, 23.4 and 24.4°. According to Barrett et al. (2007), highly alkaline precursor solutions in zeolite synthesis promote crystallisation of low-silica zeolites. This is due to the highly competitive environment created between the cation structure directing agents, in which the high molar fraction of alkali Na+ cations is susceptible to the formation of multiple zeolite mineral phases (Zhang and Ostraat 2016). On the other hand, lowering the alkalinity of the precursor gel prolongs the dissolution time of the synthesis mixture, thus increasing the polymerization degree of silicon species, which favours the synthesis of highly siliceous zeolitic materials (Liu et al. 2010). The

.

results obtained suggest that an excess of NaOH above 0.5 g is not necessary, as this could result in the formation of multiphase zeolites. Table 5.3 presents the comparable crystallinity and crystal size of the various synthesised ZSM-5 zeolite products. The crystal size was calculated from the SEM micrographs using ImageJ software.

Table 5.2: Crystallinity and crystal size for ZN-0.5, ZN-0.4, ZN-0.3, ZN-0.2, ZN- 0.1 and ZN-0.05

		Crystal size (µm)	
Sample	**Crystallisation (%)**	**Length (µm)**	**Width (µm)**
ZN-0.5	48	1.50	0.73
ZN-0.4	74	3.60	1.59
ZN-0.3	58	2.50	1.65
ZN-0.2	100	4.10	2.39
ZN-0.1	62	10.20	4.21
ZN-0.05	67	6.20	0.77

When the NaOH content in the hydrothermal gel increased from 0.05 g (ZN-0.05) to 0.1 g (ZN-0.1), an increase in crystal size, from 6.20 x 0.77 µm to 10.20 x 4.21 µm respectively, could be observed (see Table 5.3). A further increase in the NaOH content from 0.2 g (ZN-0.2) to 0.5 g (ZN-0.5) resulted in a decrease in both the crystallinity and crystal size of the zeolite products. These results correspond with those reported by Armaroli et al. (2006), who showed a correlation between the percentage crystallinity of a zeolite sample and its crystal size. Zeolites with smaller crystal size are preferred, due to their catalytic effectiveness in most catalytic reactions (Di Renzo 1998). For this reason, Sample ZN-0.3 was selected as the optimum condition, due to its sufficient crystallinity and crystal size. Even though sample ZN-0.3 was not the most crystalline, it had a percentage crystallinity of above 50, and the smallest crystal size after ZN-0.5.

The SEM micrographs of ZN-0.5, ZN-0.4, ZN-0.3, ZN-0.2, ZN-0.1 and ZN-0.05 with different NaOH contents is presented in Figure 5.4

.

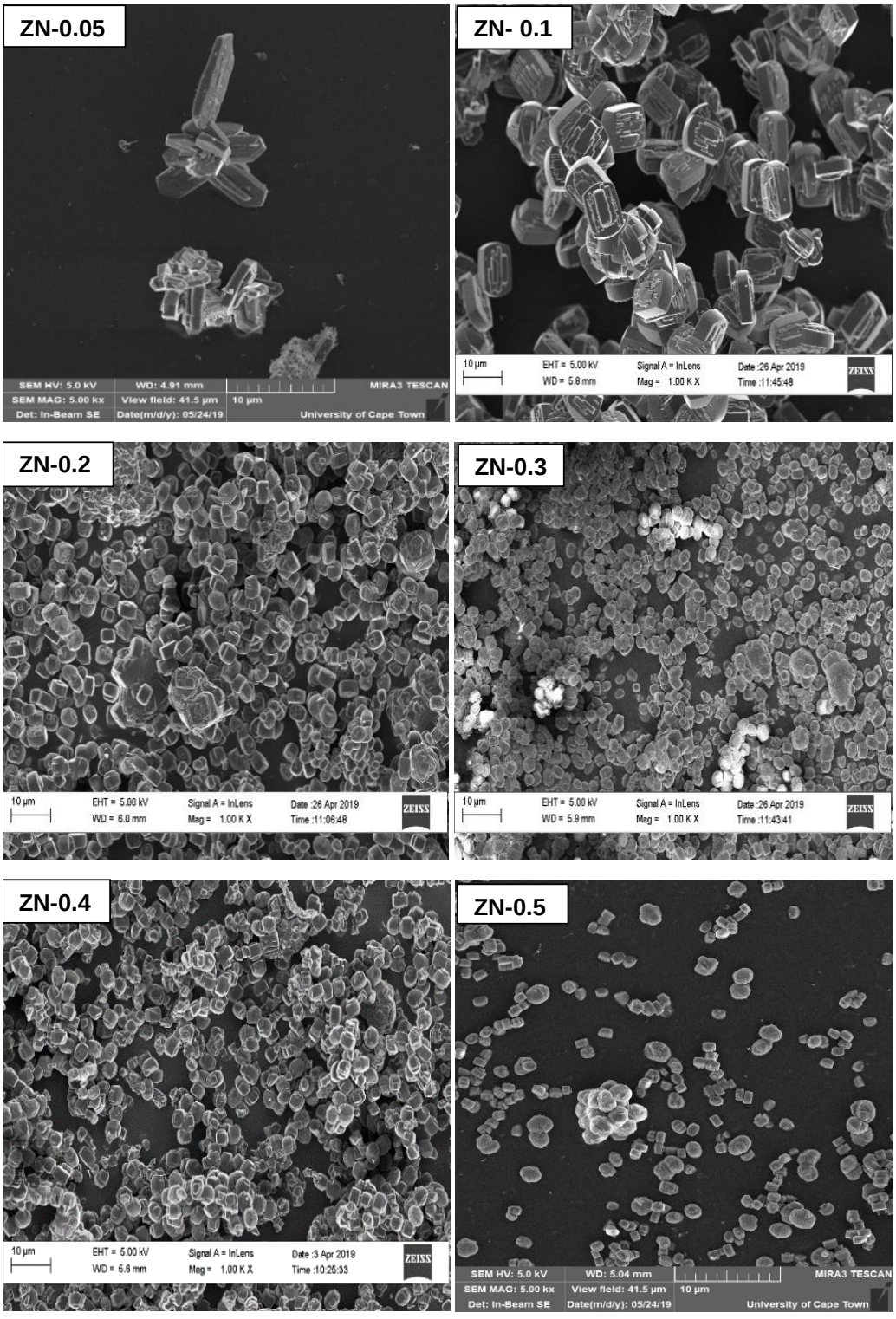

Figure 5.4: SEM micrographs showing the effect of NaOH on the morphology of ZSM-5 zeolites at 160°C for 72 h, with the following code names: ZN-0.5, ZN-0.4, ZN-0.3, ZN-0.2, ZN- 0.1 and ZN-0.05

.

The ZSM-5 zeolite crystals in sample ZN-0.5, ZN-0.4, ZN-0.3, ZN-0.2, ZN-0.1 and ZN-0.05, as observed in Figure 5.4, revealed highly intergrown and twinned crystals of three different morphologies. The crystals in ZN-0.5, ZN-0.4, ZN-0.3 and ZN-0.2 exhibited a cuboidal type morphology, sample ZN-0.1 showed a conventional ellipsoidal type morphology, while sample ZN-0.05 showed an intergrown coagulated lath-shaped (or coffin shaped) morphology. These results demonstrate that NaOH has a significant effect on the direction of crystal growth and the formation of intergrown crystals.

5.4 Effect of TPABr

This section investigates the effect of structure directing agent (TPABr) on the crystallinity, phase purity and morphology of ZSM-5 zeolite. The optimum molar composition for ZN-0.3 obtained above was used as the basis for this set of experiments. The synthesis was carried out by mixing 2 g of TFSE-H_2O, 0.3 g of NaOH and 50 mL of H_2O in a 100 ml Teflon-lined stainless autoclave, followed by the addition of x g of TPABr (x = 0.075, 0.15, 0.3, 0.6, 0.9, 1.2 and 1.5 g) while the hydrothermal conditions were kept constant at 160°C for 72 h as described in Chapter 3, Section 3.3.2. The subsequent molar regimes were assigned the following code names: ZTP-0.075, ZTP-0.15, ZTP-0.3, ZTP-0.6, ZTP-0.9, ZTP-1.2 and ZTP-1.5. The relative crystallinity, crystal size and the quality of the crystalline phases were used to determine the optimal conditions for the synthesis of ZSM-5 zeolite in this section.

Figure 5.5 compares the XRD pattern of the products ZTP-0.075, ZTP-0.15, ZTP-0.3, ZTP-0.6, ZTP-0.9, ZTP-1.2 and ZTP-1.5 obtained by varying the amount of TPABr, as described above.

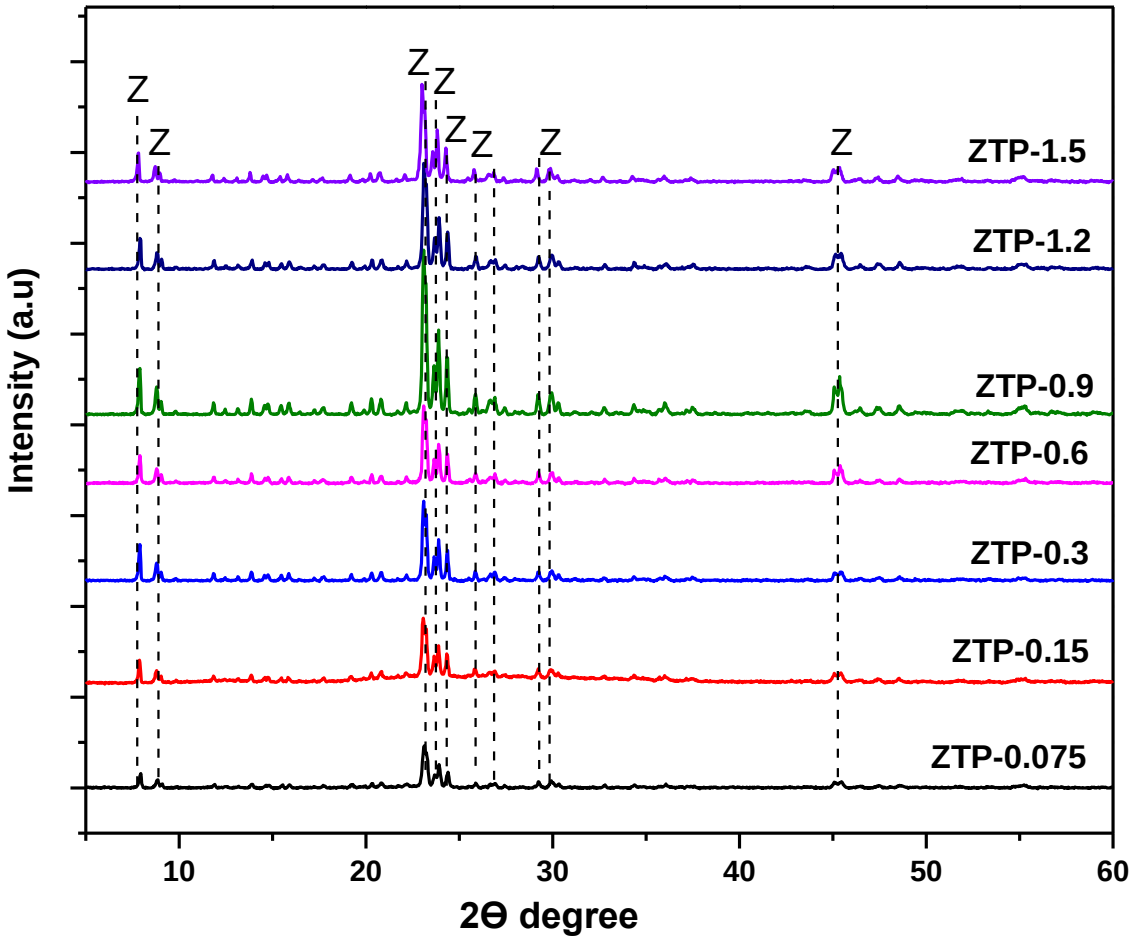

Figure 5.5: XRD spectra showing the effect of TPABr on the phase formation of ZSM-5 zeolites at 160°C for 72 h, with the following code names: ZTP-0.075, ZTP-0.15, ZTP-0.3, ZTP-0.6, ZTP- 0.9, ZTP-1.2 and ZTP-1.5, where Z = ZSM-5

Figure 5.5 shows the XRD pattern of ZSM-5 samples prepared at certain TPABr concentrations (TPABr > 0.075 g ≤ 1.5 g). All the samples displayed typical diffraction peaks of pure phase ZSM-5 zeolite without the appearance of an impure phase, as reported in literature (Panpa and Jinawath 2009; Woolery et al. 1997). It can be observed that the peak intensities for ZTP-0.075, ZTP-0.15, ZTP-0.3, ZTP-0.6 and ZTP-0.9 increased with the increase in TPABr concentration, indicating an increase in crystallinity from ZTP-0.075 to ZTP-0.9. However, further increase in TPABr concentration led to ZSM-5 zeolite products with lower peak intensities in ZTP-1.2 and ZTP-1.5, which is indicative of reduced crystallinity. The crystal size and crystallinity of the synthesised ZSM-5 zeolite products at varying TPABr concentration is summarised in Table 5.3. It can be seen from Table 5.3 that the increase in percentage crystallinity of the zeolite products from ZTP-0.075 to ZTP-0.9 was directly proportional to the increase in crystal size. However, the increase in TPABr concentration beyond 0.9 g resulted in smaller crystals, which indicate that too

.

much TPA^+ does not benefit the nucleation and crystal growth in ZSM-5 zeolite synthesis (Sashkina et al. 2017). These results agree with those of Pushparaj et al. (2013), who showed that highly crystalline zeolites ZSM-5 could be associated with increased crystal size. Although sample ZTP-0.9 was the most crystalline of the zeolite samples, it had larger average crystal size of 4.60 x 0.55 µm, which makes it unsuitable for the potential application of these materials. The crystal sizes of ZTP-0.15 and ZTP-0.075 were smaller, at 1.10 µm and 2.40 x 0.82 µm respectively, however, their relative crystallinity in both instances was below 50%. Although it would make economic sense to select either ZTP-0.15 or ZTP-0.075 as the optimum condition due to their small crystal size, their low crystallinity suggests incomplete conversion of the amorphous material into zeolite (Figure 5.5), which might impact the yield of the final product. The optimum amount of TPABr in this set of the experiment was deemed to be 1.2 g, due to sufficient crystallinity (65.75%) and small crystal size of 2.20 x 1.20 µm (length).

Table 5.3: Crystallinity and crystal size for ZTP-0.075, ZTP-0.15, ZTP-0.3, ZTP-0.6, ZTP- 0.9, ZTP-1.2 and ZTP-1.5

		Crystal size (µm)	
Sample	**Crytsallinity (%)**	**Length (µm)**	**Width (µm)**
ZTP-1.5	60.41	2.50	1.65
ZTP-1.2	65.75	2.20	1.20
ZTP-0.9	100.00	4.60	0.55
ZTP-0.6	50.28	3.50	2.00
ZTP-0.3	49.57	3.20	1.42
ZTP-0.15	33.93	1.10	_
ZTP-0.075	32.67	2.40	0.82

The morphology of ZSM-5 zeolite crystals synthesised from molar composition with different concentrations of TPABr is presented in Figure 5.6. It can be seen in Figure 5.6 that the ZSM-5 zeolite crystals for ZTP-0.075, ZTP-0.15, ZTP-0.3, ZTP-0.6, ZTP- 0.9, ZTP-1.2 and ZTP-1.5 had two distinctive morphologies of different crystal sizes. ZTP-0.075, ZTP-0.15 and ZTP-0.3 exhibited lath-shaped particles, with traces of amorphous-like particles on the surface of the crystals. The crystals of ZTP-0.6, ZTP- 0.9, ZTP-1.2 and ZTP-1.5 exhibited ellipsoidal morphology, as described by Mi et al. (2021), or prismatic-shaped crystals (Song et al. 2004). In the case of ZTP-0.3 and ZTP-0.9, highly intergrown agglomerated crystals were observed, while at high template concentrations (ZTP-0.6, ZTP-1.2 and ZTP-1.5), inter-twinned agglomerated crystal structures were observed. This could be due to the aggregation of secondary building

.

unities (SBU) caused by secondary nucleation (Mi et al. 2021). Karimi et al. (2012) investigated the effect of template concentration on the morphology of ZSM-5 zeolite crystals and reported that the increase in template concentration causes a decrease on the average particle size and crystallinity of the synthesised zeolite product. This corroborates the results presented in Table 5.3 and Figure 5.6.

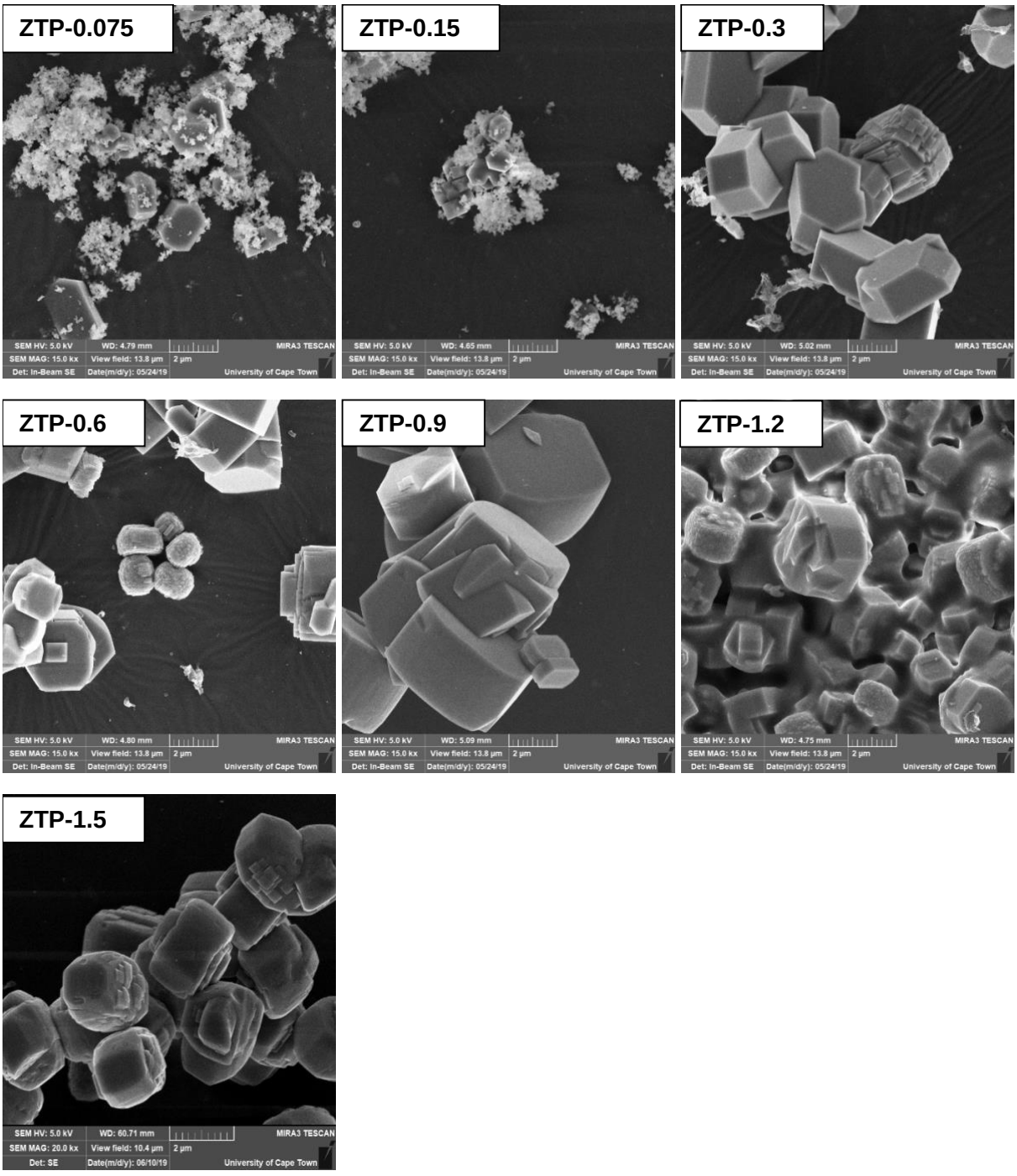

.

Figure 5.6: SEM micrographs showing the effect of TPABr on the morphology of ZSM-5 zeolites at 160°C for 72 h, with the following code names: ZTP-0.075, ZTP-0.15, ZTP-0.3, ZTP-0.6, ZTP- 0.9, ZTP-1.2 and ZTP-1.5, where Z = ZSM-5

5.5 Effect of water content

The water content plays an important role in facilitating the solubility of silica and aluminium species in the initial synthesis solution and controls the final particle size of the zeolite products (Alipour et al. (2014). This section investigated the effect of water content on the crystallinity, phase purity and morphology of CFA-based ZSM-5 zeolite. The optimum molar composition for ZTP-1.2 obtained in Section 5.4 was used as the basis for this set of experiments. The amount of water was varied as described in Table 3.5 of section 3.3.2, where x = 20, 30, 40 and 50 mL of H_2O. The hydrothermal synthesis conditions were kept constant at 160 °C for 72 hours as described in Chapter 3, section 3.3.2. The subsequent molar regimes were assigned the following code names (ZTHH-20 mL, ZTHH-30 mL, ZTHH-40 mL and ZTHH 50 mL) to reflect the amount of H_2O added in the synthesis solution. The obtained products were characterised by XRD and SEM techniques.

Figure 5.7 compares the XRD pattern of the products ZTHH-20 mL, ZTHH-30 mL, ZTHH-40 mL and ZTHH 50 mL obtained by varying the amount the water content in the synthesis solution.

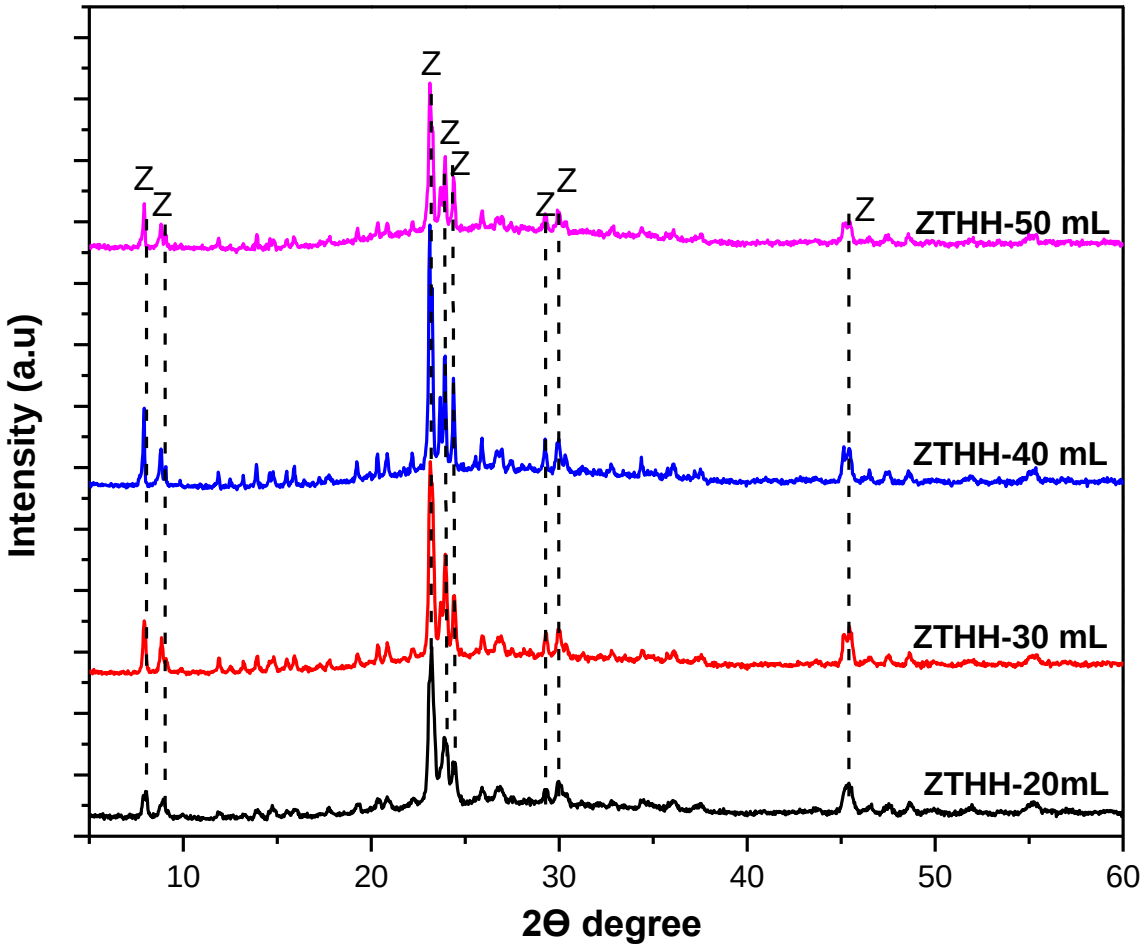

Figure 5.7: XRD spectra showing the effect of water on the phase formation of ZSM-5 zeolites at 160°C for 72 h, with the following code names: ZTHH-20 mL, ZTHH-30 mL, ZTHH-40 mL and ZTHH 50 mL, where Z = ZSM-5.

The XRD patterns presented in Figure 5.7 show the characteristic peaks of ZSM-5 zeolite synthesised with different water content. It can be seen from the XRD spectra that an increase in the water content of the synthesis hydrothermal gel by 10 mL (ZTHH-20 mL to ZTHH-30 mL) increased the peak intensity of ZTHH-30 mL, which led to a highly crystalline zeolite product. However, reduced peak intensities were observed when the water content was increased to 50 mL. This could be due to the decreased dissolution of silica and alumina species present in the hydrothermal gel caused by the reduced alkalinity. The crystallinity and crystal size of the synthesised zeolite products presented in Table 5.4 shows that a further increase in the water content beyond 30 mL led to a decrease in the crystallinity of the subsequent zeolite products. On the contrary, a decrease in the water content of the hydrothermal synthesis gel resulted in smaller crystal size of the zeolite products (ZTHH-20 mL = 1.9 µm). This could be due to the

.

supersaturated solution caused by relatively higher precursor concentrations. Petrik (2009) investigated the influence of cation, anion and water content on the rate of formation and pore size distribution of zeolite ZSM-5 and showed that at reduced water contents, the nucleation rate is most likely favoured over the crystal growth process for ZSM-5 formation. Alipour et al. (2014), investigated the effect of water content on the crystallinity and crystal size of nanosized ZSM-5 zeolite. The authors reported that reducing the water content leads to an increase in the supersaturation of the synthesis solution, which leads to the formation of smaller particle sizes. These reports are in agreement with the results presented in Table 5.4. Therefore, sample ZTHH-20 mL was deemed to contain sufficient water content for the synthesis of a highly crystalline zeolite product with small crystal size.

Table 5.4: Crystallinity and crystal size for ZTHH-20 mL, ZTHH-30 mL, ZTHH-40 mL and ZTHH-50 mL

		Crystal size (µm)	
Sample	Crystallinity (%)	Length (µm)	Width (µm)
ZTHH-50mL	62.9	2.20	1.20
ZTHH-40mL	91.4	3.10	1.84
ZTHH-30mL	100	2.40	1.30
ZTHH-20mL	90.2	1.90	1.05

The SEM micrographs of the ZSM-5 zeolite products prepared using different water contents is presented in Figure 5.8.

.

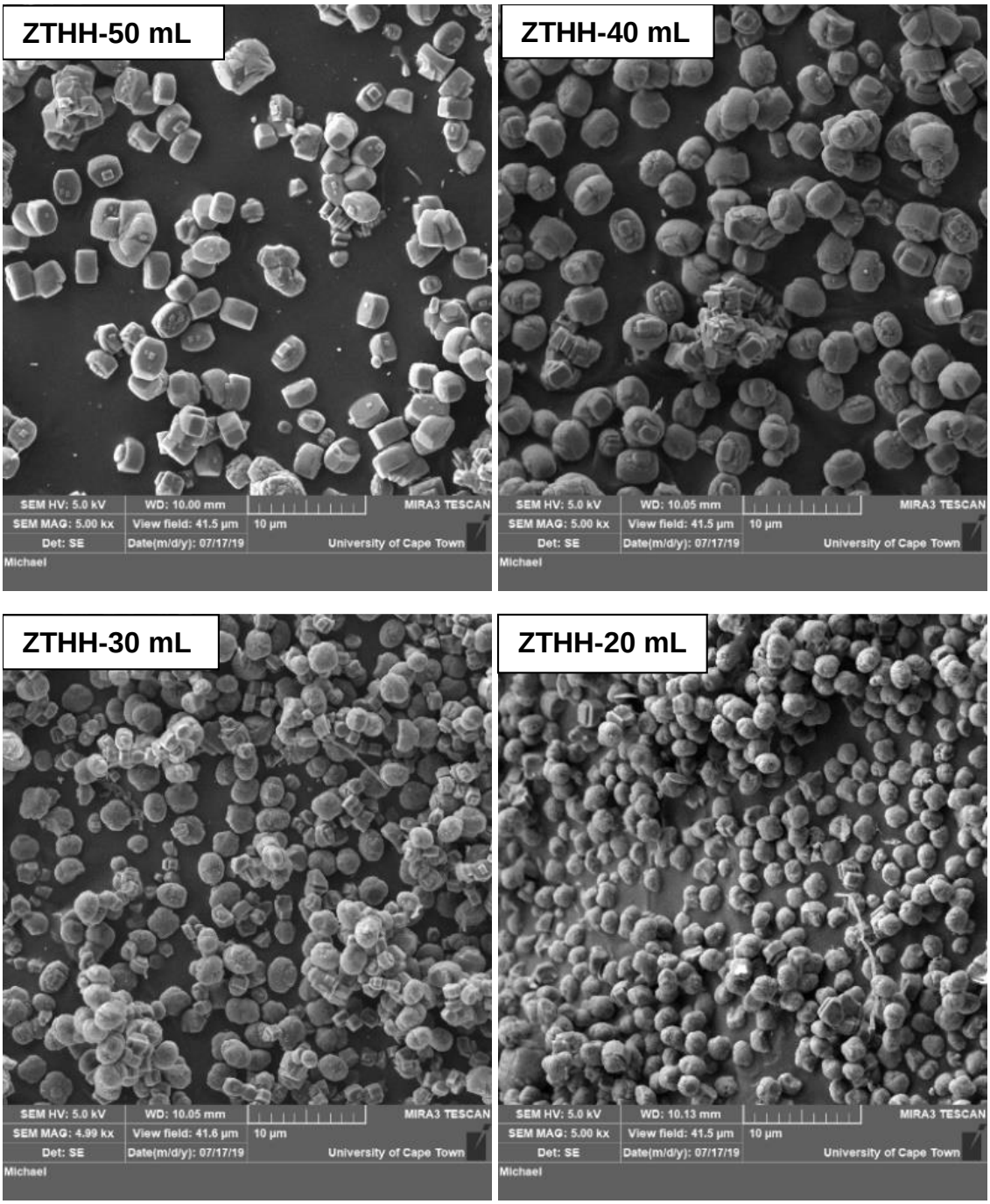

Figure 5.8: SEM micrographs showing the effect of water on the morphology of ZSM-5 zeolites at 160°C for 72 h, with the following code names: ZTHH-20 mL, ZTHH-30 mL, ZTHH-40 mL and ZTHH-50 mL, where Z = ZSM-5

The morphology of ZTHH-20 mL, ZTHH-30 mL, ZTHH-40 mL and ZTHH-50 mL, as presented in Figure 5.8, maintained the ellipsoidal type morphology of a typical ZSM-5 zeolite, as discussed in Figure 5.6. It is clear from the SEM micrographs that the decrease in water content led to zeolite

particles with reduced crystal size. ZTHH-30 mL and ZTHH-20 mL showed small crystals with an average crystal size of 2.40 x 1.30 µm and 1.90 x 1.05 µm respectively. The SEM and XRD results support the fact that reduced water in ZSM-5 zeolite synthesis promotes the formation of zeolites with smaller crystal sizes.

5.6 Effect of hydrothermal synthesis time

High-silica zeolites such as ZSM-5 have high production costs and a complex production process, which is highly influenced by time and temperature (Widayat and Annisa 2017). Given the high costs of production of these types of zeolites, this section investigated the effect of hydrothermal time on the synthesis of CFA-based ZSM-5 zeolite on the crystallinity, crystal size and morphology of ZSM-5 zeolite. The effects of hydrothermal time on ZSM-5 synthesis were studied by preparing zeolites under different hydrothermal times (0, 3, 6, 24, 48 and 72 h) while keeping the temperature constant at 160°C, as described in Chapter 3, Section 3.3.2. The optimum molar composition for ZTHH-20 mL obtained above was used as the basis in this set of experiments. The obtained products were characterised by XRD and SEM techniques.

Figure 5.9 compares the XRD pattern of the products obtained by varying the synthesis hydrothermal time.

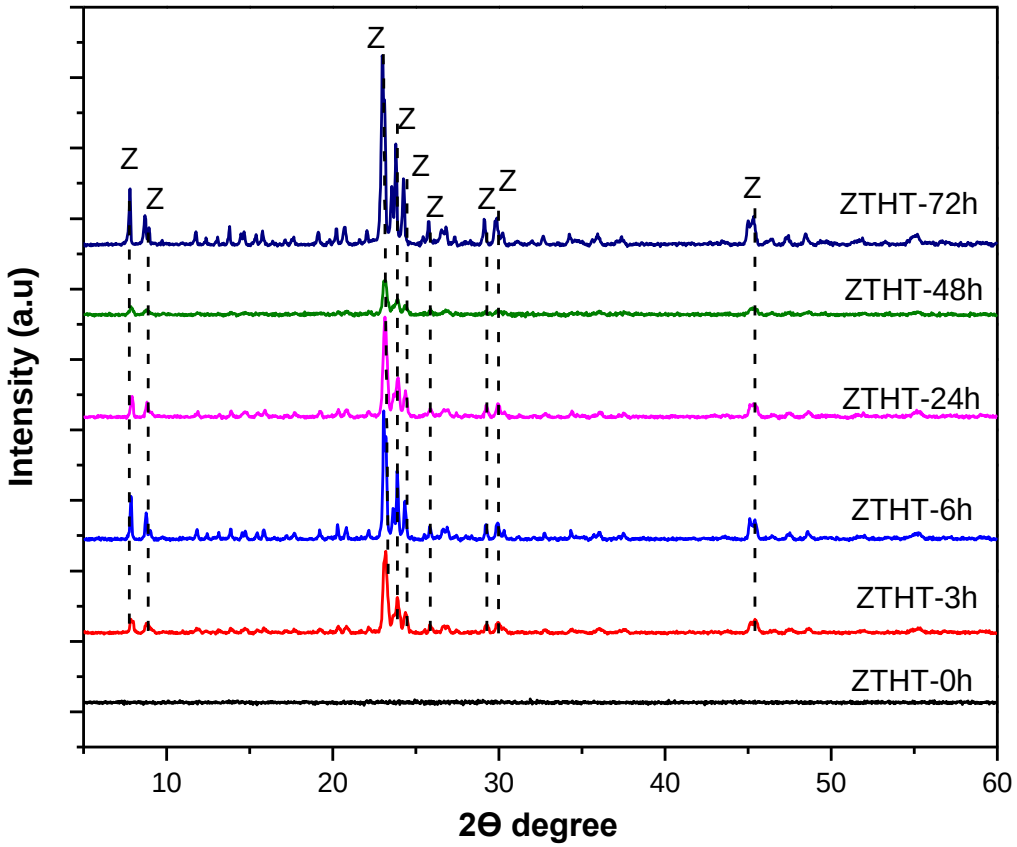

Figure 5.9: XRD spectra showing the effect of hydrothermal time on the phase formation of ZSM-5 zeolites at 160°C for (x = 0h, 3h, 6h, 24h, 48h and 72h), with the following codenames: ZTHT-0h, ZTHT-3h, ZTHT-6h, ZTHT-24h, ZTHT-48h and ZTHT-72h where Z = ZSM-5

The XRD pattern showing the effect of hydrothermal time on the crystallisation and phase purity of ZSM-5 zeolite is shown in Figure 5.9. It can be observed in the diffractogram of ZTHT-0h that no ZSM-5 crystals formed at zero-hour hydrothermal time. This observation shows that the hydrothermal process step plays an integral part in the synthesis of ZSM-5 zeolite. The diffractograms of ZTHT-3h, ZTHT-6h, ZTHT-24h, ZTHT-48h and ZTHT-72h obtained at hydrothermal times 3, 6, 24, 48 and 72 h maintained the pure phase characteristics of a ZSM-5 zeolite, as discussed in Section 5.3.3. The trend showed that an increase in the hydrothermal time from 3 to 24 h had an increasing effect on the peak intensities within the diffraction peaks 2θ = 23, 24 and 25°. This also indicated the increase in percentage crystallinity and crystal size of the synthesised ZSM-5 zeolite products in the same timeframe, with sample ZTHT-24h being the most crystalline at 100% (see Table 5.5). The results also show that at higher hydrothermal times of 48 and 72 h, the crystallinity and crystal size of the zeolite products decreases. These results confirm the findings by Petushkov et al. (2011), who reported that the increase in crystallization

.

time during ZSM-5 zeolite synthesis leads to a higher crystallinity with larger crystal size. The authors added that there is an optimum time for crystallisation, and this largely depended on the adopted synthesis procedure, and also that crystallisation time beyond the optimum time leads to a decrease in crystallinity and crystal size of the zeolite product. The results of this study showed for the first time that CFA-based pure phase ZSM-5 zeolite with average crystal size of 2.5 µm can be achieved within a hydrothermal synthesis time of 3 h, and that beyond this time, larger crystal sizes begin forming. Based on this result, crystallisation time beyond 3h is not strictly necessary. As a result, ZTHT-3h was considered to be the optimum condition for this set of experiments and its molar composition was used as a basis to investigate the effect of temperature in the subsequent subsection.

Table 5.5: Crystallinity and crystal size for ZTHT-0h, ZTHT-3h, ZTHT-6h, ZTHT-24h, ZTHT-48h and ZTHT-72h

Sample	Crystallinity (%)	Crystal size (µm)
ZTHT-72h	69.8	1.90
ZTHT-48h	23.9	3.20
ZTHT-24h	100	3.00
ZTHT-6h	58.9	2.80
ZTHT-3h	54.9	2.50
ZTHT-0h	0	0.00

The morphological structure of ZSM-5 zeolites synthesised from different hydrothermal times is presented in Figure 5.10.

.

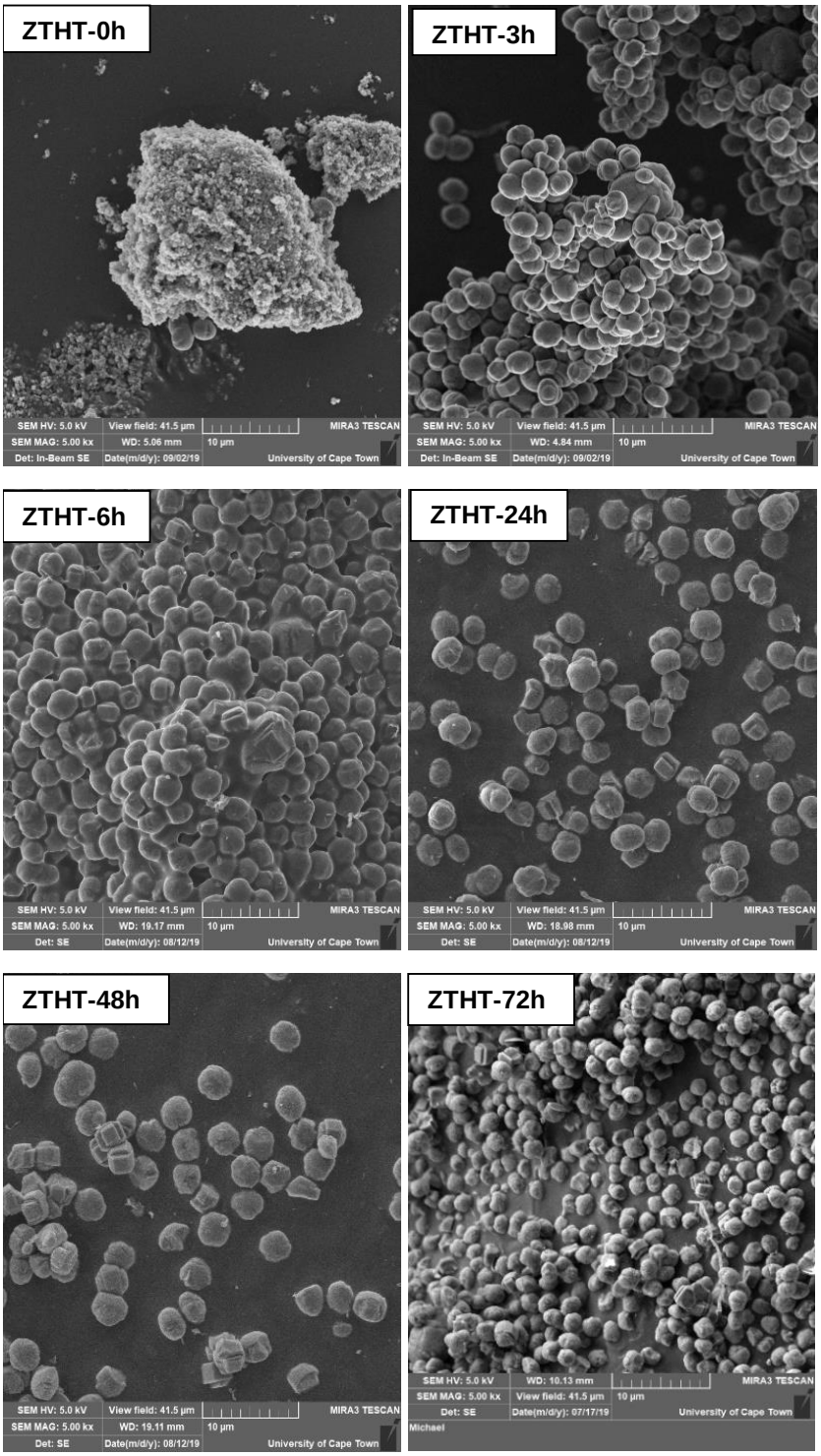

Figure 5.10: SEM micrographs showing the effect of hydrothermal time on the phase formation of ZSM-5 zeolites at 160°C for (x = 0h, 3h, 6h, 24h, 48h and 72h), with the following codes: ZTHT-0h, ZTHT-3h, ZTHT-6h, ZTHT-24h, ZTHT-48h and ZTHT-72h where Z = ZSM-5

.

Figure 5.10 presents the morphology of the synthesised ZSM-5 zeolite using different hydrothermal synthesis times. ZTHT-0h exhibited a mixture of bulky precursors agglomerated into amorphous particles. The presence of ZSM-5 was not detected in the XRD spectrum of ZTHT-0h. Sample ZTHT-3h, ZTHT-6h, ZTHT-24h, ZTHT-48h and ZTHT-72h showed ellipsoidal shaped particles of different crystal sizes ranging from 2.5 to 3.2 µm (see Table 5.5). The XRD and SEM of sample ZTHT-3h confirmed that a hydrothermal synthesis time of 3h was sufficient for the synthesis of a pure phase ZSM-5 zeolite.

5.7 Effect of hydrothermal synthesis temperature

This section investigated the effect of hydrothermal synthesis temperature on the crystallinity, crystal size and morphology of ZSM-5 zeolite. The optimum molar composition for ZTHT-3h obtained above was used as the basis in this set of experiments. As such, the synthesis was carried out at a constant hydrothermal time of 3 h, while varying the temperature as follows: 40, 70, 100, 130 and 160°C. The obtained products were thereafter characterised by XRD and SEM techniques.

The XRD spectra showing the effect of hydrothermal temperature variation on the mineral phase of ZSM-5 zeolite are presented in Figure 5.11.

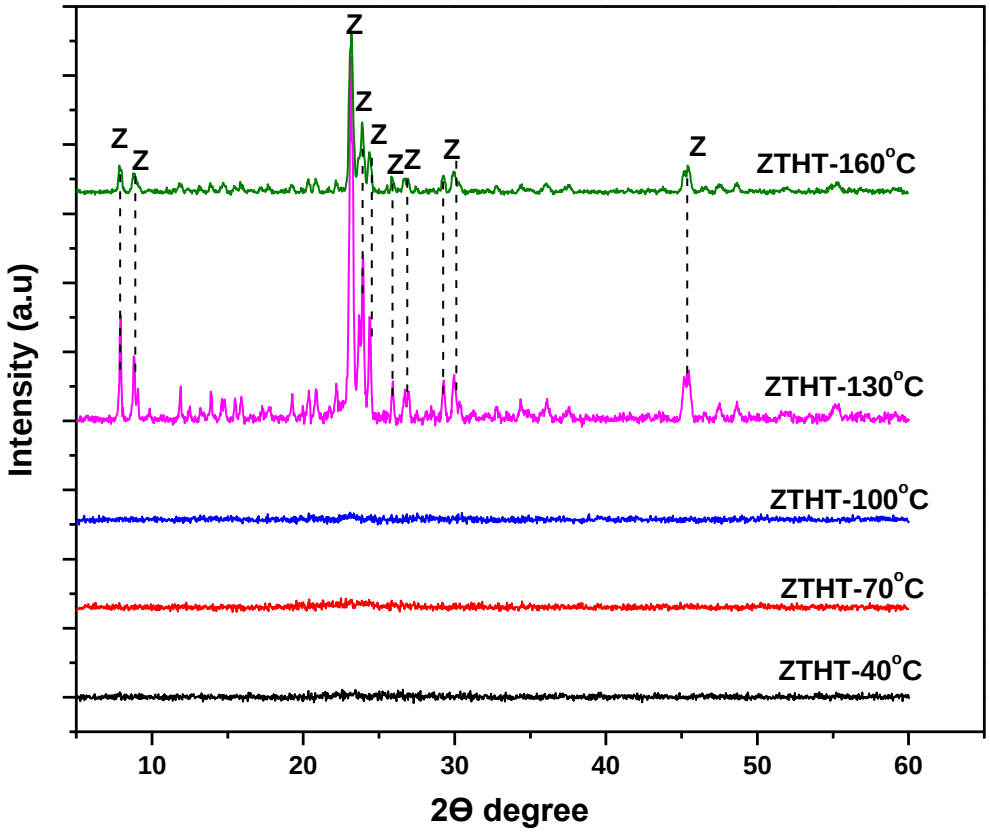

Figure 5.11: XRD spectra showing the effect of hydrothermal temperature on the phase formation of ZSM-5 zeolites at temperature (x = 40, 70, 100, 130 and 160°C) for 3 h, with the following codes: ZTHT-40°C , ZTHT-70°C, ZTHT-100°C, ZTHT-130°C and ZTHT-160°C, where Z = ZSM-5

Figure 5.11 shows the XRD pattern of ZSM-5 zeolite synthesised at different hydrothermal synthesis temperatures. It can be observed that sample ZTHT-130°C and ZTHT-160°C perfectly matched the diffractogram of ZSM-5 zeolite (Shirazi et al. 2008). However, further decreasing the synthesis hydrothermal temperature resulted in amorphous material. as observed in samples ZTHT-100°C, ZTHT-70°C and ZTHT-40°C. This shows that the crystallisation of ZSM-5 zeolite is sensitive to temperature and that at lower hydrothermal temperature. from 40 to 100°C, no ZSM-5 mineral phases can be formed under the applied synthesis conditions. In addition, a highly crystalline ZSM-5 mineral phase was obtained at 130°C (see Table 5.6). The results also showed that a further increase in the hydrothermal temperature to 160°C led to a decrease in crystallinity below 50%, as shown in Table 5.6. Larlus and Valtchev (2005) showed in their study that increasing the synthesis temperature accelerates the dissolution of the nutrients in the initial gel, as well as promoting crystal nuclei growth. In another study, Cheng et al. (2008), investigated the effect of synthesis temperature on the crystallisation of ZSM-5 zeolite obtained at temperatures ranging from approximately 100 to 200°C. The authors point out that the hydrothermal

.

temperature has a strong effect on the nucleation and crystal growth during the synthesis of ZSM-5 zeolite and that a higher synthesis temperature of 180°C reduced zeolite crystallisation time from 96 to 10 h. It was shown from their study that below a synthesis time of 10 h, the synthesised product was amorphous (4 h) and partially crystalline zeolite (8 h). Alipour et al. (2014) reported that the crystallisation temperature is directly proportional to the crystallisation time and that ZSM-5 zeolites can be crystallised at lower synthesis hydrothermal temperature and longer synthesis time. The crystallinity and crystal size for sample ZTHT-40°C, ZTHT-70°C and ZTHT-100°C could not be calculated, as no mineral phases and crystals could be detected by the XRD and SEM synthesis techniques. Even though sample ZTHT-130°C possessed the highest crystallinity, the ZSM-5 crystals were not well resolved and could not be measured by ImageJ software. Sample ZTHT-160°C showed a relative crystallinity of 49.4% and an average crystal size of 2.5 µm. Due to the lack of crystal size data for sample ZTHT-130°C, sample ZTHT-160°C was then selected as the optimum condition for this set of experiments.

Table 5.6: Crystallinity and crystal size for ZTHT-40°C, ZTHT-70°C, ZTHT-100°C, ZTHT-130°C and ZTHT-160°C

Sample	Crystallinity (%)	Crystal size (µm)
ZTHT-160˚C	49.4	2.5
ZTHT-130˚C	100	_
ZTHT-100˚C	_	_
ZTHT-70˚C	_	_
ZTHT-40˚C	_	_

Note: The dash line represents the values that could not be determined from the XRD and SEM analytic techniques.

The morphological structure of the ZSM-5 zeolite obtained at different hydrothermal temperature is presented in Figure 5.12.

.

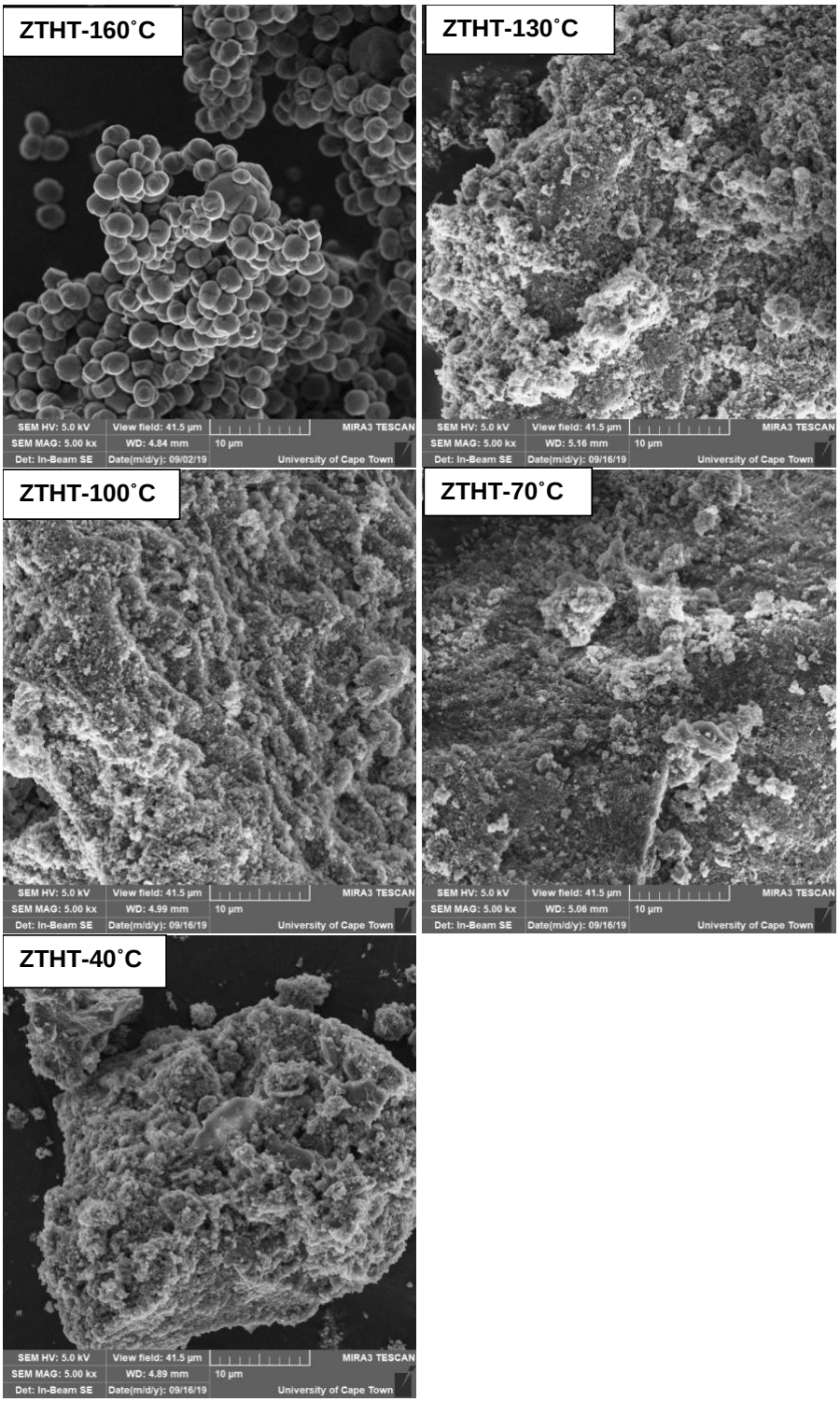

Figure 5.12: SEM micrographs showing the effect of hydrothermal temperature on the morphology of ZSM-5 zeolites at temperature (x = 40, 70, 100, 130 and 160°C) for 3 h, with the following code, ZTHT-40°C , ZTHT-70°C, ZTHT-100°C, ZTHT-130°C and ZTHT-160°C, where Z = ZSM-5

.

The micrograph of ZTHT-40°C, ZTHT-70°C and ZTHT-100°C shows finely agglomerated particles. Such morphology is associated with the presence of amorphous material (Mor et al. 2017). When the synthesis hydrothermal temperature was increased to 130°C, irregular smaller ellipsoidal crystals (0.74 μm), with some amorphous material on the surface, could be observed. A further increase in the hydrothermal temperature to 160°C showed well-resolved crystals of ellipsoidal shape (2.50 μm). The presence of amorphous material in ZTHT-130°C can be ascribed to incomplete transformation of the silica precursor species contained in the synthesis gel. This could be due to the reduced synthesis time and temperature, which decreased the dissolution of the feedstock in the initial gel, resulting in delayed crystal nuclei growth, as described by Larlus and Valtchev (2005). The XRD and SEM results support the well-established phenomenon that higher synthesis temperature and shorter synthesis time favours the formation of crystalline small-sized ZSM-5 crystals.

Therefore, the results on the effect of the synthesis temperature and time on the crystallinity and crystal size of ZSM-5 zeolite in this study showed that the optimum synthesis condition was ZTHT-160°C and ZTHT-3h respectively. The two samples were derived from the same molar composition (1Si: 0.003Al: 0.529Na: 0.114TPABr: 38.306H_2O) and hydrothermal synthesis conditions of 160°C for 3h. For this reason, sample ZTHT-3h was selected as the optimum condition for both section 5.6 and 5.7.

5.8 Comparison of the optimum conditions for the synthesis of CFA-based ZSM-5 zeolite

The effect of NaOH, structure directing agent (TPABr), water, hydrothermal time and temperature on the crystallinity, crystal size and morphology of ZSM-5 zeolite is discussed in sections 5.3, 5.4, 5.5, 5.6 and 5.7 respectively. The obtained samples following the optimisation process (H-Z-H_2O, H-ZN-0.3, H-ZTP-1.2, H-ZTHH-20mL and H-ZTHT-3h) were transformed to H-Form, as described in Chapter 3, Section 3.3.3. The samples were thereafter characterised by XRD, ICP, SEM, FTIR, BET, and TPD. This section compares the outcome of each of the characterisation results in order to determine the best conditions for the synthesis of ZSM-5 zeolite. The zeolites were synthesised from the initial molar composition of 1 Si: 0.003 Al: 0.612 Na: 0.190 TPABr: 95.766 H_2O, with Si/Al of 333.33. The best synthesis condition following the comparison study was thereafter used as the basis to evaluate the economic feasibility of producing ZSM-5 zeolite from CFA silica extract obtained from the alkaline leaching process (discussed in Chapter 6). Table 5.7 gives a summary

of the optimum conditions used during the synthesis of H-Z-H_2O, H-ZN-0.3, H-ZTP-1.2, H-ZTHH-20mL and H-ZTHT-3h.

Table 5.7: Summary of the optimum conditions applied for H-Z-H_2O, H-ZN-0.3, H-ZTP-1.2, H-ZTHH-20mL and H-ZTHT-3h

Sample	NaOH (g)	TPABr (g)	Water (mL)	Time (h)	Temperature (˚C)
H-Z-H_2O	0.4	1.5	50	72	160
H-ZN-0.3	0.3	1.5	50	72	160
H-ZTP-1.2	0.3	1.2	50	72	160
H-ZTHH-20mL	0.3	1.2	20	72	160
H-ZTHT-3h	0.3	1.2	20	3	160

The XRD spectra showing the comparative mineral phases of H-Z-H_2O, H-ZN-0.3, H-ZTP-1.2, H-ZTHH-20mL and H-ZTHT-3h is presented in Figure 5.13.

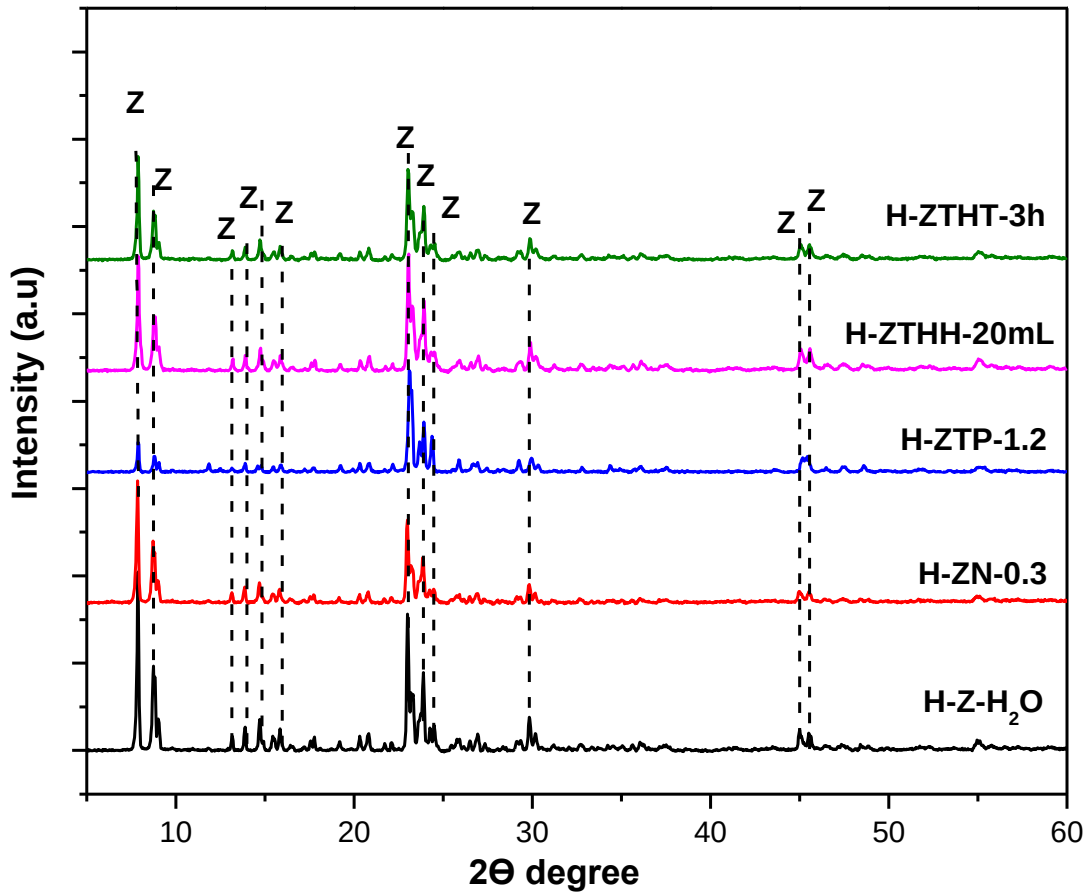

Figure 5.13: Comparison of XRD pattern of H-Z-H_2O, H-ZN-0.3, H-ZTP-1.2, H-ZTHH-20mL and H-ZTHT-3h, where Z = ZSM-5

.

Figure 5.13 shows the comparison of XRD diffractograms of H-ZSM-5 zeolites obtained from different synthesis parameters, i.e., NaOH, TPABr, water content, hydrothermal synthesis time and temperature. It is clear from the XRD spectrum that after the de-templation and ion-exchange process, no phase transformation occurred. This indicates that the modification did not destroy the zeolite primary structure. However, variation in the peak intensities of the zeolite samples is undeniably visible, with sample H-ZTP-1.2 appearing to have the lowest peak intensity in the diffraction regions 8, 9, 23, 24 and 25° 2θ, followed by samples H-ZTHT-3h, H-ZN-0.3, H-ZTHH-20mL and H-Z-H_2O respectively. Table 5.8 shows the relative percentage crystallinity, crystal size, Si/Al ratio and the yield of the zeolite products. The yield was calculated based on actual mass of the dry zeolite product per 1Kg of CFA, using Equation 5.1 presented below:

$$Zeolite\ Yield = \frac{Mass_{zeolite_{(g)}}}{1kg_{CFA}} \dots\dots\dots\dots\dots\dots\dots\dots\dots Equation\ 5.1$$

Table 5.8: Comparison of crystallinity, crystal size, Si/Al ratio and yield of the optimised ZSM-5 zeolites

Sample	Crystallinity (%)	Crystal size (µm)	Si/Al ratio	Zeolite Yield (g/Kg CFA)
H-Z-H_2O	100	3.42	184.48	89.98
H-ZN-0.3	86.41	2.84	236.40	93.48
H-ZTP-1.2	54.05	3.43	159.30	103.08
H-ZTHH-20mL	94.72	2.85	194.65	119.68
H-ZTHT-3h	74.12	2.84	204.51	82.12

Note: The Si/Al ratios were obtained from the ICP data as presented in Annexure 5.1

It can be observed in Table 5.8 that the relative percentage crystallinity of the zeolite products increased in the order of H-ZTP-1.2 < H-ZTHT-3h < H-ZN-0.3 < H-ZTHH-20mL < H-Z-H_2O, which

.

corresponded to the peak intensities of the zeolites. The crystal size ranged between 2.84 and 3.43 µm. It is noteworthy to mention that the crystal sizes of H-Z-H_2O (highly crystalline) and H-ZTP-1.2 (least crystalline) were comparable. However, no direct correlation can be deduced from this observation. Furthermore, a difference in the Si/Al ratio of the synthesis mixture and the final product can be observed. The zeolite products were synthesised from a standard precursor with a Si/Al ratio of 333.33, however after the synthesis process, the Si/Al ratio of the zeolite products ranged between 159.30 and 236.40 (Table 5.8), showing a reduction in Si/Al ratio of the final product. According to Chaves et al. (2015), the Si/Al ratio of the synthesis mixture is always higher than that of the final product, and this is especially true for high-silica zeolites. It is noteworthy to mention that reducing the water content of the synthesis mixture improved the yield of the zeolite product from 89.98 g/Kg CFA (H-Z-H_2O) to 119.68 g/Kg CFA (H-ZTHH-20mL). This could be due to the super saturation environment, which promoted nuclei crystallisation. In contrast, when the hydrothermal synthesis time was reduced to 3 h, a reduction in the product yield from 119.68 to 82.12 g/Kg CFA was observed. This is ascribed to the reduced conversion of the silica and alumina species in the initial synthesis gel into a zeolite product. According to Ding et al. (2006), shorter synthesis time results in unreacted silica and alumina in the primary solution. These species remain in the supernatant and form part of the recovered liquid waste. This study has shown for the first time that the hydrothermal synthesis time during the synthesis of CFA-based ZSM-5 zeolites can be reduced from 72 to 3 h (section 5.6) without compromising the quality of the zeolite product. On the other hand, the yield of the zeolite product obtained at 3 h (H-ZTHT-3h) indicated an increase in input material loss of approximately 31%. This is an enormous loss in chemical processes and might compromise the economic viability of the developed process. The technology economic analysis will be crucial in establishing the viability of the process at reduced hydrothermal synthesis time.

The comparison of the morphological structure of the H-form zeolites (H-Z-H_2O, H-ZN-0.3, H-ZTP-1.2, H-ZTHH-20mL and H-ZTHT-3h) is presented in Figure 5.14.

.

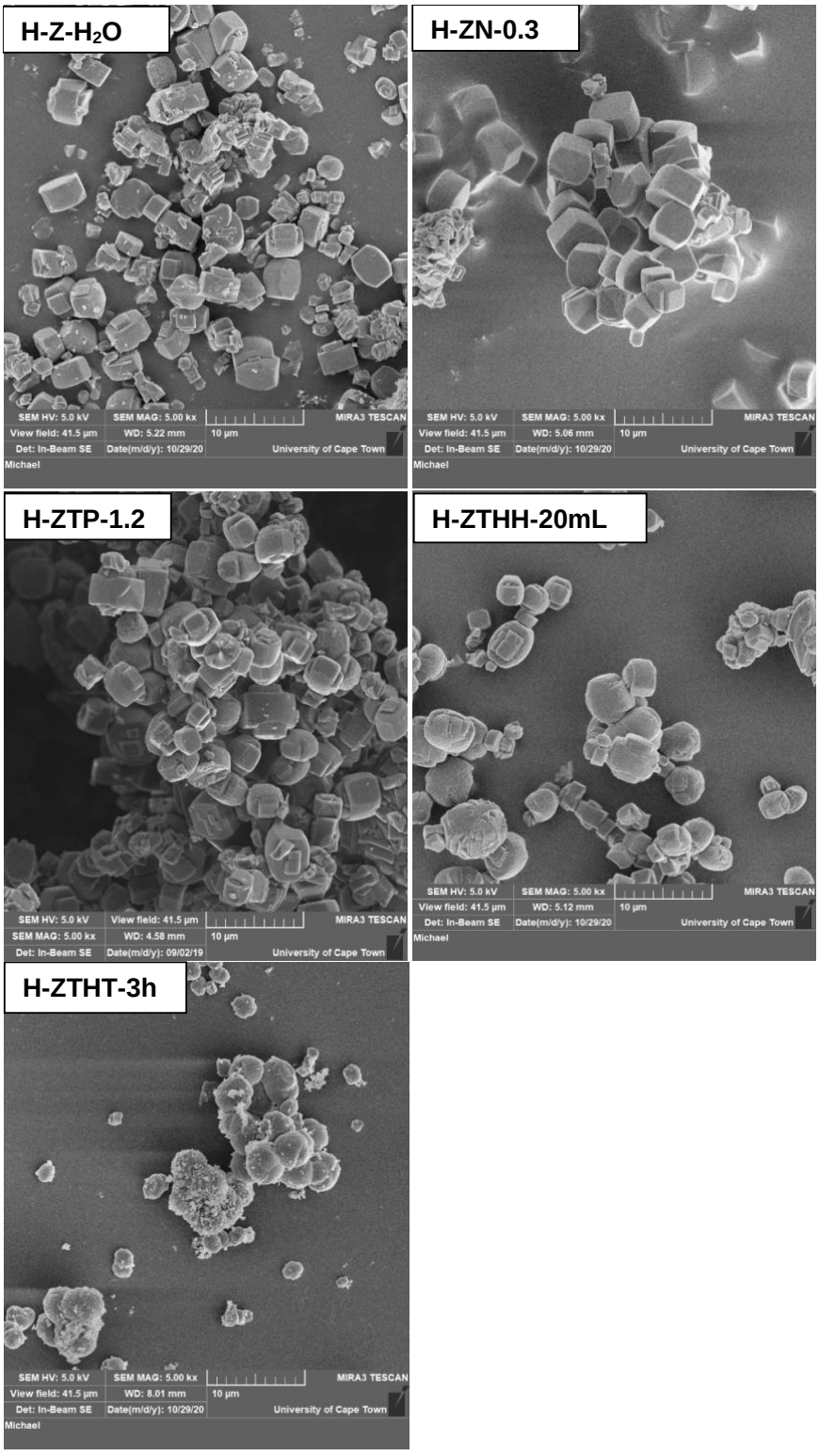

Figure 5.14: Comparison of SEM macrographs of H-Z-H_2O, H-ZN-0.3, H-ZTP-1.2, H-ZTHH-20mL and H-ZTHT-3h

Figure 5.14 shows that all the zeolite samples maintained the ellipsoidal morphological structure as observed for their Na form, as discussed in the sections above. The average zeolite crystal size ranged between 2.84 and 3.43 µm (Table 5.8), with sample H-ZTP-1.2 having the highest crystal size. It can be seen that after de-templation, cation exchange and calcination process, the difference in crystal size for H-ZTHH-20mL and H-ZTHT-3h was very minimal. This may suggest that some unreacted feedstock may have been removed during the cation exchange process. The structural analysis of the samples showing their chemical bond formation is presented in Figure 5.15.

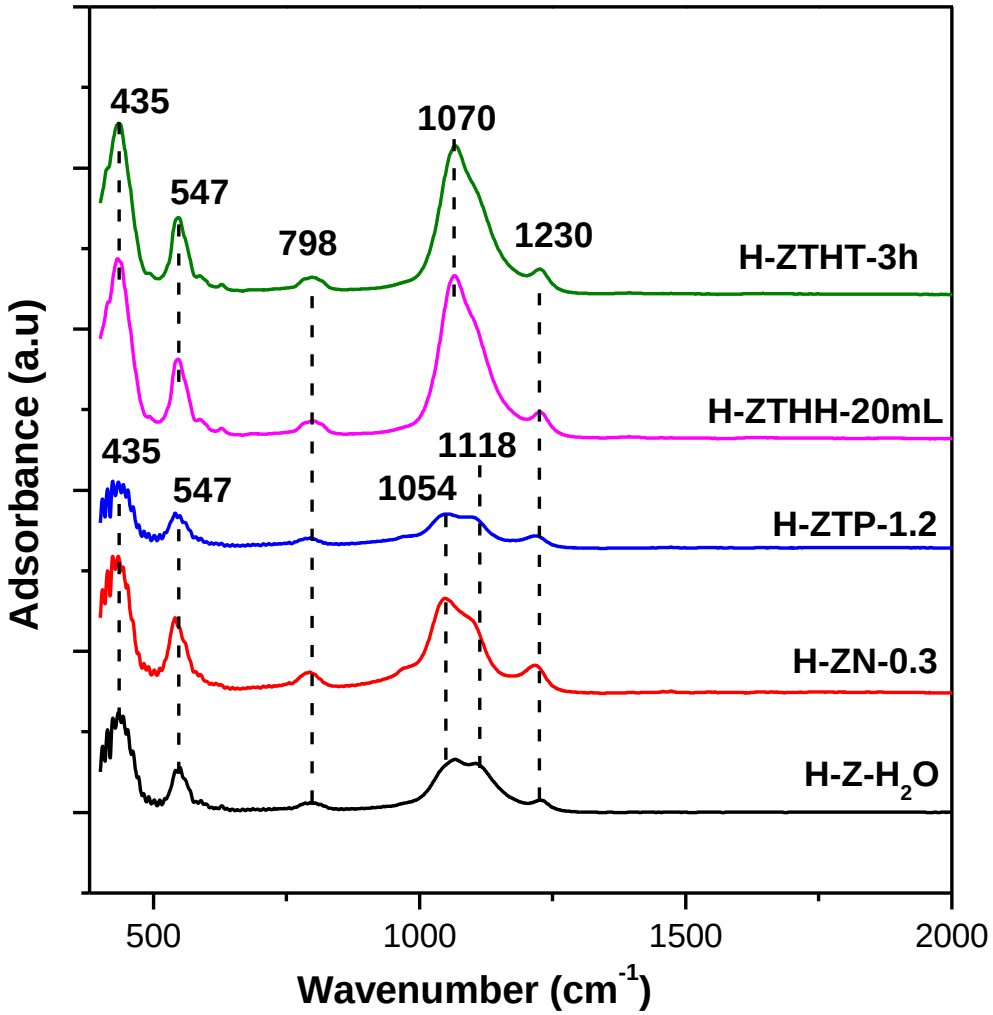

Figure 5.15: Comparison of structural profiles of H-Z-H_2O, H-ZN-0.3, H-ZTP-1.2, H-ZTHH-20mL and H-ZTHT-3h obtained by FTIR

.

The spectra of H-Z-H_2O, H-ZN-0.3 and H-ZTP-1.2 had vibration bands at 435 and 547 cm^{-1} that can be assigned to the Si-O bending which characterises highly siliceous materials and a double ring vibration respectively. The vibration band at 798 cm^{-1} is assigned to the O-T-O (T = Si or Al) symmetric stretching vibration and internal tetrahedral symmetrical stretching (Zhang et al. 2017). Two overlapping bands at 1054 and 1118 cm^{-1} were also identified. These bands correspond to Si-O internal asymmetric vibration (Ali et al. 2003), while the band at 1230 cm^{-1} is associated with asymmetric stretching vibration of Si-O-T (Oleksenko et al. 2004). The FTIR spectra of H-ZTHH-20mL and H-ZTHT-3h presented similar vibration bands as those for H-Z-H_2O, H-ZN-0.3 and H-ZTP-1.2, except that they had one band appearing at 1070 cm^{-1} instead of the double overlapping band at 1054 and 1118 cm^{-1}.

The NH_3-TPD profiles showing the strength and distribution of acid sites in H-Z-H_2O, H-ZN-0.3, H-ZTP-1.2, H-ZTHH-20mL and H-ZTHT-3h were investigated using the ammonia temperature-programmed desorption analytical technique (TPD), as described in Chapter 3, Section 3.4.8. The NH_3-TPD profiles and acidity data are presented in Figure 5.16 and Table 5.9 (a) respectively.

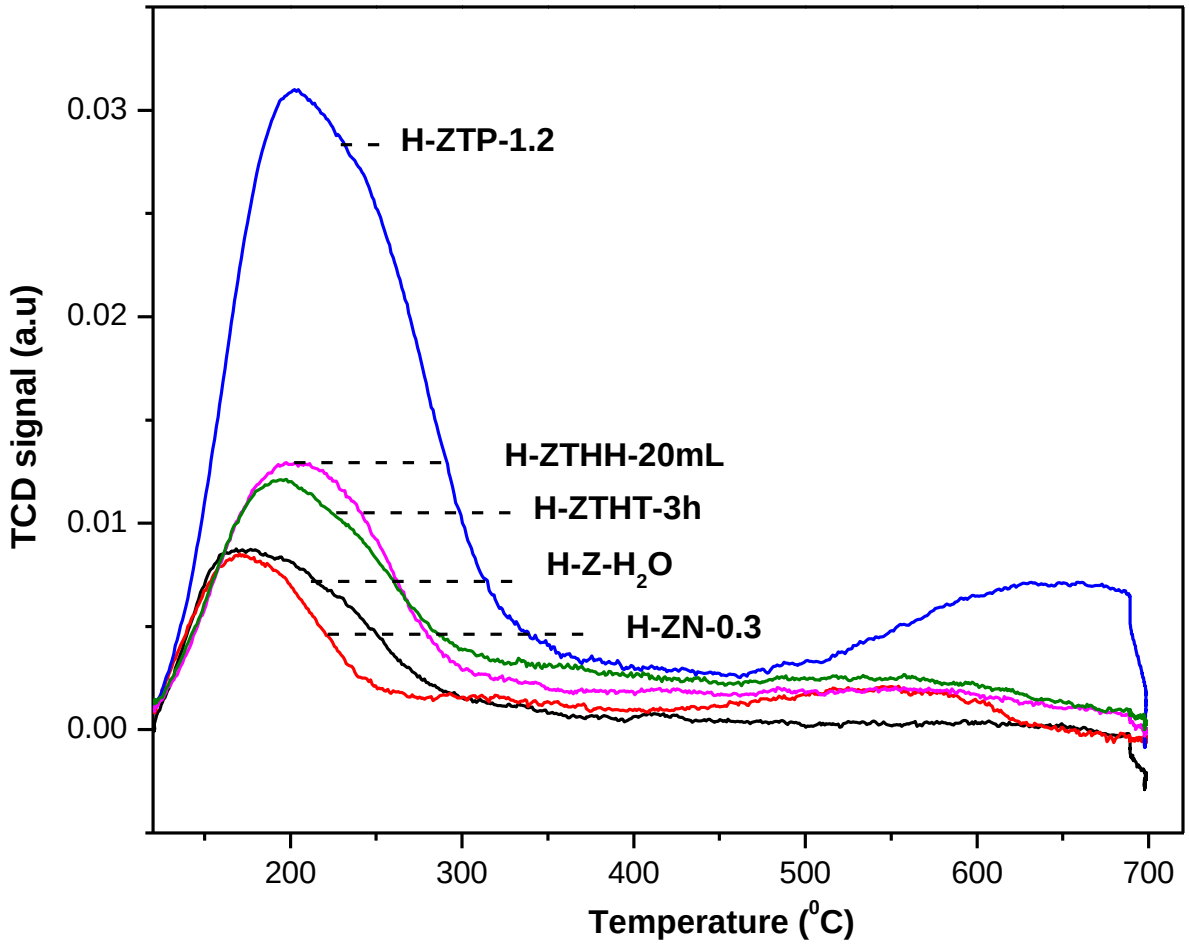

Figure 5.16: Comparative NH_3-TPD profiles of the optimised H-form ZSM-5 zeolite products obtained by varying the NaOH molar content, TPABr, water, hydrothermal time and temperature

Figure 5.16 shows the acid site distribution of H-Z-H_2O, H-ZN-0.3, H-ZTP-1.2, H-ZTHH-20mL and H-ZTHT-3h, as measured by NH_3-TPD. The TPD profiles for sample H-ZN-0.3, H-ZTP-1.2, H-ZTHH-20mL and H-ZTHT-3h exhibit two well resolved desorption peaks at low and high temperature ranges, typical of ZSM-5 zeolite (Ji et al. 2017; Wan et al. 2016). The peaks at low and high temperature ranges are generally assigned to the weak and strong acid sites respectively (Fang et al. 2017). In this study, the peak indicative of weak acid sites appeared between 160-210°C, and that of strong acid sites appeared between 540-650°C respectively. The characterisation of acid sites into weak and strong is a qualitative indication of how strongly the ammonia molecules are connected to the acid sites. For all the zeolite samples, the amount of NH_3 desorbed from the weak acid sites was higher than that absorbed at higher temperatures, as indicated by the peak intensities of the TPD profiles. The maximum adsorption of NH_3 due to the weak acid sites (0.93 mmol/g) was seen in sample H-ZTP-1.2, however the adsorption of NH_3

.

then declined to 0.17 mmol/g in sample H-ZN-0.3, while that absorbed from the strong acid site was between 0.04 and 0.21 mmol/g. It can be seen in Table 5.8 (a) that the increase in Si/Al of the zeolite product led to the decrease in the total acidity of the zeolite products, as evident from the TPD profile peak intensities.

.

Table 5.9: Acidity (a) and textural properties (b) of zeolite ZSM-5 samples obtained from the optimum conditions

Sample	Si/Al	(a) Acidic Strength				
		T1 (˚C)	Weak (mmol/g)	T2 (˚C)	Strong (mmol/g)	Total acid sites (mmol/g)
H-Z-H_2O	184.48	168.81	0.24	_	_	0.24
H-ZN-0.3	236.40	181.37	0.17	540.55	0.04	0.21
H-ZTP-1.2	159.30	202.59	0.93	645.96	0.21	1.14
H-ZTHH-20mL	194.65	200.83	0.31	540.55	0.05	0.36
H-ZTHT-3h	204.51	196.37	0.24	556.76	0.06	0.30

(b) Textural properties

Sample	S_{BET} (m^2/g)	S_{micro} (m^2/g)	S_{meso} (m^2/g)	V_{micro} (cm^3/g)
H-Z-H_2O	366.41	240.26	126.16	0.12
H-ZN-0.3	371.32	96.95	274.37	0.05
H-ZTP-1.2	402.08	185.19	216.90	0.08
H-ZTHH-20mL	345.64	149.53	196.11	0.07
H-ZTHT-3h	317.55	204.54	113.02	0.10

Notes: S_{BET}: BET surface area; S_{micro}: micropore surface area, S_{micro}: mesopore surface area; V_{micro}: micropore volume

.

This result is in accordance with that obtained by Shirazi et al. (2008), who showed that the total amount of acid sites in ZSM-5 decreases with increased Si/Al molar ratio. This is primarily due to the decrease in extra-framework aluminium content, as well as in the framework zeolite structure (Wan et al. 2016).

The nitrogen physisorption profile and surface area of the synthesised H-ZSM-5 zeolites were investigated using the Beunauer-Emmett-Teller method, described in Chapter 3, Section 3.4.7. As discussed in the former sections, the zeolite products being investigated were obtained by varying the NaOH molar content, TPABr, water, hydrothermal time and temperature. Figure 5.17 depicts the nitrogen physisorption profile of H-Z-H_2O, H-ZN-0.3, H-ZTP-1.2, H-ZTHH-20mL and H-ZTHT-3h zeolites respectively.

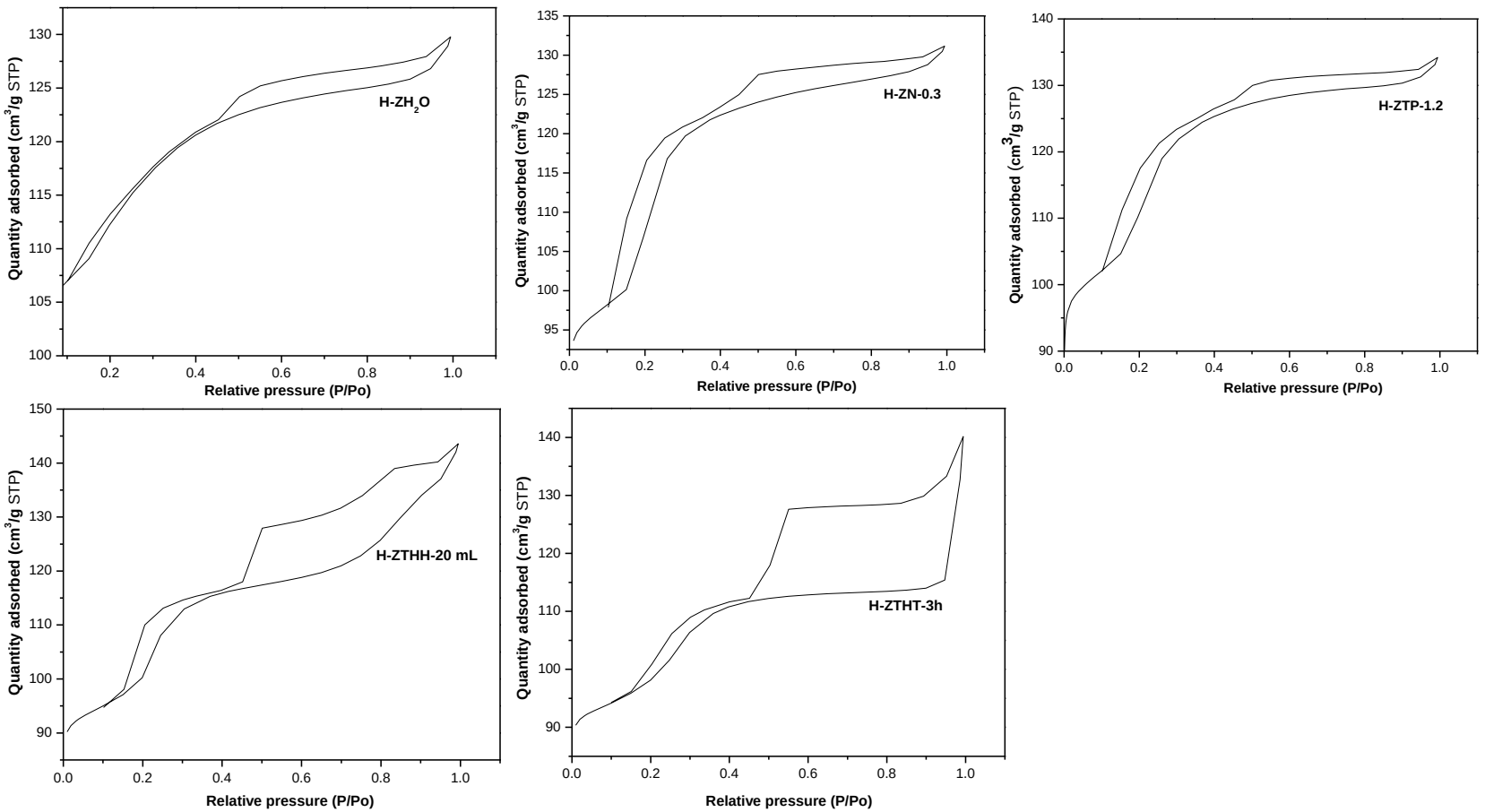

Figure 5.17: Adsorption/desorption isotherms of N_2 at 77.41 K of H-Z-H_2O, H-ZN-0.3, H-ZTP-1.2, H-ZTHH-20mL and H-ZTHT-3h

.

The nitrogen adsorption-desorption isotherms of H-Z-H_2O, H-ZN-0.3, H-ZTP-1.2, H-ZTHH-20mL and H-ZTHT-3h, prepared from varying synthesis parameters, are shown in Figure 5.17. The isotherms of H-Z-H_2O, H-ZN-0.3, H-ZTP-1.2 samples are of type I with a plateau at relative low pressure ($P/P_0 > 0.1$) and a type H4 hysteresis loop appearing at relative high pressure of $P/P_0 > 0.4$, which is typical for ZSM-5 zeolites of high Si/Al ratios. This type of hysteresis loop is common for microporous materials and characteristic of high nitrogen uptake at relatively low to high partial pressures associated with agglomerated zeolite crystals or mesoporous zeolite (Cornelius 2019; Thommes et al. 2015). On the other hand, sample H-ZTHH-20mL and H-ZTHT-3h exhibited a type IV (b) isotherm with type H5 and H2 (a) hysteresis loops appearing at relatively high pressure of $P/P_0 = 0.4$ respectively. The H5 type hysteresis loop was recently added to the IUPAC classification and is commonly observed in mesoporous materials that contain both easily accessible pores as well as relatively smaller pore openings (Thommes et al. 2015). The H2 (a) hysteresis loop exhibits delayed desorption of nitrogen from the zeolite material, due to the size of its pore opening (Thommes et al. 2015). The sharpness of the low-pressure hysteresis loop also observed in sample H-ZTHH-20mL and H-ZTHT-3h increased with the increase in Si/Al ratio. This observation and the presence of a low-pressure hysteresis loop in high-silica ZSM-5 has been reported by several authors (Carrott and Sing 1988; Hudec et al. 1998). The sorption characteristics, BET surface area, mesopore surface area, micropore surface area and micropore volume of the synthesised H-ZSM-5 zeolites, also characterised by N_2 physisorption, are presented in Table 5.9 (b). It can be seen that all the HZSM-5 samples exhibited both micropore and mesopore surface area in different proportions. The BET surface area of the H-ZSM-5 samples ranged from 318 – 402 m^2/g, and this range is in accordance with that reported in literature (Missengue et al. 2018; Triantafillidis et al. 2001; Wan et al. 2016). The proportional increase in the micropore surface area of the zeolite materials is in agreement with the literature findings (Viswanadham et al. 1997; Viswanadham et al. 2009). In contrast, high mesopore surface area was observed in samples H-ZN-0.3, H-ZTP-1.2 and H-ZTHH-20mL, which indicates intracrystalline voids in the zeolite material, as evident in Figure 5.14 (Chen et al. 2018). The pore size distribution curve (Figure 5.18) of H-Z-H_2O, H-ZN-0.3, H-ZTP-1.2, H-ZTHH-20mL and H-ZTHT-3h shows the presence of mesopores with a size distribution between 3 and 5 nm, confirming the formation of uniform mesoporous structure in these samples (Fu et al. 2017). In addition, larger mesopores (5 and 12 nm) were observed in H-ZTHH-20mL showing structural changes of pores (Zhang et al. 2003). This result agrees with similar observations reported in literature (Baerlocher et al. 2007; Petrik 2009). The physical and chemical properties of the

.

synthesised CFA-based high-silica zeolite suggest that these materials may be suitable for use as catalysts in the separation of complex mixtures (Kadja et al. 2016).

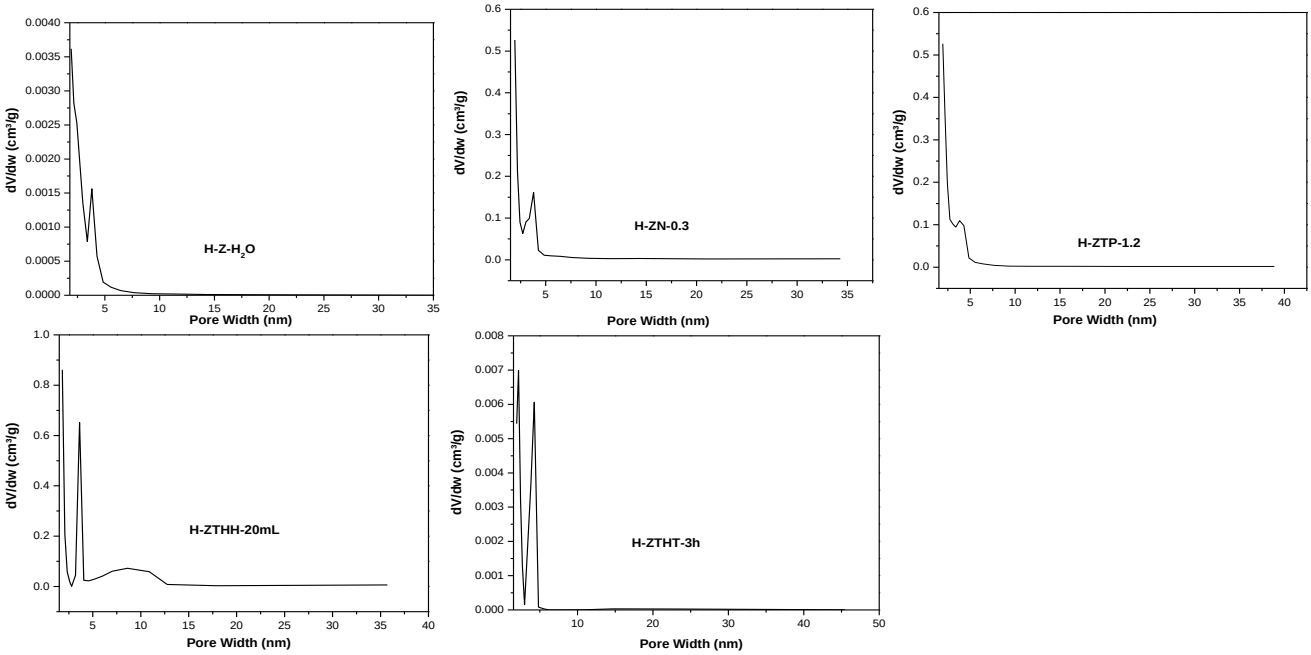

Figure 5.18: Pore size distribution curves for H-Z-H_2O, H-ZN-0.3, H-ZTP-1.2, H-ZTHH-20mL and H-ZTHT-3h

5.9 Effect of fly ash silica extract obtained from treatment with recycled liquid waste on the synthesis of ZSM-5 zeolite

The disposal and treatment of secondary liquid waste is increasingly becoming expensive, due to the variations in their chemical composition. As such, recycling of secondary liquid waste in large industrial operations has become an attractive alternative for most chemical processes, especially in coal fly ash beneficiation processes, where generation of secondary waste is inevitable. Chapter 4, Section 4.6 of this study has shown for the first time that treatment of the silica extract with water was sufficient to achieve an extract suitable for high-silica zeolite synthesis. In addition, the process showed that the resultant liquid waste can be reused in up to 4 treatment cycles without compromising the quality of the silica extract. This section investigated the effect of the fly ash silica extracts obtained after each treatment cycle, as detailed in Chapter 4, Section 4.6 on the synthesis of zeolite ZSM-5. The synthesis of ZSM-5 from TFSER1, TFSER2, TFSER3 and TFSER4 was carried out from a synthesis mixture containing 2 g of TFSERx (x =1, 2, 3 and 4), 0.4 g NaOH, 1.5 g TPABr and 50 mL of H_2O in a 100 mL Teflon-lined stainless autoclave under static conditions of 160°C for 72 h as described in Chapter 3, Section 3.3.2. The synthesis of ZSM-5 zeolite from the untreated fly ash silica extract (UFSE) was also carried out under the same conditions in order to investigate the effect of Na-rich silica extract on the morphology and

structural properties of ZSM-5 zeolite. The resulting zeolite products synthesised from the untreated fly ash silica extract and the treated silica extracts using the liquid waste, coded ZU, ZTHR1, ZTHR2, ZTHR3 and ZTHR4 respectively, were thereafter characterised by XRD, ICP, SEM, FTIR and BET.

The XRD patterns showing the mineral phases of ZU, ZTHR1, ZTHR2, ZTHR3 and ZTHR4 are presented in Figure 5.19.

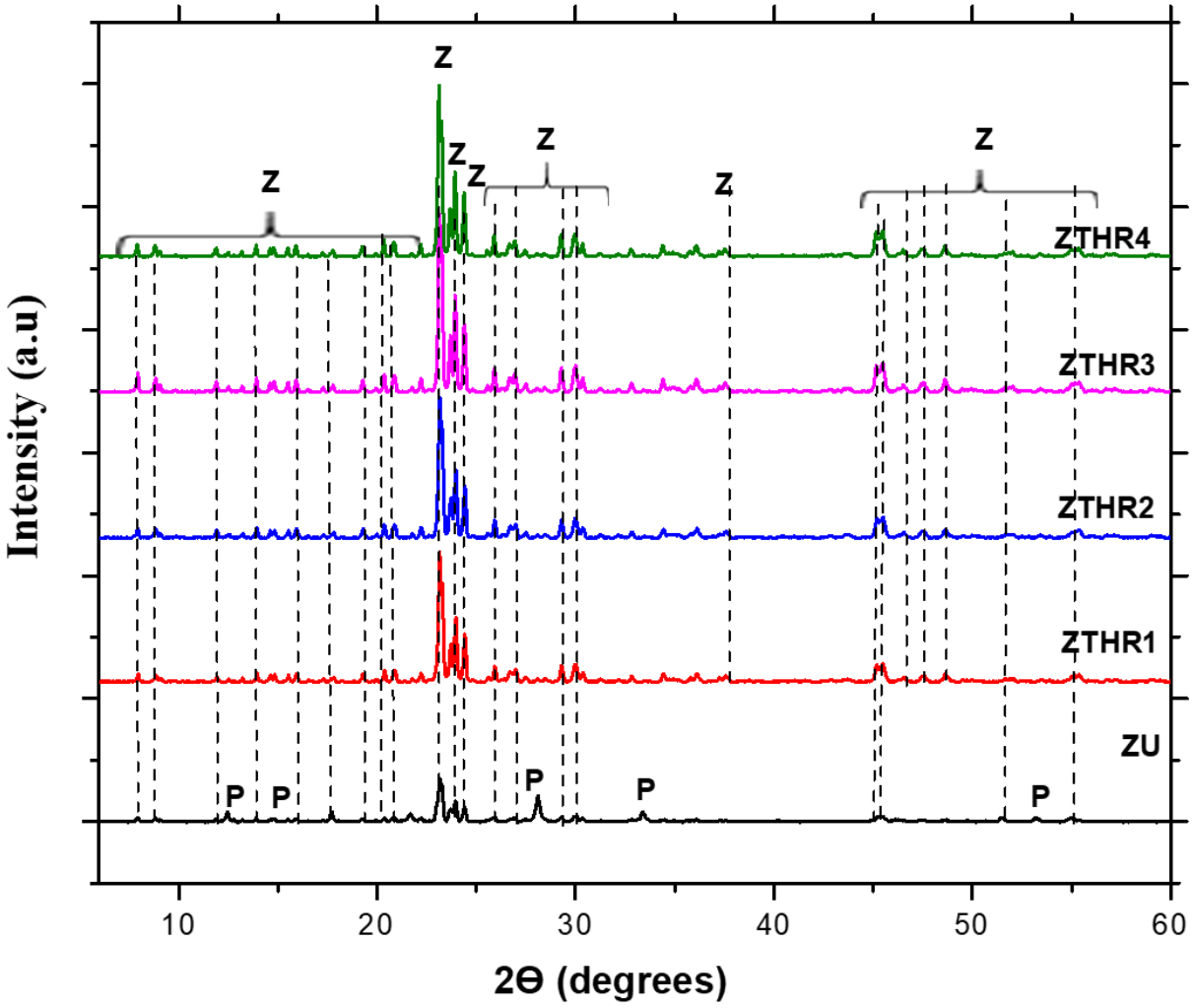

Figure 5.19: XRD spectra of ZU, ZTHR1, ZTHR2, ZTHR3 and ZTHR4 synthesised under hydrothermal conditions (160°C for 72 h) using the coal fly ash silica extracts (UFSE, TFSE1, TFSE2, TFSE3 and TFSE4) obtained in Chapter 4, Section 4.6

The spectra for ZU, ZTHR1, ZTHR2, ZTHR3 and ZTHR4 are presented in Figure 5.19. It can be seen from the XRD spectra that all the zeolite samples synthesised from treated fly ash silica

.

extracts (TFSE1, TFSE2, TFSE3 and TFSE4) displayed characteristic peaks of a pure phase ZSM-5 zeolite. An increase in the peak intensities from ZTHR1 to ZTHR4 of the three main diffractions at 2Θ = 23, 23.8 and 24.3 can be observed. This could be due to the high Na content in the TFSE1, TFSE2, TFSE3 and TFSE used as sources of Si and Al in the synthesis process, which induces quick crystallisation (Ameh et al. 2021). In contrast, the use of untreated fly ash silica extract (UFSE) as a source of Si and Al in the synthesis process resulted in the co-formation of ZSM-5 and Na-P zeolite, as shown by the XRD pattern for ZU. In addition, the major diffractions, indicative of ZSM-5 at 2Θ = 23, 23.8 and 24.3 appeared at lower intensities than those for ZTHR1, ZTHR2, ZTHR3 and ZTHR4. This could be due to the highly competitive environment created between the cation Na^+ and structure directing agent TEA^+, in which the high molar fraction of alkali Na+ cations is susceptible to the formation of multiple zeolite mineral phases (Zhang et al. 2017). Hattori and Yashima (1994) investigated the effect of Na/Si ratio on the synthesis of pure phase ZSM-5 zeolite. The authors showed that a pure phase ZSM-5 zeolite can be achieved between a Na/Si ratio of 0.016 and 0.4, and that below 0.016 or above 0.4 the formed ZSM-5 was mixed with amorphous phase or α-SiO_2. Similar observations were reported by Missengue et al. (2017), who synthesised a pure phase ZSM-5 zeolite from a CFA silica extract treated with oxalic acid solution. In this study, the TFSE3 and TFSE4 used as sources of Si and Al in the synthesis of pure phase ZSM-5 zeolite (sample ZTHR3 and ZTHR4) contained a Na/Si ratio of 0.53 and 0.59 (Chapter 4, Figure 4.11) respectively, which were 33 and 37 times higher than those reported by Hattori and Yashima (1994). It is evident from the results that even though highly crystalline pure phase ZSM-5 can be achieved at Na/Si ratios > 0.4 (ZTHR3 and ZTHR4), Na/Si ratio of > 4 resulted in an impure phase of ZSM-5 zeolite containing trace mineral phase of Na-P zeolite, which signifies the importance of the water treatment step in CFA-based ZSM-5 zeolite synthesis.

The relative percent crystallinity and the yield of the zeolite products ranged from 50-100% and 9-86.60 g/kg CFA respectively, as shown in Table 5.10. It can be seen from Table 5.10 that the synthesis of zeolite ZSM-5 from UFSE resulted in a zeolite with a lowest yield of 9 g/Kg of CFA. This could be due to the presence of high Na content (Figure 4.13) in the silica extract (UFSE) used as feedstock. However, an increase in the zeolite yield to a maximum of 86.60 g/kg of CFA (ZTHR3) was obtained after the third treatment cycle. This result corresponds to the zeolite crystallinity data, which shows that sample ZTHR3 was the most crystalline in comparison to sample ZU, ZTHR1, ZTHR2 and ZTHR4. In contrast, an instantaneous decrease in the percentage crystallinity and zeolite yield in the fourth cycle can be observed. This could be due to less Si and Al specie in the synthesis mixture, thus affecting the yield and crystallinity of the

.

final zeolite product. Similarly, a decrease in the Si/Al ratio from ZTHR3 (37.54) to ZTHR4 (21.71) can be observed in Table 5.10. It can therefore be concluded that the high sodium content in TFSE4 (Obtained in Chapter 4) facilitated crystallisation of a ZSM-5 zeolite with low Si/Al and less yield. In addition, it is clear from the results that an increase of the silica extract treatment cycles beyond 4 could lead to the formation of impure phase ZSM-5 zeolite.

Table 5.10: Percent crystallinity, crystal size, Si/Al ratio and product yield for ZU, ZTHR1, ZTHR2, ZTHR3 and ZTHR4

Sample code	Crystallinity (%)	Crystal size (µm)	Si/Al	Z_{yield} (g/Kg CFA)
ZU	50.12	2.72	5.58	9.00
ZTHR1	82.71	2.77	23.56	80.76
ZTHR2	79.20	2.59	31.83	76.90
ZTHR3	100.00	2.31	37.54	86.60
ZTHR4	70.60	1.54	21.71	66.40

Note: The Si/Al ratios were obtained from the ICP data as presented in Annexure 5.2

The morphological structure of ZU, ZTHR1, ZTHR2, ZTHR3 and ZTHR4 is presented in Figure 5.20.

.

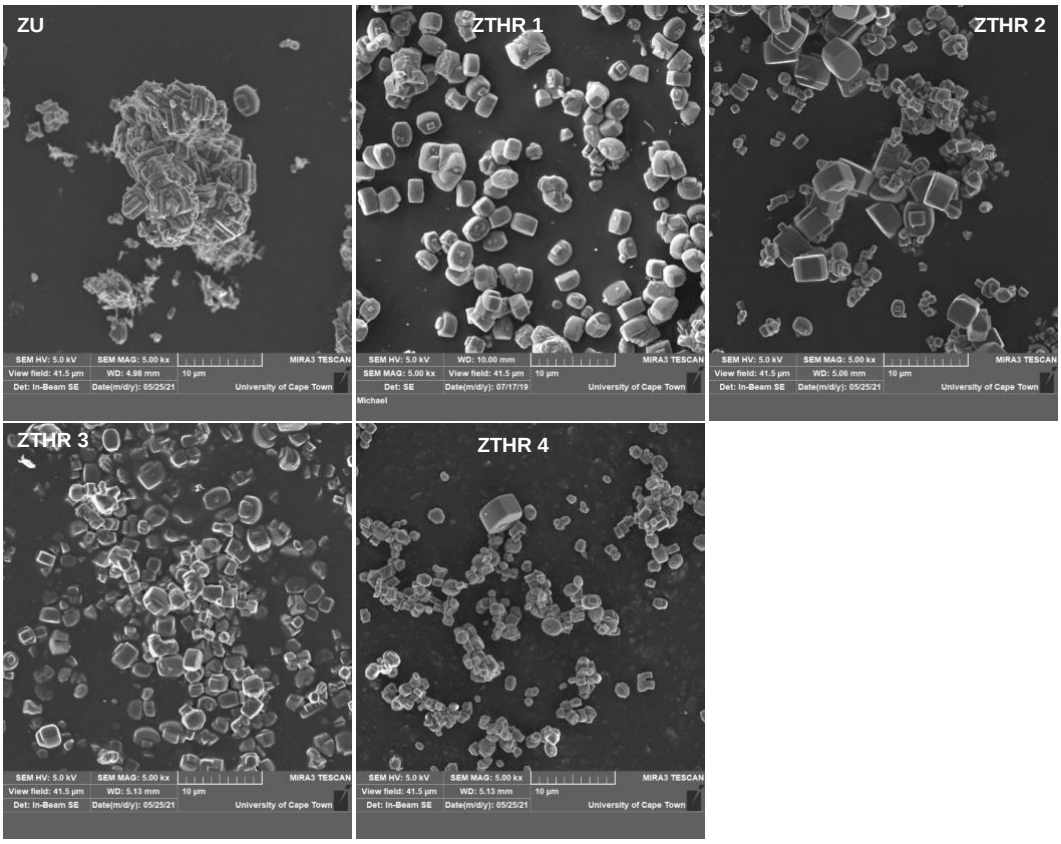

Figure 5.20: SEM micrographs of ZU, ZTHR1, ZTHR2, ZTHR3 and ZTHR4 synthesised under hydrothermal conditions (160°C for 72 h) using the coal fly ash silica extracts (UFSE, TFSE1, TFSE2, TFSE3 and TFSE4) obtained in Chapter 4, Section 4.6

Figure 5.20 shows the morphological structure of ZU, ZTHR1, ZTHR2, ZTHR3 and ZTHR4, synthesised from the untreated and treated silica extracts with recycled liquid waste. The micrograph of ZU sample shows intergrowth and twinned hexagonal prism shaped crystals (Shirazi et al. 2008), with high aggregation of an average crystal size of 2.72 µm. The SEM micrographs of ZTHR1, ZTHR2, ZTHR3 and ZTHR4 samples exhibited intergrown prismatic morphology. Such morphological structure is typical of ZSM-5 zeolite (Silva et al. 2016; Wei et al. 2020). The average crystal size of these samples ranged between 1.54 and 2.77 µm. However, an obvious decrease (ZTHR4 < ZTHR3 < ZTHR2 < ZTHR1) in the zeolite crystal size can be noticed (Table 5.10). This could be due to the occurrence of rapid nucleation reactions. Petrik et al. (1995) reported that the presence of Na^+ ions in the zeolite precursor is known to favour rapid nucleation, due to its structure-directing properties. It could then be concluded that the increasing Na content in the TFSE (Chapter 4, Figure 4.6) used in the synthesis of ZTHR1, ZTHR2, ZTHR3

and ZTHR4 may promote rapid nucleation, resulting in the formation of smaller crystal sizes as evident in Figure 5.20.

The structural configuration for ZU, ZTHR1, ZTHR2, ZTHR3 and ZTHR4 zeolite products is presented in Figure 5.21.

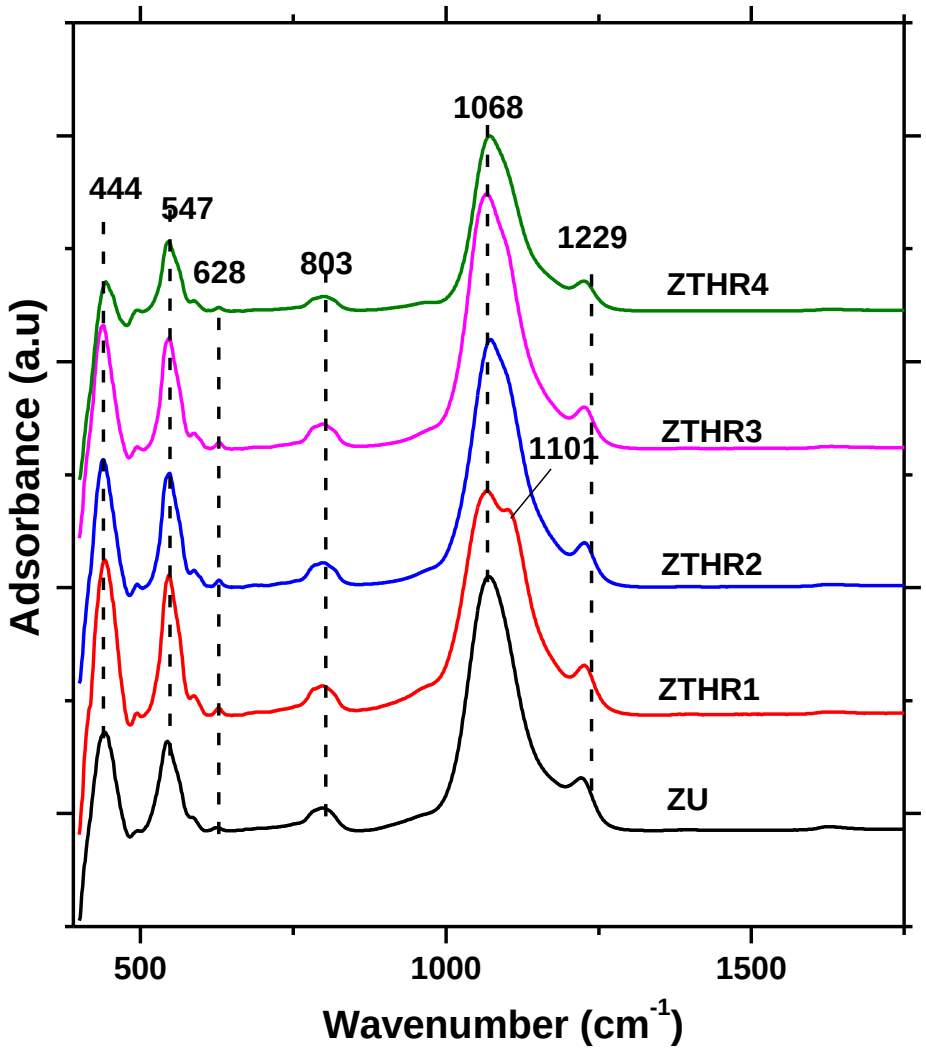

Figure 5.21: FTIR spectra for ZU, ZTHR1, ZTHR2, ZTHR3 and ZTHR4 synthesised under hydrothermal conditions (160°C for 72 h) using the coal fly ash silica extracts (UFSE, TFSE1, TFSE2, TFSE3 and TFSE4) obtained in Chapter 4, Section 4.6

The FTIR spectra (Figure 5.21) show characteristic bands of ZSM-5 zeolite at 444, 547, 628, 803, 1068 and 1229 cm^{-1} present in ZU, ZTHR1, ZTHR2, ZTHR3 and ZTHR4. The presence of 444 and 547 cm^{-1} bands in the IR spectra correspond to the Si-O bend that characterises highly siliceous materials and double ring vibration respectively (Shirazi et al. 2008). A shift on the 444

.

cm^{-1} band for ZTHR4 towards a lower wavelength can be observed, and this could be due to the low Si/Al ratio of 5.58 in the ZU sample. The bands at 628 and 1068 cm^{-1} can be attributed to internal symmetric stretching vibrations of Si-O-T bond, while the bands at 806 and 1229 cm^{-1} are associated with the external symmetric and asymmetric stretching vibration of Si-O-T respectively (Oleksenko et al. 2004). An overlap of the internal asymmetric stretch at 1068 and 1101 cm^{-1} in sample ZTHR1 can be observed. This indicates the presence of SO_4^- polymer anion in the ZSM-5 structure (Bass and Turner 1997; Shirazi et al. 2008). Shirazi et al. (2008) reported that the absorption bands around 444 and 547 cm^{-1} can be used to estimate the degree of crystallisation of the zeolite product. The XRD and SEM results of all the samples shows that the synthesised zeolite ZSM-5 exhibited good crystallinity, as confirmed by the percentage crystallinity (ranging between 50 (ZU) to 100 (ZTHR3)) shown in Table 5.10. This result further confirms the transformation of the fly ash silica extracts (UFSE, TFSE1, TFSE2, TFSE3 and TFSE4) into zeolite ZSM-5.

Figure 5.22 depicts the nitrogen physisorption profiles of UZ, ZTHR1, ZTHR2, ZTHR3 and ZTHR4 zeolite products.

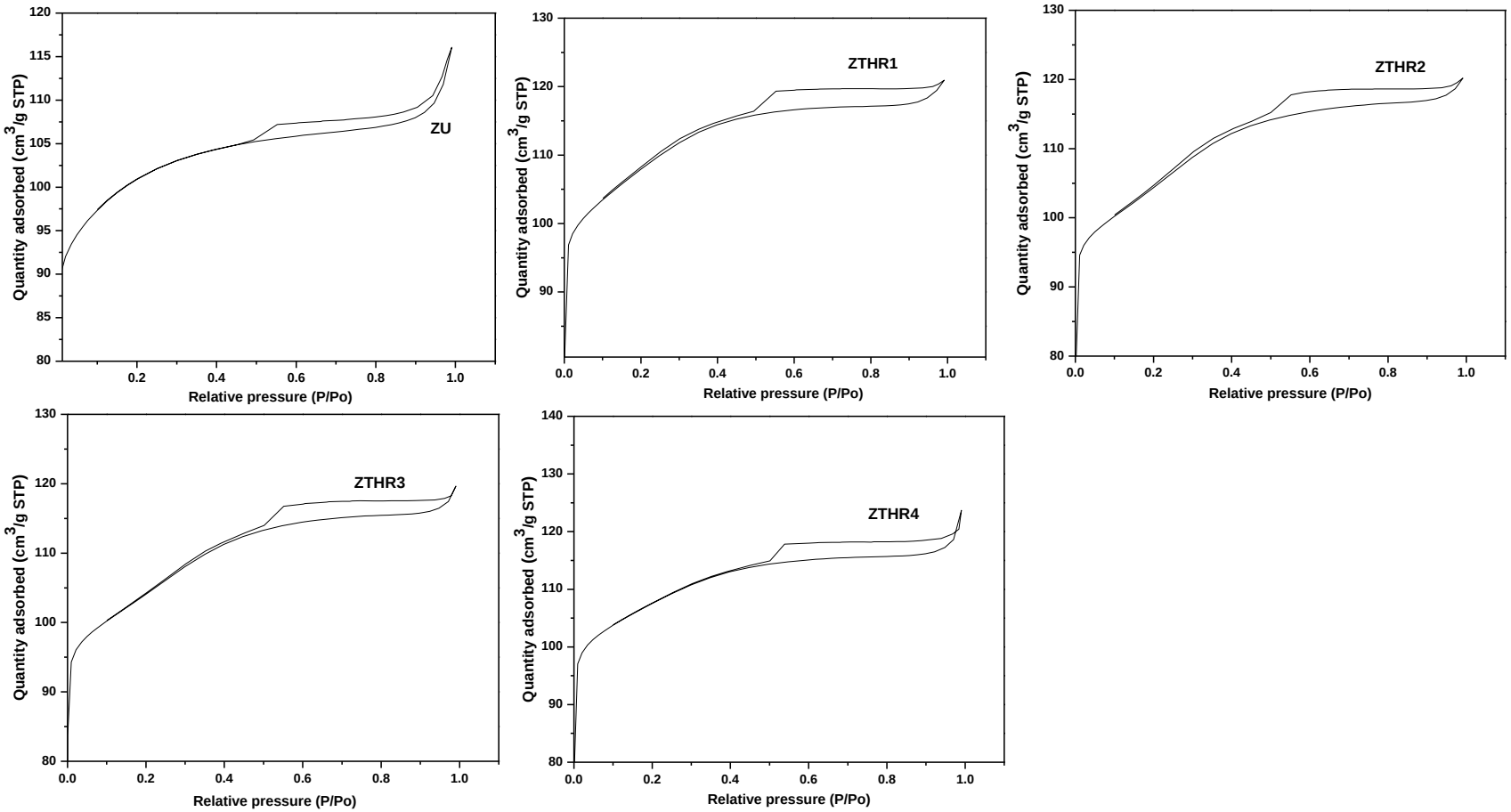

Figure 5.22: Absorption-desorption isotherms of UZ, ZTHR1, ZTHR2, ZTHR3 and ZTHR4 synthesised under hydrothermal conditions (160°C for 72 h) using the coal fly ash silica extracts (UFSE, TFSE1, TFSE2, TFSE3 and TFSE4) obtained in Chapter 4, Section 4.6

.

The N_2 adsorption-desorption isotherms of all the zeolites samples were of IUPAC type II (Figure 5.22) – indicative of micropore characteristic of high nitrogen uptake at relatively low partial pressures – with the presence of a hysteresis loop appearing in the region between 0.44 and 0.98 P/Po. This loop is common for zeolite ZSM-5 and characteristic of intra crystalline mesopores (Thommes et al. 2015). Figure 5.23 shows the pore size distribution curve of ZU, ZTHR1, ZTHR2, ZTHR3 and ZTHR4.

.

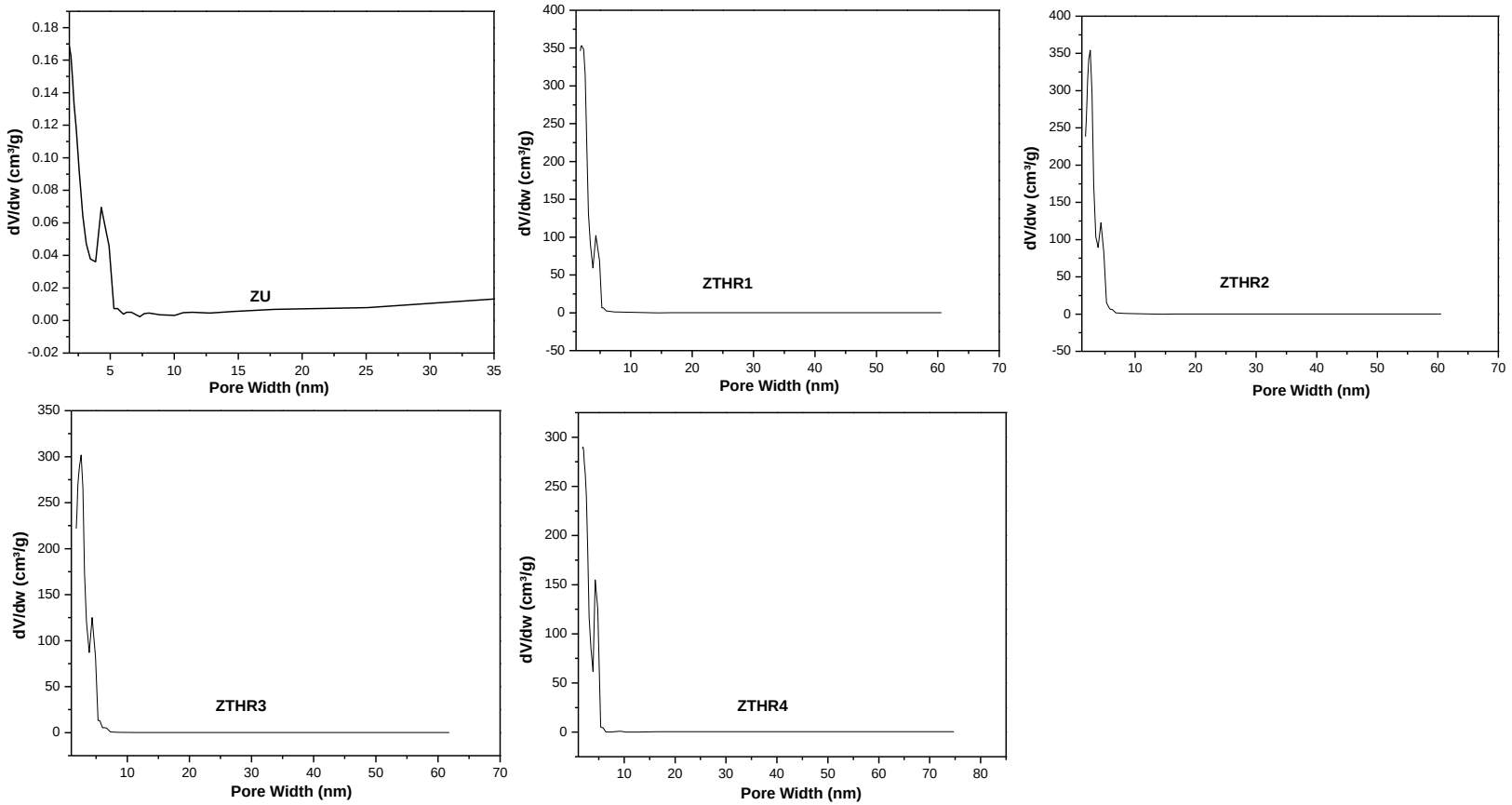

Figure 5.23: Pore size distribution curves for UZ, ZTHR1, ZTHR2, ZTHR3 and ZTHR4 synthesised under hydrothermal conditions (160°C for 72 h) using the coal fly ash silica extracts (UFSE, TFSE1, TFSE2, TFSE3 and TFSE4) obtained in Chapter 4, Section 4.6

.

The pore size distribution curves (Figure 5.23) of ZU, ZTHR1, ZTHR2, ZTHR3 and ZTHR4 show the presence of mesopores with concentrated size distribution between 3 and 5 nm respectively, confirming the formation of mesopore structure (Petrik 2009).

Table 5.11 presents the textural properties of the ZU, ZTHR1, ZTHR2, ZTHR3 and ZTHR4. All the samples possess a high surface and micropore areas between 399 to 439 m^2/g and 315 to 354 m^2/g respectively, with a mesopore area between 84 and 98 m^2/g.

Table 5.11: Textural properties UZ, ZTHR1, ZTHR2, ZTHR3 and ZTHR4

Sample code	Crystal size (µm)	S_{BET} (m^2/g)	S_{micro} (m^2/g)	S_{meso} (m^2/g)
ZU	2.72	399	315	84
ZTHR1	2.77	432	334	98
ZTHR2	2.59	415	323	92
ZTHR3	2.31	414	330	84
ZTHR4	1.54	439	354	85

These surface areas are typical of a ZSM-5 zeolite and are in good accordance with the observed high crystallinity of these samples, as presented in Table 5.10. In addition, a higher BET surface area was achieved for ZTHR4, and this could be due to its small crystal size (1.45 µm). This observation corroborates the findings by Armaroli et al. (2006). The results of this study show that the zeolite products synthesised from the TFSE1, TFSE2, TFSE3 and TFSE4 (treated with recycled liquid waste) were of good quality and can be used to synthesise pure phase ZSM-5 zeolite suitable for use as catalysts in various catalytic industries. These results present an opportunity to recycle the liquid waste obtained after the 4^{th} recycling stream (Chapter 4, Section 4.6) to a point where all the Si and Al wasted can be recovered, thus improving the yield of the final product.

.

5.10 Chapter summary

This chapter demonstrates the possibility of synthesising pure phase ZSM-5 zeolite from oxalic acid free fly ash silica extract without compromising the quality of the zeolite product. The oxalic acid and water treated fly ash silica extracts (obtained in Chapter 4), containing high Si/Al ratios were used as sources of Si and Al in the synthesis of ZSM-5 zeolite. The XRD and SEM results of the ZSM-5 zeolites synthesised either oxalic acid or water treated silica extracts were comparable, indicating that the oxalic acid treatment step in the synthesis of CFA-based ZSM-5 zeolite is not necessary and can be replaced by a single step water treatment process. Further to this, the water treated fly ash silica extract (TFSE-H_2O) was selected as the optimum molar composition (1 Si: 0.003 Al: 0.528 Na: 0.152 TPABr: 38.306 H_2O) for the synthesis of pure phase ZSM-5 with acceptable crystallinity and crystal size. This was then set as the baseline for the optimisation studies. For this, different synthesis parameters such as the effect of NaOH, TPABr, water content and hydrothermal time and temperature on the phase purity and morphology of ZSM-5 were investigated. The study demonstrated that variations in the NaOH, TPABr and water content of the synthesis precursor gel had an impact on the crystallinity, morphology and crystal size of the resulting zeolite product. In addition, the study showed for the first time that the optimum molar composition of 1 Si: 0.003 Al: 0.528 Na: 0.152 TPABr: 38.306 H_2O enhanced a fast nucleation rate and promoted crystallisation of ZSM-5 zeolite with an average crystal size of 1.9 µm within the synthesis time of 3 h. Moreover, the study has shown that the designed recycle protocols of the liquid waste (obtained after treatment of fly ash silica extract with water, Chapter 4, Section 4.6) produced good quality fly ash silica extracts suitable for the synthesis of ZSM-5 zeolite with high BET surface area ranging from 414 – 439 m^2/g. The innovative synthesis process developed in this study would be instrumental in the design of a scaled-up CFA-based zeolite synthesis process, due to its waste minimisation component.

.

CHAPTER 6
TECHNOLOGY ECONOMIC ANALYSIS OF ZSM-5 ZEOLITE SYNTHESISED FROM CFA-BASED SILICA EXTRACT

6.1 Synopsis

Technically, it has been proven in the previous chapters (Chapter 4 and Chapter 5) that coal fly ash (CFA) can be converted into ZSM-5 and sodalite zeolites with no solid waste produced. However, what has not been shown is whether the process is economically feasible. Although the synthesis of ZSM-5 zeolite from alternative inexpensive Si and Al bearing materials is well-researched (Cornelius 2019; Dey et al. 2013; Missengue et al. 2017; Vempati et al. 2006). The uptake of these processes to replace the commercially available ZSM-5 zeolite is lacking, as these techniques were limited to laboratory scale, with no economic feasibility data for large scale production (Hong et al. 2017; Wdowin et al. 2014). While most industries rely on pure silicon and aluminium sources in the synthesis of ZSM-5 zeolite, the cost of commercially sourced silica and aluminium materials is increasingly becoming expensive. The total conversion of CFA to zeolite materials will provide an alternative to use CFA as a sole source of Si and Al in a larger scale to produce zeolite materials with wide industrial applicability. It is therefore important to explore the commercial viability of CFA-based ZSM-5 and sodalite zeolites towards development of a large-scale synthesis process. This study may provide a basis to rely on CFA as a resource towards developing a commercial scaled plant for the synthesis of ZSM-5 and sodalite zeolites, thus reducing industry reliance on pure silicon and aluminium sources for ZSM-5 zeolite synthesis. This chapter, therefore, aims to investigate the economic feasibility of producing 5000 kg per year of CFA-based ZSM-5 zeolite using the proposed synthesis route.

.

6.2 Laboratory scale

6.2.1 Process description

The experimental procedure as detailed in Chapter 3, Section 3.3.1.1, 3.3.1.2, 3.3.1.3 and 3.2.2 was carried out as follows:

(1). Synthesis of sodalite and extraction of silica through a CFA alkaline leaching process

The extraction of silica and the synthesis of sodalite was carried out as detailed in Chapter 3, Section 3.3.1.2.

(2) Treatment of silica extract (UFSE)

As discussed in Chapter 5, Section 5.2, the silica extract treated with water contained the correct Si/Al ratio required for the synthesis of zeolite ZSM-5, therefore ruling out the need for oxalic acid treatment in the synthesis of high-silica CFA-based zeolite ZSM-5 as recommended by Missengue (2016) and Ndlovu et al. (2017). For this reason, the obtained UFSE in process (2), was thereafter mixed with water in a solid-to-liquid ratio of 1:6.6 in a round-bottom beaker and heated at 80˚C under reflux conditions for 6 h, while stirring at 250 rpm. The subsequent solid product (TFSE-H_2O) was then filtered and dried overnight at 70˚C as, shown in Figure 6.1 (2).

(3) Hydrothermal synthesis of ZSM-5 zeolite.

The optimum hydrothermal synthesis conditions obtained in Chapter 5, Section 5.7 were adopted as the main process conditions for the cost estimation analysis performed in this study. To account for the continuous synthesis process, the feedstock materials (TFSE-H_2O, NaOH, TPABr and water content) were scaled by a factor of 1.73, as shown in Figure 6.1 (3). As such, the dried TFSE-H_2O was mixed with 0.52 g NaOH and 34.6 mL of H_2O in a 100 mL Teflon-lined stainless autoclave. The mixture was then aged for 25 min at room temperature before adding 2.59 g of TPABr while aging for an additional 15 min. The homogenous mixture was then placed in an oven at 160°C, for 3 h. At completion, ZTHT-3h was recovered by filtration, washed with deionised water and dried overnight at 70°C.

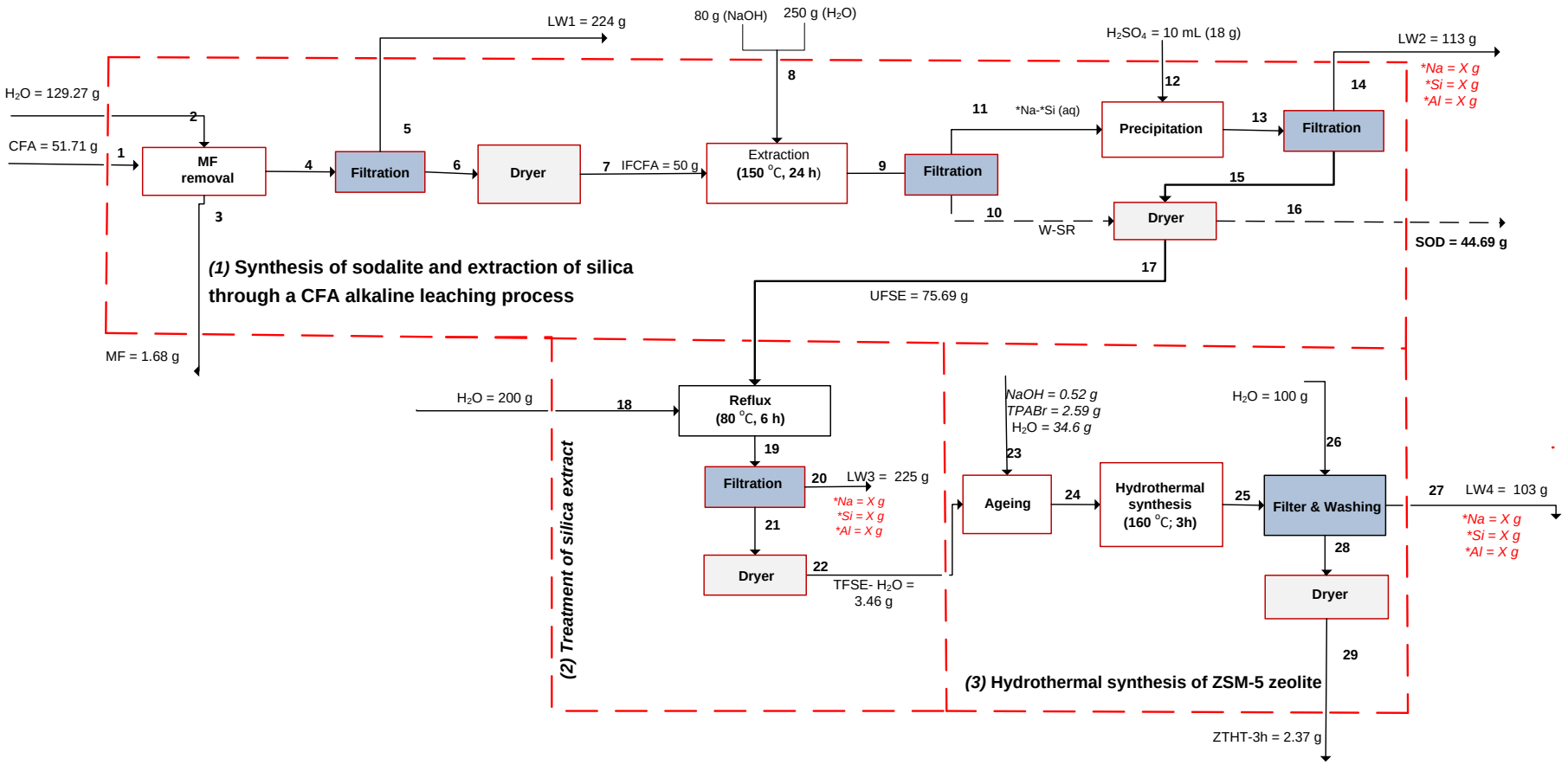

Figure 6.1: Block flow diagram for the synthesis of ZTHT-3h (hydrothermally synthesised at 160˚C for 3 h) and SOD zeolite (alkaline treatment at 150˚C for 24 h). X represents the undetermined amount of Na, Si, and Al in the liquid streams (LW2, LW3 and LW4)

.

6.2.2 Overall mass balance and product yields

The overall process mass balance for the laboratory scale is illustrated in Figure 6.2.

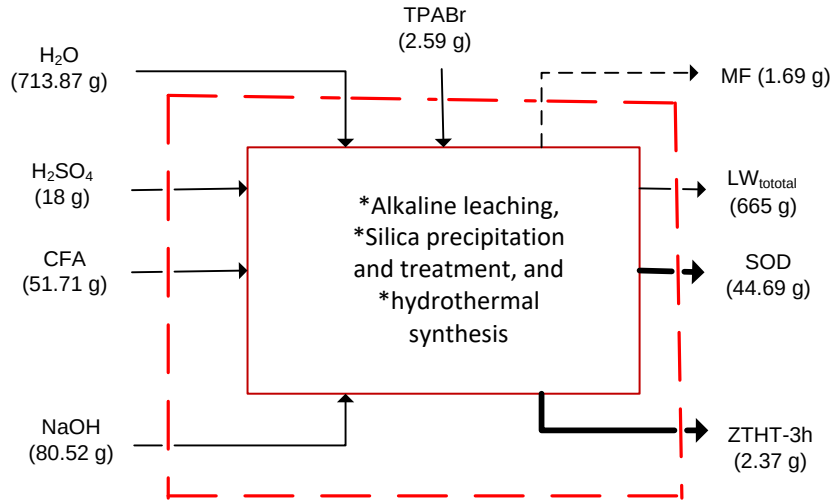

Figure 6.2: Laboratory scale overall mass balance

The generic mass balance equation is denoted by:

$$M_{feed} = M_{product} \ldots\ldots\ldots\ldots\ldots\ldots\ldots\ldots\ldots Equation\ 6.1$$

Where M_{feed} = mass of feedstock and $M_{product}$ = mass of products. The mass balance equation is therefore represented by:

$$CFA + NaOH + H_2SO_4 + H_2O + TPAB_r = SOD + ZTHT - 3h + MF + LW_{total} + M_{loss}$$

Therefore: 866.69 g = 713.75 g + M_{loss}

M_{loss} = 152.29 g

The total liquid waste (LW_{total}) is composed of LW1, LW2, LW3 and LW4 (Figure 6.1) and contains elements such as Si, Al, and Na carried over from the following process steps: silica precipitation (stream 14), treatment step (stream 20) and hydrothermal supernatant (stream 27). The total mass output was 713.75 g, which represents 82.35% of the total mass input. The total material loss (M_{loss}) in the process was 152.29 g (including liquid and solid). The mass loss represents 17.65% of the total material input. This is a huge loss in zeolite synthesis, as the input materials are costly, and any major losses could negatively impact on the process's viability. It has been

.

shown in Chapter 4, Section 3.3.2.1 that the liquid waste (LW3) resulting from the treatment of the silica extract with water can be recycled four times without compromising the quality of the silica extracts. This has demonstrated that implementing recycling protocols could decrease the amount of liquid waste produced.

The filtration and drying process steps are regarded as the main steps where material loss could have occurred due to evaporation (drying stage) and unrecovered materials remaining from the filter paper (filtration stage), which could negatively affect the product yields presented in Table 6.1. The yields were calculated using equation 6.2.

$$Y\ (\%) = \frac{W_{product}}{W_{feedstock}} * 100 \ldots\ldots\ldots\ldots\ldots\ldots\ldots\ldots\ldots\ldots\ldots\ldots\ldots\ldots Equation\ 6.2$$

Table 6.1: Product yield for MF, ZTHT-3h and SOD

Sample	Yield (%)
MF	3.27
ZTHT-3h	4.58
SOD	86.42

As shown in Table 6.1, sodalite zeolite (SOD) has a high yield of 86.42%. This is not surprising, as SOD was synthesised from the bulk solid waste recovered after the alkaline leaching process represented by stream 10 of Figure 6.1. The yield of ZTHT-3h was much lower, at 4.58%, than that of SOD zeolite, followed by MF at 3.27 g. The obtained yield for ZTHT-3h was lower than that reported by Cornelius (2019) (16.21%) for a ZSM-5 zeolite synthesised using a similar process. This could be due to the addition of extra aluminium sources added in the precursor gel during the pre-synthesis process to adjust the Si/Al prior to the hydrothermal synthesis. In the case of SOD, the obtained yield agrees with Cornelius (2019), who also reported a higher yield of sodalite zeolite (above 80%) synthesised from CFA using alkaline leaching process. On the contrary, lower yields of 26.47 and 56.30% have been reported on the synthesis of sodalite zeolite using direct hydrothermal and fusion methods respectively (Shabani et al. 2022). This result shows that the alkaline extraction process led to a higher yield of SOD.

6.3 Material cost to produce 1 kg of ZSM-5

The results obtained in the laboratory scale (discussed above) were used to extrapolate the production of 1 kg of ZSM-5 per batch and to determine the material cost of production. Figure 6.3 shows the overall mass balance for producing 1 kg of ZSM-5 zeolite.

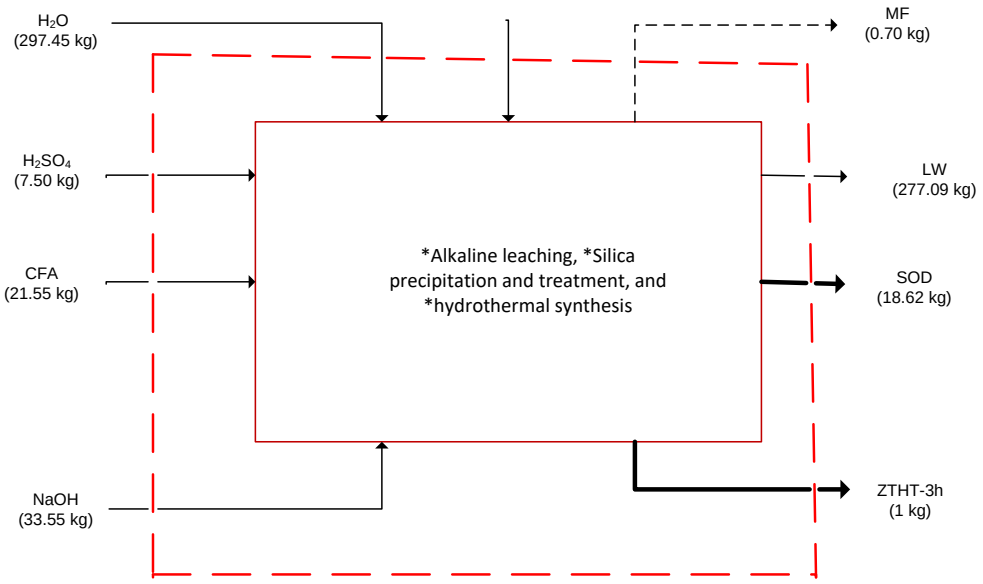

Figure 6.3: Overall mass balance for 1 kg of ZSM-5 per batch

The mass balance presented in Figure 6.3 was used to determine the material costs to produce 1 kg of ZSM-5 (ZTHT-3h) zeolite (Table 6.2).

Table 6.2: Material cost contribution to produce 1 kg of ZSM-5 per batch

Reagents	Price (R/kg)	Quantity (kg)	Material cost (R/kg of ZSM-5)	Source
Coal fly ash (CFA)	129	21.55	2779.4125	https://eparcel.co.za/courierprices.aspx
NaOH (98%)	2460.78	33.46	82333.5975	Sigma Aldrich (product no:S8045)
Water	0.033	291.36	9.6149625	City of Cape Town water and sanitation commercial / Industrial water tariffs (2021/2022)
Sulphuric acid (98%)	2681.67	7.50	20112.525	Sigma Aldrich (product no: 258105)
TPABr (98%)	4300.24	1.58	6780.94095	Sigma Aldrich (product no: 225568)
Total			**R112 016.09**	

The CFA used in this study was obtained free of charge from the Matla power plant, and for the purposes of the technology economic analysis, the transportation cost was considered as the cost price of CFA. The price of NaOH and TPABr was R2 460.78 and R4 300.24 per kg respectively

.

(sourced from Sigma-Aldrich). The water tariffs as of 2021/2022 were R32.65 per kilolitre (1000 kilograms), as per the City of Cape Town, water and sanitation for commercial or Industrial use. The price of sulphuric acid (H_2SO_4) as of June 2022 was R1 468.04 per litre. This was converted to rand per kilograms. As shown in Table 6.2, NaOH is the major cost contributor at 73.50%, followed by H_2SO_4 (24.44%), TPABr (8.24%), CFA (3.78%) and process water (0.01%). The cost implication of each reagent on the total net present value is discussed in Section 6.5 of this chapter.

6.4 Cost estimation and project evaluation at 5 000 kg per year

The cost estimation performed in this study was based on assumptions generally applied for projects within the Class 5 cost category, as recommended by American Association of Cost Engineers (AACE). This section aimed to investigate the economic feasibility to produce 5000 kg of ZTHT-3h per year. The results obtained at a laboratory scale were used as a basis to determine the cost of materials required at this scale (5 000 kg/year). For the purpose of this study, ZTHT-3h and SOD were considered as the main products for the feasibility study. The magnetic fraction (MF) obtained as a product during the first stage of the process (Figure 6.1), as well as the total liquid waste generated in the process, were not included in the cost estimation, because they both required extra treatment which was not the focus of this study. However, Chapter 4, Section 3.3.2.1 has shown that the liquid waste can be recycled to reduce the production cost. Table 6.3 details the economic analysis parameters applied in all calculations performed.

.

Table 6.3: Economic analysis base parameters

Variable	Specification
Project type	Addition into an existing plant
Process capacity	5000 kg/year of ZSM-5
Currency	South African Rands (R)
Plant operating life	20 years
Industry tax rates	33 % based on Coulson and Richardson's, (1999)
Working capital	15% of fixed cost
Interest rate	5%
Operating hours	7200 hours per year
Operating days	300 (excludes public holidays)
Inflation rate (% per year)	
Production costs	5.9%

The inflation rate was based on the current South African inflation rate as of March 2022. The annual interest rate was assumed at 5%. The industry tax was taken at 33% as suggested by Coulson and Richardson (1999). The operating hours assumed were based on 300 days per year, which excluded public holidays. The plant operating life was assumed at 20 years, which is a common life span for chemical processing plants. In addition, the cost of land and structure engineers was excluded from the calculations, as this project was assumed to be an addition into an existing plant.

6.4.2 Capital cost estimate

Capital cost plays an integral part in project cost estimation. It is required to estimate the total initial investment at the beginning of the project (Feng and Rangaiah 2011). Different methods to estimate capital costs have been extensively discussed by Coulson and Richardson (1999) (Chapter 2, Section 2.4.2). The capital estimates for chemical process plants are often based on the total purchase cost of the major equipment items required for the process (Coulson and Richardson 1999), and the other costs are estimated from the equipment costs using a Lang factor. In this study, equipment cost estimates were calculated using equation 6.3:

.

$$C_e = CS^n \ldots\ldots\ldots\ldots\ldots\ldots\ldots\ldots Equation\ 6.3$$

where C_e represents the equipment purchase cost, S = size of equipment, C = the cost constant and n represent the index for the specific type of equipment, as shown in Table 6.4.

For the purpose of the cost estimation in this study, the equipment size was estimated at the lowest size range, provided in Coulson and Richardson (1999) (Table 6.2). According to Coulson and Richardson (1999), these prices (cost constant) are based on estimates for mid-2004. The price was then converted from US dollars to South African Rands using the conversion factor: 1US $ = R16.06. The final equipment prices were therefore adjusted for inflation to 2022 using the online Inflation (2022) calculator (https://inflationcalc.co.za/?date1=2004-06-01&date2=2022-06-24&amount=136462.7565).

Table 6.4: Equipment cost estimate parameters used in equation 6.3 (adapted from Coulson and Richardson (1999)

Major equipment	Size (S)	Cost contant (R)	Index (n)	No. equipments	C_e (R)
Filter (Vacuum drum)	1 m^2	546040.00	0.6	5	7042127.96
Dryer (Pan)	2 m^2	123662.00	0.35	4	1626170.99
Reactor (jacketed)	3 m^3	240900.00	0.4	2	964261.34
				Total	**9632560.29**

The final price for equipment was multiplied by the number of equipment units selected as the major equipment for the process. The major equipment consists of two reactors (silica extraction reactor and the autoclave reactor used in the hydrothermal synthesis process), 5 filtration units and 4 dryers at different process stages. The total equipment cost was R9,632,560.29. This cost was thereafter used to estimate the total fixed capital costs expressed as a function of the total purchase equipment (Equation 2.5 – as discussed in Chapter 2, Section 2.4.2.3). For this process, the Lang factor was taken as 3.6 for a mixed fluids-solids processing plant (Table 2.4).

$$Cf = f_L C_e \ldots\ldots\ldots\ldots\ldots\ldots Equation\ 2.5$$

In addition to the equipment costs, the direct cost incurred (equipment installation + additional construction to the existing plant), which sums up the total fixed cost required in the project, were calculated using Equation 6.4 and 6.5.

.

$$PPC = PCE(1 + f_1 + \cdots + f_9) \ldots\ldots\ldots\ldots\ldots Equation\ 6.4$$

$$Fixed\ capital\ cost = PPC(1 + f_{10} + f_{11} + f_{12}) \ldots\ldots\ldots\ldots\ldots\ldots\ldots Equation\ 6.5$$

Where PPC = physical plant cost, PCE = equipment purchase cost, $f1 + f2 + f3 + + + \cdots f12$ = fixed cost estimation factors as indicated in Chapter 2, Table 2.4. The total fixed cost, which included direct and indirect costs, was R152 926 527.16. The total investment required was calculated using Equation 6.6.

$$Investment\ required = Fixed\ cost + working\ capital \ldots\ldots\ldots\ldots\ldots\ldots Equation\ 6.6$$

The working capital was based on 15% (Table 6.2) of the total fixed capital costs (R22, 938, 979.07). Therefore, the total initial investment required for this project was estimated at R175, 865, 506.24. The next section details the estimation calculations for production costs required to produce 5000 kg of ZTHH-3h per year.

6.4.3 Production cost estimate

Production costs refers to the total costs required to manufacture the desired product, in this case being ZTHT-3h and SOD. Production or operating costs are divided into fixed and variable costs (Putri 2017). Fixed costs comprise of maintenance, operating labour, laboratory costs, supervision, plant overheads, capital charges, insurance, local taxes, and royalties, whereas variable costs comprises of raw materials, miscellaneous materials, utilities, shipping and packaging. Table 6.5 presents the assumptions considered in the total production costs estimate in this study. According to Coulson and Richardson (1999), for early stage projects where detailed process information is not available, production costs estimates can be derived from the operating costs, labour costs and fixed cost, as shown in Table 6.5. The utility costs were estimated using cost of utilities Table 6.5 of Coulson and Richardson (1999). Applicable to this project were the cost of electricity and process water, for which estimates were made in US dollars and then converted to South African Rands using US1$ = R16.06, the current exchange rate. For this project, shipping and packaging as well as local taxes costs were assumed as negligible. In addition, royalty rates and research and development costs were not applicable, as the project is still at its early stages of development.

.

Table 6.5: Production cost assumptions

Production cost assumptions	
Miscellaneous materials	10% of maintenance cost
Utilities*	Assumed as R2000
Shipping and packaging	Negligible
Maintenance	5% of fixed cost
Laboratory costs	20% of operating labour
Plant overheads	50% of operating labour
Capital charges	10% fixed cost
Insurance	1% fixed cost
Local taxes	Negligible
Royalties	n/a
Sales expenses, General overheads	20% production cost (variable + fixed)
Research and development	n/a

6.4.3.1 Operating labour cost

Presented in Table 6.6 is the operating labour cost required to produce 5000 kg per year of ZSM-5 zeolite. This will require a 24-hour operating cycle for 300 days a year operated on a four-shift labour schedule.

.

Table 6.6:Total labour cost to produce ZSM-5 zeolite

Labour (Direct and Indirect)	Number	Annual Salary (TCoE R/person)	Months Employed	Total (R/year)
DIRECT LABOUR				
Chemical engineer operators	16	287,535	12	4,600,560
Chemical engineer assistant operator	5	243,123	12	1,215,615
TOTAL DIRECT LABOUR				5,816,175
INDIRECT LABOUR				
Plant				
Production Manager	1	355,954	12	355,954
Quality Assurance Technician	1	501,018	12	501,018
HR & Finance				
Bookkeeping & Finance	1	250,509	6	125,255
Other				
Stores	1	243,123	12	243,123
TOTAL INDIRECT LABOUR				1,225,350
TOTAL LABOUR COST				**7,041,525**

Note: TCoE = Total cost of employment. Salary estimates for the respective employment job titles were obtained from Payscale (2022) South Africa (Chemical Engineer Salary in South Africa | PayScale). Prices are based on an average salary for a chemical engineer in respect to the years of experience: [1] entry level with 0 -1 years of experience, [2] early career with 1-4 years of experience, [3] an experienced engineer with 10-19 years of experience and [4] salary estimate for a mid-career engineer with 5-9 years of experience.

.

A total of 25 employees were considered for this operation, which comprises of 16 chemical engineer operators, 5 assistant operators and 1x (production manager, quality assurance technician, finance person and storage keeper). The experience of the personnel ranged from 0 to 19 years. The total cost of employment for the personnel, as estimated from Payscale South Africa, was R7 041 525. The total salaries were based on a 12-month employment contract for all personnel except for the bookkeeper and finance person, which were based on a 6-month employment contract.

6.4.4 Net cashflow

The net cashflow (NCF) showing the cash inflows and outflows over a period of 20 years is presented in Table 6.7. The NCF was calculated using Equation 6.7. The price of ZSM-5 was obtained from advance chemicals supplier, from the adsorbent series with product no CAS No: 1318-02-1 and a BET surface area of greater or equal to 340 m^2/g (https://www.acsmaterial.com/zsm-5-adsorbent-series.html). The commercial price of sodalite zeolite could not be sourced from the online product prices, so for the purpose of this study a unit price of sodalite zeolite was assumed as R550 per kg.

$$Net\ cash\ flow\ (NFC) = Revenue - production\ cost - investment\ required \ldots\ldots\ldots Equation\ 6.7$$

.

Table 6.7: Net cashflow for the production of ZSM-5 and sodalite zeolite

Year	1		2		3		+…+	20	
Product	**ZTHT-3h**	**SOD**	**ZTHT-3h**	**SOD**	**ZTHT-3h**	**SOD**		**ZTHT-3h**	**SOD**
Capacity	0%	0%	50.00%	50%	75%	75%		100%	100%
Production	_	_	2500.00	48810.04	3750.00	73215.07		5000.00	97620.09
Selling price (R)	_	_	7259.88	550.00	7695.47	583.00		20722.16	1569.89
Units sold (kg)	_	_	2375.00	46369.54	3562.50	69554.31		5000.00	97620.09
Revenue (R/kg)	_	_	**17242215.00**	**25503247.82**	**27415121.85**	**40550164.03**		**103610798.65**	**153252460.57**
Total revenue (ZSM-5+SOD)	_		**42745462.82**		**67965285.88**			**256863259.21**	
Production cost (R)									
Variable	_	_	878648.62	_	931367.54	_		2507961.17	_
Fixed	_	_	37256890.45	_	39492303.87	_		106343801.12	_
Indirect production cost	_	_	7627107.81	_	8084734.28	_		21770352.46	_
Total production cost	_	_	**45762646.89**	_	**48508405.70**	_		**130622114.75**	_
Fixed capital cost	152926527.16								
Working capital	22938979.07		24315317.82						
Investment Required (IR)	**175865506.24**		**24315317.82**						
Net cashflow	-175865506.24		-27332501.89		19456880.18			126241144.47	
Net cashflow (after tax @ 33%)	-175865506.24		-27332501.89		13036109.72			84581566.79	
Cumulative net cashflow	**-175865506.24**		**-203198008.13**		**-190161898.41**			**729342578.78**	
Net present value (NPV)	**-175865506.24**		**-24791384.93**		**11261081.72**			**31877902.97**	

Note: The production of ZSM-5 per year was assumed to be (1 = 0%, 2 = 50%, 3 = 75%, 4 = 80%, 5 = 95%, 6-20 = 100%), units sold for both ZTHT-3h and SOD (1 = 0, 2-4 = 95%, 5-20 = 100%). The selling price and production costs were subjected to a year-on-year inflation rate of 5.9%. The inflation rate was assumed to be constant for the lifetime of the project.

.

Table 6.7 shows the net cashflow for the production of ZSM-5 and sodalite zeolite over a period of 20 years. The manufacturing capacity was based on the production capacity of ZTHT-3h as the main product. Conversely, the capacity of SOD was calculated based on the yield ratio of SOD and ZTHT-3h as demonstrated by Equation 6.8.

$$PC_{SOD} = \frac{Y_{SOD}}{Y_{ZSM-5}} * PC_{ZSM-5} \ldots\ldots\ldots\ldots\ldots\ldots\ldots Equation\ 6.8$$

Where Y_{SOD} = yield of sodalite zeolite, Y_{ZSM-5} = yield of ZTHT-3h, PC_{ZSM-5} = production capacity of ZTHT-3h and PC_{SOD} = production capacity of SOD. As shown in Table 6.7, no production took place in the first 12 months of operation. The 12-month leeway was given to allow for any fabrication and plant additions required to accommodate the capacity of 5000 kg per year of ZSM-5 zeolite. For this, a total investment of R200,180,824.06 was injected in the project. During the second year, the plant was allowed to operate at 50% capacity, contributing approximately R42 800 000 in total revenues. The plant capacity was increased to 75, 80 and 95% in the third, fourth and fifth year respectively, reaching full capacity from the sixth year. As can be observed from Table 6.7, even though sodalite zeolite was not the main target product for this process, it contributed approximately 60% to the total revenues. This result shows that the production of sodalite zeolite from CFA using the proposed synthesis route is more profitable than ZTHT-3h zeolite. This is not surprising, given the low yield of ZTHT-3h in comparison to that of sodalite. Although the yield of ZTHT-3h was lower, the uptake of this product in the market will be faster, given its vast application in the catalytic industry. Therefore, combining the two products in a single process would be a great benefit on the process and can be used to attract future investment. The net present value was calculated using Equation 6.9.

$$NPV = \frac{NCF}{(1+r)^n} \ldots\ldots\ldots\ldots\ldots\ldots\ldots\ldots\ldots\ldots\ldots\ldots\ldots\ldots Equation\ 6.9$$

Where NCF = net cashflow, r = interest rate and n = the number of years. The cumulative net cashflow at the end of the project life is R729,342,578.78, with an NPV of R297,306,058.61
Presented in Figure 6.4 is the cashflow curve for the manufacture of CFA-based ZTHT-3h and sodalite zeolite.

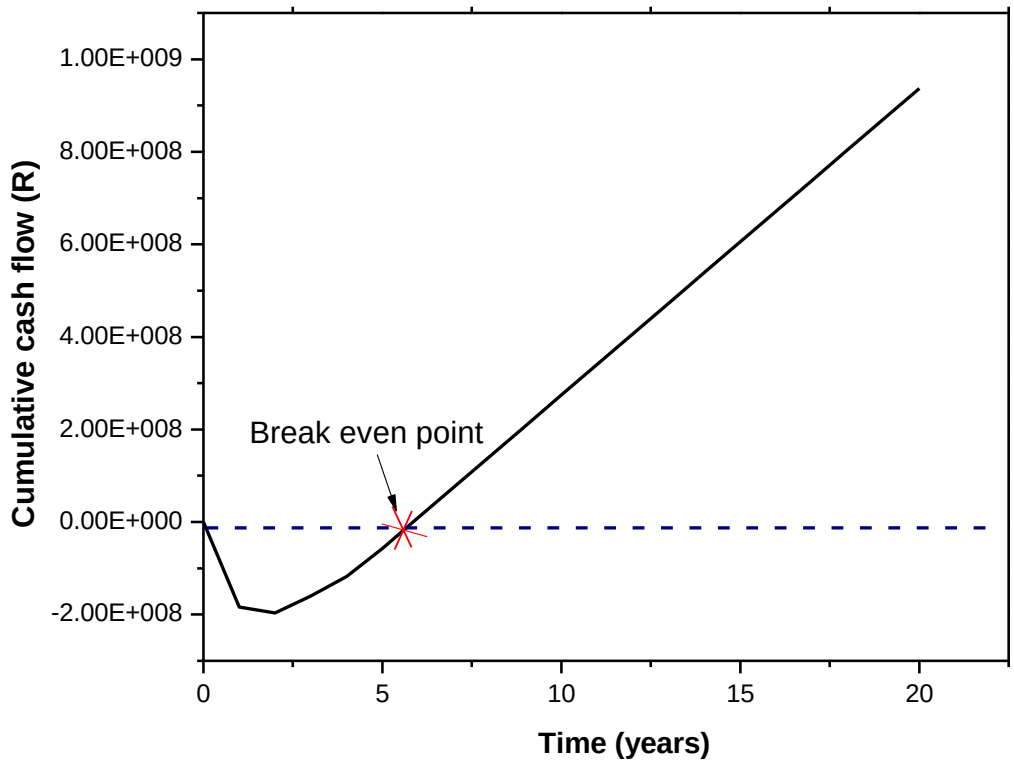

Figure 6.4: Cashflow curve for the manufacture of CFA-based ZTHT-3h zeolite and sodalite zeolite

The cashflow curve, as presented in Figure 6.4, shows that the breakeven point for this project is five years and one month. The breakeven point represents the time it would take to recover the initial investment (R200 180 824.06) made on the project. This result shows that the process was able to produce greater profitability, achieving an NPV of R297,306,058.61 for a period of 20 years and a shorter payback period of 5.1 years. Further to this, the project's profitability index, rate of return and the discounted cashflow rate of return (DCFRR) were calculated using Equations 6.10, 6.11 and 6.12 respectively.

$$Profitability\ index = \frac{NPV}{Initial\ investment} \dots\dots\dots\dots\dots\dots\dots\dots\dots\dots\dots 6.10$$

$$ROR = \frac{Cumulative\ net\ cash\ flow\ at\ end\ of\ project}{Life\ of\ project * Original\ investment}\ x\ 100\% \dots\dots\dots\dots\dots\dots\dots\dots 6.11$$

$$\sum_{n=1}^{n=t} \frac{NFW}{(1+r)^n} = 0 \dots\dots\dots\dots\dots\dots\dots\dots\dots Equation\ 6.12$$

.

Where ROR = rate of return, r = discounted cashflow rate of return and t = represents the life of the project. Based on the cost analysis assumptions made, the investment performance metric for the project is shown in Table 6.8.

Table 6.8: Investment performance metric

Profitability index	Rate of return	Discounted cash flow rate of return
1.49	18.22%	15%

The profitability index is a significant indicator in assessing the economic and financial viability of a project (Gurau 2012). A project is deemed financially viable when its profitability index is > 1. However, if the profitability index is < 1 then the project is not profitable, and it is not worth investing in such a project (Brigham and Houston 2021). The rate of return on capital invested is also an important indicator for monitoring the economic viability of a project (Feenstra and Wang 2000), which indicates a gain or loss of a project over a set period of time. In the same vein, a positive rate of return signifies project gains, whereas a negative value signifies project loss on investment. The discounted cashflow rate of return relates to the percentage rate for which, when used to discount the cashflows on the investment, it produces an NPV of zero (Haro et al. 2013). As shown in Table 6.8, the proposed CFA-based ZSM-5 synthesis route is profitable with a profitability index of 1.49, yielding a rate of return of approximately 18% and a discounted rate of return of 15%. This result shows that this project has potential and can be considered for a large-scale production of ZSM-5 and sodalite zeolite from CFA.

6.5 Sensitivity analysis

Sensitivity analysis is a quantitative risk analysis process performed to assess the impact of one variable on the net present value of the project. In this study, a sensitivity analysis on all input materials (NaOH, CFA, H_2SO_4, water and TPABr), outputs (ZSM-5 and SOD) and impact of tax on the total profits generated over the period of 20 years were investigated. Table 6.9 shows the upper and lower bounds of the variables used for the sensitivity analysis. The upper and lower bounds for each variable were based on ± 20% of the base prices.

Table 6.9: Model variables used for the sensitivity analysis

.

Variable	Units	Lower bound	base case	Upper bound
ZSM-5	R/kg	5807.90	7259.88	8711.86
SOD	R/kg	440.00	550.00	660.00
CFA	R/kg	2223.53	2779.41	3335.30
NaOH	R/kg	65866.88	82333.60	98800.32
Water	R/kg	7.61	9.51	11.42
TPABr	R/kg	5424.75	6780.94	8137.13
H_2SO_4	R/kg	16090.02	20112.53	24135.04
Tax	%	24.40	33.00	39.60

The effect of varying each of the model variables on the net present value is illustrated by Figure 6.5.

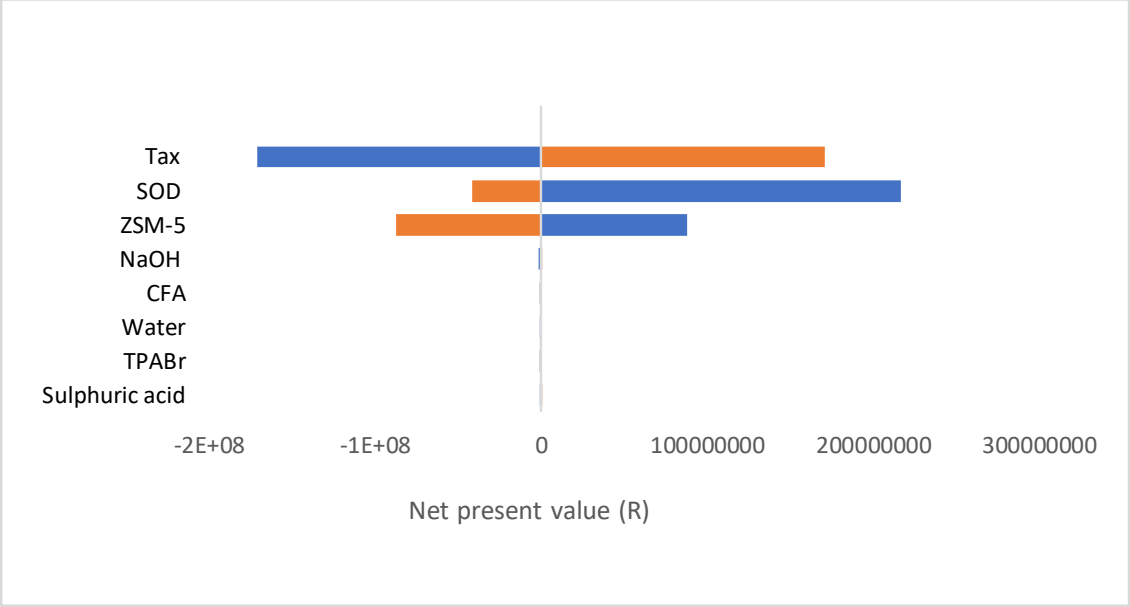

Figure 6.5: Sensitivity analysis of model variables on the net present value

As evident in Figure 6.5, lowering the interest rate by 20% had a significant impact on the NPV of the project, yielding an NPV of R 535,151,167.20 over a period of 20 years. This is expected, as a tax relief on the project would yield greater economic benefits. This indicates a ratio increase of 1.80 from the base case NPV achieved. Similarly, an increase of 20% on the tax rate yielded a

.

lower NPV of R192,712,126.20. This shows that a slight change in the tax rate will have a huge impact on the net profits reaped. The variation on ZSM-5 and SOD prices also had a great impact on the NPV. These results are similar to those reported by Hong et al. (2017). It is worth noticing that the increase in SOD price by 20% yielded a substantial NPV in comparison to ZSM-5 and other variables. Again, this shows economic dominating power of SOD zeolite as opposed to ZSM-5 zeolite in this project.

In addition, price change on the raw materials (NaOH, CFA, water, TPABr and sulphuric acid) showed no noticeable change on the NPV achieved at the end of the 20-year period, making the process a worthwhile investment venture. It is important to note that, depending on the demand for the final products (ZSM-5 and SOD) in the respective markets, the product prices might change substantially from the initial prices considered in this study. Thus, a further sensitivity analysis study was conducted to investigate the impact of product price change on the NPV beyond the 20% benchmark. The impact of ZSM-5 and SOD prices in the range of R4,259.88 – R9,259.88 and R250 – R750 per kilogram respectively on the NPV were therefore investigated.

The valuation of the net present value, profitability index and the payback period with respect to the change in price of ZSM-5 and SOD zeolite are presented in Figure 6.6 and 6.7 respectively.

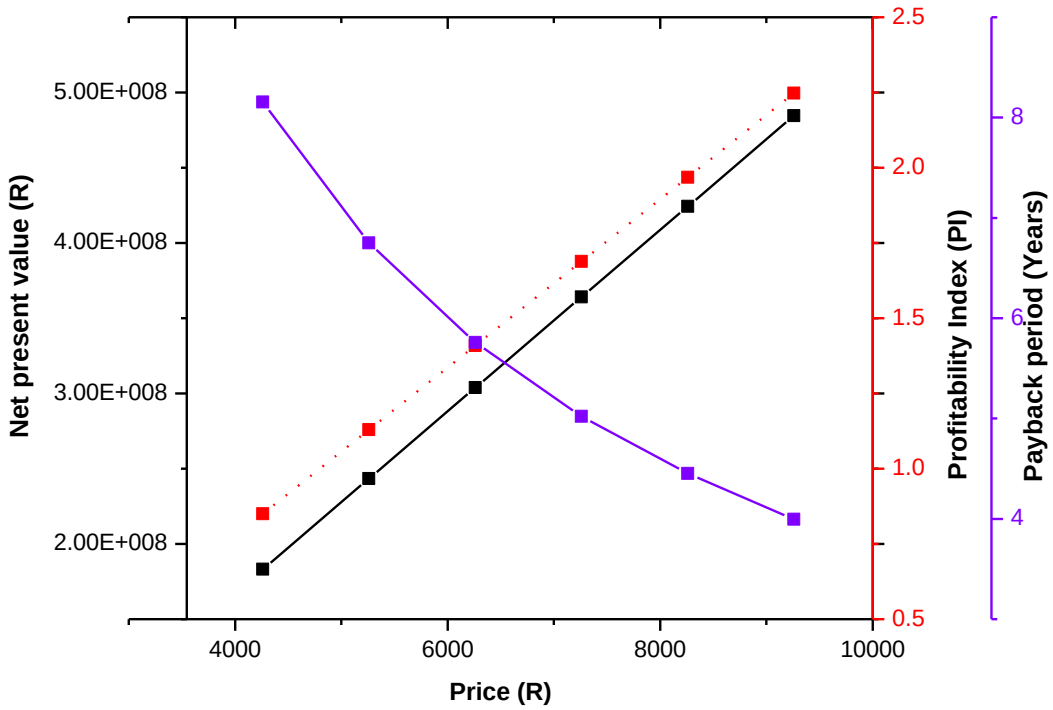

Figure 6.6: Sensitivity analysis of profitability for ZSM-5 zeolite

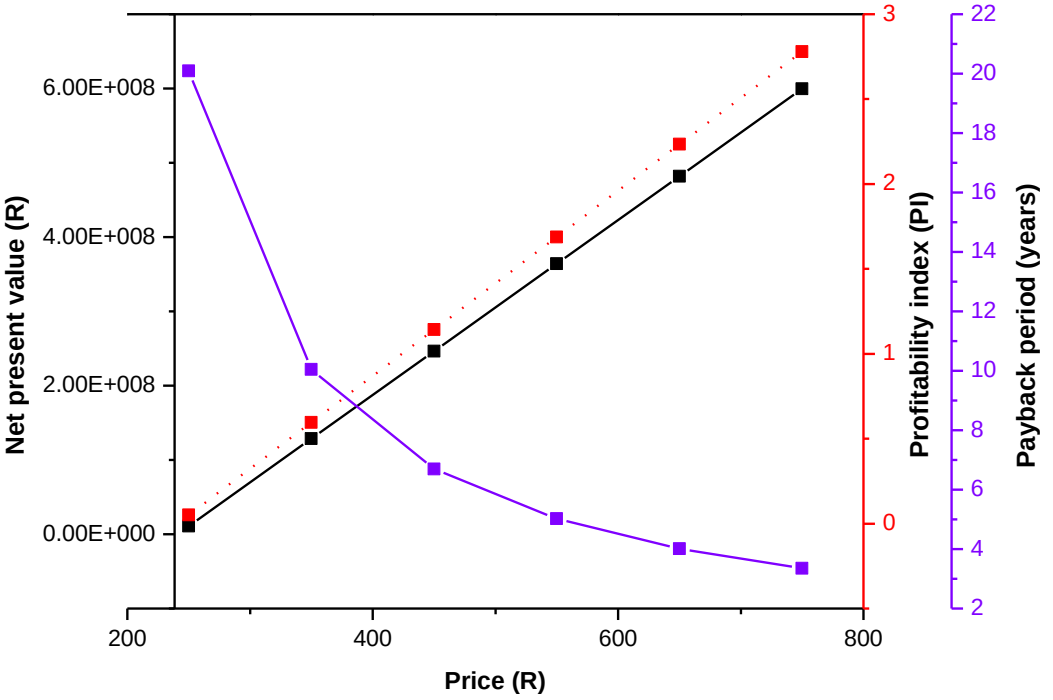

Figure 6.7: Sensitivity analysis of profitability for sodalite zeolite

.

It can be seen from Figure 6.6 that at a minimum price of R4,259.88 (ZSM-5 zeolite) the project yielded an NPV of approximately R183,200,000.00, with a profitability index of 0.85 and a payback period of 8 years 2 month. Furthermore, it was notable that increasing the selling price to R9,259.88 reduced the payback period to 4 years, which yielded a profitability index of 2.25. Observing the trend of Figure 6.6, it can be seen that below a product price of R4,259.88, the process might not be profitable, as the profitability index will be less than 1, rendering the process not viable.

Similarly, reducing the price of SOD to a minimum of R250, resulted in an NPV of approximately zero and a payback period of 20 years, as shown in Figure 6.7. This result indicates that a price range below the minimum price could result in a negative NPV, therefore deeming the process not economically viable. An in-depth market analysis on the product price is required in order to achieve a more realistic product price for both ZSM-5 and sodalite zeolite for this process.

.

6.6 Chapter summary

An economic analysis for the production of 5,000 kg of ZSM-5 per year was performed based on the optimum hydrothermal synthesis conditions obtained in Chapter 5. The actual overall mass balance results showed a total of 82.35% of the feedstock, resulting in product loss of approximately 17.65%. The results of the cost estimation revealed that the process was economically feasible, producing an NPV of R297,306,058.61 and a payback period of approximately 5 years over a period of 20 years. Further to this, a sensitivity analysis study showed that the tax rate, price of ZSM-5 and sodalite zeolite were the most sensitive variable parameters on the NPV. The cost of raw materials such as NaOH, CFA. sulphuric and TPABr, with price variation of ± 20%, did not influence the NPV making the process a worthwhile investment. In addition, the results for the sensitivity study on profitability for ZSM-5 and sodalite zeolite showed that product prices below the minimum of R4,259.88 (ZSM-5 – Figure 6) and R250 (SOD – Figure 6.7) would have a negative impact on the NPV, therefore resulting in a non-viable process. Therefore, based on the assumptions made, for the process to be profitable, the minimum market price for the synthesised ZSM-5 and SOD should be R4 259.88 and R250 respectively.

.

Chapter 7
Conclusion and recommendations

7.1 Synopsis

This chapter will conclude the study by summarising the main research findings in relation to the research aims and questions and outline the novelty contribution in the field. It will also review the limitations of the study and propose opportunities for future study.

7.2 Research main findings

The synthesis of high-silica zeolite ZSM-5 from CFA-derived silica extracts without the addition of oxalic acid or alumino silicate sources (generally used to adjust the Si/Al ratio of the feedstock) was achieved in this study. The solid residue, generated during the extraction of silica using the alkaline leaching process was converted to a low-cost high yield sodalite zeolite. This study showed for the first time that the liquid waste generated during the treatment of silica extract with water can be recycled into the process without compromising the quality of the synthesised ZSM-5 zeolite products. Furthermore, the performed technology economic analysis showed that the synthesis of ZSM-5 and sodalite zeolite from CFA using alkaline leaching process is economically viable and can be produced at a larger scale of 5000 kg of ZSM-5 per year. The total conversion of CFA into ZSM-5 and sodalite zeolite provides a zero-solid waste process for the valorisation of CFA into valuable products. This is a significant advancement in the synthesis of zeolites as this process could allow for large scale processing of CFA, thereby addressing the environmental concerns associated with its disposal into the environment.

7.2.1 Alkaline extraction of silica and treatment

It has been shown in this study that high-silica fly ash extract (UFSE) can be obtained as follows: (i) removal of magnetic fraction (MF) by way of magnetic separation process (in order to enhance the dissolution of silica from iron-free coal fly ash (IFCFA) (ii) alkaline extraction of silica (UFSE) by mixing IFCFA with 8 M NaOH solution in a solid-to-liquid ratio of 5:1 under reflux conditions at 150˚C for 24 h and (iii) treatment of the silica extract (UFSE) with oxalic acid or water under reflux at 80˚C for 6 h (to remove access Na content carried over from the leaching process). This study showed that the silica extract treated with water was comparable to those treated with oxalic acid. The successful treatment of the silica extract with water showed for the first time that the oxalic acid treatment step (recommended in literature) is not a requirement and can be replaced with a single water treatment step. Moreover, the liquid waste generated during the treatment process

.

can be recycled 4 times into the process without compromising the quality of the treated silica extracts (TFSRs). The treated silica extracts containing a Si/Al ratio, ranging from 98 to 160, were used as feedstock in the synthesis of high-silica ZSM-5 zeolites. The preparation of CFA-based high-silica extracts (suitable for use as feedstock in the synthesis of pure phase ZSM-5 zeolite) using this method presents an opportunity to eliminate the use of chemicals such as oxalic acid or alumino-silica sources during the Si/Al ratio adjustment step, thereby reducing the cost of producing CFA-based silica extracts compared to alternative extraction methods reported in literature to date.

7.2.2 Optimisation of ZSM-5 zeolite synthesis from CFA-based silica extract

The synthesis of ZSM-5 zeolite was carried out under static hydrothermal conditions (170˚C at 72 h) using the oxalic acid and water-treated silica extracts as feedstocks. The ZSM-5 zeolite synthesised from the water treated silica extract was pure phase, with relative high crystallinity (84%) and smaller crystal size (3.60 x 1.59 μm), which was comparable to those synthesised with oxalic acid treated extracts. The formulated molar composition of the water-treated silica extract (1 Si: 0.003 Al :0.612 Na: 0.190 TPABr: 95.766 H_2O) was thereafter set as a baseline for the optimisation studies. The effect of NaOH, TPABr, water content, hydrothermal temperature and time on the synthesis of ZSM-5 zeolite were investigated in this study. The variation in concentration of NaOH had a significant effect on the morphology, crystallinity and crystal size of the zeolite products. At relatively low Na content of 0.10 g and 0.05 g, the ZSM-5 products exhibited an ellipsoidal type morphology of large crystals (10.20 x 4.21 μm and 6.20 x 0.77 μm) and yielded a higher crystallinity of 62% and 67% respectively. Upon an increase of the Na content to 0.5 g, cuboidal type morphology of ZSM-5 zeolite of smaller crystals (1.50 x 0.73 μm) and a relative crystallinity of 48% were observed. This demonstrated that Na content can be used to alter the morphology and crystal size of the synthesised ZSM-5 zeolites. Similarly, reduced water content from 50 to 20 mL led to ZSM-5 zeolite made up of smaller crystals (2.20 x 1.20 μm to 1.90 x 1.05 μm). No major observations can be deduced on the effect of TPABr on the synthesis of ZSM-5 zeolite, except that reduced TPABr content of 0.3, 0.15 and 0.075 resulted in a zeolite product with traces of amorphous-like particles on the surface of the crystals, which suggested incomplete conversion of the amorphous material into ZSM-5 zeolite. The optimum molar formulation (1Si: 0.003Al: 0.529Na: 0.152TPABr: 95.766H_2O -ZTP-1.2), resulting from the variation of NaOH, TPABr and water content was further used to investigate the effect of hydrothermal synthesis time (0, 3, 6, 24, 48 and 72 h) and temperature (40, 70, 100, 130 and 160°C) on the synthesis of ZSM-5. This study showed for the first time that ZSM-5 zeolite can be

.

crystallised within 3 h, at a hydrothermal temperature of 160°C. The study further showed that a decrease in the hydrothermal synthesis time from 72 to 3 h facilitated the formation of ZSM-5 with relatively larger crystals (2.50 μm) (ZTHT-3h) compared to those obtained at 72 h (1.90 μm) (ZTHT-72h). In contrast, no ZSM-5 zeolites were formed at lower temperature of 40, 70 and 100°C. The result suggested that the shorter hydrothermal synthesis time (3 h) and high temperature (160°C) enhanced a fast nucleation rate and promoted crystallinity and crystal growth of the ZSM-5 zeolite. Furthermore, pure phase ZSM-5 zeolites were synthesised from the silica extracts treated with recycled liquid waste (TFSR1, TFSR2, TFSR3 and TFSR4). All the zeolite products exhibited intergrowth and twinned hexagonal crystals with crystal size ranging from 1.54 to 2.77 μm. The successful synthesis of a pure phase ZSM-5 zeolite from all the liquid waste treated silica extracts presents an opportunity to recycle the liquid waste beyond the 4 cycles until all the Si and Al in the liquid waste can be recovered.

7.2.3 Process technology economic (TEA) analysis

A cost economic analysis was performed in this study to evaluate the viability of the process. The optimum synthesis conditions for ZTHT-3h (160°C for 3 h) were used as the basis for the TEA. The mass balance showed that 17.65% of the total input materials (including solids and liquids) was lost during different process stages (e.g., drying, filtration and etc.). The total material cost to produce 1 kg of ZSM-5 per year was over R100 000, however the sensitivity analysis showed that price variation of ± 20% on the raw materials (NaOH, CFA, water, TPABr and sulphuric acid) showed no significant change on the net present value. Based on the assumptions made, the cost estimation showed that the process was economically feasible at 5000 kg of ZSM-5 a year and obtained a net present value of R297,306,058.61 and a payback period of approximately 5 years over a period of 20 years, with sodalite zeolite contributing approximately 60% to the total revenues. This was expected, given the yield of sodalite (86.42%) compared to that of ZSM-5 zeolite (4.58%).

7.3 Recommendations for future studies

The research aims, questions, and objectives have been successfully addressed in this study. However, there have been some intriguing developments, although not within the scope of this study, which require further investigation. The following is therefore recommended for future research.

.

- While it has been shown in this study that the liquid waste (resulting from the treatment of the silica extract with water – stream 20, Figure 6.1) can be recycled, it has also been shown that the supernatant from the hydrothermal synthesis (stream 27, Figure 6.1) can be reused in the synthesis process (Du Plessis 2014). Further studies need to be conducted to investigate the threshold beyond which recycling of the liquid waste (treatment and hydrothermal step) might be detrimental to the purity of the zeolite products, due to accumulation of Na and other elements which might interfere with the synthesis of the final product.

- This study has shown for the first time that a product yield of up to 120 g/kg CFA can be synthesised from CFA silica extract without treatment with oxalic acid or addition of silicate or aluminate sources. However, it is important to investigate the effect of agitation during the hydrothermal synthesis. Mainganye et al. (2013) showed that agitation during the zeolite aging step increases the dissolution of the feedstock, thereby reducing the synthesis time and improve the yield of the final product. Considering scale-up, stirring during the hydrothermal synthesis will be a necessity in order to facilitate even heat transfer and avoid any variabilities in the synthesis mixture, with the aim to produce uniform zeolite crystal size.

- Although this study has shown for the first time that the synthesis of ZSM-5 from CFA-derived silica extracts using alkaline leaching process is economically viable, there is still a need to investigate treatment of the magnetic fraction (recovered as a by-product in the process) in order to include it as a commercial third product stream for the synthesis process

- Studies on the application of ZSM-5, sodalite zeolite and the magnetic fraction is required to determine the catalytic activity of these materials compared to commercially available products.

- It should be noted that the technology economic analysis conducted in this study was based on assumptions made for early-stage research. It is therefore necessary to conduct a more detailed cost estimation for this process once the above recommendations have been addressed and the process can be considered at its advanced stages.

.

APPENDICES

Annexure A.1: Elemental composition for H-Z-H_2O, H-ZN-0.3, H-ZTP-1.2, H-ZTHH-20mL and H-ZTHT-3h.

	ICP (Wt%), n=3				
Elements	**H-Z-H_2O**	**H-ZN-0.3**	**H-ZTP-1.2**	**H-ZTHH-20 mL**	**H-ZTHT-3h**
Si	95.93 ± 2.09	94.56 ± 2.80	97.17 ± 0.78	95.38 ± 3.01	96.12 ± 1.96
Al	0.52 ± 0.00	0.40 ± 0.01	0.61 ± 0.01	0.49 ± 0.01	0.47 ± 0.01
Ca	0.61 ± 0.03	0.72 ± 0.01	0.41 ± 0.01	0.66 ± 0.01	0.47 ± 0.00
Fe	0.06 ± 0.01	0.70 ± 0.02	0.06 ± 0.00	0.18 ± 0.17	0.05 ± 0.00
Ti	0.06 ± 0.00	0.06 ± 0.00	0.10 ± 0.00	0.06 ± 0.00	0.06 ± 0.00
Mg	0.11± 0.02	0.13 ± 0.00	0.05 ± 0.00	0.11 ± 0.00	0.09 ± 0.00
P	0.00 ± 0.00	0.00 ± 0.00	0.00 ± 0.00	0.00 ± 0.00	0.00 ± 0.00
K	0.05 ± 0.00	0.05 ± 0.01	0.00 ± 0.00	0.04 ± 0.00	0.03 ± 0.00
Na	2.66 ± 0.15	3.20 ± 0.05	1.59 ± 0.14	3.08 ± 0.03	2.72 ± 0.24
Mn	0.00 ± 0.00	0.02 ± 0.00	0.01 ± 0.00	0.00 ± 0.00	0.00 ± 0.00
Cr	0.01 ± 0.00	0.16 ± 0.00	0.00 ± 0.00	0.01 ± 0.00	0.01 ± 0.00

Annexure A.2: Elemental composition for ZU, ZTHR1, ZTHR2, ZTHR3 and ZTHR4

	ICP (Wt%), n=3				
Elements	**ZU**	**ZTHR1**	**ZTHR2**	**ZTHR3**	**ZTHR4**
Si	70.99 ± 2.54	88.82 ± 2.21	90.07 ± 3.02	90.84 ± 2.94	89.01 ± 1.49
Al	12.72 ± 0.93	3.77 ± 0.49	2.83 ± 0.27	2.42 ± 0.14	4.10 ± 0.52
Ca	2.75 ± 0.12	0.85 ± 0.48	0.71 ± 0.11	0.57 ± 0.15	0.76 ± 0.16
Fe	1.89 ± 0.14	0.23 ± 0.07	0.47 ± 0.10	0.38 ± 0.11	0.27 ± 0.06
Ti	1.76 ± 0.02	0.41 ± 0.05	0.31 ± 0.03	0.31 ± 0.05	0.42 ± 0.02
Mg	0.36± 0.01	0.17 ± 0.01	0.13 ± 0.02	0.13 ± 0.02	0.14 ± 0.00
P	0.05 ± 0.00	0.02 ± 0.01	0.02 ± 0.01	0.02 ± 0.01	0.03 ± 0.00
K	1.92 ± 0.21	0.50 ± 0.07	0.49 ± 0.11	0.52 ± 0.16	0.71 ± 0.17
Na	6.99 ± 0.21	5.16 ± 0.46	4.85 ± 0.23	4.70 ± 0.08	4.46 ± 0.05
Mn	0.67 ± 0.00	0.01 ± 0.00	0.02 ± 0.00	0.02 ± 0.00	0.03 ± 0.00
Cr	0.39 ± 0.00	0.05 ± 0.01	0.09 ± 0.01	0.08 ± 0.01	0.09 ± 0.01
Si/Al	5.58	23.56	31.83	37.54	21.71

.

REFERENCES

Aboudi, K., L. A. Fernández-Güelfo, C. J. Álvarez-Gallego & L. I. Romero-García, 2021. Biogas, biohydrogen, and polyhydroxyalkanoates production from organic waste in the circular economy context Sustainable Biofuels. 305-343.

Abrishamkar, M., S. N. Azizi & H. Kazemian, 2010. Ultrasonic-Assistance and Aging Time Effects on the Zeolitation Process of BZSM-5 Zeolite. Wiley Online Library.

Ahmaruzzaman, M., 2010. A review on the utilization of fly ash. *Progress In Energy and Combustion Science* 36(3):327-363.

Aldahri, T., J. Behin, H. Kazemian & S. Rohani, 2016. Synthesis of zeolite Na-P from coal fly ash by thermo-sonochemical treatment. *Fuel* 182:494-501.

Ali, M., B. Brisdon & W. Thomas, 2003. Synthesis, characterization and catalytic activity of ZSM-5 zeolites having variable silicon-to-aluminum ratios. *Applied Catalysis A: General* 252(1):149-162.

Alipour, S. M., R. Halladj & S. Askari, 2014. Effects of the different synthetic parameters on the crystallinity and crystal size of nanosized ZSM-5 zeolite. *Reviews in Chemical Engineering* 30(3):289-322.

Ameh, A. E., O. O. Fatoba, N. M. Musyoka, B. Louis & L. F. Petrik, 2020. Transformation of fly ash based nanosilica extract to BEA zeolite and its durability in hot liquid. *Microporous and Mesoporous Materials* 305:110332.

Ameh, A. E., N. M. Musyoka, O. Oyekola, B. Louis & L. F. Petrik, 2021. Acylation of Anisole With Benzoyl Chloride Over Rapidly Synthesized Fly Ash–Based HBEA Zeolite. *Frontiers in Chemistry* 9:683125.

Ameh, E. A., 2019. Sustainable synthesis of BEA zeolite from fly ash-based amorphous silica. Thesis (PhD), University of the Western Cape.

Andaç, Ö., M. Tatlıer, A. Sirkecioğlu, I. Ece & A. Erdem-Şenatalar, 2005. Effects of ultrasound on zeolite A synthesis. *Microporous and Mesoporous Materials* 79(1-3):225-233.

Ansari, M., A. Aroujalian, A. Raisi, B. Dabir & M. Fathizadeh, 2014. Preparation and characterization of nano-NaX zeolite by microwave assisted hydrothermal method. *Advanced Powder Technology* 25(2):722-727.

Anuwattana, R., K. J. Balkus Jr, S. Asavapisit & P. Khummongkol, 2008. Conventional and microwave hydrothermal synthesis of zeolite ZSM-5 from the cupola slag. *Microporous and Mesoporous Materials* 111(1-3):260-266.

Arafat, A., J. Jansen, A. Ebaid & H. Van Bekkum, 1993. Microwave preparation of zeolite Y and ZSM-5. *Zeolites* 13(3):162-165.

Armaroli, T., L. Simon, M. Digne, T. Montanari, M. Bevilacqua, V. Valtchev, J. Patarin & G. Busca, 2006. Effects of crystal size and Si/Al ratio on the surface properties of H-ZSM-5 zeolites. *Applied Catalysis A: General* 306:78-84.

Aronne, A., S. Esposito & P. Pernice, 1997. FTIR and DTA study of lanthanum aluminosilicate glasses. *Materials Chemistry and Physics* 51(2):163-168.

Askari, S., S. M. Alipour, R. Halladj & M. H. D. A. Farahani, 2013. Effects of ultrasound on the synthesis of zeolites: a review. *Journal of Porous Materials* 20(1):285-302.

BABIC, V., 2021. Increasing the porosity of zeolites. PhD Thesis, Université de Poitiers.

Baerlocher, C., L. B. McCusker & D. H. Olson, 2007. Atlas of zeolite framework types. Structure Commission on the International Zeolite Association.

Bai, G., Y. Qiao, B. Shen & S. Chen, 2011. Thermal decomposition of coal fly ash by concentrated sulfuric acid and alumina extraction process based on it. *Fuel Processing Technology* 92(6):1213-1219.

Barrett, P., Q. Huo & N. Stephenson, 2007. Recent advances in low silica zeolite synthesis. *Studies in Surface Science and Catalysis* 170:250-257.

Bass, J. L. & G. L. Turner, 1997. Anion distributions in sodium silicate solutions. Characterization by 29Si NMR and infrared spectroscopies, and vapor phase osmometry. *The Journal of Physical Chemistry B* 101(50):10638-10644.

Bayati, B., A. Babaluo & R. Karimi, 2008. Hydrothermal synthesis of nanostructure NaA zeolite: The effect of synthesis parameters on zeolite seed size and crystallinity. *Journal of the European Ceramic Society* 28(14):2653-2657.
Behin, J., S. S. Bukhari, V. Dehnavi, H. Kazemian & S. Rohani, 2014. Using coal fly ash and wastewater for microwave synthesis of LTA zeolite. *Chemical Engineering & Technology* 37(9):1532-1540.
Belviso, C., 2018. State-of-the-art applications of fly ash from coal and biomass: A focus on zeolite synthesis processes and issues. *Progress in Energy and Combustion Science* 65:109-135.
Belviso, C., F. Cavalcante & S. Fiore, 2013. Ultrasonic waves induce rapid zeolite synthesis in a seawater solution. *Ultrasonics Sonochemistry* 20(1):32-36.
Belviso, C., F. Cavalcante, A. Lettino & S. Fiore, 2011. Effects of ultrasonic treatment on zeolite synthesized from coal fly ash. *Ultrasonics Sonochemistry* 18(2):661-668.
Berkgaut, V. & A. Singer, 1996. High capacity cation exchanger by hydrothermal zeolitization of coal fly ash. *Applied Clay Science* 10(5):369-378.
Bhanarkar, A., A. Gavane, D. Tajne, S. Tamhane & P. Nema, 2008. Composition and size distribution of particules emissions from a coal-fired power plant in India. *Fuel* 87(10-11):2095-2101.
Bhandari, R. B., A. Pathak & V. K. Jha, 2012. A Laboratory Scale Synthesis of Geopolymer from Locally Available Coal Fly Ash from Brick Industry. *Journal of Nepal Chemical Society* 29:18-23.
Bindhu, J. & S. Sugunan, 1998. A comparative study of medium and large pore zeolites in alkylation reactions. Cochin University of Science and Technology.
Bjørgen, M., S. Svelle, F. Joensen, J. Nerlov, S. Kolboe, F. Bonino, L. Palumbo, S. Bordiga & U. Olsbye, 2007. Conversion of methanol to hydrocarbons over zeolite H-ZSM-5: On the origin of the olefinic species. *Journal of Catalysis* 249(2):195-207.
Bleken, F. L., S. Chavan, U. Olsbye, M. Boltz, F. Ocampo & B. Louis, 2012. Conversion of methanol into light olefins over ZSM-5 zeolite: Strategy to enhance propene selectivity. *Applied Catalysis A: General* 447:178-185.
Blissett, R. & N. Rowson, 2012. A review of the multi-component utilisation of coal fly ash. *Fuel* 97:1-23.
Bogdanov, B., D. Georgiev, K. Angelova & Y. Hristov, Synthetic zeolites and their industrial and environmental applications. In: International Science Conference, Bulgaria, 2009.
Bohra, S., D. Kundu & M. K. Naskar, 2014. One-pot synthesis of NaA and NaP zeolite powders using agro-waste material and other low cost organic-free precursors. *Ceramics International* 40(1):1229-1234.
Booker, N., E. Cooney & A. Priestley, 1996. Ammonia removal from sewage using natural Australian zeolite. *Water Science and Technology* 34(9):17-24.
Brigham, E. F. & J. F. Houston, 2021. Fundamentals of financial management, 11 Addition edn. Cengage Learning.
Bukhari, S. S., S. Rohani & H. Kazemian, 2016. Effect of ultrasound energy on the zeolitization of chemical extracts from fused coal fly ash. *Ultrasonics Sonochemistry* 28:47-53.
Burt, E., P. Orris & S. Buchanan, 2013. Scientific evidence of health effects from coal use in energy generation. University of Illinois and Health Care Without Harm, Chicago and Washington: .
Canellas, J., A. Soares & B. Jefferson, 2019. Removing Ammonia From Wastewater Using Natural and Synthetic Zeolites: A Batch Experiment. *Chemical Engineering and Industrial Chemistry* doi:https://doi.org/10.26434/chemrxiv.9831542.v1.
Carlson, C. L. & D. C. Adriano, 1993. Environmental impacts of coal combustion residues. *Journal of Environmental Quality* 22(2):227-247.
Carrott, P. & K. Sing, 1988. Assessment of microporosity Studies in Surface Science and Catalysis. vol 39, 77-87.
Cejka, J., H. van Bekkum, A. Corma & F. Schueth, 2007. Introduction to zeolite molecular sieves, 3rd Addition edn. Studies in Surface Science and Catalysis.
Chandrasekhar, S. & P. Pramada, 2008. Microwave assisted synthesis of zeolite A from metakaolin. *Microporous and Mesoporous Materials* 108(1-3):152-161.
Chang, H.-L. & W.-H. Shih, 2000. Synthesis of zeolites A and X from fly ashes and their ion-exchange behavior with cobalt ions. *Industrial & Engineering Chemistry Research* 39(11):4185-4191.
Chareonpanich, M., O. Jullaphan & C. Tang, 2011. Bench-scale synthesis of zeolite A from subbituminous coal ashes with high crystalline silica content. *Journal of Cleaner Production* 19(1):58-63.

Chareonpanich, M., T. Namto, P. Kongkachuichay & J. Limtrakul, 2004. Synthesis of ZSM-5 zeolite from lignite fly ash and rice husk ash. *Fuel Processing Technology* 85(15):1623-1634.
Chaves, T. F., H. O. Pastore, P. Hammer & D. Cardoso, 2015. As-synthesized TEA-BEA zeolite: Effect of Si/Al ratio on the Knoevenagel condensation. *Microporous and Mesoporous Materials* 202:198-207.
Chen, H., X. Shi, J. Liu, K. Jie, Z. Zhang, X. Hu, Y. Zhu, X. Lu, J. Fu & H. Huang, 2018. Controlled synthesis of hierarchical ZSM-5 for catalytic fast pyrolysis of cellulose to aromatics. *Journal of Materials Chemistry A* 6(42):21178-21185.
Chen, Z., J. Wang, Z. Pu, Y. Zhao, D. Jia, H. Chen, T. Wen, B. Hu, A. Alsaedi & T. Hayat, 2017. Synthesis of magnetic Fe3O4/CFA composites for the efficient removal of U (VI) from wastewater. *Chemical Engineering Journal* 320:448-457.
Cheng, Y., R. Liao, J. Li, X. Sun & L. Wang, 2008. Synthesis research of nanosized ZSM-5 zeolites in the absence of organic template. *Journal of materials processing technology* 206(1-3):445-452.
Chester, A. W. & E. G. Derouane, 2009. Zeolite characterization and catalysis, 1 edn. A Tutorial, New York.
Chigondo, M., U. Guyo, M. Shumba, F. Chigondo, B. Nyamunda, M. Moyo & T. Nharingo, 2013. Synthesis and characterisation of zeolites from coal fly ash (CFA). *Engineering Science and Technology* 3(4):714-718.
Christensen, P., L. R. Dysert, J. Bates, D. Burton, R. Creese & J. Hollmann, 2005. Cost Estimate Classification system-as applied in engineering, procurement, and construction for the process industries. *AACE International Recommended Practices*:1-30.
Chudasama, C. D., J. Sebastian & R. V. Jasra, 2005. Pore-size engineering of zeolite A for the size/shape selective molecular separation. *Industrial & Engineering Chemistry Research* 44(6):1780-1786.
Colella, C., 1999. Environmental applications of natural zeolitic materials based on their ion exchange properties Natural microporous materials in environmental technology. Springer, 207-224.
Conner, W. C., G. Tompsett, K.-H. Lee & K. S. Yngvesson, 2004. Microwave synthesis of zeolites: 1. Reactor engineering. *The Journal of Physical Chemistry B* 108(37):13913-13920.
Cornelius, M.-L. U., 2015. The role of aluminium content in the control of the morphology of fly ash based hierarchical zeolite X. Masters Thesis, University of the Western Cape
Cornelius, M.-L. U., 2019. Synthesis and characterisation of high silica zeolites with MOR and MFI framework type from South African coal fly ash. Full Research University of the Western Cape
Coulson, J. & J. F. Richardson, 1999. Chemical Engineering. *Elsevier* 6:35.
Crea, F., A. Nastro, J. Nagy & R. Aiello, 1988. Synthesis of silicalite 1 from systems with different TPABr/SiO2 ratios. *Zeolites* 8(4):262-267.
Cronshaw, I., 2015. World Energy Outlook 2014 projections to 2040: natural gas and coal trade, and the role of China. *Australian Journal of Agricultural and Resource Economics* 59(4):571-585.
Cruciani, G., 2006. Zeolites upon heating: Factors governing their thermal stability and structural changes. *Journal of Physics and Chemistry of Solids* 67(9-10):1973-1994.
Cundy, C. S. & P. A. Cox, 2003. The hydrothermal synthesis of zeolites: history and development from the earliest days to the present time. *Chemical Reviews* 103(3):663-702.
Daniels, W. L., M. Beck & M. Eick, Guidance for the beneficial use of fly ash on coal mines in Virginia (USA). In: In Z Agioutantis & K Komnitsas (Eds), 2nd International conference on advances in mineral resources management and geotechnics, 2006.
Davison, R. L., D. F. Natusch, J. R. Wallace & C. A. Evans Jr, 1974. Trace elements in fly ash. Dependence of concentration on particle size. *Environmental Science & Technology* 8(13):1107-1113.
Derouane, E. G., 1984. Molecular shape-selective catalysis in zeolites-selected topics Studies in Surface Science and Catalysis. vol 19. Elsevier, 1-17.
Dey, K. P., S. Ghosh & M. K. Naskar, 2013. Organic template-free synthesis of ZSM-5 zeolite particles using rice husk ash as silica source. *Ceramics International* 39(2):2153-2157.
Di Renzo, F., 1998. Zeolites as tailor-made catalysts: control of the crystal size. *Catalysis Today* 41(1-3):37-40.
Ding, L., Y. Zheng, Z. Zhang, Z. Ring & J. Chen, 2006. Effect of agitation on the synthesis of zeolite beta and its synthesis mechanism in absence of alkali cations. *Microporous and Mesoporous Materials* 94(1-3):1-8.

Ding, Y.-L., H.-Q. Wang, M. Xiang, P. Yu, R.-Q. Li & Q.-P. Ke, 2020. The effect of Ni-ZSM-5 catalysts on catalytic pyrolysis and hydro-pyrolysis of biomass. *Frontiers in Chemistry* 8:790.

Dorin, R. M., H. Sai & U. Wiesner, 2014. Hierarchically porous materials from block copolymers. *Chemistry of Materials* 26(1):339-347.

Du Plessis, P. W., 2014. Process design for the up-scale zeolite synthesis from South African coal fly ash. Cape Peninsula University of Technology.

Ensminger, D. & L. J. Bond, 2011. Ultrasonics: fundamentals, technologies, and applications. CRC press.

Eskom Holdings, S., 2011. Limited. 2013. *Rustenburg strengthening Project Phase* 2.

Eze, C. P., 2014. Determination of toxic elements, rare earth elements and radionuclides in coal fly ash, products and waste. University of the Western Cape

Fang, Y., X. Su, X. Bai, W. Wu, G. Wang, L. Xiao & A. Yu, 2017. Aromatization over nanosized Ga-containing ZSM-5 zeolites prepared by different methods: Effect of acidity of active Ga species on the catalytic performance. *Journal of Energy Chemistry* 26(4):768-775.

Feenstra, D. W. & H. Wang, 2000. Economic and accounting rates of return. *Research School Systems, Organisation and Management*:5-33.

Feng, R., K. Chen, X. Yan, X. Hu, Y. Zhang & J. Wu, 2019. Synthesis of ZSM-5 zeolite using coal fly ash as an additive for the methanol to propylene (MTP) reaction. *Catalysts* 9(10):788.

Feng, Y. & G. P. Rangaiah, 2011. Evaluating capital cost estimation programs; five capital-cost-estimation programs are compared using a set of case studies. *Chemical Engineering* 118(8):22-30.

Fernández-Jiménez, A. & A. Palomo, 2005. Mid-infrared spectroscopic studies of alkali-activated fly ash structure. *Microporous and Mesoporous Materials* 86(1-3):207-214.

Fisher, G. L., B. A. Prentice, D. Silberman, J. M. Ondov, A. H. Biermann, R. C. Ragaini & A. R. McFarland, 1978. Physical and morphological studies of size-classified coal fly ash. *Environmental Science & Technology* 12(4):447-451.

Fu, T., J. Chang, J. Shao & Z. Li, 2017. Fabrication of a nano-sized ZSM-5 zeolite with intercrystalline mesopores for conversion of methanol to gasoline. *Journal of Energy Chemistry* 26(1):139-146.

Gao, Y., B. Zheng, G. Wu, F. Ma & C. Liu, 2016. Effect of the Si/Al ratio on the performance of hierarchical ZSM-5 zeolites for methanol aromatization. *Rsc Advances* 6(87):83581-83588.

Georgiev, D., B. Bogdanov, K. Angelova, I. Markovska & Y. Hristov, 2009. Synthetic zeolites-structure, classification, current trends in zeolite synthesis. Paper presented at the Internation Science Conference Stara Zagora, Bulgaria.

Gilbert, C., O. S. Ayanda, O. O. Fatoba, G. Madzivire & L. F. Petrik, 2019. A novel method of using iron nanoparticles from coal fly ash or ferric chloride for acid mine drainage remediation. *Mine Water and the Environment* 38(3):617-631.

Gitari, M. W., L. F. Petrik & N. M. Musyoka, 2016. Hydrothermal conversion of south african coal fly ash into pure phase zeolite Na-P1. *Zeolite-Useful Minerals* 2:25-42.

Golbad, S., P. Khoshnoud & N. Abu-Zahra, 2017. Hydrothermal synthesis of hydroxy sodalite from fly ash for the removal of lead ions from water. *International Journal of Environmental Science and Technology* 14(1):135-142.

Goodarzi, F., 2006. Characteristics and composition of fly ash from Canadian coal-fired power plants. *Fuel* 85(10-11):1418-1427.

Gouzinis, A. & M. Tsapatsis, 1998. On the preferred orientation and microstructural manipulation of molecular sieve films prepared by secondary growth. *Chemistry of Materials* 10(9):2497-2504.

Groen, J., L. A. Peffer, J. Moulijn & J. Pérez-Ramırez, 2004. On the introduction of intracrystalline mesoporosity in zeolites upon desilication in alkaline medium. *Microporous and Mesoporous Materials* 69(1-2):29-34.

Gupta, D. K., U. N. Rai, R. D. Tripathi & M. Inouhe, 2002. Impacts of fly-ash on soil and plant responses. *Journal of Plant Research* 115(6):401-409.

Gurau, M. A., 2012. The use of profitability index in economic evaluation of industrial investment projects. *Proceedings in Manufacturing Systems* 7(1):55-58.

Hahn, A., H. Vogel, S. Andó, E. Garzanti, G. Kuhn, H. Lantzsch, J. Schüürman, C. Vogt & M. Zabel, 2018. Using Fourier transform infrared spectroscopy to determine mineral phases in sediments. *Sedimentary Geology* 375:27-35.

Harja, M., S. M. Cimpeanu, M. Dirja & D. Bucur, 2016. Synthesis of Zeolite from Fly Ash and their Use as Soil Amendment *Zeolites-Useful Minerals*. IntechOpen.
Haro, P., P. Ollero, A. V. Perales & A. Gómez-Barea, 2013. Thermochemical biorefinery based on dimethyl ether as intermediate: Technoeconomic assessment. *Applied Energy* 102:950-961.
Hattori, T. & T. Yashima, 1994. Zeolites and Microporous Crystals. Paper presented at the Internation Symposium on Zeolites and Microporous Crystals, Nagoya.
Hölderich, W. & H. Van Bekkum, 1991. Zeolites in organic syntheses Studies in Surface Science and Catalysis. vol 58, 631-726.
Holler, H. & U. Wirsching, 1985. Zeolite formation from fly-ash. *Fortschritte der Mineralogie* 63(1):21-43.
Hong, J. L. X., T. Maneerung, S. N. Koh, S. Kawi & C.-H. Wang, 2017. Conversion of coal fly ash into zeolite materials: synthesis and characterizations, process design, and its cost-benefit analysis. *Industrial & Engineering Chemistry Research* 56(40):11565-11574.
Hu, T., W. Gao, X. Liu, Y. Zhang & C. Meng, 2017. Synthesis of zeolites Na-A and Na-X from tablet compressed and calcinated coal fly ash. *Royal Society Open Science* 4(10):170921.
Huang, S., X. Liu, L. Yu, S. Miao, Z. Liu, S. Zhang, S. Xie & L. Xu, 2014. Preparation of hierarchical mordenite zeolites by sequential steaming-acid leaching-alkaline treatment. *Microporous and Mesoporous Materials* 191:18-26.
Hudec, P., A. Smiešková, Z. Židek, M. Zúbek, P. Schneider, M. Kočiřík & J. Kozánková, 1998. Adsorption properties of ZSM-5 zeolites. *Collection of Czechoslovak Chemical Communications* 63(2):141-154.
Hui, K. & C. Y. H. Chao, 2006. Effects of step-change of synthesis temperature on synthesis of zeolite 4A from coal fly ash. *Microporous and Mesoporous Materials* 88(1-3):145-151.
Hums, E., 2017. Synthesis of phase-pure zeolite sodalite from clear solution extracted from coal fly ash. *J Thermodyn Catal* 8(02):1000187.
Iliopoulou, E. F., S. Stefanidis, K. Kalogiannis, A. Delimitis, A. Lappas & K. Triantafyllidis, 2012. Catalytic upgrading of biomass pyrolysis vapors using transition metal-modified ZSM-5 zeolite. *Applied Catalysis B: Environmental* 127:281-290.
Inada, M., Y. Eguchi, N. Enomoto & J. Hojo, 2005. Synthesis of zeolite from coal fly ashes with different silica–alumina composition. *Fuel* 84(2-3):299-304.
Inflation, S. A., 2022. South African Inflation.
Itabashi, K., Y. Kamimura, K. Iyoki, A. Shimojima & T. Okubo, 2012. A working hypothesis for broadening framework types of zeolites in seed-assisted synthesis without organic structure-directing agent. *Journal of the American Chemical Society* 134(28):11542-11549.
Iyer, R., 2002. The surface chemistry of leaching coal fly ash. *Journal of Hazardous Materials* 93(3):321-329.
Izidoro, J. d. C., D. A. Fungaro, F. S. dos Santos & S. Wang, 2012. Characteristics of Brazilian coal fly ashes and their synthesized zeolites. *Fuel Processing Technology* 97:38-44.
Jacobs, P., E. M. Flanigen, J. Jansen & H. van Bekkum, 2001. Introduction to zeolite science and practice, 1 edn. Technology and Engineering
Jala, S. & D. Goyal, 2006. Fly ash as a soil ameliorant for improving crop production—a review. *Bioresource Technology* 97(9):1136-1147.
Jha, B. & D. Singh, 2011. A review on synthesis, characterization and industrial applications of flyash zeolites. *Journal of Materials Education* 33(1):65.
Jha, B. & D. N. Singh, 2016. Fly ash zeolites: innovations, applications, and directions, vol 78. Springer.
Ji, Y., H. Yang & W. Yan, 2017. Strategies to enhance the catalytic performance of ZSM-5 zeolite in hydrocarbon cracking: A review. *Catalysts* 7(12):367.
Juan, R., S. Hernández, J. M. Andrés & C. Ruiz, 2007. Synthesis of granular zeolitic materials with high cation exchange capacity from agglomerated coal fly ash. *Fuel* 86(12-13):1811-1821.
Julbe, A., J. Motuzas, F. Cazevielle, G. Volle & C. Guizard, 2003. Synthesis of sodalite/αAl2O3 composite membranes by microwave heating. *Separation and Purification Technology* 32(1-3):139-149.
Kadja, G. T., R. R. Mukti, Z. Liu, M. Rilyanti, I. N. Marsih, M. Ogura, T. Wakihara & T. Okubo, 2016. Mesoporogen-free synthesis of hierarchically porous ZSM-5 below 100° C. *Microporous and Mesoporous Materials* 226:344-352.
Kalyankar, A., A. Choudhari & A. Joshi, 2011. Low frequency dielectric properties of fly ash based zeolite ZSM-5. *IJBAS* 1:59-63.

Karimi, R., B. Bayati, N. C. Aghdam, M. Ejtemaee & A. A. Babaluo, 2012. Studies of the effect of synthesis parameters on ZSM-5 nanocrystalline material during template-hydrothermal synthesis in the presence of chelating agent. *Powder Technology* 229:229-236.

Kasture, M. W., V. V. Bokade & P. N. Joshi, 2005. Conversion of fly ash—an environmentally detrimental waste to zeolite beta (BEA) for commercial catalytic applications. *Journal of the American Ceramic Society* 88(11):3260-3263.

Kazemimoghadam, M. & T. Mohammadi, 2011. Preparation of nano pore hydroxysodalite zeolite membranes using of kaolin clay and chemical sources. *Desalination* 278(1-3):438-442.

Koike, N., K. Iyoki, B. Wang, Y. Yanaba, S. P. Elangovan, K. Itabashi, W. Chaikittisilp & T. Okubo, 2018. Increasing the ion-exchange capacity of MFI zeolites by introducing Zn to aluminosilicate frameworks. *Dalton Transactions* 47(28):9546-9553.

Kolay, P. & D. Singh, 2002. Characterization of an alkali activated lagoon ash and its application for heavy metal retention. *Fuel* 81(4):483-489.

Konno, H., T. Okamura, T. Kawahara, Y. Nakasaka, T. Tago & T. Masuda, 2012. Kinetics of n-hexane cracking over ZSM-5 zeolites–Effect of crystal size on effectiveness factor and catalyst lifetime. *Chemical Engineering Journal* 207:490-496.

Köroğlu, H. J., A. Sarıoğlan, M. Tatlıer, A. Erdem-Şenatalar & Ö. T. Savaşçı, 2002. Effects of low-temperature gel aging on the synthesis of zeolite Y at different alkalinities. *Journal of Crystal Growth* 241(4):481-488.

Kovo, A., 2012. Effect of temperature on the synthesis of zeolite X from Ahoko Nigerian kaolin using novel metakaolinization technique. *Chemical Engineering Communications* 199(6):786-797.

Kumar, N., V. Nieminen, K. Demirkan, T. Salmi, D. Y. Murzin & E. Laine, 2002. Effect of synthesis time and mode of stirring on physico-chemical and catalytic properties of ZSM-5 zeolite catalysts. *Applied Catalysis A: General* 235(1-2):113-123.

Larlus, O. & V. P. Valtchev, 2004. Crystal morphology control of LTL-type zeolite crystals. *Chemistry of Materials* 16(17):3381-3389.

Larlus, O. & V. P. Valtchev, 2005. Control of the morphology of all-silica BEA-type zeolite synthesized in basic media. *Chemistry of Materials* 17(4):881-886.

Lee, S.-R., Y.-H. Son, A. Julbe & J.-H. Choy, 2006. Vacuum seeding and secondary growth route to sodalite membrane. *Thin Solid Films* 495(1-2):92-96.

Li, J., X. Zeng, X. Yang, C. Wang & X. Luo, 2015. Synthesis of pure sodalite with wool ball morphology from alkali fusion kaolin. *Materials Letters* 161:157-159.

Li, Y. & W. Yang, 2008. Microwave synthesis of zeolite membranes: A review. *Journal of Membrane Science* 316(1-2):3-17.

Liu, S., P. Zhang, X. Meng, D. Liang, N. Xiao & F.-S. Xiao, 2010. Cesium-free synthesis of aluminosilicate RHO zeolite in the presence of cationic polymer. *Microporous and Mesoporous Materials* 132(3):352-356.

Liu, Y., F. Zeng, B. Sun, P. Jia & I. T. Graham, 2019. Structural characterizations of aluminosilicates in two types of fly ash samples from Shanxi Province, North China. *Minerals* 9(6):358.

Lv, G., Z. Li, W.-T. Jiang, C. Ackley, N. Fenske & N. Demarco, 2014. Removal of Cr (VI) from water using Fe (II)-modified natural zeolite. *Chemical Engineering Research and Design* 92(2):384-390.

Ma, M., M. Su, S. Li, F. Jiang & R. Li, 2018. Predicting coal consumption in South Africa based on linear (metabolic grey model), nonlinear (non-linear grey model), and combined (metabolic grey model-Autoregressive Integrated Moving Average Model) Models. *Sustainability* 10(7):2552.

Machado, N. R. C. F. & D. M. M. Miotto, 2005. Synthesis of Na–A and–X zeolites from oil shale ash. *Fuel* 84(18):2289-2294.

Madrid, R., C. Nogueira & F. Margarido, Production and characterisation of amorphous silica from rice husk waste. In: WasteEng'2012: Proceedings of the 4th International Conference on Engineering for Waste and Biomass Valorisation, 2012.

Madzivire, G., L. F. Petrik, W. M. Gitari, T. V. Ojumu & G. Balfour, 2010. Application of coal fly ash to circumneutral mine waters for the removal of sulphates as gypsum and ettringite. *Minerals Engineering* 23(3):252-257.

Mainganye, D., T. Ojumu & L. Petrik, 2013. Synthesis of zeolites Na-P1 from South African coal fly ash: effect of impeller design and agitation. *Materials* 6(5):2074-2089.

Mallapur, V. P. & J. U. K. Oubagaranadin, 2017. A brief review on the synthesis of zeolites from hazardous wastes. *Transactions of the Indian Ceramic Society* 76(1):1-13.
Manique, M. C., L. V. Lacerda, A. K. Alves & C. P. Bergmann, 2017. Biodiesel production using coal fly ash-derived sodalite as a heterogeneous catalyst. *Fuel* 190:268-273.
Matjie, R., J. Bunt & J. Van Heerden, 2005. Extraction of alumina from coal fly ash generated from a selected low rank bituminous South African coal. *Minerals Engineering* 18(3):299-310.
Medina, A., P. Gamero, J. M. Almanza, A. Vargas, A. Montoya, G. Vargas & M. Izquierdo, 2010. Fly ash from a Mexican mineral coal. II. Source of W zeolite and its effectiveness in arsenic (V) adsorption. *Journal of Hazardous Materials* 181(1-3):91-104.
Mewes, D., 1997. Chemical Engineering Design. vol 6. Wiley Online Library.
Mi, X., Z. Hou & X. Li, 2021. Controllable synthesis of nanoscaled ZSM-5 aggregates with multivariate channel under the synergistic effect of silicate-1 and TPABr using dual-silica source. *Microporous and Mesoporous Materials* 323:111224.
Miar Alipour, S., R. Halladj, S. Askari & E. BagheriSereshki, 2016. Low cost rapid route for hydrothermal synthesis of nano ZSM-5 with mixture of two, three and four structure directing agents. *Journal of Porous Materials* 23(1):145-155.
Missengue, R., 2016. Synthesis of ZSM-5 zeolite from South African fly ash and its application as solid catalyst. Research based (PhD) Thesis, University of the Western Cape
Missengue, R., P. Losch, N. Musyoka, B. Louis, P. Pale & L. Petrik, 2018. Conversion of South African coal fly ash into high-purity ZSM-5 zeolite without additional source of silica or alumina and its application as a methanol-to-olefins catalyst. *Catalysts* 8(4):124.
Missengue, R. N. M., P. Losch, G. Sedres, N. M. Musyoka, O. O. Fatoba, B. Louis, P. Pale & L. F. Petrik, 2017. Transformation of South African coal fly ash into ZSM-5 zeolite and its application as an MTO catalyst. *Comptes Rendus Chimie* 20(1):78-86.
Modhera, B., M. Chakraborty, P. Parikh & R. Jasra, 2009. Synthesis of nano-crystalline zeolite β: Effects of crystallization parameters. *Crystal Research and Technology: Journal of Experimental and Industrial Crystallography* 44(4):379-385.
Mohiuddin, E., Y. M. Isa, M. M. Mdleleni, N. Sincadu, D. Key & T. Tshabalala, 2016. Synthesis of ZSM-5 from impure and beneficiated Grahamstown kaolin: Effect of kaolinite content, crystallisation temperatures and time. *Applied Clay Science* 119:213-221.
Mohiuddin, E., M. M. Mdleleni & D. Key, 2018. Catalytic cracking of naphtha: The effect of Fe and Cr impregnated ZSM-5 on olefin selectivity. *Applied Petrochemical Research* 8(2):119-129.
Moisés, M. P., C. T. P. da Silva, J. G. Meneguin, E. M. Girotto & E. Radovanovic, 2013. Synthesis of zeolite NaA from sugarcane bagasse ash. *Materials Letters* 108:243-246.
Moliner, M., C. Franch, E. Palomares, M. Grill & A. Corma, 2012. Cu–SSZ-39, an active and hydrothermally stable catalyst for the selective catalytic reduction of NO x. *Chemical Communications* 48(66):8264-8266.
Mor, S., C. K. Manchanda, S. K. Kansal & K. Ravindra, 2017. Nanosilica extraction from processed agricultural residue using green technology. *Journal of Cleaner Production* 143:1284-1290.
Moreno, N., X. Querol, C. Ayora, C. F. Pereira & M. Janssen-Jurkovicová, 2001. Utilization of zeolites synthesized from coal fly ash for the purification of acid mine waters. *Environmental Science & Technology* 35(17):3526-3534.
Morsi, R. E. & R. S. Mohamed, 2018. Nanostructured mesoporous silica: influence of the preparation conditions on the physical-surface properties for efficient organic dye uptake. *Royal Society Open Science* 5(3):172021.
Mosca, A., O. Öhrman, J. Hedlund, I. Perdana & D. Creaser, 2009. NO2 and N2 sorption in MFI films with varying Si/Al and Na/Al ratios. *Microporous and Mesoporous Materials* 120(3):195-205.
Mousavi, S. F., M. Jafari, M. Kazemimoghadam & T. Mohammadi, 2013. Template free crystallization of zeolite Rho via Hydrothermal synthesis: Effects of synthesis time, synthesis temperature, water content and alkalinity. *Ceramics International* 39(6):7149-7158.
Mozgawa, W., M. Król, J. Dyczek & J. Deja, 2014. Investigation of the coal fly ashes using IR spectroscopy. *Spectrochimica Acta Part A: Molecular and Biomolecular Spectroscopy* 132:889-894.
Mukherjee, S. & S. K. Srivastava, 2006. Minerals transformations in northeastern region coals of India on heat treatment. *Energy & Fuels* 20(3):1089-1096.

Musyoka, N. M., L. F. Petrik, G. Balfour, W. M. Gitari & E. Hums, 2011. Synthesis of hydroxy sodalite from coal fly ash using waste industrial brine solution. *Journal of Environmental Science and Health, Part A* 46(14):1699-1707.

Musyoka, N. M., L. F. Petrik, W. M. Gitari, G. Balfour & E. Hums, 2012. Optimization of hydrothermal synthesis of pure phase zeolite Na-P1 from South African coal fly ashes. *Journal of Environmental Science and Health, Part A* 47(3):337-350.

Na, K. & G. A. Somorjai, 2015. Hierarchically nanoporous zeolites and their heterogeneous catalysis: current status and future perspectives. *Catalysis Letters* 145(1):193-213.

Nada, M. H., E. G. Gillan & S. C. Larsen, 2019. Mechanochemical reaction pathways in solvent-free synthesis of ZSM-5. *Microporous and Mesoporous Materials* 276:23-28.

Natusch, D., J. Wallace & C. Evans, 1974. Toxic trace elements: preferential concentration in respirable particles. *Science* 183(4121):202-204.

Ndlovu, N. Z., R. N. Missengue, L. F. Petrik & T. Ojumu, 2017. Synthesis and characterization of faujasite zeolite and geopolymer from South African coal fly ash. *Journal of Environmental Engineering* 143(9):04017042.

Ndlovu, N. Z. N., 2016. Synthesis of zeolite (ZSM-5 and Faujasite) and geopolymer from South African coal fly ash. Maters Thesis (Research), Cape Peninsula University of Technology.

Nishiyama, N., M. Miyamoto, Y. Egashira & K. Ueyama, 2001. Zeolite membrane on catalyst particles for selective formation of p-xylene in the disproportionation of toluene. *Chemical Communications*(18):1746-1747.

Novembre, D., D. Gimeno, A. Pasculli & B. Di Sabatino, 2010. Synthesis and characterization of sodalite using natural kaolinite: an analytical and mathematical approach to simulate the loss in weight of chlorine during the synthesis process. *Fresenius Environmental Bullettin* 19(6):1109-1117.

Nyale, S. M., O. O. Babajide, G. D. Birch, N. Böke & L. F. Petrik, 2013. Synthesis and characterization of coal fly ash-based foamed geopolymer. *Procedia Environmental Sciences* 18:722-730.

Ocampo, F., H.-S. Yun, M. M. Pereira, J.-P. Tessonnier & B. Louis, 2009. Design of MFI zeolite-based composites with hierarchical pore structure: a new generation of structured catalysts. *Crystal Growth and Design* 9(8):3721-3729.

Ojumu, T. V., P. W. Du Plessis & L. F. Petrik, 2016. Synthesis of zeolite A from coal fly ash using ultrasonic treatment–A replacement for fusion step. *Ultrasonics Sonochemistry* 31:342-349.

Oleksenko, L. P., V. K. Yatsimirsky, G. M. Telbiz & L. V. Lutsenko, 2004. Adsorption and catalytic properties of Co/ZSM-5 zeolite catalysts for CO oxidation. *Adsorption Science & Technology* 22(7):535-541.

Oleksiak, M. D. & J. D. Rimer, 2014. Synthesis of zeolites in the absence of organic structure-directing agents: factors governing crystal selection and polymorphism. *Reviews in Chemical Engineering* 30(1):1-49.

Oumi, Y., S. Nemoto, S. Nawata, T. Fukushima, T. Teranishi & T. Sano, 2003. Effect of the framework structure on the dealumination–realumination behavior of zeolite. *Materials Chemistry and Physics* 78(2):551-557.

Ozin, G. A., A. Kuperman & A. Stein, 1989. Advanced zeolite, materials science. *Angewandte Chemie International Edition in English* 28(3):359-376.

Palčić, A. & V. Valtchev, 2020. Analysis and control of acid sites in zeolites. *Applied Catalysis A: General* 606:117795.

Pan, F., X. Lu, Y. Wang, S. Chen, T. Wang & Y. Yan, 2014. Organic template-free synthesis of ZSM-5 zeolite from coal-series kaolinite. *Materials Letters* 115:5-8.

Panitchakarn, P., N. Laosiripojana, N. Viriya-Umpikul & P. Pavasant, 2014. Synthesis of high-purity Na-A and Na-X zeolite from coal fly ash. *Journal of the Air & Waste Management Association* 64(5):586-596.

Panpa, W. & S. Jinawath, 2009. Synthesis of ZSM-5 zeolite and silicalite from rice husk ash. *Applied Catalysis B: Environmental* 90(3-4):389-394.

Panzarella, B., G. A. Tompsett, K. S. Yngvesson & W. C. Conner, 2007. Microwave synthesis of zeolites. 2. Effect of vessel size, precursor volume, and irradiation method. *The Journal of Physical Chemistry B* 111(44):12657-12667.

Papaioannou, D., P. Katsoulos, N. Panousis & H. Karatzias, 2005. The role of natural and synthetic zeolites as feed additives on the prevention and/or the treatment of certain farm animal diseases: a review. *Microporous and Mesoporous Materials* 84(1-3):161-170.

Parikh, S. J. & J. Chorover, 2006. ATR-FTIR spectroscopy reveals bond formation during bacterial adhesion to iron oxide. *Langmuir* 22(20):8492-8500.
Passaglia, E. & R. A. Sheppard, 2001. The crystal chemistry of zeolites. *Reviews in Mineralogy and Geochemistry* 45(1):69-116.
Payscale, 2022. Average Chemical Engineer Salary in South Africa.
Petrik, L., 2009. The influence of cation, anion and water content on the rate of formation and pore size distribution of zeolite ZSM-5. *South African Journal of Science* 105(7):251-257.
Petrik, L., C. O'Connor & S. Schwarz, 1995. The influence of various synthesis parameters on the morphology and crystalsize of ZSM-5 and the relationship between morphology and crystal size and propene oligomerization activity. *Studies in Surface Science and Catalysis*:517-524.
Petushkov, A., S. Yoon & S. C. Larsen, 2011. Synthesis of hierarchical nanocrystalline ZSM-5 with controlled particle size and mesoporosity. *Microporous and Mesoporous Materials* 137(1-3):92-100.
Pfenninger, A., 1999. Manufacture and use of zeolites for adsorption processes Structures and Structure Determination. Springer, 163-198.
Praharaj, T. & G. Ray, 2001. Percutaneous transluminal coronary angioplasty with stenting of anomalous right coronary artery originating from left sinus of Valsalva using the Voda guiding catheter: a report of two cases. *Indian Heart Journal* 53(1):79-82.
Prasad, B. & R. J. Mortimer, 2011. Treatment of acid mine drainage using fly ash zeolite. *Water, Air, & Soil Pollution* 218(1):667-679.
Prasetyoko, D., N. Ayunanda, H. Fansuri, D. Hartanto & Z. Ramli, 2012. Phase transformation of rice husk ash in the synthesis of ZSM-5 without organic template. *J Math Fund Sci* 44:250-262.
Prasomsri, T., W. Jiao, S. Z. Weng & J. G. Martinez, 2015. Mesostructured zeolites: bridging the gap between zeolites and MCM-41. *Chemical Communications* 51(43):8900-8911.
Purnomo, C. W., C. Salim & H. Hinode, 2012. Synthesis of pure Na–X and Na–A zeolite from bagasse fly ash. *Microporous and Mesoporous Materials* 162:6-13.
Pushparaj, H., M. Ganesh, P. Muthiahpillai, M. Velayutham, P. Yong-Ki, W. C. Choi & H. T. Jang, 2013. Effects of crystallinity of ZSM-5 zeolite on para-selective tert-butylation of ethylbenzene. *Chinese Journal of Catalysis* 34(2):294-304.
Putri, R. L., 2017. Analysis Of Production Cost Calculations Using Process Costing Method In Suli Tofu Factory. *Ekonomika45: Jurnal Ilmiah Manajemen, Ekonomi Bisnis, Kewirausahaan* 5(1):6-13.
Querol, X., N. Moreno, J. t. Umaña, A. Alastuey, E. Hernández, A. Lopez-Soler & F. Plana, 2002. Synthesis of zeolites from coal fly ash: an overview. *International Journal of Coal Geology* 50(1-4):413-423.
Querol, X., F. Plana, A. Alastuey & A. López-Soler, 1997. Synthesis of Na-zeolites from fly ash. *Fuel* 76(8):793-799.
Querol, X., J. Umana, F. Plana, A. Alastuey, A. Lopez-Soler, A. Medinaceli, A. Valero, M. Domingo & E. Garcia-Rojo, 2001. Synthesis of zeolites from fly ash at pilot plant scale. Examples of potential applications. *Fuel* 80(6):857-865.
Ramesh, K. & D. D. Reddy, 2011. Zeolites and their potential uses in agriculture. *Advances in Agronomy* 113:219-241.
Rani, P., R. Srivastava & B. Satpati, 2016. One-step dual template mediated synthesis of nanocrystalline zeolites of different framework structures. *Crystal Growth & Design* 16(6):3323-3333.
Ren, N., J. Bronić, B. Subotić, X.-C. Lv, Z.-J. Yang & Y. Tang, 2011. Controllable and SDA-free synthesis of sub-micrometer sized zeolite ZSM-5. Part 1: Influence of alkalinity on the structural, particulate and chemical properties of the products. *Microporous and Mesoporous Materials* 139(1-3):197-206.
Robson, H., 2001. Verified synthesis of zeolitic materials. Gulf Professional Publishing.
Ruen-ngam, D., D. Rungsuk, R. Apiratikul & P. Pavasant, 2009. Zeolite formation from coal fly ash and its adsorption potential. *Journal of the Air & Waste Management Association* 59(10):1140-1147.
Rungsuk, D., R. Apiratikul, V. Pavarajarn & P. Pavasant, Zeolite synthesis from fly ash from coal-fired Power plant by fusion method. In: E-042 The 2nd Joint International Conference on “Sustainable Energy and Environment (SEE 2006)” Bangkok, Thailand, 2006. p 1-4.
Saikia, B. J. & G. Parthasarathy, 2010. Fourier transform infrared spectroscopic characterization of kaolinite from Assam and Meghalaya, Northeastern India. *J Mod Phys* 1(4):206-210.

.

Santos, J., Â. Barreto, J. Nogueira, A. L. Daniel-da-Silva, T. Trindade, M. J. Amorim & V. L. Maria, 2020. Effects of amorphous silica nanopowders on the avoidance behavior of five soil species—a screening study. *Nanomaterials* 10(3):402.

Sashkina, K. A., Z. Qi, W. Wu, A. B. Ayupov, A. I. Lysikov & E. V. Parkhomchuk, 2017. The effect of H2O/SiO2 ratio in precursor solution on the crystal size and morphology of zeolite ZSM-5. *Microporous and Mesoporous Materials* 244:93-100.

Schmidt, R., J. Prado-Gonjal & E. Morán, 2015. Microwave-assisted hydrothermal synthesis of nanoparticles. *CRC Concise Encyclopedia of Nanotechnology Boca Raton (USA): CRC Press Taylor & Francis Group*.

Scott, J., D. Guang, K. Naeramitmarnsuk, M. Thabuot & R. Amal, 2002. Zeolite synthesis from coal fly ash for the removal of lead ions from aqueous solution. *Journal of Chemical Technology & Biotechnology: International Research in Process, Environmental & Clean Technology* 77(1):63-69.

Sedres, G., 2016. Recovery of SiO_2 and Al_2O_3 from coal fly ash. Full Thesis, University of the Western Cape

Seidel, A., A. Sluszny, G. Shelef & Y. Zimmels, 1999. Self inhibition of aluminum leaching from coal fly ash by sulfuric acid. *Chemical Engineering Journal* 72(3):195-207.

Serrano, D. & P. Pizarro, 2013. Synthesis strategies in the search for hierarchical zeolites. *Chemical Society Reviews* 42(9):4004-4035.

Shabani, J. M., A. E. Ameh, O. Oyekola, O. O. Babajide & L. Petrik, 2022. Fusion-Assisted Hydrothermal Synthesis and Post-Synthesis Modification of Mesoporous Hydroxy Sodalite Zeolite Prepared from Waste Coal Fly Ash for Biodiesel Production. *Catalysts* 12(12):1652.

Shen, W., M. Zhou, W. Ma, J. Hu & Z. Cai, 2009. Investigation on the application of steel slag–fly ash–phosphogypsum solidified material as road base material. *Journal of Hazardous Materials* 164(1):99-104.

Shigemoto, N., H. Hayashi & K. Miyaura, 1993. Selective formation of Na-X zeolite from coal fly ash by fusion with sodium hydroxide prior to hydrothermal reaction. *Journal of Materials Science* 28(17):4781-4786.

Shirazi, L., E. Jamshidi & M. Ghasemi, 2008. The effect of Si/Al ratio of ZSM-5 zeolite on its morphology, acidity and crystal size. *Crystal Research and Technology: Journal of Experimental and Industrial Crystallography* 43(12):1300-1306.

Shirazian, S., S. Ghafarnejad Parto & S. N. Ashrafizadeh, 2014. Effect of water content of synthetic hydrogel on dehydration performance of nanoporous LTA zeolite membranes. *International Journal of Applied Ceramic Technology* 11(5):793-803.

Sibanda, V., S. Ndlovu, G. Dombo, A. Shemi & M. Rampou, 2016. Towards the utilization of fly ash as a feedstock for smelter grade alumina production: a review of the developments. *Journal of Sustainable Metallurgy* 2(2):167-184.

Silva, A. V., L. S. Miranda, M. Nele, B. Louis & M. M. Pereira, 2016. Insights to achieve a better control of silicon-aluminum ratio and ZSM-5 zeolite crystal morphology through the assistance of biomass. *Catalysts* 6(2):30.

Singh, R. & P. K. Dutta, 2003. MFI: A case study of zeolite synthesis Handbook of Zeolite Science and Technology. CRC Press, 25-79.

Sinnott, R. & G. Towler, 2019. Chemical engineering design: SI Edition. Butterworth-Heinemann.

Song, W., R. Justice, C. Jones, V. Grassian & S. Larsen, 2004. Synthesis, characterization, and adsorption properties of nanocrystalline ZSM-5. *Langmuir* 20(19):8301-8306.

Srinivasan, A. & M. W. Grutzeck, 1999. The adsorption of SO2 by zeolites synthesized from fly ash. *Environmental Science & Technology* 33(9):1464-1469.

Tauanov, Z., P. Tsakiridis, D. Shah & V. Inglezakis, 2019. Synthetic sodalite doped with silver nanoparticles: Characterization and mercury (II) removal from aqueous solutions. *Journal of Environmental Science and Health, Part A* 54(9):951-959.

Thommes, M., K. Kaneko, A. V. Neimark, J. P. Olivier, F. Rodriguez-Reinoso, J. Rouquerol & K. S. Sing, 2015. Physisorption of gases, with special reference to the evaluation of surface area and pore size distribution (IUPAC Technical Report). *Pure and Applied Chemistry* 87(9-10):1051-1069.

Treacy, M. M. & J. B. Higgins, 2007. Collection of simulated XRD powder patterns for zeolites fifth (5th) revised edition edn. Structure Commission of the International Zeolite Association

Triantafillidis, C. S., A. G. Vlessidis, L. Nalbandian & N. P. Evmiridis, 2001. Effect of the degree and type of the dealumination method on the structural, compositional and acidic characteristics of H-ZSM-5 zeolites. *Microporous and Mesoporous Materials* 47(2-3):369-388.
Trigueiro, F., D. Monteiro, F. Zotin & E. F. Sousa-Aguiar, 2002. Thermal stability of Y zeolites containing different rare earth cations. *Journal of Alloys and Compounds* 344(1-2):337-341.
Vaičiukyniene, D., K. Baltakys & A. Kantautas, 2009. Hydrosodalite ion exchange in saturated Ca (OH) 2 solution. *Materials Science-Poland* 27(2).
Valdés, M. G., A. Perez-Cordoves & M. Diaz-Garcia, 2006. Zeolites and zeolite-based materials in analytical chemistry. *TrAC Trends in Analytical Chemistry* 25(1):24-30.
Valeev, D., A. Mikhailova & A. Atmadzhidi, 2018. Kinetics of iron extraction from coal fly ash by hydrochloric acid leaching. *Metals* 8(7):533.
van Amsterdam, M., 1918. Factorial techniques applied in chemical plant cost estimation: A comparative study based on literature and cases. TU Delft.
Van Niekerk, A., 2005. Direct crystallisation of hydroxysodalite and MFI membranes on α-alumina supports. North-West University.
Vempati, R. K., R. Borade, R. S. Hegde & S. Komarneni, 2006. Template free ZSM-5 from siliceous rice hull ash with varying C contents. *Microporous and Mesoporous Materials* 93(1-3):134-140.
Viswanadham, N., G. M. Dhar & T. P. Rao, 1997. Pore size analysis of ZSM-5 catalysts used in n-heptane aromatization reaction: an evidence for molecular traffic control (MTC) mechanism. *Journal of Molecular Catalysis A: Chemical* 125(2-3):L87-L90.
Viswanadham, N., R. Kamble, M. Singh, M. Kumar & G. M. Dhar, 2009. Catalytic properties of nano-sized ZSM-5 aggregates. *Catalysis Today* 141(1-2):182-186.
Vom Berg, W., Utilization of fly ash in Europe. In: Proc of Int Conf on Fly ash disposal and utilization, 1998. vol 1. p 8-14.
Walton, J. L. S. T. G. & J. Sorrels, 2017. Cost Estimation: Concepts and Methodology. *Air Economics Group, Health and Environmental Impacts Division* 1:8e14.
Wan, Z., W. Wu, G. K. Li, C. Wang, H. Yang & D. Zhang, 2016. Effect of SiO2/Al2O3 ratio on the performance of nanocrystal ZSM-5 zeolite catalysts in methanol to gasoline conversion. *Applied Catalysis A: General* 523:312-320.
Wang, C.-F., J.-S. Li, L.-J. Wang & X.-Y. Sun, 2008. Influence of NaOH concentrations on synthesis of pure-form zeolite A from fly ash using two-stage method. *Journal of Hazardous Materials* 155(1-2):58-64.
Wang, L., Y. Wang, L. Cui, J. Gao, Y. Guo & F. Cheng, 2020. A sustainable approach for advanced removal of iron from CFA sulfuric acid leach liquor by solvent extraction with P507. *Separation and Purification Technology* 251:117371.
Wang, X., X. Hu, C. Song, K. W. Lux, M. Namazian & T. Imam, 2017. Oligomerization of biomass-derived light olefins to liquid fuel: Effect of alkali treatment on the HZSM-5 catalyst. *Industrial & Engineering Chemistry Research* 56(42):12046-12055.
Wdowin, M., M. Franus, R. Panek, L. Badura & W. Franus, 2014. The conversion technology of fly ash into zeolites. *Clean Technologies and Environmental Policy* 16(6):1217-1223.
Weckhuysen, B. M. & J. Yu, 2015. Recent advances in zeolite chemistry and catalysis. *Chemical Society Reviews* 44(20):7022-7024.
Wei, Q., P. Zhang, X. Liu, W. Huang, X. Fan, Y. Yan, R. Zhang, L. Wang & Y. Zhou, 2020. Synthesis of Ni-modified ZSM-5 zeolites and their catalytic performance in n-octane hydroconversion. *Frontiers in Chemistry* 8:586445.
Weitkamp, J., 2000. Zeolites and catalysis. *Solid State Ionics* 131(1-2):175-188.
Widayat, W. & A. Annisa, Synthesis and characterization of ZSM-5 catalyst at different temperatures. In: IOP Conference Series: Materials Science and Engineering, 2017. vol 214. IOP Publishing, p 012032.
Woolery, G., G. Kuehl, H. Timken, A. Chester & J. Vartuli, 1997. On the nature of framework Brønsted and Lewis acid sites in ZSM-5. *Zeolites* 19(4):288-296.
Wright, P. A. & M. Lozinska, Structural Chemistry and Properties of zeolites. In: Martínez, C. & J. Pérez-Pariente (eds) 5th Internation Feza Conference, Valencia Spain, 2011. p 1.
Wu, C.-y., H.-f. Yu & H.-f. Zhang, 2012. Extraction of aluminum by pressure acid-leaching method from coal fly ash. *Transactions of Nonferrous Metals Society of China* 22(9):2282-2288.

.

Xu, H., J. Van Deventer & G. Lukey, 2001. Effect of alkali metals on the preferential geopolymerization of stilbite/kaolinite mixtures. *Industrial & Engineering Chemistry Research* 40(17):3749-3756.

Xu, J., J. Sun, Y. Wang, J. Sheng, F. Wang & M. Sun, 2014. Application of iron magnetic nanoparticles in protein immobilization. *Molecules* 19(8):11465-11486.

Xue, Q.-f. & S.-g. Lu, 2008. Microstructure of ferrospheres in fly ashes: SEM, EDX and ESEM analysis. *Journal of Zhejiang University-Science A* 9(11):1595-1600.

Xue, T., Y. M. Wang & M.-Y. He, 2012. Synthesis of ultra-high-silica ZSM-5 zeolites with tunable crystal sizes. *Solid State Sciences* 14(4):409-418.

Yang, X.-Y., L.-H. Chen, Y. Li, J. C. Rooke, C. Sanchez & B.-L. Su, 2017. Hierarchically porous materials: synthesis strategies and structure design. *Chemical Society Reviews* 46(2):481-558.

Yao, J., H. Wang, K. R. Ratinac & S. P. Ringer, 2006. Formation of colloidal hydroxy-sodalite nanocrystals by the direct transformation of silicalite nanocrystals. *Chemistry of Materials* 18(6):1394-1396.

Yao, Z., X. Ji, P. Sarker, J. Tang, L. Ge, M. Xia & Y. Xi, 2015. A comprehensive review on the applications of coal fly ash. *Earth-Science Reviews* 141:105-121.

Yao, Z., M. Xia, Y. Ye & L. Zhang, 2009. Synthesis of zeolite Li-ABW from fly ash by fusion method. *Journal of Hazardous Materials* 170(2-3):639-644.

Yu, J., 2007. Synthesis of zeolites. *Introduction to Zeolite Science and Practice* 168:39.

Yuvakkumar, R., A. J. Nathanael, V. Rajendran & S. Hong, 2014. Rice husk ash nanosilica to inhibit human breast cancer cell line (3T3). *Journal of Sol-Gel Science and Technology* 72(1):198-205.

Zhang, C., Q. Liu, Z. Xu & K. Wan, 2003. Synthesis and characterization of composite molecular sieves with mesoporous and microporous structure from ZSM-5 zeolites by heat treatment. *Microporous and Mesoporous Materials* 62(3):157-163.

Zhang, K., Z. Liu, X. Yan, X. Hao, M. Wang, C. Li & H. Xi, 2017. In situ assembly of nanoparticles into hierarchical Beta zeolite with tailored simple organic molecule. *Langmuir* 33(50):14396-14404.

Zhang, K. & M. L. Ostraat, 2016. Innovations in hierarchical zeolite synthesis. *Catalysis Today* 264:3-15.

Zhang, L., S. Xie, W. Xin, X. Li, S. Liu & L. Xu, 2011. Crystallization and morphology of mordenite zeolite influenced by various parameters in organic-free synthesis. *Materials Research Bulletin* 46(6):894-900.

Zhang, X., D. Tang & G. Jiang, 2013. Synthesis of zeolite NaA at room temperature: The effect of synthesis parameters on crystal size and its size distribution. *Advanced Powder Technology* 24(3):689-696.

Zhu, M., R. Ji, Z. Li, H. Wang, L. Liu & Z. Zhang, 2016. Preparation of glass ceramic foams for thermal insulation applications from coal fly ash and waste glass. *Construction and Building Materials* 112:398-405.

.

Website based references:

Payscale.2022. Average Chemical Engineer Salary in South Africa. Chemical Engineer Salary in South Africa | PayScale. [22 June 2022].

SA Inflation. 2022. South African Inflation. https://inflationcalc.co.za/?date1=2004-06-01&date2=2022-06-24&amount=136462.7565. [24 June 2022]

World Data. 2022. Development of inflation rates in South Africa. https://www.worlddata.info/africa/south-africa/inflation-rates.php#:~:text=The%20inflation%20rate%20for%20consumer,rate%20was%207.9%25%20per%20year. [29 June 2022]

.